



The
University
Of
Sheffield.

**The evolution and development of structural colour in *Heliconius*
butterflies**

Victoria Jayne Lloyd

A thesis submitted in partial fulfilment of the requirement for the degree of Doctor of
Philosophy

The University of Sheffield
Faculty of Science
Department of Biosciences

Submission Date
September 2022

Declaration

The work presented in this thesis was performed at the University of Sheffield between October 2018 and September 2022 under the supervision of Dr. Nicola Nadeau. Unless stated otherwise, the work is that of the author. No part of this thesis has previously been submitted for a degree or any other qualification at this University or any other institution.

Victoria Lloyd

September 2022

Abstract

In nature, nanostructures can interact with light to produce a striking array of colours called structural colours. Such colours have gained considerable attention in evolutionary biology and, more recently, as potential routes for the design of advanced optical materials. Vivid examples of structural colour are found in butterflies, resulting from the modification of their wing scales to contain optically precise nanostructures. In *Heliconius*, such optical nanostructures take the form of multilayer reflectors on the cuticle scale ridges which reflect light through constructive interference. While structural colours in *Heliconius* have been characterised optically, their underlying development remains unknown. Throughout this thesis, I explore the development of structural colour in *Heliconius*, both in terms of the cellular processes guiding the precise formation of the multilayer reflectors as well as the underlying genetic control.

Using high-resolution microscopy and perturbation experiments, I demonstrate a crucial role of the actin cytoskeleton in the development of optical nanostructures in *Heliconius sara*. In addition, I reveal a previously undescribed network of actin in developing butterfly scale cells which forms at the time of optical nanostructure formation. I then use differential expression analysis between structurally coloured and non-structurally coloured subspecies of *Heliconius erato* and *Heliconius melpomene* to reveal a number of candidate genes that may control optical nanostructure formation. Furthermore, I reveal a lack of convergence in the genes controlling structural colour development in *Heliconius*. Finally, I demonstrate the development of structural colour in *Heliconius* is subject to environmental influences, specifically dietary stress. This thesis lays the foundation for investigations into the study of structural colour development in diverse butterfly species.

Acknowledgments

I extend my most sincere gratitude to my supervisor, Dr. Nicola Nadeau, whose support and encouragement has been absolutely invaluable over the last four years. I could not have asked for better supervision undertaking this PhD and I am forever grateful for the opportunity to work together. I truly appreciated the freedom to ask my own questions and the unwavering support the entire way.

I also thank my second supervisor, Dr. Andrew Parnell. His enthusiasms and passion for the subject has given me a great determination going forward beyond my PhD. I thank him for the selfless dedication of time to my project and for guiding me through the physics of structural colour. His unfaltering support and dedication have truly helped make this project cross-disciplinary.

I thank my past and present lab colleagues, who became good friends along the way, particularly Dr. Melanie Brien, Dr. Juan Enciso-Romero and Angel Nguyen. Thank you for keeping me grounded throughout these last four years and for generously offering your time, whether it was painstaking Linux scripting or just a cup of tea and a biscuit – I always appreciated it.

This project would not have possible without the support of numerous people within the Biosciences and Physics department, who are too many to name individually. I thank the lab technicians and staff who supported this project, particularly those at the Arthur Willis Environment Centre involved with keeping the population of *Heliconius* butterflies going, even in the most difficult of circumstances.

I thank my parents, to whom this thesis is dedicated to. I thank my father, who took me on many wonderful adventures all over the world and gave me the opportunities which he never had growing up. Our journeys together have served as a constant source of inspiration and joy in my studies of the natural world. Equally I thank my mother, for not only showing me the strength and fortitude of women but also for enduring my menagerie of animals over the years - even when it meant sharing a house with numerous geese and a rhea. I am forever indebted to you both.

Last but certainly not least I thank my fiancé, Lewis. I do not think he imagined that when I told him I was going to study biology at the University of Sheffield that I would still be there eight years later. Thank you for always being my rock.

Table of Contents

Chapter 1

General introduction	10
<i>Structural colour in the natural world</i>	10
<i>The scale as a unit of colour in butterflies.....</i>	13
<i>The model: Heliconius butterflies</i>	20
Thesis rationale	26
Research summary	27
<i>Chapter 2 summary</i>	27
<i>Chapter 3 summary</i>	27
<i>Chapter 4 summary</i>	28
<i>Chapter 5 summary</i>	29
<i>Chapter 6 summary</i>	30

Chapter 2

The evolution and development of structural colour in butterflies	31
Author contributions	31
Abstract	32
Keywords	32
Introduction	32
Surface nanostructures – ridge reflectors.....	35
Lower lamina reflectors.....	37
Internal nanostructures – lumen multilayers and photonic crystals.....	40
Beyond butterflies – evolutionary insights from other systems.....	41
Conclusions.....	42
Acknowledgments	43
Supplementary information	44

Chapter 3

The actin cytoskeleton plays an essential role in structural color formation in <i>Heliconius sara</i> butterflies.....	46
Author contributions	47
Abstract	48
Significance statement.....	48
Introduction	49
Results	51
<i>Development of H. sara scales.....</i>	54
<i>F-actin patterning differs between developing iridescent and non-iridescent scales.....</i>	57
<i>TauSTED super-resolution microscopy reveals detailed remodelling of the actin cytoskeleton</i>	58
<i>The actin cytoskeleton plays a direct role in optical nanostructure formation.....</i>	61
Discussion	65
<i>Conclusion</i>	69
Materials and Methods	69
<i>Butterfly rearing</i>	69
<i>Electron Microscopy.....</i>	69
<i>Scanning electron microscopy (SEM).....</i>	70
<i>Transmission electron microscopy (TEM).....</i>	70
<i>Atomic force microscopy (AFM).....</i>	70
<i>Synchrotron X-ray nanotomography.....</i>	71
<i>Immunofluorescence.....</i>	71

<i>Confocal microscopy</i>	72
<i>TauSTED microscopy</i>	72
<i>Comparative analyses of iridescent and non-iridescent scales</i>	72
<i>SEM Analysis of adult scale H. sara morphology</i>	72
<i>SEM Analysis of adult Heliconius erato demophoon scale morphology</i>	73
<i>Confocal analysis of actin in developing scales</i>	73
<i>Statistical analyses</i>	74
<i>Chemical perturbation of actin</i>	75
<i>Reflectance spectroscopy</i>	76
<i>Phenotypic analyses of actin perturbation</i>	76
Acknowledgments	77
Supplementary information	78
<i>Supplementary results</i>	78
<i>Supplementary figures</i>	79

Chapter 4

Differential expression analysis reveals the genetic basis of iridescent structural colour in

<i>Heliconius butterflies</i>	93
Author contributions	94
Abstract	95
Keywords	96
Introduction	96
Methods	101
<i>Animal husbandry</i>	101
<i>RNA extraction, library preparation and sequencing</i>	102
<i>Filtering, alignment and assembly</i>	102
<i>Differential expression analysis</i>	103
<i>Functional annotation</i>	104
<i>Overlap of genes between the androconial and iridescent wing regions in iridescent species</i> . 104	
<i>Gene Set Enrichment Analysis (GSEA)</i>	105
<i>Overlap of differentially expressed genes with Quantitative Trait Loci (QTL)</i>	105
<i>Overlap of differentially expressed genes with bristle (chaeta) and cuticle development genes...</i>	
.....	106
<i>Identification of convergent differentially expressed genes</i>	107
<i>Identification of candidate genes</i>	107
<i>Immunofluorescence</i>	108
<i>Confocal microscopy</i>	109
Results	110
<i>Differential expression</i>	110
<i>Gene set enrichment analysis</i>	114
<i>Narrowing down candidate genes</i>	116
<i>Overlap of differentially expressed genes with QTL</i>	116
<i>Overlap with Drosophila bristle genes</i>	120
<i>Overlap with cuticle development genes</i>	121
<i>Convergent genes in Heliconius</i>	122
<i>Candidate gene identification and immunofluorescent staining</i>	123
Discussion	128
<i>Conclusion</i>	131
Acknowledgments	132
Supplementary information	133

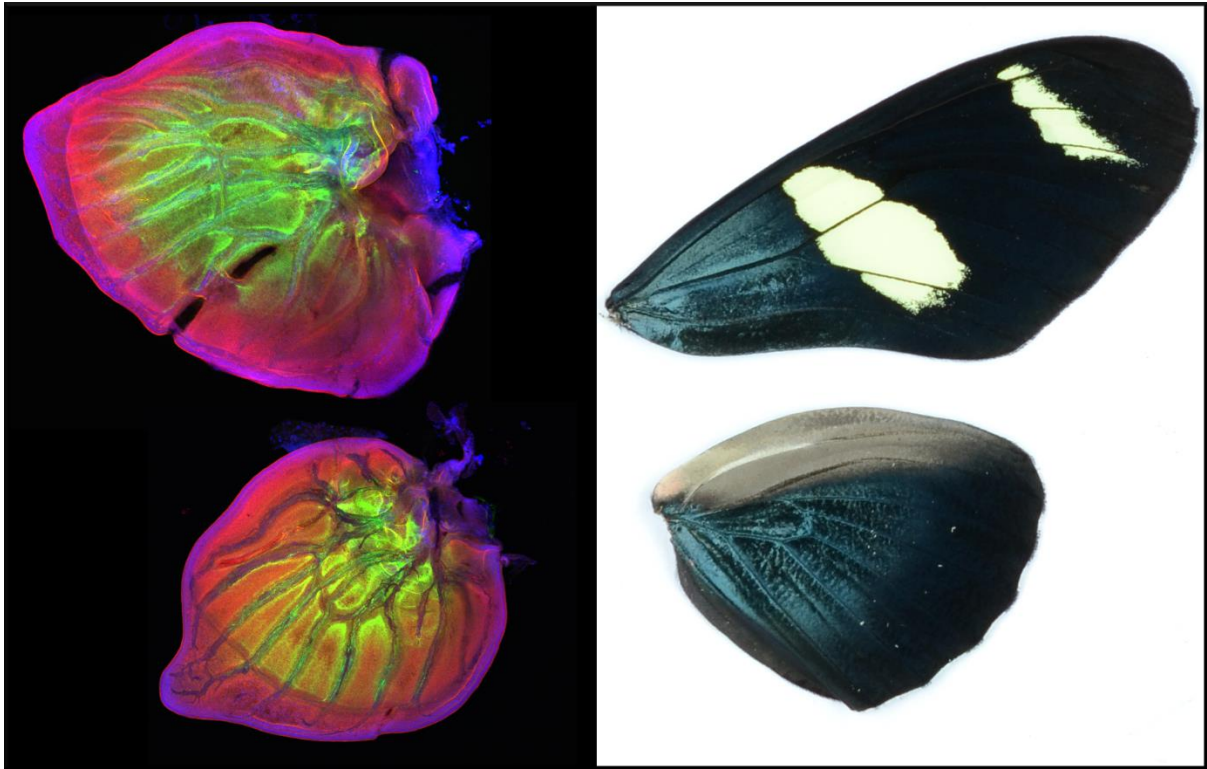
Chapter 5

Impact of dietary stress on the development of structural colour in the butterfly *Heliconius*

<i>sara</i>	173
Author contributions	173
Abstract	174
Keywords	175
Introduction	175
Materials and methods	179
<i>Butterfly husbandry</i>	179
<i>Diet manipulation</i>	180
<i>Leaf chemistry</i>	181
<i>Digital imaging</i>	181
<i>Wing area analysis</i>	181
<i>Colour area analysis</i>	182
<i>Reflectance spectrometry</i>	183
<i>Atomic force microscopy (AFM)</i>	185
<i>Transmission Electron Microscopy (TEM)</i>	185
<i>Scanning Electron Microscopy (SEM)</i>	186
<i>Structural analysis</i>	186
<i>Optical modelling</i>	187
Results	189
<i>Diet Manipulation and leaf chemistry</i>	189
<i>Impacts of dietary stress on development and size</i>	190
<i>Impacts of dietary stress on wing colouration</i>	193
<i>Iridescent area</i>	193
<i>Reflectance of iridescent blue</i>	193
<i>Angular variation</i>	194
<i>Impact of diet on pigmentary colouration</i>	196
<i>Structural analysis</i>	198
<i>Optical modelling</i>	201
<i>Reduction in reflectance</i>	203
<i>Shift in hue to shorter wavelengths</i>	205
Discussion	208
<i>Conclusion</i>	213
Acknowledgments	214
Supplementary Tables, Figures and Information	215
<i>Supplementary information: Thin-film interference, multilayers and simulating the optical properties of Heliconius sara</i>	226

Chapter 6

General Discussion	232
<i>Research summary</i>	232
<i>A broader insight into optical nanostructure development</i>	235
<i>Convergence in structural colour formation</i>	238
<i>Future directions and challenges</i>	240
<i>Conclusion</i>	244
References	246
Appendix	267



The developing and adult wings of *Heliconius sara*.

Left: Final-instar larval wing of *Heliconius sara* stained with Anti-notch (red), Phalloidin (green) and DAPI (blue). Imaged with a Nikon A1 confocal microscope.

Right: Adult wing of a male *Heliconius sara* bred at the University of Sheffield. Imaged with a fix mounted Nikon DSLR camera.

Chapter 1

General Introduction

Structural colour in the natural world

Vivid structural colours are the result of light interacting with nanostructures within an animals or plants integument (Kinoshita, 2008). Such colours are the governed by physical processes such as diffraction and interference, as oppose to pigments which use chemicals to selectively absorb specific wavelengths of light (Kinoshita, 2008; Thayer et al., 2020). Robert Hooke (1665) presented the first microscopic explorations of structural colour in the Peacock feather (Hooke, 1665). Despite early observations it was several centuries before full appreciation of these structures. The advent of electron microscopy and the superior resolution which it permitted paved the way for revolutionary new insights. Anderson and Richards (1942) presented the first detailed optical characterisations of beetles and butterfly photonic architectures (Anderson and Richards, 1942). Structural colours have since been described in numerous taxa including plants, fish, insects and birds (Kinoshita, 2008)(Figure 1).

Structural colours have generated much interest from an evolutionary perspective, including their role in sexual selection (reviewed in Doucet and Meadows, 2009) as well as investigations into the underlying genetic basis (Brien et al., 2022; Thayer et al., 2020). Examination of the fossil record points to an evolution of structural colour half a billion years ago (Parker, 2000). Throughout this long evolutionary history structural colouration has evolved diverse functions, including thermoregulation (Shi et al., 2015), camouflage (Kjernsmo et al., 2020; Wilts et al., 2012), sexual signalling (Kemp, 2007) and warning colouration (Waldron et al., 2017). More recently the appreciation of structural colours has broadened beyond an evolutionary

perspective towards application-based approaches (Barrows and Bartl, 2014). Replicating such structures is at the forefront of numerous technologies including paints (Saito, 2011), textiles (Chen et al., 2021), tactile sensors (Zhu et al., 2019) and solar cell technologies (Siddique et al., 2017). However, while human-replicated technologies often use sophisticated and energy-demanding materials such as metal oxide layers (Chen et al., 2011b, 2011a; Zhang et al., 2006), natural systems harness common biopolymers, such as keratin and chitin. Furthermore, natural systems encompass a degree of disorder while still maintaining coherent scattering mechanisms (Zhang and Chen, 2015). An understanding of how such natural photonic structures develop will lay the groundwork for future attempts to replicate such structures. Given the current climate crisis, exploring novel bio-inspired technological approaches to answer energy-harvesting challenges has never been so imperative.

Insects display prominent examples of structural colour. For example, the iridescent blue *Morpho* butterfly is visible from an aircraft, demonstrating the power of structural colours as long-range visual signals (Silberglied, 1984). Nevertheless, structural colours can also represent a mechanism to blend in; for example, the shiny elytra of Jewel beetles helps them camouflage by making them appear inconspicuous on the glossy surface of a leaf (Kjernsmo et al., 2020). As such the function of structural colours cannot always be assumed by their visual appearance alone without an appreciation of the underlying ecological context (for a review of functions see Doucet and Meadows, (2009).

Structural colouration can be broadly categorised into coherent and incoherent scattering (Prum et al., 2006). Incoherent scattering manifests from light scattering structures that are randomly distributed (and commensurate to the size of the wavelength of light) such that the phases of the scattered waves are not correlated e.g., the blue colour of some Amphibians (Bagnara et al., 2007; Prum et al., 2006; Sun et al., 2013). In contrast and more frequently observed in insects is coherent scattering. Coherent scattering requires structures that have

spatial variation in the refractive index which is periodic and therefore scattered waves have correlated phases (Prum et al., 2006). Diverse butterfly scale optical structures (e.g. thin films, photonic crystals and multilayer reflectors) function by coherent scattering (discussed in Prum et al., (2006)). A common feature of coherent scattering is iridescence, in which the hue or intensity of light changes depending on the angle of incoming light or observation (Doucet and Meadows, 2009; Prum et al., 2006). Overall, underlying all these structural colour mechanisms in insects is a recurrent theme, involving a manipulation of the cuticle to form a layer (or layers) capable of light reflection (Ghiradella, 2010; Ghiradella and Butler, 2009).

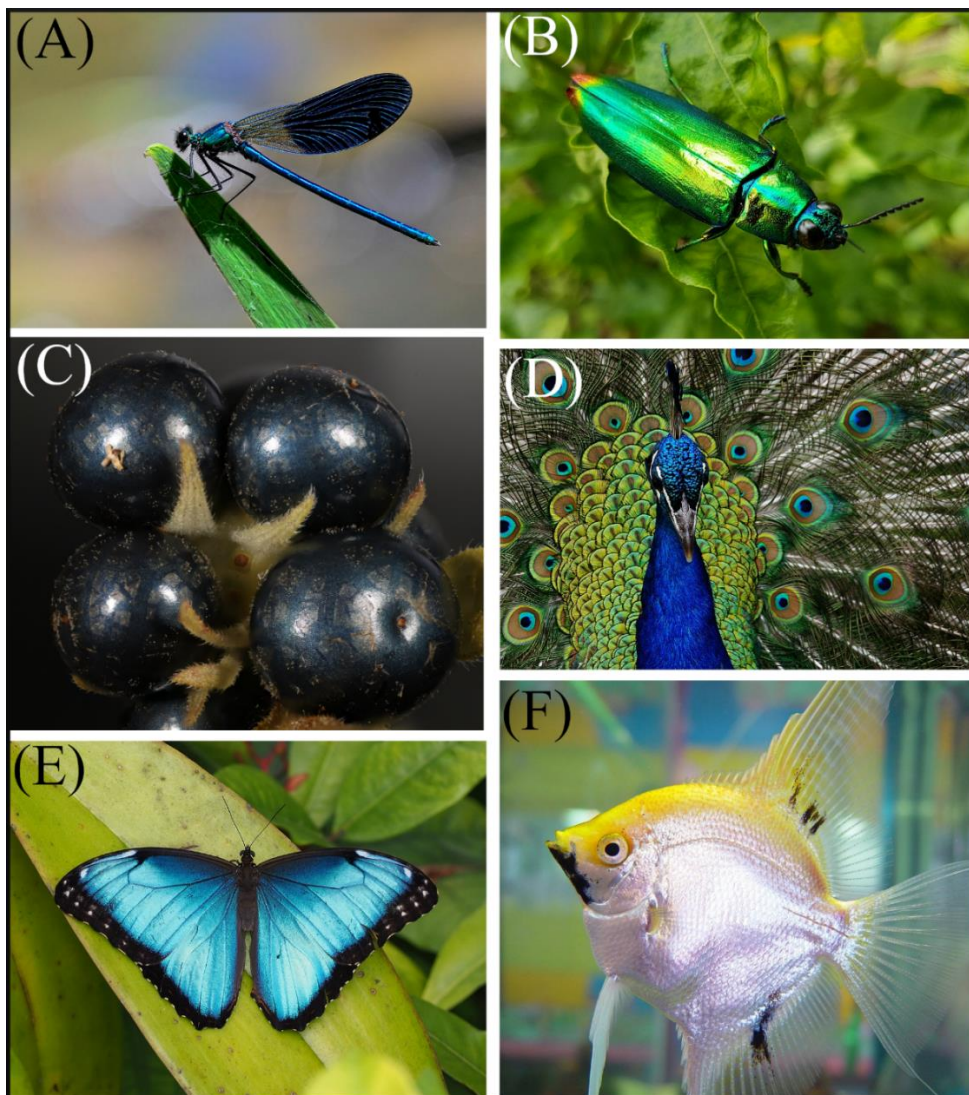


Figure 1. A diversity of structural colour in nature. (A) Blue iridescent colour of a Damselfly (Zygoptera). (B) Shiny elytron of a Jewel beetle (Coleoptera). (C) Iridescent berries of a lantana plant (Lamiales). (D) Elaborate display of a male Peacock (Galliformes). (E) The vivid flash of *Morpho helenor* (Lepidoptera). (F) Silvery scales of an Angelfish (Cichliformes). Image credits: (A) Frayle (B) Obsidian Soul (C) Paul Richards (D) Bernard Spragg, NZ (E) Nosferattus (F) Leon Brooks. All images except (C) were obtained from Wikimedia and made available under a Creative Commons CC0 1.0 Universal Public Domain Dedication license or released without license into the public domain (F).

The scale as a unit of colour in butterflies

Lepidoptera possess scales on their wings, which sit in a regular array, comparable to tiles on a roof (Figure 2). The scale is empty cuticle skeleton which is predominantly composed of the polysaccharide chitin, but also contains proteins, lipids and pigments (Moussian, 2010). A typical scale has a flat undifferentiated lower layer and an elaborate upper layer consisting of parallel ridges connected perpendicularly at regular intervals by struts of cuticle, known as crossribs. Supporting pillars of cuticle, called trabeculae, extend into the scale lumen (Figure 2) (Ghiradella, 1991; Nijhout, 1991). Scales assist in several functions, such as aerodynamic flight (Slegers et al., 2017) and wing hydrophobicity (Chen et al., 2004), but they are predominantly utilised as sources of colour for the wing. A huge diversity of scale morphologies has evolved through tweaking of the microstructural elements and these are associated with various pigmentary and nanostructural colours (Ghiradella and Butler, 2009; Nijhout, 1991). A detailed review exploring the evolutionary genetics and development of structural colour in butterflies and other systems is presented in Chapter 2.

Wing scales develop from single epidermal cells. Division of a sensory organ precursor (SOP) cell leads to several daughter cells, one of which becomes the future scale and another forms the socket which anchors the scale into the wing. SOPs are the developmental origin of several insect structures, including chemosensory bristles and chordotonal organs, and cell identity is guided by a suite of early specification genes (Blochlinger et al., 1991; Ghiradella, 2010).

Final scale morphology is determined by numerous factors. Pigmentation of the scale is associated with microstructure (ridges, crossribs, microribs) patterning (Liu et al., 2021; Matsuoka and Monteiro, 2018). Knockouts of melanin pathway genes in *Bicyclus anyana* by Matsuoka and Monteiro (2018) resulted in structural changes to the wing scale, demonstrating an association between pigments and the underlying structure (Matsuoka and Monteiro, 2018). Fluorescent microscopy of developing scales demonstrated the importance of the actin cytoskeleton in controlling scale cell shape; driving both the elongation of the scale cells along the proximal-distal axis as well as positioning the cuticle ridges on the scale surface (Day et al., 2019; Dinwiddie et al., 2014). Comparisons between structurally coloured and non-structurally coloured scales suggests variation in actin patterning may contribute to optical nanostructure formation (Dinwiddie et al., 2014). Furthermore, recent work by Liu et al., (2021) suggests cuticle proteins within the scale are vital for the patterning of scale microstructural elements. Knockouts of several cuticle proteins in *Bombyx mori* led to significant alterations to the ridge and crossrib architecture (Liu et al., 2021).

Despite these inroads, much of the process of scale development remains unknown; both in terms of cellular development as well as the regulatory network directly controlling the cellular effectors underpinning scale formation (Smith et al., 2018). From a developmental and mechanistic perspective, the scale cell requires a close association between the membrane, actin cytoskeleton and cuticle (Ghiradella, 2010, 1974). How these cellular components

interact together remains poorly understood; for example, how the membrane protrudes from between the actin bundles prior to ridge formation and how the cuticle ridges are shaped during deposition – particularly in systems where the ridges form optical nanostructures. As is common in the field of Evolutionary Development (Evo Devo) insights can be gleaned from comparisons with homologous structures. The bristles of *Drosophila* are a well characterised homologous structure to butterfly scales (Zhou et al., 2009). Gene knockouts, histochemical analyses and chemical perturbations, particularly those performed by Tilney (Tilney et al., 2003, 2000a, 2000b, 1998, 1996, 1995; Tilney and DeRosier, 2005) and Adler (Adler, 2019; Fei et al., 2002; Nagaraj and Adler, 2012), led to advancements in the understanding of actin dynamics, cell polarisation and cuticle deposition. Nagaraj and Adler (2012) showed that Zona pellucida domain proteins, microtubules and exosomes are crucial for patterned cuticle deposition of bristles and present an avenue of future exploration for butterfly scales (Nagaraj and Adler, 2012).

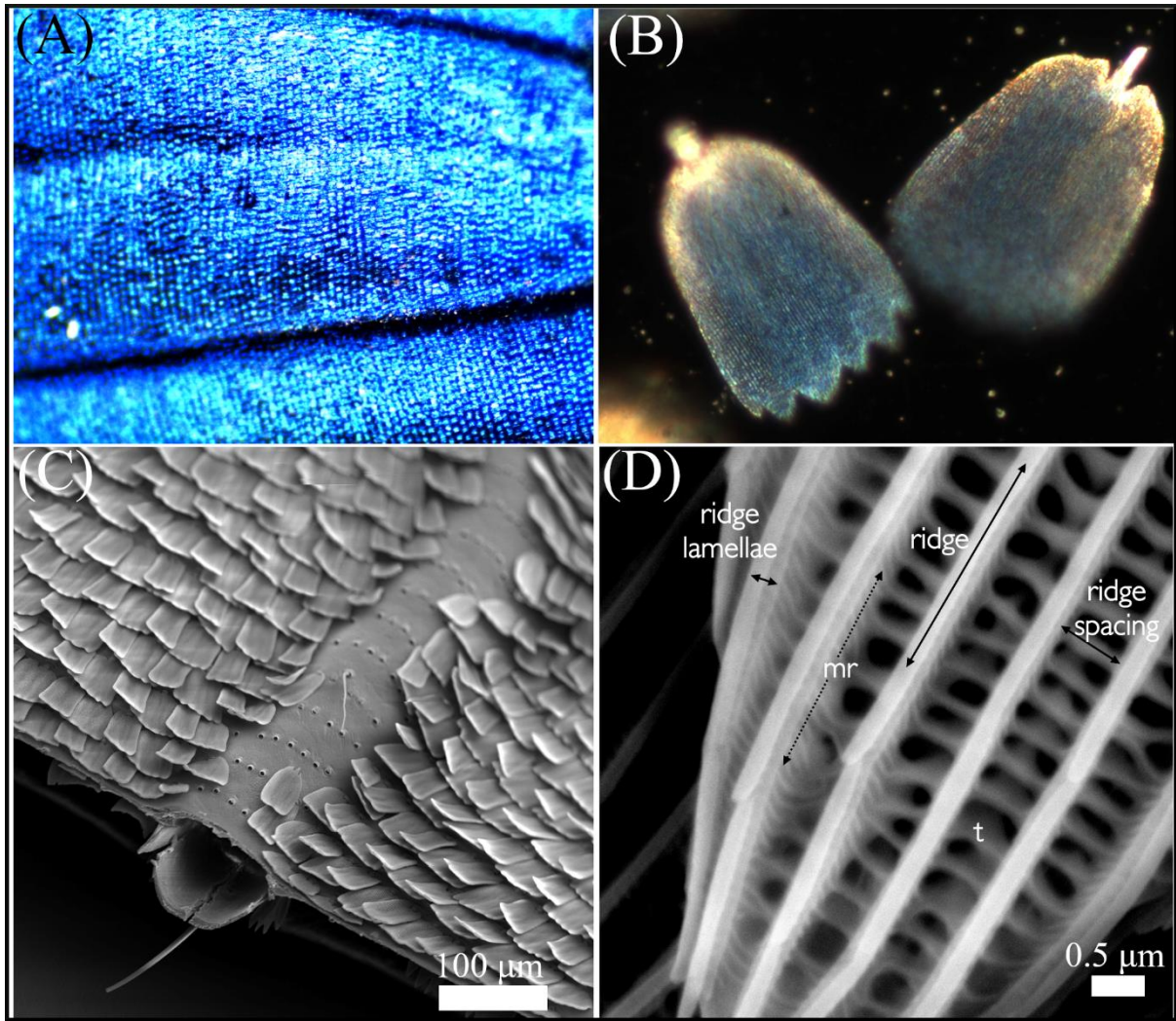


Figure 2. Wing scales of *Heliconius* butterflies. (A) Blue iridescent wing scales are point sources of colour. (B) Individual iridescent scales. (C) SEM image of a cross-section through a wing with scales overlapping either side of the large vein. (D) Microstructural layout of a typical wing scale showing the large parallel ridges connected by crossribs. Smaller pleats of cuticle run down the side of the ridge and are called microribs (mr). Crossribs connect the ridges perpendicularly and extend into the scale lumen forming the trabeculae (t). Scale windows are the hollow openings into the scale lumen. Image (D) reproduced from Parnell et al., (2018) ,where it is made available under a CC-BY 4.0 license (<https://creativecommons.org/licenses/by/4.0/>).

A key goal of Evo Devo is to understand how developmental pathways are tweaked to generate phenotypic diversity (Joron et al., 2006a; Nunes et al., 2013). Central to this question is an understanding of the direct and indirect interactions between molecular regulators within a cell and their targets, known as a Gene Regulatory Network (GRN)(Liu et al., 2019). GRN's shape the cellular environment and provide a coupling between the genotype and the phenotype (Emmert-Streib et al., 2014). Inference of the GRN provides an understanding of how the cell functions at the mechanistic level and reveals specific molecular interactions from a large number of potential genes. Such inferences can drive hypotheses on biological processes which can be tested experimentally (Emmert-Streib et al., 2014; Liu et al., 2019). GRN's have been used to infer broad patterns of evolution, such as the animal body plan (Fernandez-Valverde et al., 2018) but also to gain insight into the formation novel anatomical features such as vertebrate tooth shape (Sadier et al., 2020) and *Drosophila* dorsal appendage formation (reviewed by Smith et al., 2018).

The GRN underpinning scale cell development and microstructure patterning are understudied. Much of what we know about the genes and regulatory interactions controlling scale development comes from studies of wing patterning in Lepidoptera. In *Heliconius* wing patterning is controlled by a small number of conserved 'toolkit' loci, which form hotspots of evolution for diverse wing patterns (Livraghi et al., 2021; Nadeau, 2016). Knockouts of patterning genes can alter scale microstructure. For example, CRISPR-Cas9 knockouts of *cortex* resulted in a switch from red/black type scales to white scales and was accompanied by microstructural changes, including a sheet like upper lamina in the scale windows (Livraghi et al., 2021). Knockouts of major developmental genes in other Lepidoptera species also result in scale structure changes (Prakash et al., 2022; Thayer et al., 2020). Knockouts of *Antennapedia* in *Bicyclus anynana* result in scale cell shape changes, with fingers forming at the distal scale axis in conjunction with alterations to ridge and crossrib direction (Prakash et al., 2022). Table

1 presents a list of some the known genes, including major developmental patterning genes, which have been shown to control scale structure regulation.

Nonetheless, the majority of identified genes thus far represent early pre-patterning factors which set in motion a series of scale cell differentiation pathways specific to certain colours and scale types. Instead, comparatively little is known about the downstream parts of the GRN which regulate the cellular effectors that build and control the shape of the scale microstructures. For example, the blue structurally coloured and black non-structurally coloured scales in *Heliconius* are regulated by the same set of pre-patterning factors (*optix* and *cortex*) but little is known about the downstream developmental pathways directly controlling the formation of the optical nanostructures in the blue scales (Livraghi et al., 2021). Gene expression data acts as starting point to explore the GRN's controlling scale cell development and ultimately how this set of molecular interactions are tweaked to form microstructures capable of structural colour production (Chouvardas et al., 2016; Emmert-Streib et al., 2014; Liu et al., 2019).

Table 1. Summary of gene knockout studies in various species of Lepidoptera where there has been an effect on scale cell development (microstructural alterations and/or colouration changes).

Gene	Species	Scale development knockout effect	Reference
Cortex	<i>Heliconius sp.</i>	Scale pigment switch; alteration of crossribs, upper lamina and microrib morphology	(Livraghi et al., 2021)
Lac2	<i>Bombyx mori</i>	Ridge organisation; crossribs, microribs altered patterning	(Liu et al., 2021)
	<i>Vannessa cardui</i>	Loss of scales; pigmentation switch	(Peng et al., 2020)
Th	<i>Bicyclus anynana</i>	No cuticle; curled scale appearance; reduced pigmentation	(Matsuoka and Monteiro, 2018)
Ddc		Disorganised and fused crossribs; trabeculae architecture alteration	
Yellow		Lamina layer alterations; crossrib alterations; pigmentary changes in dark coloured scales	
Ebony		Scale size slightly larger; small changes crossrib thickness	
Optix	<i>Junonia sp.</i>	Lower lamina thickness; pigment alterations	(Thayer et al., 2020; Zhang et al., 2017)
	<i>Bicyclus anynana</i>	Scale shape change	(Prakash et al., 2022)
Antp	<i>Bicyclus anynana</i>	Scale fingers induced; ridge crossrib axis alteration; lost pigmentation	
Ubx	<i>Bicyclus anynana</i>	Lamina thickness; lost pigmentation	(Prakash et al., 2022)
	<i>Junonia coenia</i>	Scale morphology alterations corresponding to pigmentary changes	(Tendolkar et al., 2021)
	<i>Vanessa cardui</i>	Scale identity switch; pigmentary changes	
ApA	<i>Bicyclus anynana</i>	Lamina thickness; lost pigmentation	
BarH1	<i>Colias crocea</i>	Scale pigmentation switch	(Woronik et al., 2019)
WntA	<i>Heliconius sp.</i>	Scale pigmentation switch; crossrib alterations; ridge spacing change	(Concha et al., 2019)
Dll	<i>Bicyclus anynana</i>	Missing scales; reduced pigmentation	(Connahs et al., 2019)
	<i>Pieris canidia</i>	Missing scales; pigmentation switch	(Wee et al., 2022)
Bab	<i>Colias sp.</i>	Switch to structurally coloured scales; female-specific pigmentation switch	(Ficarrotta et al., 2022)
Spalt	<i>Pieris canidia</i>	Scale pigmentation switch; pigment granules around crossribs; windows, upper lamina alteration	(Wee et al., 2022)

The model: Heliconius butterflies

The diverse and vibrant wing patterns of *Heliconius* butterflies have captured the interests of biologists for centuries and the genus features widely in evolutionary studies of diversity, speciation and population genetics (Merrill et al., 2015; Van Belleghem et al., 2021). The genus is part of a larger tribe known as the Heliconiinae (Nymphalidae), made up of 8 genera, with *Heliconius* being the most species rich having 48 described species. The butterflies are found throughout the neotropics from South and Central America to the southern reaches of the USA. They may also be referred to as the ‘longwings’, owing to their wing shape which gives them their leisurely but purposeful flight. The diverse patterns on their wings typically follow a general theme of a black background with gaudy patterns of red, orange, yellow, white and (occasionally) blue (Jiggins, 2017). Such wing pattern diversity captured the attention of the naturalist Henry Walter Bates during his explorations to the Amazon basin and provided inspiration for his writings on adaptation and mimicry (Bates, 1862; Brown, 1981).

The bright colour patterns serve as aposematic warning signals, signalling their toxicity to predators which is accrued from their cyanogenic *Passiflora* hostplants (Cardoso and Gilbert, 2013). Evolutionary divergent species of *Heliconius* converge on a particular warning signal within a geographic area, forming mimicry rings encompassing both *Heliconius* and other butterflies such as the Ithomiinae (Figure 3) (Brown, 1981; Brown and Benson, 1974; Jiggins, 2017; Joron et al., 2006b). Where different colour forms meet geographically, they establish narrow hybrid zones maintained by frequency-dependent selection (Joron et al., 2006a; Kronforst and Papa, 2015; Mallet and Barton, 1989). Field studies of translocated butterflies to areas where the colour pattern is different show reduced survival, owing to predator recognition of the prevalent colour pattern within a local area (Mallet and Barton, 1989). Strong selective forces drive pre- and post-mating reproductive isolation and therefore assist in speciation (Jiggins et al., 2001; Kozak et al., 2015). Nonetheless, many related species can co-

occur within the same region leading to ecological divergence, with partitioning of host-plant niches and habitat preferences from thick understorey to open clearings (Jiggins, 2017; Jiggins et al., 1997; Kozak et al., 2015; Mallet and Gilbert, 1995). The adaptive radiation of the genus has also been associated with key innovations, such as pollen feeding in adult butterflies (Gilbert, 1972; Jiggins, 2017; Kozak et al., 2015). The acquisition of this amino acid rich resource underpins their long adult lifespan and extended reproductive period and has been linked to mushroom body expansion and novel feeding strategies such as trapline foraging (review by Young and Montgomery, 2020).

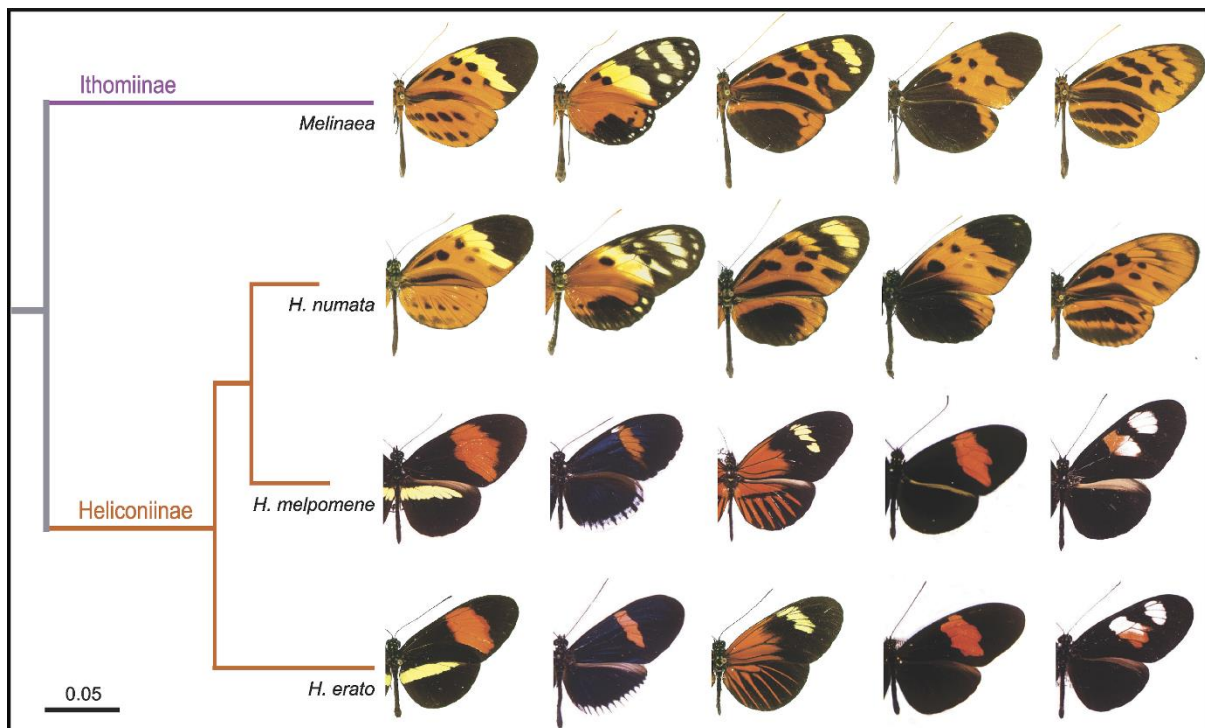


Figure 3. Diversity and convergence of colour patterns in several species and subspecies of *Heliconius* and the distantly related *Melinaea* (Ithomiinae). Image reproduced from Joron et al., (2006) where it is made available under a CC-BY 4.0 license (<https://creativecommons.org/licenses/by/4.0/>).

Studies of *Heliconius* wing patterns and colours took on a new direction with the advent of genomic technologies. Discovering the genetic basis of wing pattern diversity has contributed greatly to the knowledge of the evolution of novelty (Joron et al., 2006a; Kronforst and Papa, 2015). Colour pattern variation in *Heliconius* is attributed to a ‘toolkit’ of a restricted number of major effect loci (Nadeau, 2016). Various genomic methodologies coupled with recent advances in gene knockout technologies, such as CRISPR-Cas9, have elucidated the genes responsible for wing pattern variation at these loci, including: *cortex* (Livraghi et al., 2021), *optix* (Zhang et al., 2017), *WntA* (Mazo-Vargas et al., 2017) and *aristaless1* (Westerman et al., 2018). The gene *cortex* controls the specification of red and melanic (blue or black) scale identity and is regulated by modular enhancers that play a role in yellow bar patterning in *Heliconius erato* and *Heliconius melpomene* (Livraghi et al., 2021). *Optix* specifies the red colour pattern by acting as a switch between ommochrome (red and orange) and melanin (black and grey) pigments and acts downstream of *cortex* (Livraghi et al., 2021; Zhang et al., 2017). *WntA* demarks the spatial patterning of colour boundaries on the wing. Loss of *WntA* in *Heliconius erato demophoon* causes the expansion of the red wing bar into the typically black regions (Concha et al., 2019; Mazo-Vargas et al., 2017). Finally, the transcription factor *aristaless1*, which has been traced back to a butterfly-specific tandem duplication event, controls the white versus yellow colour through modification of the deposition of the yellow pigment 3-hydroxykynurenine (3-OHK) (Westerman et al., 2018).

Interestingly, many of these key patterning genes are deeply conserved in insects (Jiggins et al., 2017) with roles in colour patterning across Lepidoptera. For example, *cortex* and *WntA* control melanic colour variation and patterning in various butterfly and moth species (Gallant et al., 2014; Hof et al., 2016; Mazo-Vargas et al., 2017; Nadeau, 2016). The diversity of wing patterns in *Heliconius* lies in the tweaking of the expression of regulatory components which underpin these genetic elements (Hanly et al., 2019; Jiggins et al., 2017).

While pigmentary colours and patterns in *Heliconius* have received much attention, several species also possess structural colours (Parnell et al., 2018). There have been multiple independent origins of structural colour within the genus (Kozak et al., 2015). In the case of the monophyletic ‘iridescent specialists’, all seven species possess iridescent blue colour with a common ancestor between 2-5 million years ago. In contrast, a considerably more recent origin of structural colour (<10,000 years) has occurred in divergent species, such as the subspecies *Heliconius erato cyrbia* and *Heliconius melpomene cythera*, associated with co-mimicry (Figure 4) (Parnell et al., 2018).

The iridescent blue colour is produced from multilayer stacks of cuticle along the parallel ridges of wing scales. The individual layers reflect light through the principles of thin-film interference and when several layers are stacked they form a Bragg mirror; creating an intense reflection of the blue wavelength. In *Heliconius sara* the phenomenon of iridescence is particularly noticeable owing to the flat and continuous nature of their ridge layers (Figure 4B). In contrast, species such as *Heliconius erato cyrbia* have a more curved ridge profile, creating a less intense reflection (Figure 4D) (Parnell et al., 2018). In addition, reduced cuticle ridge spacing correlates with an increase in brightness of the reflected colour (Brien et al., 2018). Ridge multilayer reflectors are also found in numerous other unrelated species such as *Morpho* (Giraldo and Stavenga, 2016) and *Colias eurytheme* (Ghiradella, 1974). Green structural colour is also found in a subspecies of *Heliconius doris*. Instead of multilayer stacks, this particular species utilises a thin-film lower lamina to reflect blue light which is then spectrally filtered by the yellow pigment 3-OHK to produce the green appearance (Wilts et al., 2017a).

The adaptive role of structural colouration in *Heliconius* remains understudied. In *Hypolimnas bolina* structural colour functions as a mating signal, with female preference for male brightness (Kemp, 2007). Mate choice experiments in *Heliconius* have demonstrated a female preference for polarised light signals that arise from structural colour (Sweeney et al.,

2003). Conversely, the adaptive roles of pigmentary colours have been explored to a greater extent in *Heliconius*. For example, recent studies have shown UV reflection from the 3-OHK pigment in the yellow bar can be used to signal to conspecifics (Bybee et al., 2012; Finkbeiner et al., 2017; Finkbeiner and Briscoe, 2021) and can potentially function as a private communication channel (Dell’Aglia et al., 2018). *Heliconius erato* females have a duplicate UV opsin, suggesting the signal may be utilised for a sex-specific function (Briscoe et al., 2010; Finkbeiner and Briscoe, 2021; McCulloch et al., 2016). Further study on the adaptive role of iridescent structural colour is warranted.

Initial studies have begun to elucidate the genetic basis of structural colour. Iridescence in *Heliconius* is likely controlled by multiple genes (Brien et al., 2018; Curran, 2018; Appendix). Hybrid zones form between structurally coloured and non-structurally coloured subspecies of *H. erato* and *H. melpomene*. Within these zones there is an intermediate level of iridescence (Curran et al., 2020). In addition, recent phenotypic crosses between the structurally coloured *H. e. cyrbia* and the non-structurally coloured *H. e. demophoon* demonstrated a quantitative nature of the trait but with a potential major effect locus on the Z chromosome (Brien et al., 2018). This contrasts to pigmentary colours which show a simpler inheritance, corresponding to major effect loci such as *cortex*.

The advent of high-throughput genomic methods led to a boom in Evo Devo study species with a goal of increasing phylogenetic sampling (Jenner and Wills, 2007). Many in the field questioned the motive behind such wide sampling and posited that most evolutionary themes could be elucidated through focus on a few select species (Sommer, 2009). Nevertheless, the study of structural colour evolution and development requires us to look beyond the typical model species. In the classical definition of a ‘model system’, *Heliconius* fulfils many of the requirements. There is a long history of evolutionary study, annotated species genomes and the system is suitable for genomic tools such as CRISPR-Cas9 (*Heliconius* Genome Consortium,

2012). In addition, the butterflies can be maintained in the lab with short generational turnover (29 days from egg to adult) and a long lifespan (up to 6 months). Furthermore, the recent evolution of iridescent subspecies (Parnell et al., 2018) is commensurate with comparative genetic studies – a key method in Evo Devo. Taken together, *Heliconius* is a suitable model for studies of the evolution and development of structural colour. Furthermore, insights gleaned from these studies will likely be applicable at a broader level given the conservation of mechanisms and regulatory components controlling cuticle deposition in insects (Ghiradella, 2010). While the underlying genes may be different, understanding the developmental processes controlling structural colour will likely provide insights into numerous systems beyond *Heliconius*.

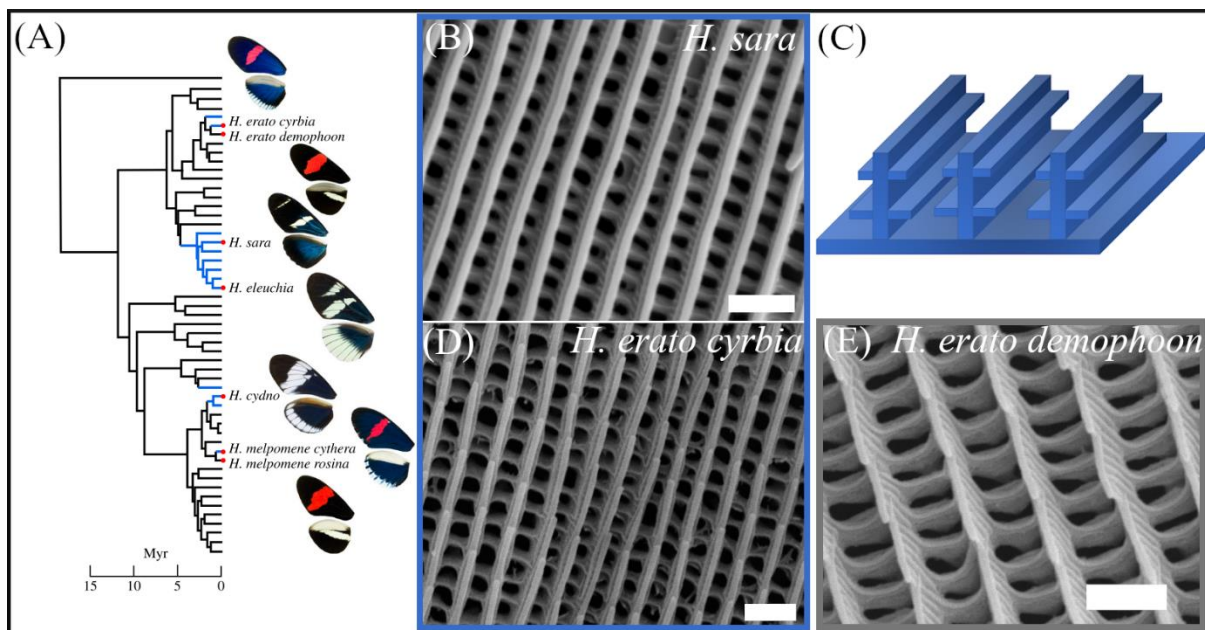


Figure 4. Structural colour in *Heliconius* butterflies. (A) Phylogenetic positions of some of the structurally coloured species of *Heliconius*. Branches which are blue indicates a species with blue structural colour. (B) The layered ridges of a blue iridescent *Heliconius sara* wing scale. The layers are continuous on the ridge. (C) A schematic diagram of the ridges of *H. sara*, forming a multilayer optical nanostructure. (D) Layered ridges of a blue, iridescent *Heliconius erato cyrbia* wing scale. The ridges are less continuous than in *H. sara*, visible as termination

points on the upper layer. (E) Ridges of the non-iridescent *Heliconius erato demophoon* wing scale. All scale bars: 1 μm . Image (A) reproduced from Parnell et al., (2018), where it is made available under a CC-BY 4.0 license (<https://creativecommons.org/licenses/by/4.0/>).

Thesis rationale

Structural colours are widespread in nature and have received considerable attention in birds and butterflies (Ghiradella and Butler, 2009; Sun et al., 2013). Many species of *Heliconius* possess iridescent, blue structural colour (Parnell et al., 2018). The nanostructures responsible for generating structural colour have been well characterised from an optical perspective. Furthermore, recent studies have presented initial inroads into the genetic basis of structural colour in *Heliconius* (Brien et al., 2018; Curran et al., 2020). However, the developmental basis of optical nanostructure formation remains poorly understood. Advances in developmental imaging technologies, such as super-resolution microscopy, have opened the door to characterising the nano-level formation of such structures (Hell et al., 2015). In addition, advances in high-throughput sequencing technologies and their application beyond traditional models means that Evo Devo studies can move beyond observational characterisation towards a deeper understanding of the gene pathways and molecular interactions underpinning structure formation. In this thesis I aim to understand the development of structural colour in *Heliconius* by addressing three primary questions: (1) How do iridescent scales and optical nanostructures develop at the cellular level? (2) What are the genes controlling structural colour development and are these convergent between different species? (3) how sensitive is the development of these structures to environmental conditions?

Research summary

Chapter 2 summary

This chapter builds on the introduction I presented in Chapter 1. I present a timely review on the evolution and development of structural colour in butterflies. I discuss the latest insights into the development and genetics of structural colours, primarily focusing on lower lamina reflectors, ridge reflectors and internal multilayers and photonic crystals. Finally, I take a step back from butterflies and discuss the broader understanding of structural colour evolution across the diversity of animals and plants.

Chapter 3 summary

The actin cytoskeleton is an intracellular network which controls numerous key functions including force generation and cell shape (Fletcher and Mullins, 2010). In butterfly scale cells the actin cytoskeleton controls proximal-distal scale elongation and the positioning of the cuticle ridges on the cell surface. The actin cytoskeleton may also play a role in structural colour development, although evidence for this is limited (Day et al., 2019; Dinwiddie et al., 2014; Ghiradella, 1974). This chapter aims to understand the role of the actin cytoskeleton in the formation of optical nanostructures in the butterfly *Heliconius sara*.

We find the actin cytoskeleton is crucial in structural colour development. Firstly, we show that iridescent scales have an increased actin bundle number compared to non-iridescent black scales and this leads to an increase in cuticle ridge density, thereby maximising the scales light reflecting surface area. We then use TauSTED super-resolution microscopy to reveal a previously undescribed network of branched actin filaments in butterfly scale cells, which may be contributing to structural colour development. Finally, through chemical perturbation of

actin in developing iridescent scales we diminish the blue structural colour from adult wings. Electron microscopy reveals that actin perturbation results in significant disruption the regularity of the ridges and alterations to layered optical nanostructures. This suggests that the actin cytoskeleton has a direct role in the construction of the multilayer nanostructure.

Chapter 4 summary

The genetic basis of structural colour in butterflies is poorly understood. The few genes which have been identified to date are likely upstream of the regulatory network controlling scale structure formation (Smith et al., 2018). Having characterised the cellular development of *Heliconius* scales and uncovered a crucial role of the actin cytoskeleton in Chapter 3, I now focus on the genetic basis of optical nanostructure formation. In this chapter I aim to uncover the genes controlling structural colour development in *Heliconius* and whether these genes are convergent between species which have independently evolved blue iridescent colour. Differential gene expression analysis is performed between iridescent and non-iridescent subspecies of *Heliconius erato* and *Heliconius melpomene*. We identify a large number of differentially expressed (DE) genes in both study species. Further comparisons are made within iridescent subspecies between the iridescent wing region and the non-structurally coloured androconial wing region. DE genes upregulated in both the iridescent species and the iridescent wing region are likely involved specifically in structural colour development. This leads us to identify *chitin deacetylase 1* as an important candidate.

We then perform Gene Set Enrichment Analysis (GSEA) to identify over represented classes of genes. Next, we interrogate our list of differentially expressed genes by: i) identifying DE genes which are located in QTL intervals associated with structural colouration. ii) Overlap of DE genes with genes involved in homologous structure development. In addition, we

identify concordantly expressed genes between *H. erato* and *H. melpomene*, where we find little evidence of convergent genes controlling structural colour development. Finally, we construct a table of candidate genes based on the occurrence frequency of DE genes within the above analyses and immunofluorescent staining is performed on the top candidate. Our final list contains several genes associated with the actin cytoskeleton, supporting our findings in Chapter 3 of an important role of this network in optical nanostructure formation.

Chapter 5 summary

Condition dependence of structural colour has been observed in several butterfly species, however such studies are lacking in *Heliconius* (Fenner et al., 2019; Kemp, 2008). Understanding the condition dependence of structural colouration in *Heliconius* will lay the groundwork for future studies on its potential adaptive function as a sexually selected signal. Dietary stress experiments are performed on larval stages to test the condition dependence of iridescent blue and yellow pigmentary colouration in *Heliconius sara*. Brightness and hue of the blue, iridescent colour is reduced following dietary stress and the effect is sexually dimorphic with a greater impact on males. Conversely, the yellow pigmentary colour is robust to dietary stress.

Having shown a condition dependent impact of dietary stress on structural colouration we next sought to understand the effect on the underlying scale ultrastructure. Scanning electron microscopy showed that dietary stress led to gaps in the optical nanostructure layers. To determine the optical effect of such nanostructural alterations we performed optical modelling of the *Heliconius sara* multilayer (a walk-through of the optical modelling theory is provided in the supplementary). Simulations of the nanostructure show the reduction in reflection is caused by loss of the reflective layers, linking our microscopic observations with optical theory.

The shift in hue was attributed to a relatively minor reduction in the thickness of either the air or chitin layers of the nanostructure. Overall, the development of structural colour in *Heliconius* is subject to environmental influences such as dietary stress.

Chapter 6 summary

This final chapter unifies the key findings of this thesis and how this work builds on our current knowledge of the topic. I end by discussing the future directions, challenges and how new technologies will present exciting avenues for the study of the evolution and development of structural colour.

Chapter 2

The evolution of structural colour in butterflies

Victoria J. Lloyd^{1*} and Nicola J. Nadeau¹

¹*Animal and Plant Sciences, University of Sheffield, Alfred Denny Building, Western bank, Sheffield S10 2TN, UK*

* Corresponding author

Email Victoria Lloyd: vjlloyd1@sheffield.ac.uk

Email Nicola Nadeau: n.nadeau@sheffield.ac.uk

Citation: Lloyd, V. J., Nadeau, N. J. (2021) ‘The evolution of structural colour in butterflies’.

Current Opinion in Genetics & Development. 69, 28 – 34. doi:

<https://doi.org/10.1016/j.gde.2021.01.004>

Author contributions

This chapter is published in *Current Opinion in Genetics and Development* (Lloyd and Nadeau, 2021). Myself and Nicola Nadeau designed the review. I wrote the manuscript with editing and revision performed by myself and Nicola Nadeau.

Abstract

Butterflies display some of the most striking examples of structural colour in nature. These colours originate from cuticular scales that cover the wing surface, which have evolved a diverse suite of optical nanostructures capable of manipulating light. In this review we explore recent advances in the evolution of structural colour in butterflies. We discuss new insights into the underlying genetics and development of the structural colours in various nanostructure types. Improvements in -omic and imaging technologies have been paramount to these new advances and have permitted an increased appreciation of their development and evolution.

Keywords

Structural colour, butterfly, evolution, development, iridescence

Introduction

In nature some of the most conspicuous colours come not from pigments but instead from physical structures within the integument of some animals and plants (Airoidi et al., 2019; Ingram and Parker, 2008). These structures, on the order of a few hundred nanometres or less, selectively reflect light to create a vivid repertoire of colours known as ‘structural colours’ (Supplementary information: **box 1**). A diverse range of organisms produce structural colours, including birds (Burg and Parnell, 2018), plants (Airoidi et al., 2019), fish (Denton, 1970) and invertebrates (Barrows and Bartl, 2014; Kramer et al., 2007; Onelli et al., 2017; Trzeciak and Vukusic, 2009). Structural colours have evolved to fill diverse roles including camouflage (Kjernsmo et al., 2020) and intra- (Sweeney et al., 2003) and interspecific communication (Waldron et al., 2017).

Butterflies have long been subjects of study for their pigmentary colours, and they have also been firmly at the forefront of our understanding of structural colouration. Vivid displays of structural colours are found across the butterfly phylogeny and utilize diverse optical

mechanisms (**Figure 1**)(Ren et al., 2020). Nevertheless, all butterfly structural colours originate from tiny (approximately 100µm long) scales which adorn the wing surfaces. Each scale is a flattened cuticular extension, with an intricate upper lamina (layer) of parallel ridges connected transversely by crossribs which extend down through a lumen to a flat lower lamina (**Figure 1a**)(Ghiradella and Radigan, 1976; Nijhout, 1991). Remarkably, each highly-intricate scale is a result of the expansion of a single cell (Ghiradella and Radigan, 1976). Pigments are also crucial for scale colour, with spectral purity of structurally coloured scales achieved by including pigments, such as melanin, into the scale structure (Stavenga et al., 2014; Thayer et al., 2020). Additional mechanisms such as scale stacking can further modify and enhance the colour (Siddique et al., 2016).

Varied ecological pressures and the underlying malleability of the arthropod cuticle has contributed to the evolution of diverse structural colour mechanisms in butterflies (Ghiradella, 2010; Vukusic, 2006). While the vivid blue scales of *Morpho* are a classic example of a complex scale reflector (Vukusic et al., 1999), bright colouration also occurs in other species, such as metalmarks (Riodininae), which have a comparatively simple optical nanostructure (Ren et al., 2020). Indeed, even within a single genus several divergent optical nanostructures may be found (Wilts et al., 2014), highlighting the flexibility of the underlying cellular mechanisms governing the evolution and development of structural colour.

In this review we aim to highlight the recent advancements in understanding butterfly structural colour evolution from a genetic and developmental perspective. We group butterfly optical nanostructures into three major types based on their location within the scale and discuss each one in turn. The seminal works of Ghiradella (Ghiradella, 1989, 1974; Ghiradella et al., 1972) have served as a foundation for understanding both the optics of butterfly structural colours as well as their development *in vivo*. Following a period of relatively little activity, the last five years has seen tremendous advancements, including new insights into the genes

controlling structural colour (Brien et al., 2018; Thayer et al., 2020; Zhang et al., 2017). These insights have been aided by the molecular revolution of the past decade, with tools such as CRISPR-Cas9 pioneering our understanding of the underlying genetics. Furthermore, advances in microscopy technologies have reaffirmed our appreciation for wing scale formation at the nanoscale.

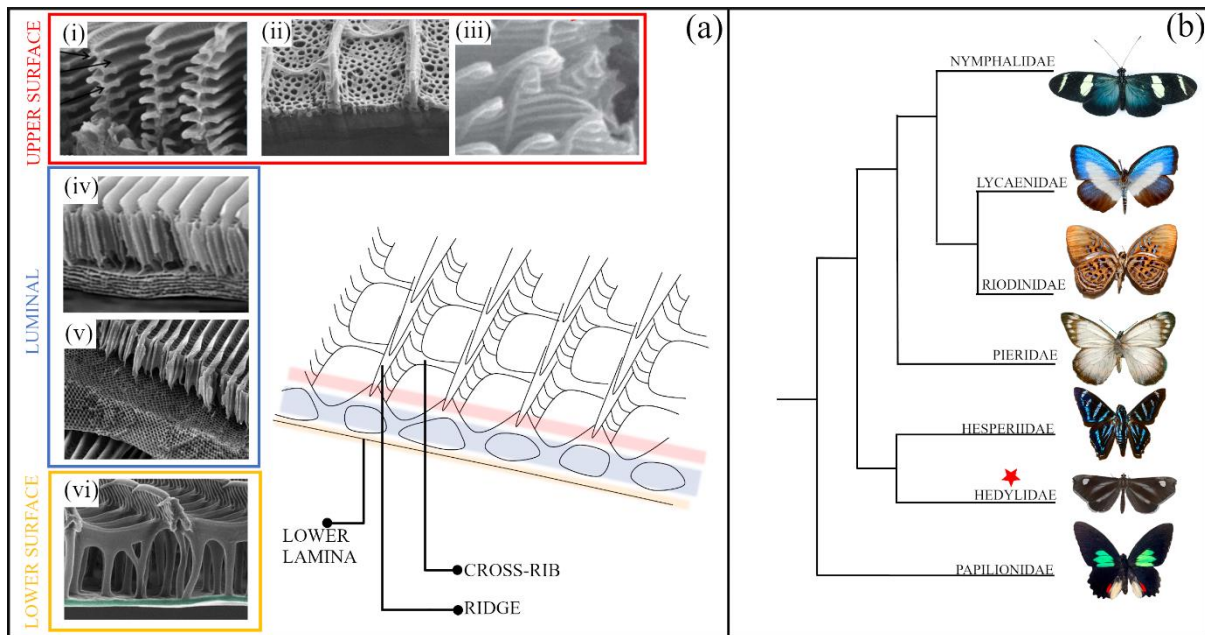


Figure 1. The diversity of structural colour in butterflies. (a) Morphologically diverse optical nanostructures have evolved through modifications to a basic scale ‘ground plan’. Modifications can be grouped depending on their location within a scale (upper surface, lumen, lower surface). Several features of the upper surface may be modified, including the ridges (i), inter-ridge cuticle (ii), and microribs (iii). The hollow lumen may also contain nanostructures, including multilayers (iv) and highly-ordered photonic crystals (v). Changes in cuticle thickness of the lower lamina can produce lower lamina reflectors (vi). (b) Examples of structural colour in the major families of Papilionoidea (butterflies). Structural colour remains undescribed for the Hedyliidae (star), but are presumed present due to the existence of white scales in some species. Phylogeny drawn from Espeland et al., (2018). SEM images in (a) reprinted from: (i) Potyrai et al., (2015) (iv, v) Wilts et al., (2014) (vi) Thayer et al., (2020).

All made available under a CC-BY 4.0 license (<https://creativecommons.org/licenses/by/4.0/>).

Image (ii) reprinted with permission from Trzeciak et al., (2012) © The Optical Society. Image (iii) used with permission of The Royal Society (U.K.), from Wickham et al., (2006); permission conveyed through Copyright Clearance Center, Inc. Images of Lycaenidae (https://commons.wikimedia.org/wiki/File:Lycaenidae_-_Danis_species.JPG) , Riodininae (https://commons.wikimedia.org/wiki/File:Riodinidae_-_Paralaxita_tesia-001.JPG) , Pieridae (https://commons.wikimedia.org/wiki/File:Pieridae_-_Delias_harpalyce-001.jpg) , Hesperidae (https://commons.wikimedia.org/wiki/File:Hesperidae_-_Jemadia_menechmus.JPG) and Papilionidae (https://commons.wikimedia.org/wiki/File:Papilionidae_-_Parides_sesostris_zestos.JPG) obtained from Wikimedia, where they were made available by Hectonichus under a CC-BY-SA-3.0 (<https://creativecommons.org/licenses/by-sa/3.0/legalcode>) license. Image of Hedyliidae obtained from Wikimedia ([https://commons.wikimedia.org/wiki/File:Hedyliid_Moth_\(Macrosoma_lucivittata\)_254659_99377.jpg](https://commons.wikimedia.org/wiki/File:Hedyliid_Moth_(Macrosoma_lucivittata)_254659_99377.jpg)) , where it was made available by Bernard DUPONT under a CC-BY-SA-2.0 license (<https://creativecommons.org/licenses/by-sa/2.0/legalcode>).

Surface nanostructures – ridge reflectors

Several features of the upper scale surface can be modified into reflective structures (**Figure 1**). The parallel ridges, which all butterfly scales possess, can become elaborated into a series of layered lamellae, creating an intense reflection through constructive interference (Supplementary information: **Box 1**)(Ghiradella et al., 1972). Remarkably, this can result in around 75% of the light being reflected in cases such as the blue *Morpho* scale (Vukusic et al., 1999). However, the light reflected by these structures is not solely limited to the human visible

spectrum, for example UV reflectance is present in species such as *Eurema lisa* (Ghiradella et al., 1972). Ridge reflectors have evolved independently in multiple lineages and in some cases several times within a lineage, for example in *Heliconius*, driven by convergent evolution for mimicry (Parnell et al., 2018).

Ridge reflectors form during wing scale development, with alternating air and chitin layers attaining optically precise spacing through drying post-eclosion (Ghiradella, 2010). Electron micrographs by Ghiradella (1974) led her to propose that ridge multilayers form by elastic buckling of the cuticle in response to intracellular stresses (Ghiradella, 1974). Notably though, this hypothesis draws on a purportedly similar process Locke (1958) proposed for the formation of taenidial folds in the tracheae of insects; where cuticle folds formed through mechanical buckling (Ghiradella, 1974; Locke, 1958). Subsequent re-evaluation of taenidial fold formation now suggests a more active role of the actin cytoskeleton and chitin synthases, rather than mechanical buckling (Öztürk-Çolak et al., 2016; Uv and Moussian, 2010). While much work is still needed on the development of ridge reflectors it is plausible that these nanostructures also require an active role for the actin cytoskeleton and chitin synthases in their formation. Indeed, recent studies have highlighted the importance of the actin cytoskeleton in wing scale development (Day et al., 2019; Dinwiddie et al., 2014).

Brien *et al.*, (2018) present some of the first insights into the genetic basis of ridge reflector evolution. Using phenotypic analyses of crosses between iridescent and non-iridescent races of *Heliconius erato*, they show that structural colour is a quantitative trait not associated with any of the major effect loci previously linked to pigmentary wing patterning in *Heliconius* (Brien et al., 2018). Interestingly, a moderate effect locus was detected on the sex chromosome, reminiscent of much older work showing that differences in ridge-reflector-based UV colouration between *Colias* species is due to a sex-linked locus (Silberglied and Taylor, 1973).

Perhaps unsurprisingly, given the precise nanostructures involved, ridge reflector formation shows sensitivity to developmental conditions in many species (Fenner et al., 2019; Kemp et al., 2006). Together, with a sex-linked genetic architecture, this has interesting implications for the evolution of ridge reflector colour as a sexual signal. Sex-linkage would aid the evolution of sexually dimorphic colour, important if the sexes have different evolutionary optima; while condition dependence could increase the information content of these colour signals to potential mates.

Lower lamina reflectors

The scale's lower-most cuticle layer can function as a thin-film capable of scattering light (Supplementary information: **Box 1**). Often this nanostructure is accompanied by pigments which function as 'optical filters' by absorbing wavelengths of light to enhance the structural colour (Stavenga et al., 2014). Lower lamina reflectors are often considered an optically and developmentally simple mechanism of achieving structural coloration. From an optical perspective, the lower lamina is a simple interface of contrasting refractive indexes which can scatter light (Thayer et al., 2020). This optical process is reminiscent of that present in ancient Lepidopteran structurally coloured scales from the Jurassic (albeit possessing a slightly different scale morphology of a fused lower and upper lamina) (Zhang et al., 2018). Lower lamina reflectance is an "evolutionarily accessible" optical phenotype because all scales possess a flat lower lamina. As such, this removes the need to evolve complex ridge or crossrib structures, which may impact on other intrinsic scale properties including thermoregulation, aerodynamics, hydrophobicity or self-cleaning (Chen et al., 2004; Krishna et al., 2020; Slegers et al., 2017).

Artificial selection experiments in both *Bicyclus anyana* (Wasik et al., 2014) and *Junonia coenia* (Thayer et al., 2020) have demonstrated that within a short period of time (6 generations and 12 generations, respectively) the colour produced by lower lamina reflectors can be considerably modified (**Figure 2**). Selection in both these species resulted in changes in thickness of the lower lamina, demonstrating the ease with which this scale element can be sculpted. Indeed, in both *Bicyclus* and *Junonia*, between-species variation in structural colour appears to have evolved through tuning the lower lamina thickness. This reinforces suggestions that the lower lamina is a common evolutionary target for selection in diverse species and that relatively small, quantitative changes to just one part of the scale architecture can have profound micro- and macroevolutionary consequences (Smith et al., 2018; Thayer et al., 2020).

Zhang *et al.* (2017) demonstrated that knockouts of the developmental patterning gene *optix* also results in a brown to blue colour change in *J. coenia* (Zhang et al., 2017). Thayer *et al.* (2020) showed this switch in colouration through *optix* deletion was the result of lower lamina thickening, recapitulating what occurs in both the artificial selection experiments and within natural populations (**Figure 2**)(Thayer et al., 2020). This hints at the possibility of *optix* and its associated gene regulatory networks being the target for selection in naturally evolving, structurally-coloured populations. Interestingly, Thayer *et al.*, (2020) also showed that in other coloured scales of *Junonia*, such as gold scales, the lower lamina was tuned to a thickness to produce a complementary reflected wavelength. By regulating lamina thickness, *optix* and its downstream targets could therefore control the range of wavelengths produced through thin film interference (Thayer et al., 2020). Future work on the downstream targets of *optix* should aid our understanding of the regulatory networks and cellular control of structural colouration.

Optix also plays a conserved role in pigmentation and scale structure in butterflies (Martin et al., 2014; Zhang et al., 2017). This suggests that the evolution of pigments and some nanostructures may be more intertwined than previously thought and may be controlled by a

few ‘adaptive hotspots’ such as *optix* (Zhang et al., 2017). Indeed, several recent studies have highlighted a regulatory link between both scale structure and pigments (Fenner et al., 2020; Matsuoka and Monteiro, 2018; Peng et al., 2020; Thayer et al., 2020; Zhang et al., 2017). Future studies should continue to address the link between scale structure, pigments and nanostructures.

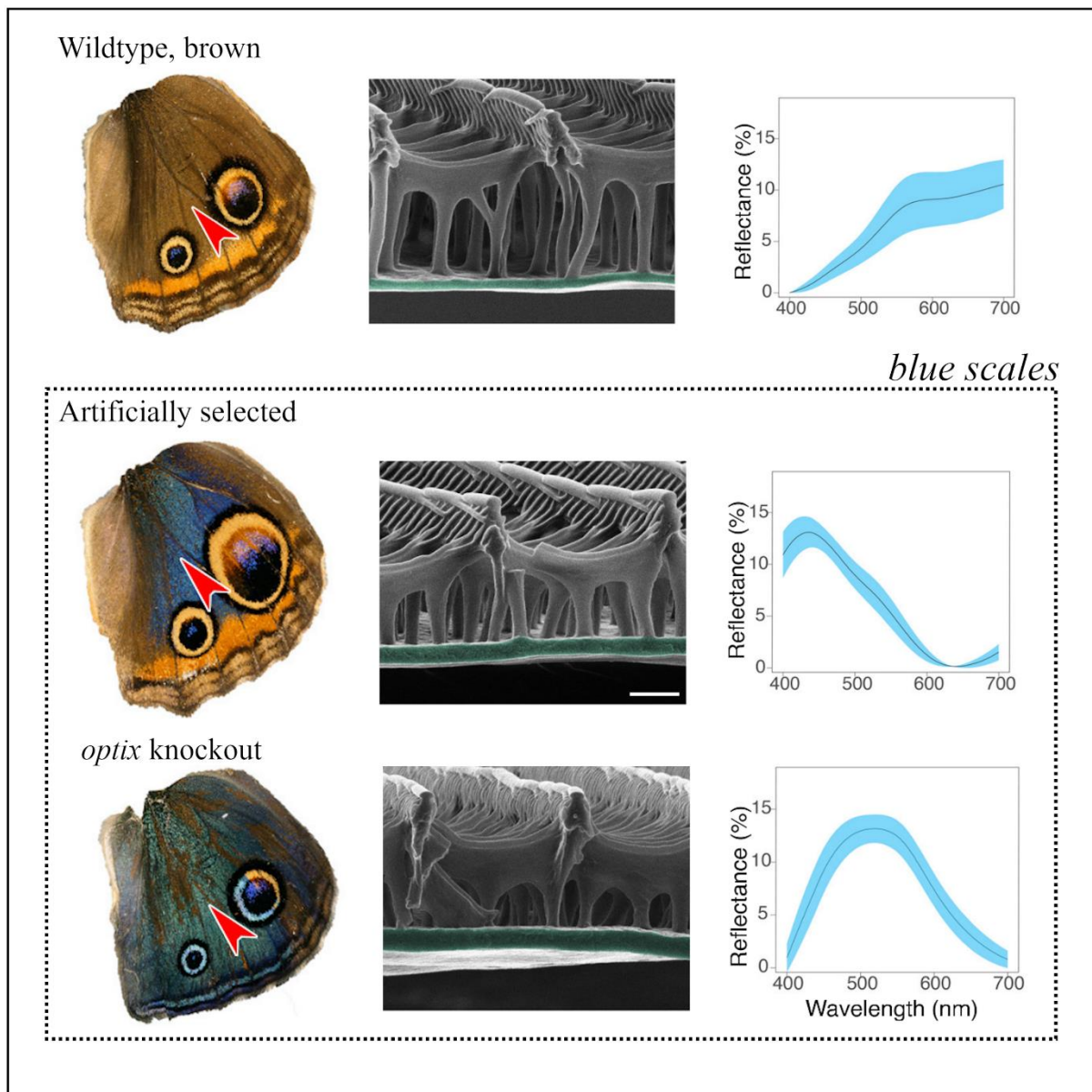


Figure 2. Insights into the genetic and structural control of lower lamina structural colour in *Junonia coenia* through artificial selection experiments and *optix* knockouts. Wildtype

J. coenia hindwings are predominantly brown in colour. A blue colouration is observed in wings which have been artificially selected for blue scales and in CRISPR-Cas9 knockouts of the developmental patterning gene *optix*. Changes in the observed colour of artificially selected and *optix* knockout wings can be seen in reflectance plots, with a shift to the blue end of the spectrum compared to wildtype brown scales. Helium ion microscopy (HIM) cross-sections showing scale morphology, with the lower lamina false coloured in green. The lower lamina is considerably thicker in *optix* knockout wings and artificially selected wings compared to wildtype wings. Images reproduced from Thayer et al., (2020) with permission and under a CC-BY-4.0 license (<https://creativecommons.org/licenses/by/4.0/>).

Internal nanostructures – lumen multilayers and photonic crystals

Diverse nanostructures may be present within the scale lumen, ranging from simple multilayers to complex 3D photonic crystals (**Figure 1**) (Wilts et al., 2014). While often considered as highly-ordered structures, lumen nanostructures may also encompass a degree of disorder, for instance in the lumen multilayers of *Ornithoptera* (birdwing) scales (Kazama et al., 2017).

Focusing on photonic crystal formation, Ghiradella *et al.* (1989) provided the first insights into the role of the smooth endoplasmic reticulum (SER) as a templating network for highly ordered chitin deposition within the developing scale (Ghiradella, 1989). Subsequently, electron microscopy deduced a gyroid structure of the photonic crystals, consistent with a process of templating by intracellular membranes (**Box 1**)(Michielsen and Stavenga, 2008). Recently, techniques such as SAXS and X-ray tomography have permitted deeper understanding of not just the optical properties of such highly ordered structures but also the underlying cellular processes guiding their formation (Saranathan et al., 2010; Wilts et al., 2017b). Indeed, recent insights by Wilts *et al.* (2017) showed that the photonic crystals in the

scales of *Thecla opisena* were arranged in a size gradient over the scale's proximo-distal axis. Investigations over this gradient demonstrated a time-dependent growth process of crystal formation and that crystals do not form in the same orientation. The authors concluded that rather than a pre-folding template of SER, gyroid formation more likely involves simultaneous membrane templating and chitin deposition (Wilts et al., 2017b).

Characterising the optical properties of diverse luminal structures while considering the underlying phylogenetic relationships has provided deeper insights into the evolution of such structures. For example, gyroid structures and multilayers are found in closely-related species of Cattlehearts (*Parides*). This may suggest an underlying commonality in the developmental pathways and cellular effectors governing such structures. Wilts *et al.* (2014) suggest that minor deviations in developmental parameters may shift scale cell fate between multilayers or gyroid structures within the scale lumen (Wilts et al., 2014).

Similarly, Ren *et al.*, (2020) used comparative studies across butterfly families to understand the diversity of scale ultrastructures underlying metallic reflectance. Scales of Lycaenids were able to produce metallic, silver scales through an internal multilayer-type architecture. The authors suggested that differences in the number of chitin layers and perforation of the upper lamina could have led to a transition from blue to silver scales (Ren et al., 2020). The next major breakthrough will be in identifying the molecular switches involved in these evolutionary transitions between nanostructure types.

Beyond butterflies – evolutionary insights from other systems

We are beginning to gain an appreciation of the underlying evolutionary development of structural colours in many systems. Knowledge from these systems may present unique insights into the evolution of structural colour in butterflies. For example, photonic crystals within

weevils evolved only once, involving a transition from a hollow scale to one in which the spongy network within the lumen becomes increasingly ordered (Seago et al., 2019). This bears similarity to the evolution of photonic crystals in butterflies, which likely required a transition from a hollow lumen to one with an increasingly ordered multilayer (Wilts et al., 2014). In weevils, photonic crystal evolution was associated with shifts in feeding strategy and the need for crypsis (Seago et al., 2019), raising the question as to whether similar ecological pressures also shaped butterfly structural colour evolution.

While much focus has been placed on structural colouration in animals, diverse structural colours are also present in the petals, leaves and fruits of plants (Airoldi et al., 2019). Remarkably, despite disparity in cell types and cuticular materials used for nanostructures, many of the underlying cellular principles are likely conserved between animals and plants. For example, multilayer reflectors in fruits form through microtubule cytoskeleton guided deposition of cellulose into layered, helicoidal structures (Airoldi et al., 2019). In butterfly scales, the actin cytoskeleton guides chitin deposition on the ridges and may also play a role in nanostructure formation (Dinwiddie et al., 2014). Additionally, light-reflecting ridges on the epidermal layer of petals form through buckling of the cuticle (Antoniou Kourounioti et al., 2013), similar to the suggested mechanism of ridge reflector formation in butterflies, which could involve stress-mediated buckling of the chitin cuticle (Ghiradella et al., 1972). Overall, different systems may give universal insights into the underlying principles governing structural colour evolution.

Conclusions

Butterflies have evolved a diverse suite of optical nanostructures to produce vivid displays of structural colour. Advances in molecular genetic tools, such as CRISPR, in addition to much

improved resolution of microscopy techniques have provided tantalising new insights into the evolution and development of optical nanostructures in butterflies. Whilst much of the underlying cellular dynamics and developmental pathways remain unknown, the next few years is set to see major advances in our knowledge of structural colour evolution. By its very nature, the study of structural colours is a highly interdisciplinary topic, involving collaborations between physicists, material scientists and biologists alike. Such collaborations will not just give unique insights into evolutionary processes governing structural colouration but will open the doors to a whole range of biomimetic technologies, taking inspiration from the photonic structures which evolution has been finely sculpting over millennia.

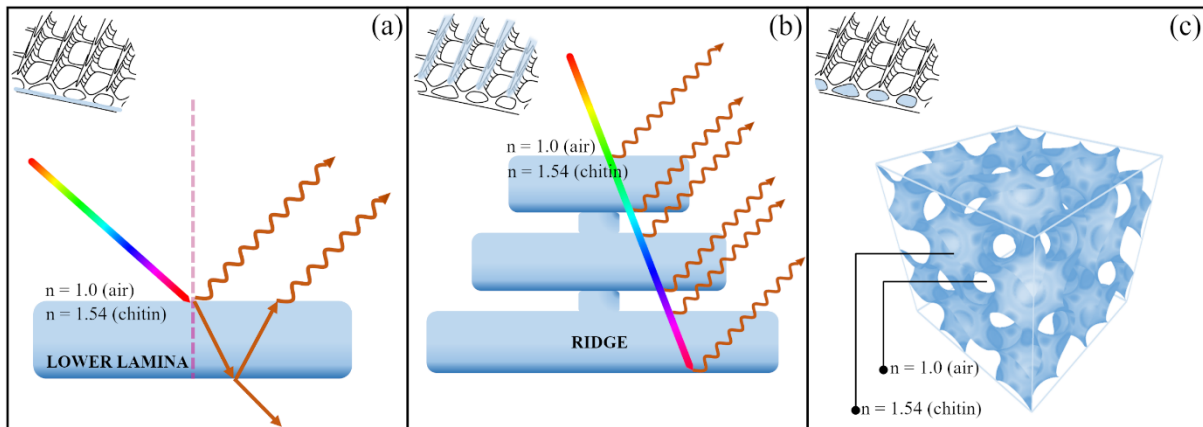
Acknowledgements

We thank Bodo Wilts (University of Fribourg), Rachel Thayer (University of California) and Radislav Potyrailo (General Electric Global Research Center) for permission to use their images. We also extend thanks to Andrew Parnell and Melanie Brien for their feedback on the manuscript. V.J.L is supported by a NERC doctoral training partnership (Adapting to the Challenges of a Changing Environment, NE/L002450/1).

Conflict of interest statement

The authors declare no conflict of interest.

Supplementary Information



Box 1. Optical nanostructures in butterflies. Diverse optical mechanisms in butterflies are governed by the same basic principle – to generate structural colour light must pass through materials of differing refractive indexes (n). The cuticle of butterflies is composed of chitin, which has a refractive index of 1.54 (at 590 nm). To attain a contrasting refractive index, butterfly nanostructures also encompass air spaces which have a refractive index of 1.0 (Burg and Parnell, 2018).

Thin films are the simplest optical mechanism present in butterfly scales. The lower lamina of the scale can form an optically precise thin-film reflector (a). Light waves are reflected by both the upper and lower surface of the lamina. When these reflected light waves are in phase, so that they peak at the same time, they can interfere constructively to accentuate particular wavelengths of light. The colour produced depends on the thickness of the chitin layer as well as the viewing and incidence angles (Thayer et al., 2020).

Thin film reflectors may also be stacked upon each other to form a multilayer-type nanostructure (Burg and Parnell, 2018). Examples of multilayers in butterfly scales may be found on both the upper surface as well in the lumen. The same principle of differences in refractive indexes applies, with the alternating air and chitin layers forming the contrasting indexes necessary to generate the phase change required for light interference. In the example

of the ridge reflector multilayer (b) light is reflected and transmitted by each layer, producing a colour through constructive interference. Changing the number of layers governs the intensity of reflection while modifying the spacing of the air and chitin layers changes the colour produced (Ingram and Parker, 2008).

3D photonic crystals in butterflies are highly-ordered, repeating structures on the order of the wavelength of light (c). As the light waves enter the structure, only certain wavelengths of light may propagate, producing a specific colour (Burg and Parnell, 2018). This reflectance of a certain wavelength occurs regardless of the angle of light entering. Such structures are found in the lumen of butterfly scales, as highly periodic 3D crystals of chitin. One particularly interesting type is the 'gyroid' structure, having a nanoscale bicontinuous structure surrounding air spaces, which can be described by a mathematical concept in which a curved structure is maximally connected through the smallest surface area possible (Ingram and Parker, 2008).

Chapter 3

The actin cytoskeleton plays an essential role in structural color formation in *Heliconius sara* butterflies

Victoria J. Lloyd^{1*}, Stephanie L. Burg², Jana Harizanova^{3,4}, Olivia Hill², Juan Enciso-Romero¹, Rory L. Cooper^{1,5}, Silja Flenner⁶, Elena Longo⁶, Imke Greving⁶, Nicola J. Nadeau^{1,†} and Andrew J. Parnell^{2,†}

¹*Ecology and Evolutionary Biology, School of Biosciences, University of Sheffield, Alfred Denny Building, Western bank, Sheffield S10 2TN, UK*

²*Department of Physics and Astronomy, University of Sheffield, Hicks Building, Hounsfield Road, Sheffield S3 7RH, UK*

³*Central Laser Facility—Science & Technology Facility Council, The Research Complex at Harwell, Rutherford Appleton Laboratory, Harwell Campus, Didcot, Oxfordshire, OX11 0FA, UK*

⁴*Core Facility for Integrated Microscopy, Department of Biomedical Sciences, University of Copenhagen, 2200N Copenhagen, Denmark*

⁵*Department of Genetics and Evolution, University of Geneva, Sciences III, Geneva 1205, Switzerland*

⁶*Helmholtz-Zentrum Hereon, Max-Planck-Strasse 1, 21502 Geesthacht, Germany*

[†]*These authors contributed equally to this work*

* Corresponding authors

Email: n.nadeau@sheffield.ac.uk, vjlloyd1@sheffield.ac.uk, a.j.parnell@sheffield.ac.uk

Author contributions

This chapter is formatted for submission to PNAS and is presented in its submitted format. Methods have been expanded on in the chapter to provide full descriptions of the undertaken research. The project was designed by myself, Andrew Parnell, Nicola Nadeau and Rory Cooper. Myself and Andrew Parnell performed most of the data collection. I performed the immunofluorescent staining, confocal microscopy, scanning electron microscopy, chemical perturbation treatments, reflectance spectrometry and the corresponding data analysis for these methods. X-ray nanotomography was performed by myself, Nicola Nadeau, Andrew Parnell and Juan Enciso-Romero, led by the beamline scientists Silja Flenner, Elena Longo, Imke Greving at the Deutsches Elektronen-Synchrotron, Hamburg, Germany. X-ray nanotomography rendering and the corresponding analyses were performed by Stephanie Burg at the University of Sheffield. The TauSTED experiment was performed at the Central Laser Facility, Harwell, Oxford, UK and was led by the microscope scientist Jana Harizanova. I performed the immunofluorescent staining. Image acquisition was performed by Jana Harizanova, Olivia Hill and myself. TauSTED images were processed by myself and Jana Harizanova and image interpretation performed by all authors. Andrew Parnell performed the Atomic Force Microscopy (AFM) and rendering and analysis of the AFM was performed by myself and Andrew Parnell. Juan Enciso-Romero wrote the Python script for the reflectance spectrometry data collection and the R script for the subsequent analysis. I wrote the manuscript and all authors contributed to editing and revision.

Abstract

The captivating displays of structural color in butterflies are caused by nanostructures physically interacting with light through diffraction or interference. From an optical perspective these photonic nanostructures are well understood, however the developmental processes underpinning their formation remain largely uncharacterized. This is particularly true for the layered lamellae which form multilayer reflectors on the wing scale surface of some butterfly species. Previous research has suggested that F-actin, which controls wing scale ridge positioning, may possibly play a direct or indirect role in controlling structural color development. Here, we demonstrate that F-actin is involved in the formation of structural color in the butterfly *Heliconius sara*. Using comparisons between iridescent and non-iridescent scales in adult and developing *H. sara* we show that iridescent scales have more densely packed actin bundles compared to non-iridescent scales, leading to decreased ridge spacing. Using super-resolution microscopy, we find that actin is repeatedly re-arranged in the later stages of pupal development, when the optical nanostructures form. Experimental perturbation of actin during these later stages results in significant reduction of structural coloration in adult *H. sara*. Together these findings show that actin plays an important role during structural color formation in iridescent *Heliconius* butterflies.

Significance statement

In nature, structural colours are brilliant and intense colours produced by light reflecting off sub-micron structures. Butterflies demonstrate vivid examples of structural colour originating from tiny scales on their wings containing light-reflecting nanostructures. While the optical properties of these nanostructures are well characterised, how they develop remains largely unknown. The actin cytoskeleton is a protein network which controls butterfly scale cell shape and may contribute to nanostructure formation. We use TauSTED super-resolution microscopy

to uncover a previously undescribed, branched actin network within scale cells. We show that not only does the actin cytoskeleton control the density of light reflecting surfaces but through actin perturbation experiments we demonstrate a direct involvement of actin in stabilising and building the nanostructure layers.

Introduction

Structural color produced by the interaction of light with nanostructures enable a diverse and tremendously vivid array of colors (Ingram and Parker, 2008). They are particularly important in low light environments, for example in the forest understory, as they achieve superior visual signal propagation over pigmentary color (Douglas et al., 2007). Despite the importance of biological photonic nanostructures from both an evolutionary perspective and as potential routes for the design of advanced optical materials (Kinoshita et al., 2008; Saito, 2011), the structural formation process remains poorly understood.

The photonic nanostructures within the wing scales responsible for structural color seen in butterflies and moths (Zhang et al., 2015) include; photonic crystals (Prum et al., 2006; Saranathan et al., 2010), multilayer reflectors (Giraldo and Stavenga, 2016) and thin-films (Stavenga et al., 2014; Thayer et al., 2020). Each wing scale develops from a single cell, forming a chitinous, cuticle envelope with an undifferentiated lower layer and a complex structured upper layer covered in longitudinal parallel ridges (Ghiradella, 1989; Ghiradella and Radigan, 1976; Nijhout, 1984; Overton, 1966). Multilayer reflectors are found in numerous structurally-colored butterfly species and are situated in the parallel scale ridges as a stack of layered lamellae (Ghiradella, 1991, 1989, 1974; Vukusic et al., 1999). Ghiradella (1974) postulated that developing ridges buckle due to intracellular stress (potentially from actin bundles) and this is responsible for layered lamellae formation.

Studying the actin cytoskeleton during scale formation can improve our understanding of how layered lamellae form, as for many cell types it plays an important role in controlling cell shape (Pollard et al., 2009). The scale ridges (on which the layered lamellae form) are the result of chitin deposition between parallel actin bundles (Day et al., 2019; Dinwiddie et al., 2014). The actin bundles are temporary and are stabilized through polymerisation and cross-linking of F-actin within developing scale cells (Guild et al., 2005; Tilney et al., 2000b, 1996).

The actin cytoskeleton within *Drosophila* bristles, a homologous structure to butterfly scales, has been extensively studied (Galant et al., 1998). Knockouts of actin organization genes have shown that the actin cytoskeleton is important in controlling the number and shape of the ridges in bristles, as well as the localization of chitin synthase enzymes, required to deposit the ridges (Adler, 2019; Shapira et al., 2011; Tilney et al., 2000b; Wu et al., 2016). In butterfly scales the actin bundles may not just be limited to guiding ridge positioning but could be crucial in sculpting finer-scale aspects of scale morphology, including the photonic nanostructures.

H. sara is a member of a monophyletic group of iridescent butterflies in the *Heliconius* genus and displays blue iridescent wing coloration (Parnell et al., 2018; Sweeney et al., 2003; Wilts et al., 2017a) (Fig 1A,1B). *H. sara* has both structurally colored blue iridescent and non-structurally colored, black scales (Fig 1A-1C), facilitating direct comparative analyses in both adult and pupal stages. The structural color of *H. sara* is generated through layered lamellae on the parallel scale ridges (Fig 1E-1G) (Parnell et al., 2018; Wilts et al., 2017a).

Here, we examine F-actin organization during wing scale development in the butterfly *H. sara*, focusing on the formation of the nanostructures responsible for iridescence. Using scanning electron microscopy (SEM) and fluorescence microscopy we investigate whether patterning of F-actin differs between iridescent and non-iridescent wing scales. We use

TauSTED (Stimulated emission depletion) super-resolution microscopy (Alvarez et al., 2021) to gain insight into actin remodeling during scale development. We then chemically perturb actin dynamics to elucidate whether the actin cytoskeleton plays a direct role in the formation of the optical nanostructure in *H. sara*.

Results

To compare the adult morphology of the iridescent and non-iridescent scales on the dorsal forewing of *H. sara* we used SEM (Fig. 2) and X-ray tomography (S1). We examined both upper cover scales and basal ground scales (Fig. 1D). The general structure of iridescent and non-iridescent scales is almost identical (S2 Movie, S3 Movie), both having a flat smooth lower layer (lamina) and a highly intricate upper layer (lamina). The parallel ridges on the upper lamina are joined together by crossribs, with the spaces between crossribs forming a regular series of windows into the interior scale lumen (Fig. 2C). Both cover and ground iridescent scales were smaller in size than non-iridescent scales (mean \pm SE scale area, blue (cover $2700\mu\text{m}^2\pm 21$, ground $3708\mu\text{m}^2\pm 35$), black (cover $3044\mu\text{m}^2\pm 25$, ground $4123\mu\text{m}^2\pm 30$), likelihood ratio, $\chi^2=208$, d.f. = 1, $p<0.001$), which can be attributed to the decreased width of iridescent scales (mean \pm SE scale width, blue (cover $29.5\mu\text{m}\pm 0.22$, ground $42.9\mu\text{m}\pm 0.3$), black (cover $31.3\mu\text{m}\pm 0.22$, ground $47.8\mu\text{m}\pm 0.33$), likelihood ratio, $\chi^2=24$, d.f. = 1, $p<0.001$, Fig 2D, S5B).

Having confirmed the general structure of iridescent and non-iridescent scales are similar we next quantified differences in the finer scale elements, focusing first on the parallel ridges (Fig. 2C, S4). The iridescent blue scales had significantly reduced ridge spacing compared to the non-iridescent black scales (mean \pm SE ridge spacing, blue $0.804\mu\text{m}\pm 0.007$, black $0.962\mu\text{m}\pm 0.004$; likelihood ratio, $\chi^2=446$, d.f. = 2, $p<0.001$; Fig. 2E-2F). The reduced ridge spacing in blue scales was also confirmed via a correlation function analysis of the tomography data (S1E-1F)(Strobl and Schneider, 1980). This is consistent with prior work which found

iridescent *Heliconius* species have reduced scale ridge spacing compared to non-iridescent species (Parnell et al., 2018). The decreased ridge spacing in iridescent scales can be attributed to an overall increase in ridge number, rather than a smaller scale width, with iridescent scales consistently having a greater ridge number for a given scale width (Fig. 2D). There was also an effect of scale type (cover or ground) upon ridge spacing (likelihood ratio, $\chi^2=27$, d.f. = 2, $p<0.001$). Iridescent cover scales had significantly reduced ridge spacing compared to iridescent ground scales (Tukey comparison, $p < 0.001$), but there was no difference in ridge spacing between cover and ground scales for non-iridescent scales (Tukey comparison, $p=0.633$). There was a skewed distribution of ridge spacing in the iridescent scales, with a truncation of the distribution of ridge spacing at the lowest spacing values (S5A). This suggests that there is likely to be an absolute physical limit to which ridges can be packed together within the scale.

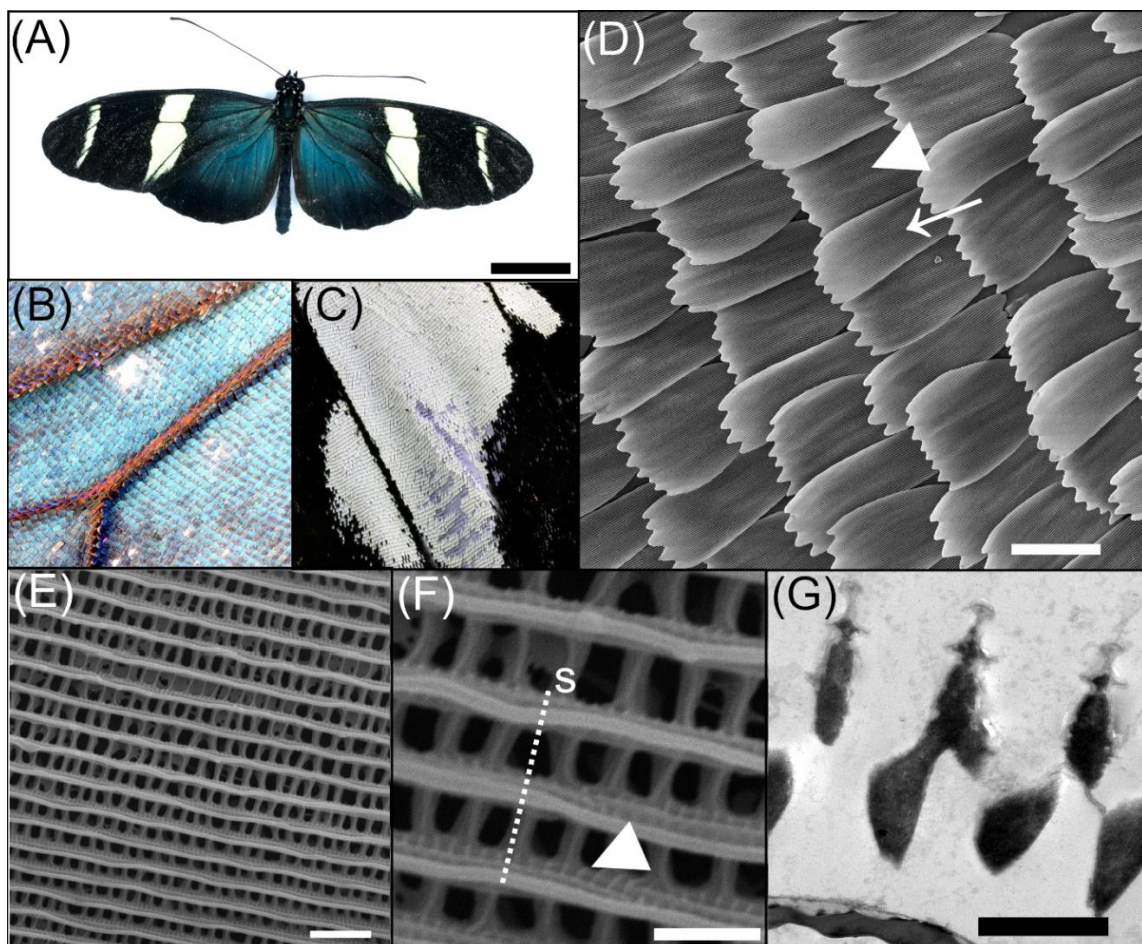


Fig 1: The neotropical butterfly *Heliconius sara*. (A) Dorsal view of a *Heliconius sara* individual. (B) Region of blue, iridescent wing scales on the proximal forewing. (C) Region of black and white, non-iridescent wing scales on the distal forewing. (D) SEM image of the overlapping scales on the dorsal wing surface. Cover scales (arrow) sit directly on top of the basal ground scales (arrowhead). (E) Dorsal view of an iridescent wing scale surface, with many periodically ordered longitudinal ridges running parallel to scale length. (F) High-magnification view of an iridescent wing scale showing ridge ultrastructure; with open windows into the scale lumen separated by crossribs. Microribs (arrowhead) pattern the sides of the ridges and are perpendicular to ridge direction. Dotted line (s) indicates sectioning axis for the image in (G). Transmission electron microscope (TEM) cross-section through the scale ridges (G). The layers on the ridges form a multilayer photonic nanostructure. Scale bars lengths: (A) 10 mm, (D) 50 μm , (E) 2 μm , (F, G) 1 μm .

To confirm that differences in ridge spacing were not the result of sampling from two different wing regions (proximal vs distal) we measured ridge spacing in the closely-related, non-iridescent species *Heliconius erato demophoon* (S6). Ridge spacing did not significantly differ between the proximal (comparable to *H. sara* iridescent region) and distal (comparable to *H. sara* non-iridescent region) forewing (mean \pm SE ridge spacing, proximal = $0.906\mu\text{m} \pm 0.0101$, distal = $0.956\mu\text{m} \pm 0.0125$; paired t-test, $t = 1.94$, d.f. = 4, $p = 0.125$; S6 C-D). This suggests observed differences in ridge spacing in *H. sara* is associated with the presence of iridescent structural colour and not dependent on position of the scale along the wing.

Finally, correlation function analysis of the X-ray nano-tomography measured scales indicates a greater crossrib spacing in the black scale compared to the iridescent scale (iridescent $0.483\mu\text{m}$; non-iridescent $0.607\mu\text{m}$)(S1). An expanded crossrib spacing in black scales allows more light to enter the scale lumen and so be absorbed by melanin pigments (Siddique et al., 2017).

Whilst the general morphology of adult *H. sara* iridescent and non-iridescent scales is similar, morphological differences of the scale ridges are observed, with adult iridescent scales displaying considerably reduced ridge spacing compared to non-iridescent scales.

Development of *H. sara* scales

Our wing scale development series spans from 25% to 62.5% of total pupal development, encompassing scales emerging from the wing epithelium to the formation of final scale morphology (S7). At approximately 25% nascent scales begin to emerge as small actin-dense, cytoplasmic projections from the wing epithelium (S7A). Scale cell nuclei sit directly within the wing epithelium and are considerably larger than surrounding nuclei. Alpha-tubulin staining at 31% reveals the emerging scale buds are rapidly filling with cytoplasm (S7B) and are beginning to differentiate into cover (S7C, arrowhead) and ground scales (S7C, arrow), with the larger ground scales containing more cytoplasm. In some cases, the tubulin appears organized into dense arrays, suggesting ordered microtubules are beginning to form (S7C). By 37.5% the scales are essentially elongated sacs, containing thick longitudinal actin bundles (S7D). Previous research has shown that actin bundles are required for scale elongation and form through polymerization of actin into filaments (F-actin), followed by cross-linking of filaments together into thick bundles (Day et al., 2019; Dinwiddie et al., 2014). The actin bundles are most clearly discernible at the proximal portion of the scale where it buds from the epithelium through the developing socket (S7F, arrowhead).

At 50%-56% the scales become flattened and long finger-like projections form on the distal tip (S7G-4I). At this stage the actin bundles are highly ordered in appearance and cover the entire proximal-distal portion of the scale (S7I). At approximately 62.5%-69% chitin is deposited between the parallel actin bundles to form the parallel ridges.

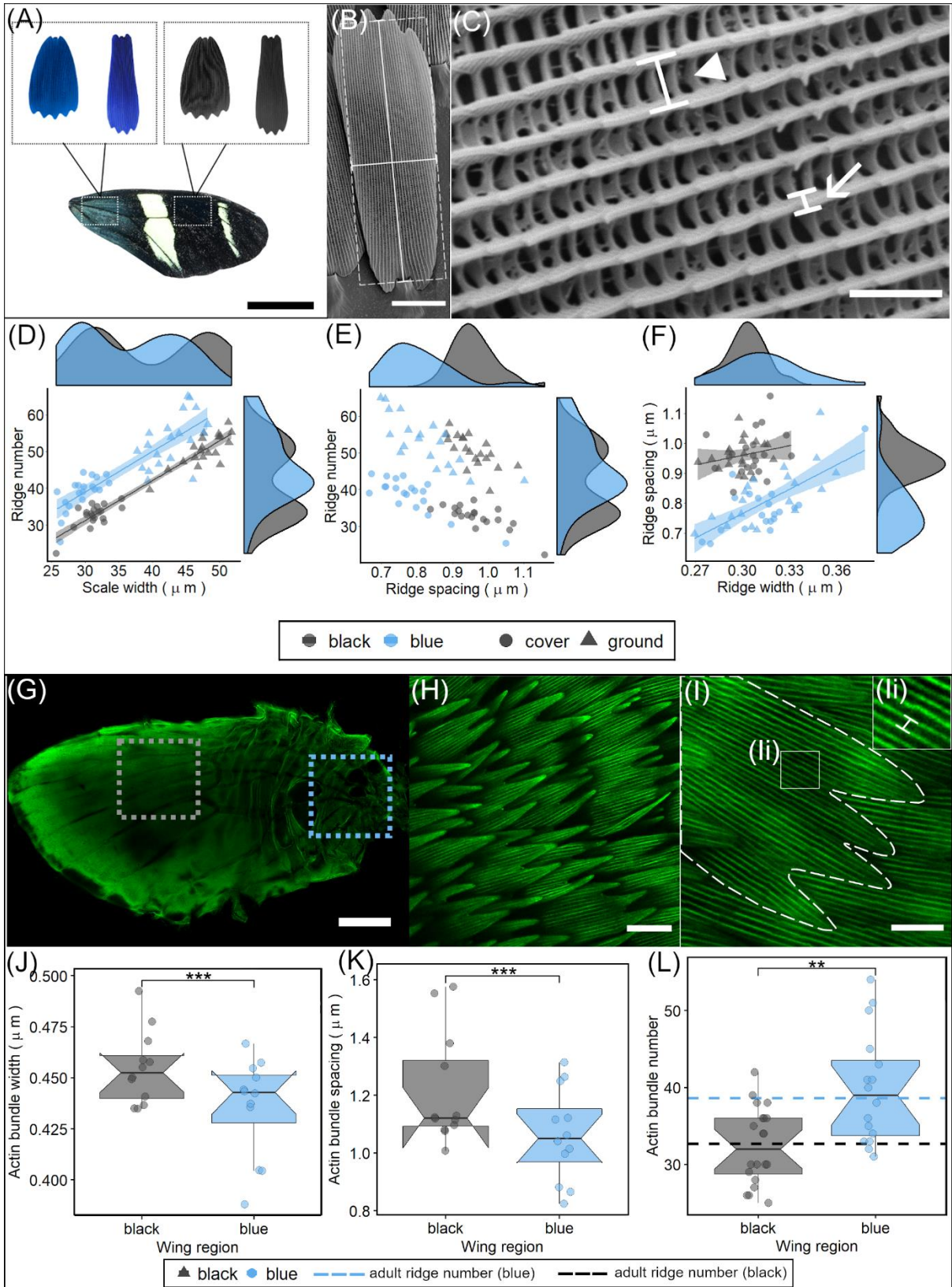


Fig 2: Morphological analyses of adult ridge organisation and pupal actin patterning. (A) Cover and ground scales (SEM images, false coloured) were sampled from the proximal, iridescent (blue) wing region and the distal, non-iridescent (black) wing region. Representative SEMs showing measurements of (B) scale length (vertical solid line), width (horizontal solid line) and approximate area (dashed line); and (C) ridge spacing (arrowhead) and ridge width (arrow). Comparison of cover and ground scales in blue and black wing regions for (D) ridge number and scale width (μm)(E) ridge number and ridge spacing (μm) (F) ridge spacing (μm) and ridge width (μm). Each point is the mean value grouped by individual, region and scale type. Shaded areas around regression lines indicate 95 % confidence intervals. Density plots on the axes give the distribution of each parameter for iridescent and non-iridescent scales separately (cover and ground combined). (G) Whole-mounted, phalloidin-stained *H. sara* forewing, showing the iridescent region (blue box) and non-iridescent region (grey box). (H) Overlapping wing scales at 50%, with actin bundles visualised through phalloidin staining. (I) Extraction of measurements of actin bundles from an individual developing scale. (Ii) High-magnification zoom of the individual actin bundles showing the spacing between two adjacent bundles. (J) Actin bundle width (μm) for 50% iridescent (blue) and non-iridescent (black) scales. (K) Actin bundle spacing (μm) for 50% iridescent (blue) and non-iridescent (black) scales. (L) Actin bundle number for iridescent (blue) and non-iridescent (black) scales, dashed lines indicate ridge number in adult cover scales. Points in (J, K) represent mean measurements for each individual grouped by region, points in (L) represent individual scales. Scale bar lengths: (A) = 10 mm, (B, H) = 20 μm , (C) = 2 μm , (G) = 1 mm, (I) = 10 μm .

F-actin patterning differs between developing iridescent and non-iridescent scales

We determined the optimal developmental stage to quantify actin organization as 50% of total pupal development. At this stage actin bundles are highly regular and have reached the distal portion of the scale (S7I and Fig. 2I) (Day et al., 2019; Dinwiddie et al., 2014). Additionally, chitin ridge deposition is beginning, suggesting that the actin bundles are correctly positioned for ridge formation to occur.

Using confocal microscopy of phalloidin-stained wings, we quantified the spacing and thickness of actin bundles within developing scales (Fig. 2G-L). Iridescent scales had slightly thinner actin bundles compared to non-iridescent scales (mean \pm SE bundle width, iridescent $0.438\mu\text{m}\pm 0.004$, non-iridescent $0.456\mu\text{m}\pm 0.003$; likelihood ratio, $\chi^2=19$, $p<0.001$; Fig. 2J). Differences in bundle width may be influenced by slight differences in development stages observed between the proximal and distal forewing scales (Dinwiddie et al., 2014). The developing iridescent scales had reduced actin spacing compared to the non-iridescent, black scales (mean \pm SE bundle spacing, iridescent $1.07\mu\text{m}\pm 0.02$, non-iridescent $1.22\mu\text{m}\pm 0.03$; likelihood ratio, $\chi^2=40$, $p<0.001$; Fig. 2K). Furthermore, we also found that iridescent scales had a greater number of actin bundles compared to non-iridescent scales (mean \pm SE actin bundle number, iridescent 40 ± 1.8 , non-iridescent 32 ± 1.1 ; likelihood ratio, $\chi^2=11$, $p<0.001$; Fig 2L)

This result is consistent with previous findings, indicating a tight coupling between the spacing of actin bundles and spacing of chitin ridges (Day et al., 2019). The mean number of actin bundles in iridescent and non-iridescent cover scales closely matched the mean number of ridges found in adult cover scales of both types (Fig. 2L).

Our results show that the patterning of actin in developing *Heliconius* scale cells plays an important role in governing the density of adult scale ridges, which is an important morphological parameter for controlling the iridescent properties.

TauSTED super-resolution microscopy reveals detailed remodeling of the actin cytoskeleton

Next, we used TauSTED to observe the ultrastructural remodeling of the actin cytoskeleton during the development of *H. sara* scales (Fig. 3, S8). At 44% of total pupal development we observe smaller peripheral actin bundles as well as larger internal actin bundles described previously by Dinwiddie et al., (2014) (Fig. 3 A-C). In scales with incipient finger formation, observed as distinct joints forming on the previously smooth distal edge, the location of finger origination coincided with the point at which prominent internal actin bundles attach to the membrane (Fig 3C, arrow). This hints at a possible role of these larger internal actin bundles in specifying spatial positioning of the fingers. Previous actin inhibition experiments performed by Dinwiddie et al., (2014) resulted in scales lacking fingers, consistent with a role of actin bundles in specifying finger position and elongation.

At 50% the actin bundles are maximally spaced in agreement with our confocal microscopy observations (S7). Z-projections of the optical sections suggest re-structuring of the actin bundles, with the continuous uniform actin bundles, now displaying a more intricate ultrastructural arrangement (Fig. 3D-F). In addition, some actin appears to be present between the large bundles (Fig. 3F), reminiscent of the transient ‘actin snarls’ described in *Drosophila* bristle development (Frank et al., 2006; Tilney et al., 2003, 2000b; Wu et al., 2016).

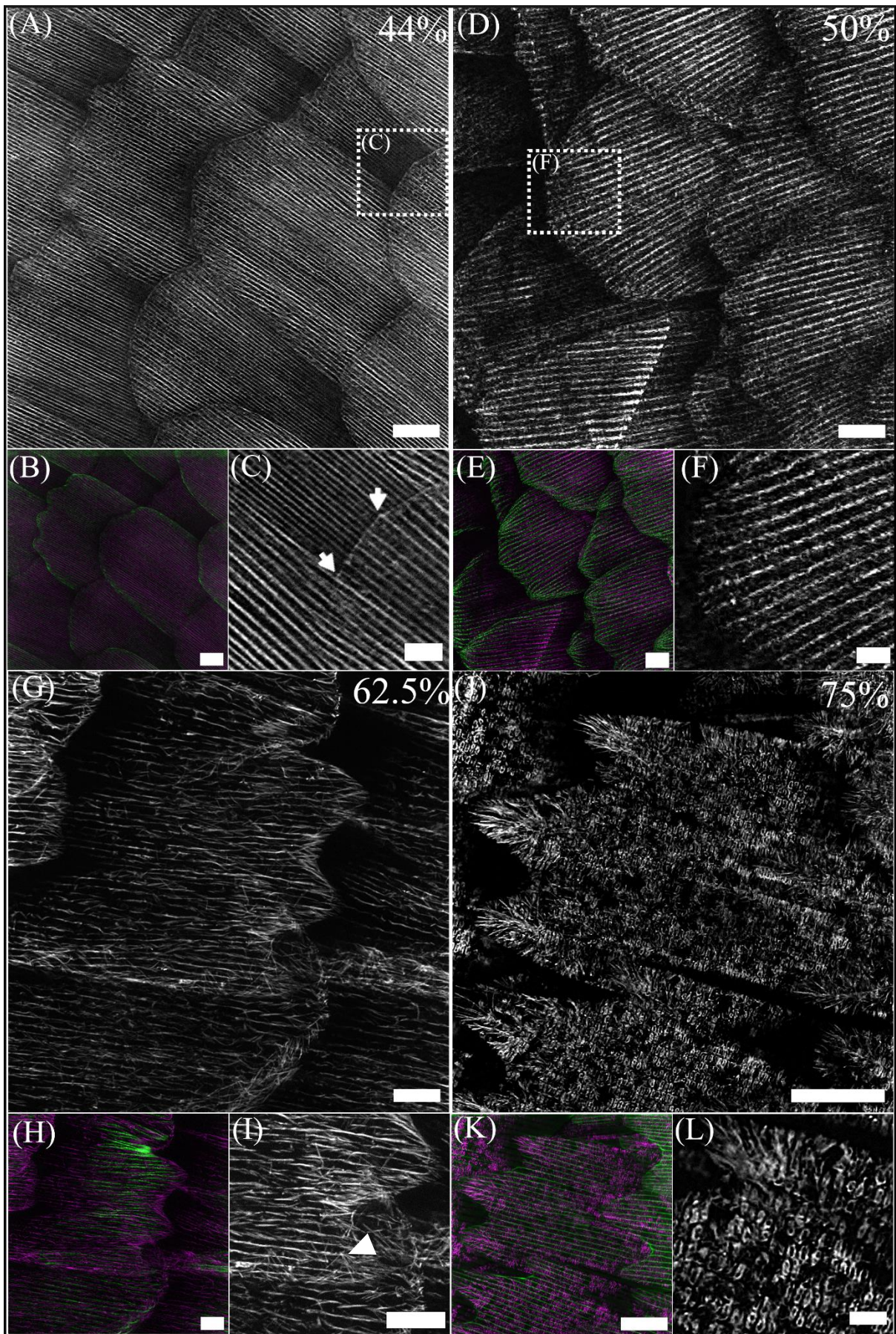


Fig 3: TauSTED super-resolution microscopy of the rearranging actin cytoskeleton during the development of *H. sara* scales. Grayscale images show F-actin stained with phalloidin. Colored images represent merge of actin (phalloidin, magenta) and chitin (CBD-TMR, green). (A) At 44% development small, numerous actin bundles are visible on the surface of each scale, with large actin bundles located internally. (B) Merged image indicating incipient cuticle formation at the periphery of the scale cells. (C) Enlarged section of actin bundles on the distal portion of a cover scale cell. Points of finger origination (arrows) correspond to locations of larger, internal actin bundles associating with the scale tip. (D) At 50% the actin bundles are maximally spaced as the scale cell becomes increasingly flattened. (E) Cuticle formation between the actin bundles is evident across the entirety of the scale. (F) Zoom of the actin bundles at the tip of a scale cell. (G, H) At 62.5% the large continuous, parallel actin bundles are dissociating. A second network of branched F-actin is located more internally of the larger actin bundles and is particularly evident along the scale edges and the fingers. (I) Many of the individual filaments appear to radiate from single points (arrowhead) and span across several microns before apparently attaching to the edge of the scale cell. (J) At 75% the actin network within the cell undergoes a final rearrangement. At the finger tips, highly branched actin projects from within the middle portion of the fingers towards the distal edges. Within the scale body no parallel bundles or branched filaments are visible, instead the actin has taken on ‘block’ like appearance. (K) by 75% ridge cuticle formation is complete and ultrastructures such as the crossribs are visible. (L) Enlarged section of the ‘blocks’ of actin, which are hollow in the middle where the crossribs are present. Scale bars: (A, B D, E, G, H) 5 μ m; (J, K) 10 μ m; (C, F, I, L) 2 μ m.

At 62.5% development the large actin bundles are undergoing disassembly, with fracturing of the bundles into disjointed sub-bundles (Fig. 3G-I). A previously undescribed second population of branched actin is now present and is particularly evident at the scale edges as well as the fingertips (Fig. 3I). These branched actin filaments are smaller in diameter, located more internally and are orientated multi-directionally compared to the actin bundles. Along the scale edge, multiple filaments appear to radiate like spokes from single points further inside the scale and connect with the scale edge (Fig. 3I).

At 75% the actin cytoskeleton undergoes a final, further reorganization with a highly branched network present in the fingers, radiating towards the distal fingertips (Fig 3J-L). In contrast, the main scale body is now entirely filled with square ‘blocks’ of actin which run the length of the scale and sit between the cuticle ridges. Z-projections indicate each block forms around the crossribs, though they do not fill the entirety of the nascent windows. By 81% (within 12 hours) this remaining actin network shows evidence of dissociation, beginning at the peripheral margins of the cell (S7 C, F). At 87.5% and beyond TauSTED imaging was not possible due to the presence of pigments.

Our TauSTED microscopy reveals novel aspects of actin cytoskeleton remodeling during butterfly scale development. The actin cytoskeleton plays a multifaceted role in butterfly scale development, from specifying finger location to a role in the development of certain ultrastructures such as the crossribs.

The actin cytoskeleton plays a direct role in optical nanostructure formation

SEM and optical imaging have shown that actin organization plays an important role in mediating the iridescent properties of *H. sara*, through the control of ridge spacing in adult scales. TauSTED imaging also revealed a complex network of actin present during the

formation of cuticle nanostructures. However, whether actin plays other, more direct roles, in optical nanostructure formation is unclear. To address this, we treated pupae with Cytochalasin D (cyto-D) at 50% of total pupal development, during ridge ultrastructure formation and incipient chitin deposition, to assess the effects of actin disruption on structural color production (Dinwiddie et al., 2014).

We observed substantial loss of structural color in cyto-D treated forewings, with wings appearing visibly dark blue-black in color (Fig. 4A, B) and a significant reduction in brightness (t-test, $t=4.34$, $d.f.=33$, $p<0.001$). Such structural color loss was not observed in the non-injected left forewing of treated individuals (Fig. 4A), nor the right forewing of controls (injected with Graces insect medium) (Fig. 4C, D). Reflectance spectroscopy of the proximal right forewing of cyto-D treated ($n=21$) and controls ($n=15$) was performed to quantify structural color loss. Cyto-D treated wings displayed a dramatic reduction in reflectance and flattening of the peak reflectance curve compared to control wings (Fig. 4E). A subtle peak in the cyto-D treated spectra is evident, likely resulting from individuals in which the treatment was unsuccessful. Indeed, this is evident from individual spectra plots (S9). Most cyto-D treated individuals exhibited a completely flat reflectance spectrum, no change in angular intensity (i.e., no iridescence) and significant structural color loss (S9).

We observed no discernible differences in the size of cyto-D treated scales compared to control scales (Fig. 4F-G, J-K). In some extreme cases we observed deformation of scale shape, with flexing of the fingers outwards and a ‘pinching’ of the central ridges (S10). There was no difference in the average ridge number between cyto-D treated and control scales (t-test, $t=-0.41$, $df=5$, $p=0.70$, Fig. 4O). This suggests that by 50% development, ridge number and position has already been established in scale cells.

SEM imaging of cyto-D treated scales revealed significant deformation of ridge structure compared to controls (Fig. 4I, M). This includes loss of ridge uniformity, evidenced by severe curving and collapse of the ridges (Fig. 4H, I and S10). We also observed that in some cyto-D treated individuals the window regions become filled entirely with cuticle (S10 B, E). In addition, we noted evidence of ridge layering disruption, with ‘breakpoints’ apparent in ridge layers of cyto-D scales (S11A, arrowheads) compared to the more continuous ridge layering seen in controls (S11B). To quantify ridge disruption, we compared curvature (κ) of the ridges between treated and control scales (Fig 4N). Cyto-D treated scales had significantly greater average ridge curvature (κ) (μm^{-1}) compared to controls (mean \pm SE curvature (κ), cyto-D treated $0.0566 \pm 0.0018 \mu\text{m}^{-1}$, control $0.0158 \pm 0.0006 \mu\text{m}^{-1}$; t-test, $t = -2.78$, $df = 12$, $p < 0.05$; Fig. 4N). We also noted a large distribution in the average curvature values of treated scales, consistent with the differing levels of scale disruption observed in SEM images.

Overall, these results show that perturbation of the actin cytoskeleton during scale ridge formation results in significant loss of structural color. This can be directly attributed to the disruption of the scale ultrastructural elements responsible for iridescent color production.

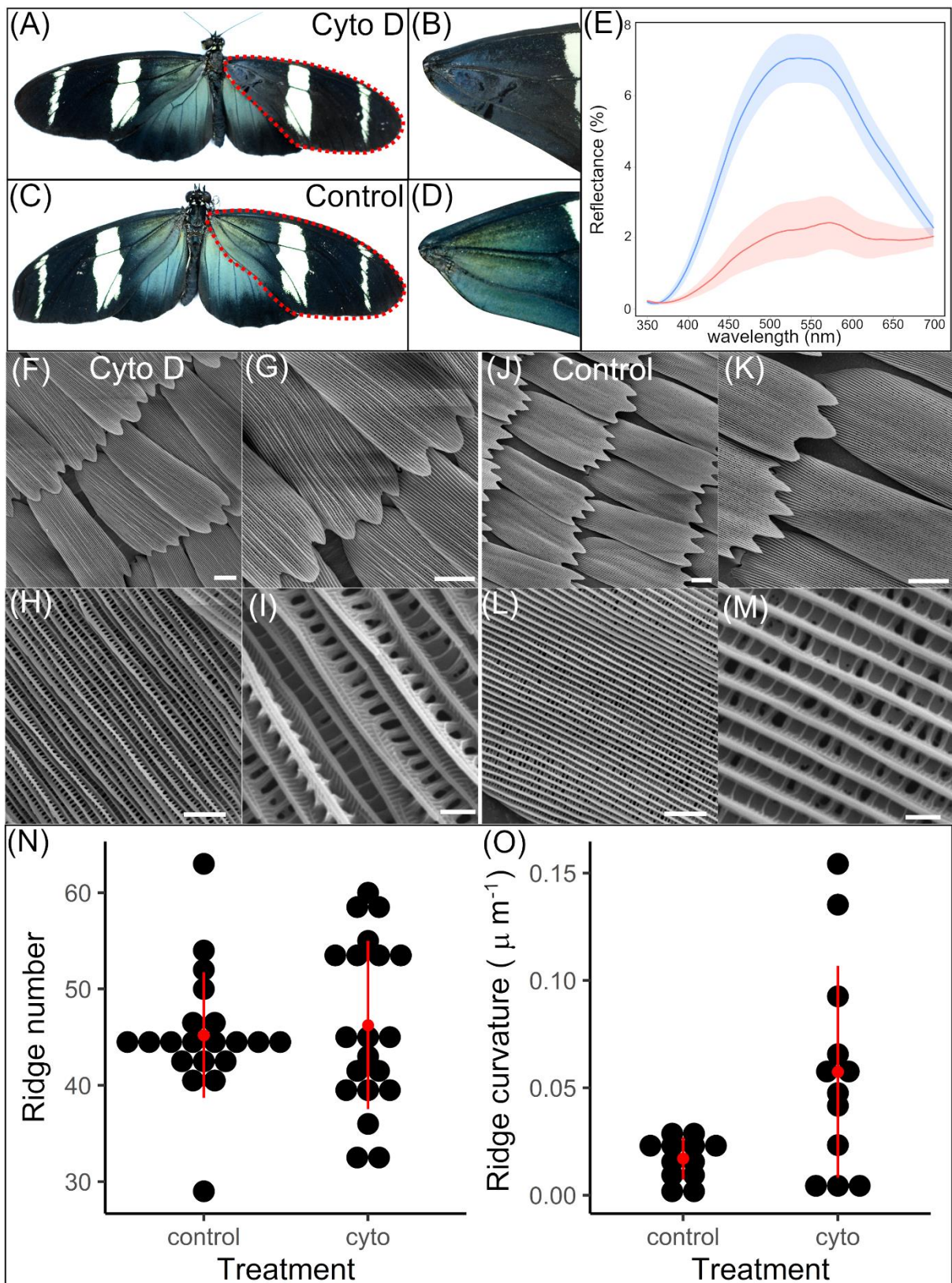


Fig 4: Chemical perturbation of actin with cytochalasin D at 50% development (A-D)

Typical morphological phenotype of butterflies injected with cytochalasin D (A) and graces insect medium/DMSO (control, C) into the right forewing at 50% development and zooms of each (A→B, C→D) showing the discernible color change of the iridescent region. (E) Reflectance spectra at the angle of maximum reflectance for control (blue) and cyto-D treated (red) wings. Shaded areas indicate standard error of the mean (for n=15 (control) and n=21 (cyto-d) measured individuals). (F-M) SEM imaging of typical cyto-d treated (F-I) and control (J-K) individual's wing scales in the treated region at different magnifications. Differences in brightness of the ridges indicates differences in height. (N) Ridge curvature (κ) for cyto-d treated and control scales. (O) Ridge number for cyto-d treated and control scales. Black points indicate individual scales. Red points and lines indicate the mean and standard deviation respectively. Scale bars lengths: (F, G, J, K) 15 μ m, (H, L) 5 μ m, (I, M) 1 μ m.

Discussion

The gross adult morphology of iridescent and non-iridescent *H. sara* scales does not differ dramatically. However, our results show that iridescent scales exhibit a substantial decrease in the spacing of parallel ridges (Fig. 2). Through comparisons between developing iridescent and non-iridescent scales, we determined that the reduced ridge spacing associated with adult iridescent scales can be attributed to the denser packing of actin bundles during pupal development (Fig. 2). Tighter ridge spacing is crucial for maximizing reflectance and therefore iridescent scale properties (Brien et al., 2018; Kinoshita et al., 2002). The layered lamellae responsible for iridescence in *H. sara* are present within these ridges and closer ridge spacing increases the density of light-reflecting surfaces within an individual scale. In the butterfly

Morpho adonis, (which also contains layered lamellae optical nanostructures), a reduction in ridge spacing of just 0.13 μm yields a 30% increase in reflectivity (Kinoshita et al., 2002). Our results show the actin cytoskeleton is crucial for controlling close spacing of ridges in iridescent scales, through denser packing of actin bundles during scale development (Fig. 2K).

The developmental control of total actin bundle number within scale cells warrants further investigation. *Drosophila* bristle studies have highlighted several actin binding proteins that may be key regulators of actin bundle abundance (Hopmann and Miller, 2003; Tilney et al., 2000b). Perturbation of two such proteins, Actin-binding protein 1 (Abp1) and Scar, within developing *Drosophila* bristles resulted in extra bristle ridges. These may be promising candidates for future studies of butterfly scale formation (Koch et al., 2012).

Dinwiddie et al., (2014) observed that structurally colored, silver scales of *Vanessa cardui* possessed double bundles of actin between ridges. In contrast, we observed little difference in actin bundle organisation between iridescent and non-iridescent scales of *H. sara* (Fig. 6). Although, subtle differences may be indiscernible due to variation in phalloidin staining (Hopmann and Miller, 2003) we suggest the incongruity of these results may be due to differences in morphology linked to structural colour production. Although, the gross morphology of *H. sara* iridescent and non-iridescent scales is similar (Fig. 2A-2F), the morphology of these different units in *Agraulis vanillae* is distinct. The iridescent scales of *A. vanillae* have fused windows, with chitin between their ridges, reduced crossribs, and precisely patterned microribs. This distinction in scale architecture is linked to the optical phenomena which *A. vanillae* harnesses to produce structural color; whose formation involves dramatic shifts in chitin deposition likely controlled by actin patterning (Adler, 2019; Dinwiddie et al., 2014). In contrast, layered lamellae in iridescent in *H. sara* develop upon an existing structure – the parallel scale ridges. There is no dramatic shift in architecture between iridescent and non-iridescent scales in *H. sara* and therefore the actin organisation is similar.

If, as proposed by Ghiradella (1974), F-actin provides the stress forces necessary to induce elastic buckling of the cuticle layer into layered lamellae, then we may expect to observe differences in actin dynamics, such as compressive forces, rather than large-scale differences in organization (Ghiradella, 1974). Indeed, our perturbation of the actin cytoskeleton using cyto-D and the resultant reduction in iridescence (Fig. 6A) could be indicative of an additional, more direct role of F-actin in controlling the layered lamellae architecture.

Cyto-D promotes sub-bundling of actin, resulting in wavy and distorted actin bundles within cells (Guild et al., 2002; Tilney et al., 2000a). We saw that disruption of the mechanical integrity of actin during optical nanostructure formation causes considerable reduction in iridescence (Fig. 4) indicative of an additional, more direct role of actin in forming the layered lamellae. The deformed ridges observed in our cyto-D treated butterfly scales (Fig. 4I) display similarities to bristle phenotypes observed in fly mutants for actin organization proteins (Hopmann et al., 1996; Shapira et al., 2011; Tilney et al., 1995). Similar to fly bristles, actin bundles in butterfly scales are crucial for ridge formation, which occurs through extracellular chitin deposition in the inter bundle regions (Frank et al., 2006; Shapira et al., 2011; Tilney et al., 1996). Without actin bundles correctly guiding these projections the final chitin ridges form in an aberrant manner, leading to ridges of varying geometries (Shapira et al., 2011). We predict that the primary loss of structural color in our treated samples is likely attributed to collapse of ridges into varying angles, resulting in the multilayer photonic nanostructures no longer in registry with one another and therefore preventing concerted light reflection.

Interestingly, we observed additional phenotypic effects of actin perturbation on ridge ultrastructure. Harnessing both SEM and AFM (S10, S11 arrowheads) we noted regular ‘breakpoints’ appearing on the usually continuous ridge layers. We interpret this observation with caution as the ridge layering is more visible on the collapsed ridges of treated scales compared to the more perpendicular ridges of controls (Fig. 4I, M). The disruption of ridge

layering suggests a further role of actin in directly controlling the formation of layered lamellae. Whether this perturbation of actin disrupts stress forces required to buckle the cuticle into layers, as predicted by Ghiradella, (1974) or instead prevents correct localization of chitin synthase enzymes to deposit the ridges (Adler, 2019) presents an interesting topic for future investigation.

Cyto-D may also have disrupted the secondary branched actin network present within scales (Fig. 3I, L). Our TauSTED imaging showed this network was particularly prominent after 63.5% of total pupal development, when the cuticle ridges had already formed, and the parallel actin bundles were breaking down (Fig. 3G-I). We speculate that this network may be involved in stabilizing the scale cuticular structures as the prominent parallel actin bundles break down. During this stage the scale is still filled with cytoplasm and therefore likely subject to high cytoplasmic pressure (Clark et al., 2014). In support of this prediction, we see actin filaments in between the cuticle ridges, as well as a high density of branched actin at the scale edges and in the fingers (Fig. 3I). Furthermore, some scales treated with cyto-D exhibited loss of overall uniformity, such as splayed fingers, consistent with disruption to a scale-wide stabilizing mechanism (S10A). The branched actin filaments may act as a series of intracellular ‘struts’, keeping the complex cuticular ultrastructure in a fixed registry until cuticle deposition is completed. Interestingly, at 75% of total pupal development the actin becomes ‘block-like’ as it arranges around the crossribs (Fig. 3 J-L), suggesting that this stabilizing mechanism of actin may follow the path of the depositing cuticle internally as scale development progresses.

Overall, our study shows that the actin cytoskeleton plays a crucial role in the development of structural color in the butterfly *H. sara*. Through denser packing of actin bundles during development, iridescent *H. sara* scales attain a higher density of chitin ridges enhancing optical reflectance. In addition, using actin perturbation experiments we demonstrate that the actin cytoskeleton likely plays a more direct role in the development of layered lamellae. The actin

“scaffold” appears to template the chitin deposition and make the chitin structures (as they are forming) more mechanically stable during this process. Absence or diminution of the actin results in photonic structures that are out of registry with one another leading to dramatic changes in the overall reflected intensity and directionality of the structural color.

We postulate that the role of actin may be akin to the layout and pinning stage used in dressmaking, so it is crucial to achieving high levels of long-range order and perfection across an entire scale cell. As such, this result observed in *H. sara* may be at play in the formation of ridge reflectors in across many Lepidoptera species. Ultimately, we show the actin cytoskeleton within butterfly scales cells plays a crucial and multifaceted role in precise optical nanostructure development underpinning structural coloration.

Materials and Methods

Butterfly rearing

Stocks of *Heliconius sara* were purchased from Stratford-upon-Avon Butterfly Farm, United Kingdom. Adult butterflies were maintained in breeding cages at 25 °C, at the Arthur Willis Environment Centre, University of Sheffield. Adults were fed on 10 % sugar water solution with ~1 gram of added pollen per 200 ml. Shoots of *Passiflora auriculata* were provided for adults to lay eggs on. The eggs were collected twice weekly and caterpillars kept at 25 °C, 75 % humidity and fed on shoots of *Passiflora biflora*. Pre-pupation caterpillars were checked regularly and the time of pupation was recorded as the point of pupal case formation.

At the desired stage, wings were dissected from pupae in phosphate buffered saline (PBS) and immediately fixed for 15 minutes in 4 % paraformaldehyde in PBS, at room temperature. Developmental stages of pupae were recorded as a percentage, with *H. sara* taking 8 days from pupation to adult eclosion.

Electron Microscopy

Scanning electron microscopy (SEM)

Adult wing samples were cut from regions of interest and adhesive tape was lightly applied to remove some cover scales. Samples were then adhered onto SEM mounting stubs using 9 mm carbon tabs (Agar Scientific). Mounted samples were vacuum coated with several nanometres of gold using a sputter coater (Agar Scientific). SEM was undertaken using a JEOL JSM-6010LA SEM, equipped with InTouchScope software.

Transmission electron microscopy (TEM)

TEM protocols followed Shawkey et al., (2003). Adult iridescent *H. sara* wing scales were removed and washed with 0.25M sodium hydroxide with 0.1% Tween. Samples were transferred to a 2:3 solution of formic acid to EtOH for several hours and then dehydrated in 100% EtOH. Samples were infiltrated with Epon epoxy resin through washes of 15%, 50%, 70% and 100% Epon in propylene oxide. Samples were placed in resin molds and cured in a 60 °C oven overnight. Thin sections of the sample (70-100 nm) were cut using a Leica ultramicrotome and placed on a copper grid. Uranyl acetone staining was performed on the samples for 10 minutes before two washes in distilled water for 5 minutes. Further staining was undertaken using Lead nitrate, sodium citrate and 1M sodium hydroxide. This was followed by two additional washes in distilled water. Imaging was performed on a Phillips CM100 Transmission electron microscope with an accelerating voltage of 100 kv.

Atomic force microscopy (AFM)

AFM imaging of wing scales was undertaken using a Digital Instrument Dimension 3100 Scanning probe microscope equipped with a Nanoscope IV controller. AFM was performed in tapping mode as previously described (Parnell et al., 2018). Data visualisation and image reconstruction was performed using the freely available software Gwyddion (Nečas and Klapetek, 2012).

Synchrotron X-ray nanotomography

Individual scales were mounted vertically onto fine needle tips using a 3-axis optical alignment stage and UV-curable adhesive. X-ray nanotomography was performed at the PO5 imaging beamline at PETRAIII, Deutsches Elektronen-Synchrotron facility (DESY), Hamburg. Samples were rotated through 360° while scanning. Axis alignment, thresholding and 3D volume reconstruction was performed manually in Python, using High Speed Tomography in Python (PyHST) software. See (Burg, 2018) for full rendering methods. Values of ridge spacing and crossrib spacing were extracted from the reconstructed images using correlation function analysis (Strobl and Schneider, 1980).

Immunofluorescence

Fixed wings (4% PFA in PBS (phosphate buffered saline)) were washed several times in PBSTx (0.5-1% Triton-X 100). For microtubule staining, samples were then blocked in 5% Goat serum in PBSTx, rocking at room temperature for two hours. Primary antibody labelling was conducted using a mouse Anti- α -Tubulin antibody (T6199, Sigma) at 1:1000 in PBSTx, overnight at 4 °C. Secondary antibody incubation used Cy3 AffiniPure Donkey Anti-Mouse (Jackson ImmunoResearch) at 1:300 and samples were incubated at room temperature for 2-3 hours. For staining of the actin cytoskeleton and/or membrane wings were left overnight at 4 °C in Phalloidin (Alexa Fluor 555/ ATTO-647; Invitrogen) or SiR-actin (Spirochrome) at 1:200 in PBS and/or Wheat Germ Agglutinin (WGA) (Alexa Fluor 647 conjugate; Invitrogen) at 1:300 in PBS. For the STED microscopy dye concentrations were increased and WGA was replaced by a Chitin Binding Domain (TMR) (New England Biolabs; special request). Finally, DAPI (1 μ g/mL) was used for counterstaining. Wings were mounted onto slides with Fluoroshield (Merck) for confocal microscopy and Mowiol or Prolong Diamond Antifade (Invitrogen) for

STED microscopy and a coverslip applied. Left hindwings were used as controls, following the above protocol but omitting the fluorescent dye and/or primary antibody.

Confocal microscopy

Confocal microscopy imaging was performed on a Nikon A1 confocal laser microscope equipped with NIS elements software. Z-stacks were assembled into single images using FIJI (Schindelin et al., 2012).

TauSTED microscopy

Super resolution imaging was performed on a Leica TCS SP8 STED microscope with Falcon module at the Central Laser Facility, Oxford, UK. Stained wings were mounted onto slides using Mowiol and #1.5 High Precision coverslips (Marienfeld). Slides were stored at 4 °C until imaging. For each slide, both the proximal iridescent region and distal non-iridescent region was 3D imaged (voxel size 23x23x156 nm) using Leica HC PL APO CS2 100x/1.40 Oil objective and HyD SMD detectors. To achieve the STED effect we used 660 nm, 1.5 W CW (continuous wave) laser and 775 nm, 1.5W pulsed laser, for the corresponding fluorophores with 20% laser power. The acquired images were processed using as phasor based TauBackground Suppression (background removal from lifetime contributions uncorrelated to the STED process) and TauStrength (resolution increase) tools from the Leica LAS X software (Alvarez et al., 2021).

Comparative analyses of iridescent and non-iridescent scales

*SEM analysis of adult scale *H. sara* morphology*

H. sara butterflies were taken from breeding stocks maintained at the University of Sheffield. 20 individuals, consisting of 10 males and 10 females, were used for analysis. For each individual a forewing was removed and a 5 mm x 5 mm section of both the iridescent region

and non-iridescent, black region was used for SEM. For each region, images were taken of 10 cover and 10 ground scales.

ImageJ (Schneider et al., 2012) was used to measure the length of each scale, taken from the distal edge of the socket to the distal tip of the scale. Ridge spacing was calculated using PeakFinder Tool (Vischer, 2011) (S1 Fig). At the midpoint of scale length, a 90 ° transect was taken across the scale to measure its width and the numbers of ridges were calculated using the PeakFinder Tool. The average ridge spacing was calculated as scale width divided by total number of ridges. Scale area was calculated using scale length multiplied by scale width, using the rectangular area as an approximation of true scale area. Ridge width was calculated using the Ridge Detection plugin (Steger, 1998) (S4). For each individual, 5 ground and 5 cover scales per region were used to calculate ridge width. For each scale, a 600 x 600 pixel section from the middle of scale was selected for analysis. Contrast and brightness levels were adjusted manually to optimal levels using FIJI (Schindelin et al., 2012). The Ridge Detection parameters were set as follows: Sigma = 3.10, Lower Threshold = 0.51, Upper Threshold = 3.40, Minimum Line Length = 40.00, Maximum Line Length = 0.00.

*SEM analysis of adult *Heliconius erato demophoon* scale morphology*

H. erato demophoon butterflies were taken from University of Sheffield collections (captive reared individuals), with 5 individuals used for the analysis. For each individual a 5 mm x 5 mm section from both the proximal forewing and distal hindwing were mounted for SEM. For each region images were taken of 5 ground and 5 cover scales. Ridge spacing measurements followed the methods described above.

Confocal analysis of actin in developing scales

The dissected forewings of 12 individuals were phalloidin stained following the protocol above. Stained wings were mounted on slides and imaged on a Nikon A1 confocal. For each

slide, several Z-stack images were taken from both iridescent and non-iridescent regions using a x40 oil objective lens. From each wing region, we selected 5 scales for analysis which showed minimal disruption and the least overlap with other scales. Images were converted into 8-bit grayscale images in FIJI. A 100 x 100 pixel section of the scale was cropped out and stacked using the sum slices. Actin spacing was calculated as the mean distance between the centre of the actin bundles. The Ridge Detection plugin (Steger, 1998) in FIJI was used to calculate the mean actin bundle width. The Ridge Detection parameters were set as follows: Sigma = 1.22, Lower Threshold = 4.76, Minimum Line Length = 10.00, Maximum Line Length = 0.00. The upper threshold was set between 12.58 and 21.93 to account for slight differences in brightness between experiments. At least 4 ridges per scale were used to calculate mean actin bundle width. In addition, the total number of actin bundles per scale was calculated from 20 black and 16 blue scales from across 11 individuals.

Statistical analyses

All statistical analyses were performed in R (Version 3.5.2) (R Core team, 2018). For SEM analyses of adult iridescent and non-iridescent *H. sara* scales, we constructed a linear mixed effect model for each response variable (scale area, scale length, scale width, ridge spacing, ridge width) using the lme4 package (Bates et al., 2015). Prior to fitting the mixed effect model for ridge width, we averaged individual ridge measurements per scale. For models of ridge spacing, scale area and ridge width we included 'individual' as an intercept only random effect and for the model of ridge spacing, we included an interaction term between scale type and region. For scale length and scale width we fitted a random slope mixed model, allowing a different response to wing region for each individual. We used likelihood ratio tests between models with the Chi-squared distribution to assess statistical significance of sequentially dropped terms. For pairwise comparisons, Tukey multiple comparison tests were performed using the emmeans package in R (Lenth et al., 2018). For analyses of the ridge spacing between

the proximal and distal scales of *H. e. demophoon*, we firstly averaged measurements for each region per individual. Given the lower sample size we performed a paired t-test.

For analyses of actin bundle width, bundle spacing and bundle number in developing iridescent and non-iridescent scales, we constructed linear mixed effects models using the Lme4 package (Bates et al., 2015). For bundle spacing and bundle width we firstly averaged bundle measurements per scale to account for multiple bundle measurements. For all models we fitted ‘individual’ as an intercept only random effect and tested statistical significance using likelihood ratio tests with a Chi-squared distribution.

All figures were constructed with ggplot2 (Wickham, 2016), GIMP (v.2.8.22.) (The Gimp Development Team, 2014) and ImageJ (Schneider et al., 2012).

Chemical perturbation of actin

Actin inhibition experiments followed the protocol of Dinwiddie et al., (2014). Ready-made cytochalasin D solution (Merck) (5 mg/ml in DMSO) was diluted to a final concentration of 20 μ m in Graces insect medium (Merck). Pupae were injected at 4- days post pupation using a Hamilton microliter syringe (701N). 5 μ l of drug was injected directly into the proximal portion of the right wing blade. Control pupae followed the same protocol but were injected with 5 μ l of 20 μ m DMSO in Graces insect medium. Pupae were allowed to continue development until eclosion. Immediately after the wings had dried post-eclosion, butterflies were humanely killed. Butterflies which failed to emerge properly were discarded from further analyses. Only batches with an eclosion rate of over 50% were included in further analyses. A chi-squared test was used to assess differences in emergence rate between control and treated pupae. Whole wing imaging was performed on a Nikon D7000 DSLR camera. Scale imaging was performed using SEM and AFM (see above).

Reflectance spectroscopy

Reflectance spectrometry was undertaken using an Ocean Optics USB2000+ Spectrometer connected to a PX=2 pulsed xenon light source with a fibre-optic probe. Right forewings from 15 controls and 21 treated individuals were mounted onto a rotating optical stage and measurements taken following the methods of Parnell et al., (2018). Spectra Suite (Ocean Optics) software was used to acquire scans. Integration times were set at 350 ms, using 5 scans to average and a boxcar width of 3 nm. Data was analysed in R, using the package PAVO (v. 2.4.0) (Maia et al., 2013). Spectra were smoothed using the 'Prospec' function and peaks extracted using the 'Peakshape' function. Average spectra for control and treated individuals were plotted using the 'Aggplot' function.

Phenotypic analyses of actin perturbation

SEM was used to acquire ridge number measurements for 4 control and 4 treated individuals following the methods outlined previously. Five scales per individual were selected from regions across the sample. Statistical comparisons of ridge number between control and treated samples were analysed using a Welch two-sample t-test in R. High magnification SEM images of three scales per individual were selected for curvature analysis. The FIJI package Kappa (Mary and Brouhard, 2019) was used to acquire measurements of curvature (κ) for 10 ridges per scale. Using control points plotted along individual ridges, curves were inputted as open B-splines and fitted using a 'Point Distance Minimisation' algorithm. The parameters were set as follows: Data Threshold Radius = 15, Global Threshold Level = 0.05 and Local Error Threshold = 0.05. All other parameters were maintained at default levels. Average ridge curvature was calculated per scale and comparisons performed using a Welch two-sample t-test. AFM was performed on scales from the right forewing of 2 control and 2 treated individuals, using the methods outlined above. For each scale four transverse cross-sections

were taken across the image encompassing as many ridges as possible and the profiles plotted. Several replicates were taken per individual. From these profiles, ridge height measurements were calculated using the absolute minimum value of the data to the top of the ridge peak. Average height per ridge was plotted for the treatment and control scales.

Acknowledgements

We thank Dr. Alan Dunbar (CBE, University of Sheffield) for use of the scanning electron microscope (funded via the EPSRC grant EP/K001329/1). We are grateful to Chris Hill (Department of Biomedical Science, University of Sheffield) and Frane Babarović (School of Biosciences, University of Sheffield) for assistance in transmission electron microscopy. We thank Darren Robinson (Light Microscope Facility, University of Sheffield) for assistance with optical imaging. We also thank Dr. Natalia Bulgakova and Dr. Miguel Ramirez (Biomedical science department, University of Sheffield) for provision of an Anti- α -tubulin antibody and their expertise in immunofluorescent staining. We thank William Hentley (Department of Animal and Plant Sciences, University of Sheffield) for assistance in the high-magnification imaging of the wings. Finally, we thank Gonzalo Castiella Ona who provided invaluable assistance within the laboratory during his Erasmus funded internship.

Funding

This research was supported by the following grants: Natural Environment Research Council (NERC) Fellowship to N.J.N (NE/K008498/1). This work was also funded from through a NERC doctoral training partnership (Adapting to the Challenges of a Changing Environment) (V.J.L).

Author contributions

Specific contributions of authors are detailed at the start of the chapter.

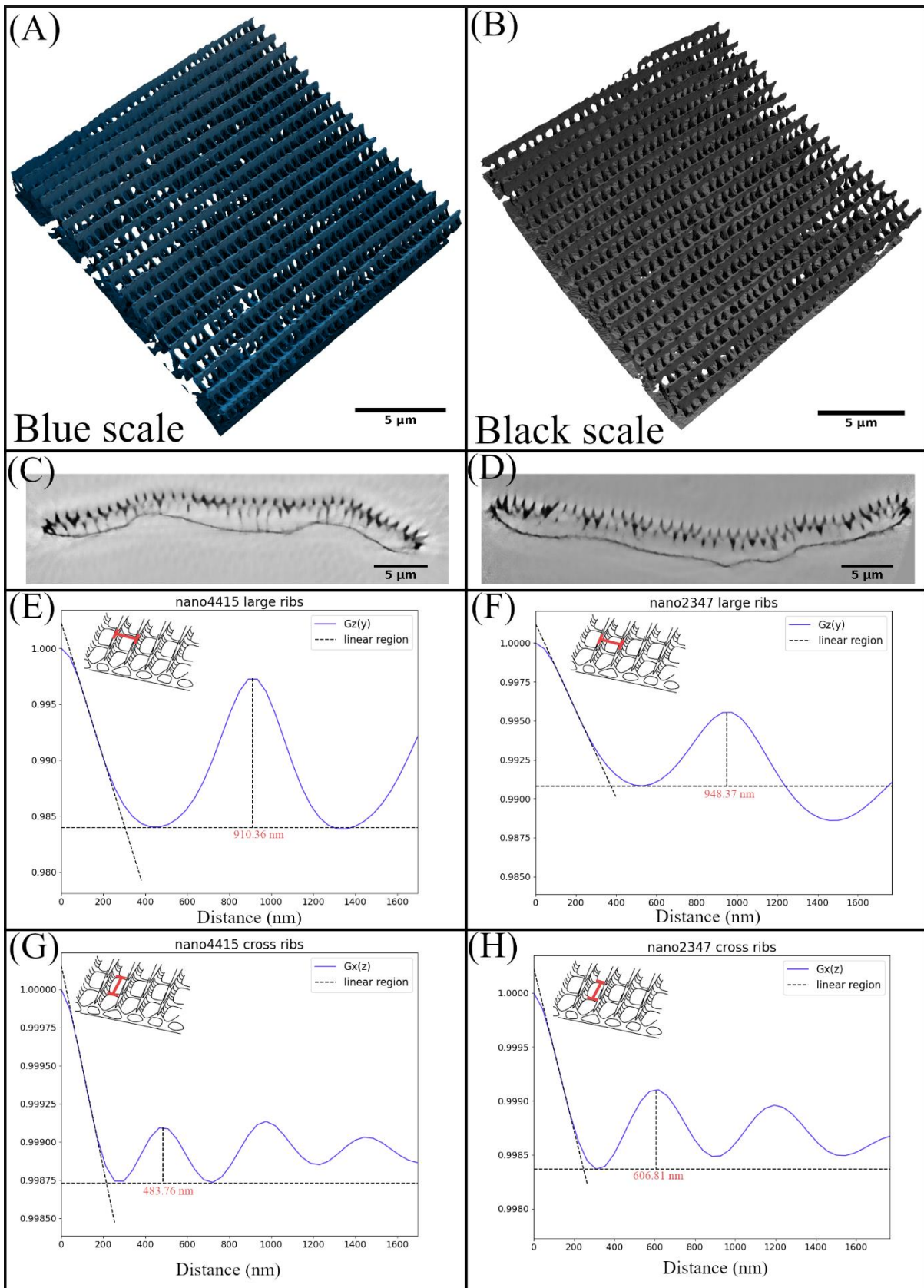
Supplementary information

Supplementary results

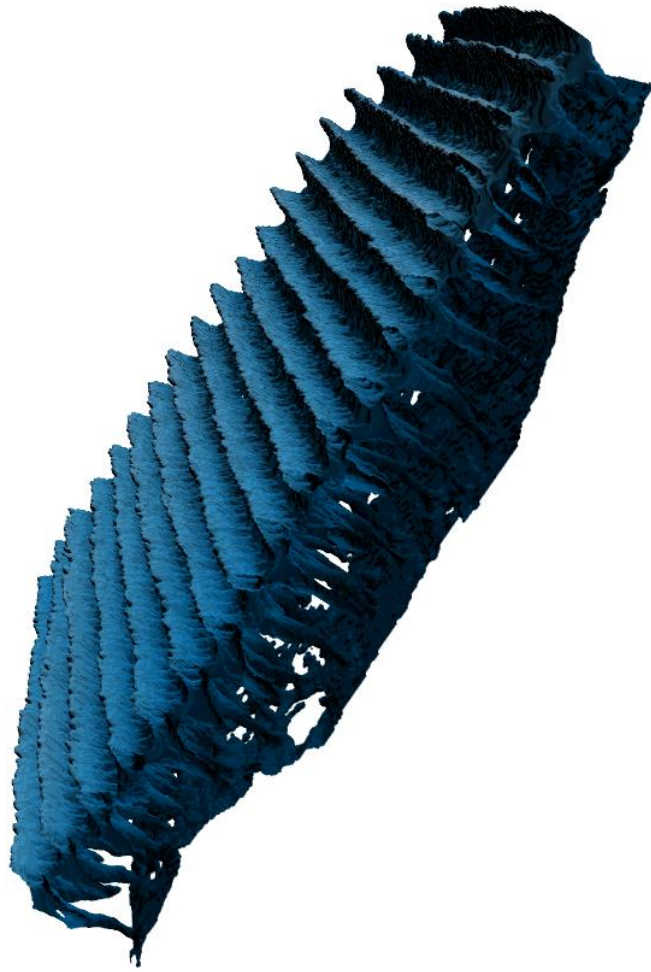
There was a significant difference in the length of iridescent and non-iridescent cover scales (Tukey comparison, $p < 0.001$), but not ground scales (Tukey comparison, $p = 0.99$) (mean \pm SE scale length, blue (cover, ground) = $91.7 \mu\text{m} \pm 0.48$, $86.6 \mu\text{m} \pm 0.47$; black (cover, ground) = $97.4 \pm 0.56 \mu\text{m}$, $86.4 \mu\text{m} \pm 0.41$).

Ridge width was slightly greater in iridescent scales compared to non-iridescent scales (mean \pm SE ridge width, iridescent $0.315 \mu\text{m} \pm 0.002$, non-iridescent $0.302 \mu\text{m} \pm 0.001$; likelihood ratio, $\chi^2=43$, d.f. = 1, $p < 0.001$; Fig. 2F). There was no difference in ridge width between cover and ground scales (likelihood ratio, $\chi^2=0.24$, d.f. = 1, $p=0.622$, Fig. 2F). Interestingly, the distribution of ridge width in iridescent scales was much greater than that of non-iridescent scales (S5C). However, measurements of ridge width from SEM images could be sensitive to the imaging angle, with ridge height being confounded in some cases with ridge width. The X-ray nanotomography data did not support this difference in ridge width between iridescent and non-iridescent scales (iridescent scale, 303nm; non-iridescent scale, 373 nm).

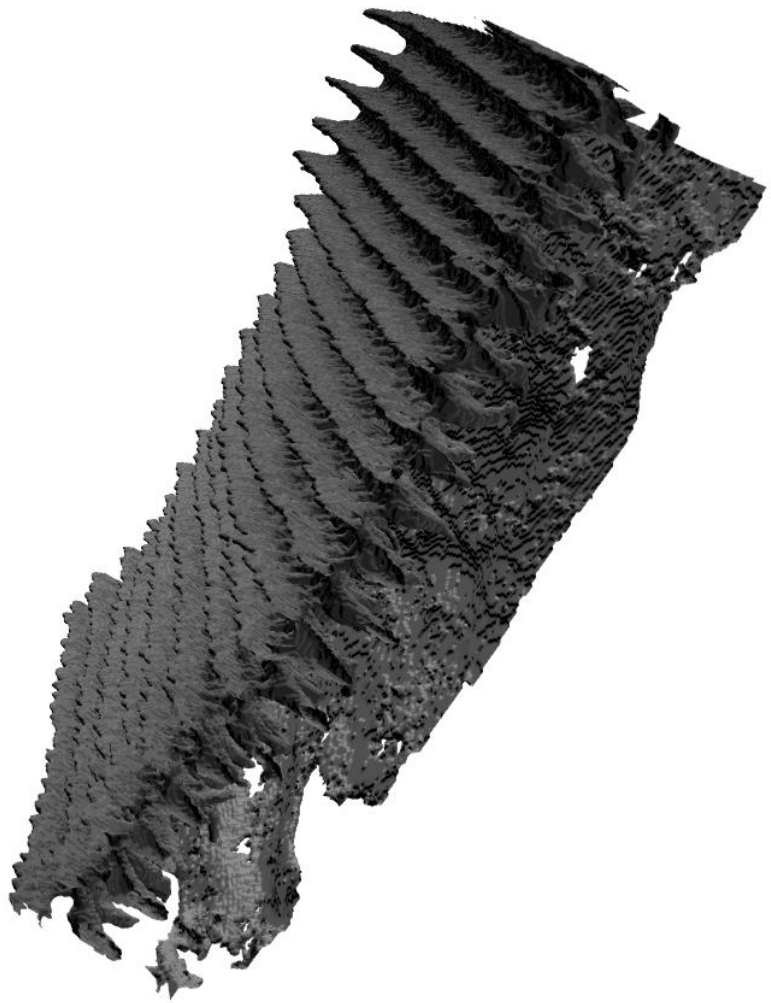
Supplementary figures



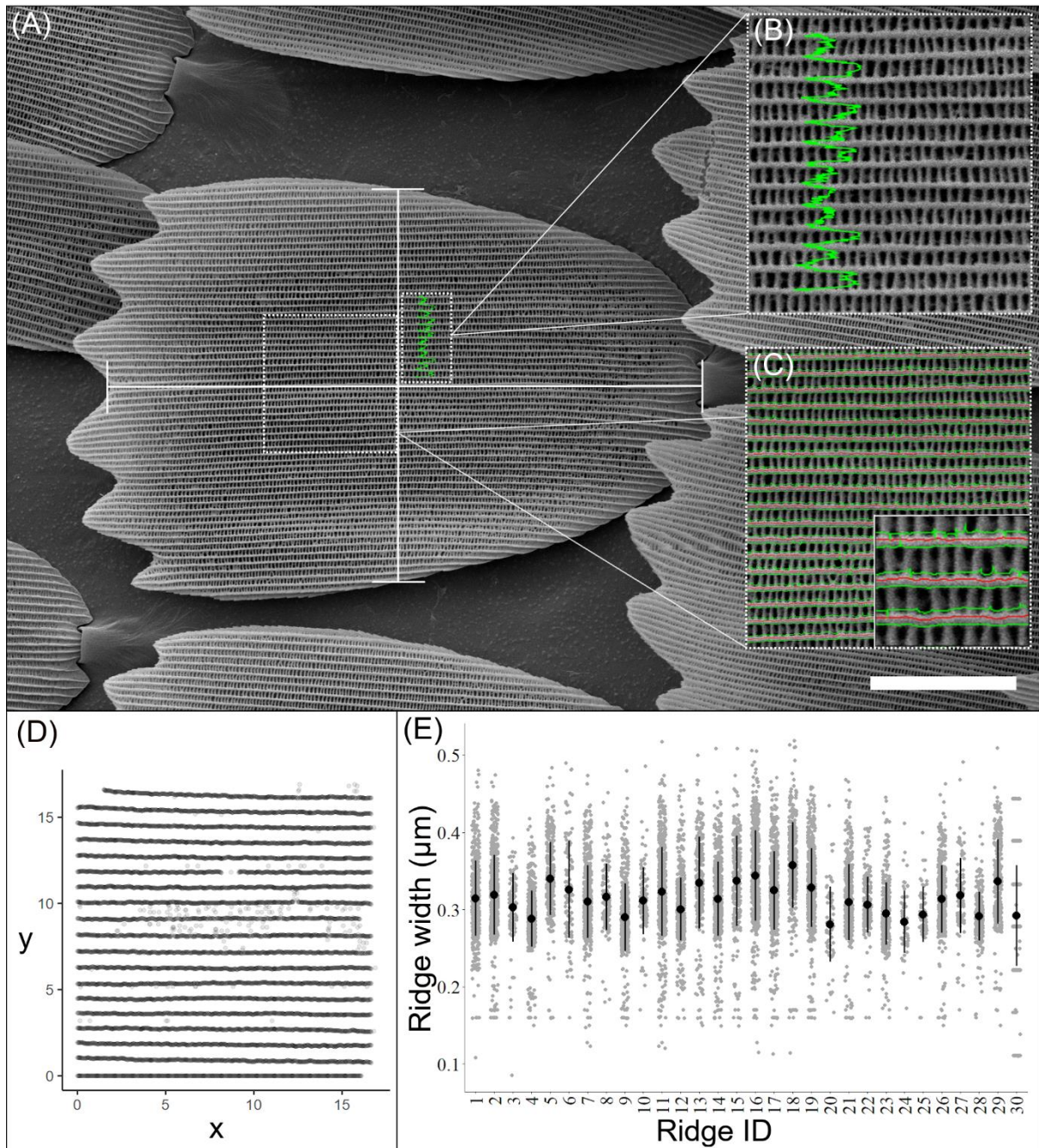
S1: Synchrotron X-ray nanotomography of an adult iridescent and non-iridescent scale of *H. sara*. Reconstructed 3D images of the central region of a blue, iridescent (A) and a black, non-iridescent scale (B) demonstrating the similarities in general morphology of both scale types. Sliced view (YZ plane) of the rendered iridescent (C) and non-iridescent (D) scales. (E-H) Extraction of morphological parameters from the rendered images using correlative function analysis. Red number indicates measured parameter value. Extraction of ridge spacing from the iridescent (E) and non-iridescent scale (F). Extraction of crossrib spacing of the iridescent (G) and non-iridescent scale (H). Scale bar lengths: (A, B) = 5 μm , (C, D) = 5 μm



S2: Movie of an X-ray nanotomography reconstructed blue, iridescent scale. False coloured, blue.

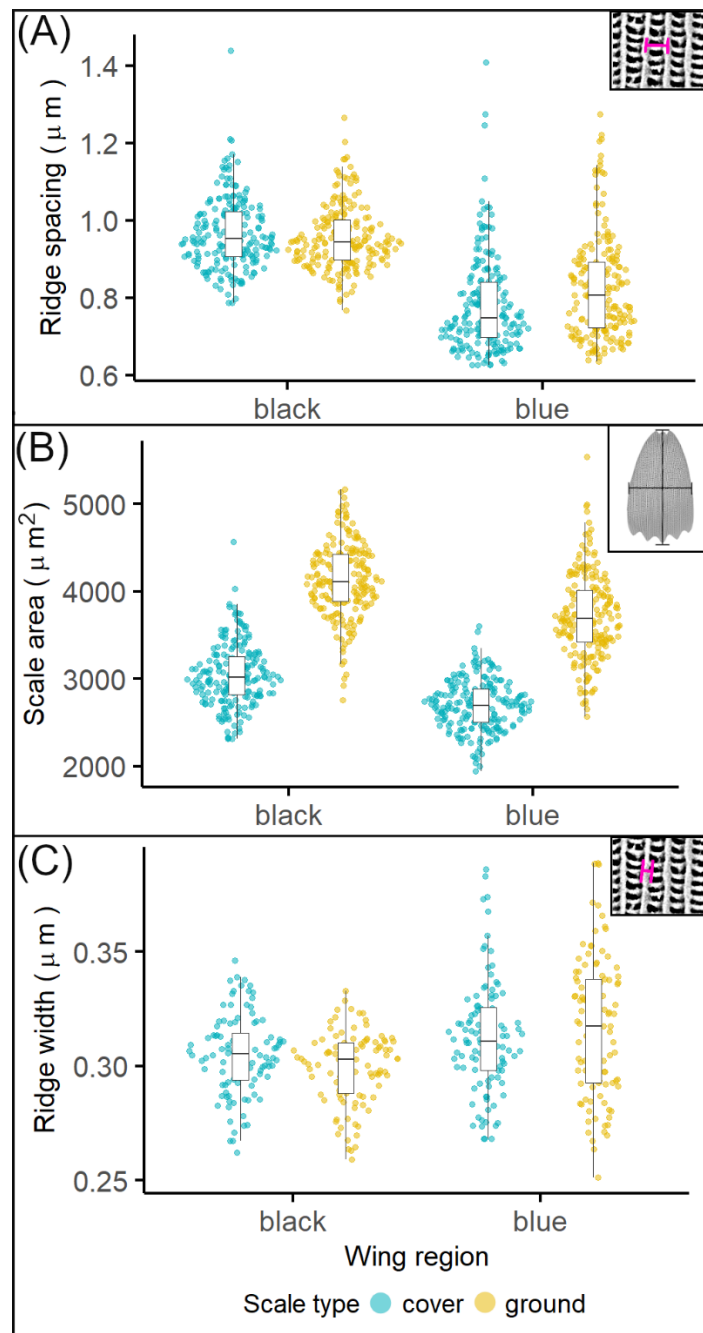


S3: Movie of an X-ray nanotomography reconstructed non-iridescent, black scale. False coloured, black.

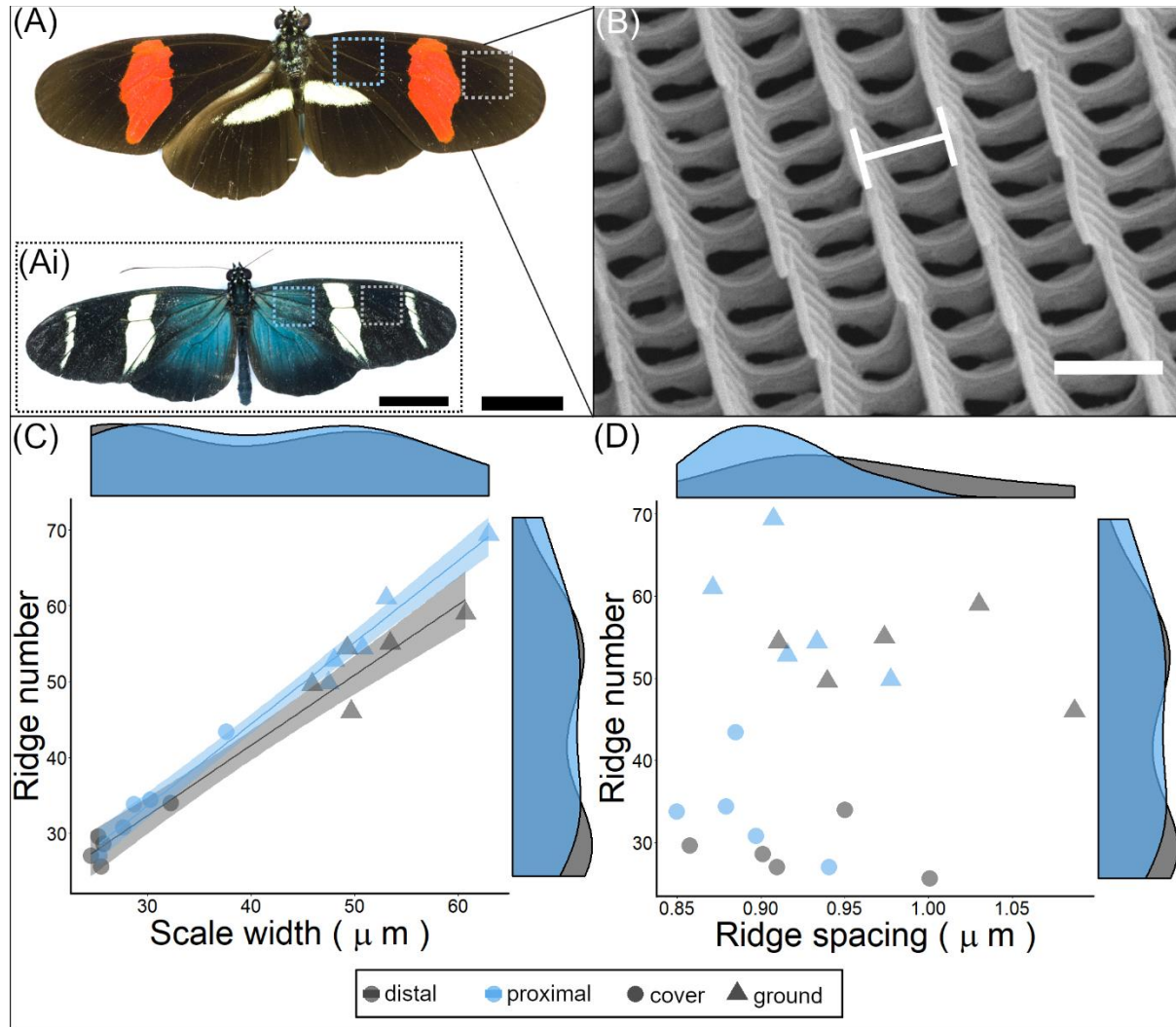


S4: Methods of morphological analysis for an adult *Heliconius sara* wing scale. (A) SEM image of a *Heliconius sara* ground scale. The length of the scale is measured as the distance from the edge of the socket to the distal tip of the scale blade (horizontal line). The scale width is taken as a 90° transect at the midpoint of scale length (vertical line). (B) PeakFinder tool can be used to select the longitudinal ridges from an SEM image. Each green peak highlights a separate longitudinal ridge, with the space between peaks forming a trough. (C) The ridge detector plugin selects individual ridges (red lines) within the selected area of the scale. Each

detected ridge is assigned a unique ridge ID. The green lines highlight the edges of an individual ridge and are used to calculate ridge width. Measurements of ridge width are taken along the full length of each selected ridge (D) Positioning of all the 11361 individual measurements of ridge width taken from the detected ridges in the selected scale area. (E) Measurements of ridge width (μm), mean ridge width μm (black dot) and standard deviation (black lines) for each selected ridge. Scale bar length = $20\ \mu\text{m}$.

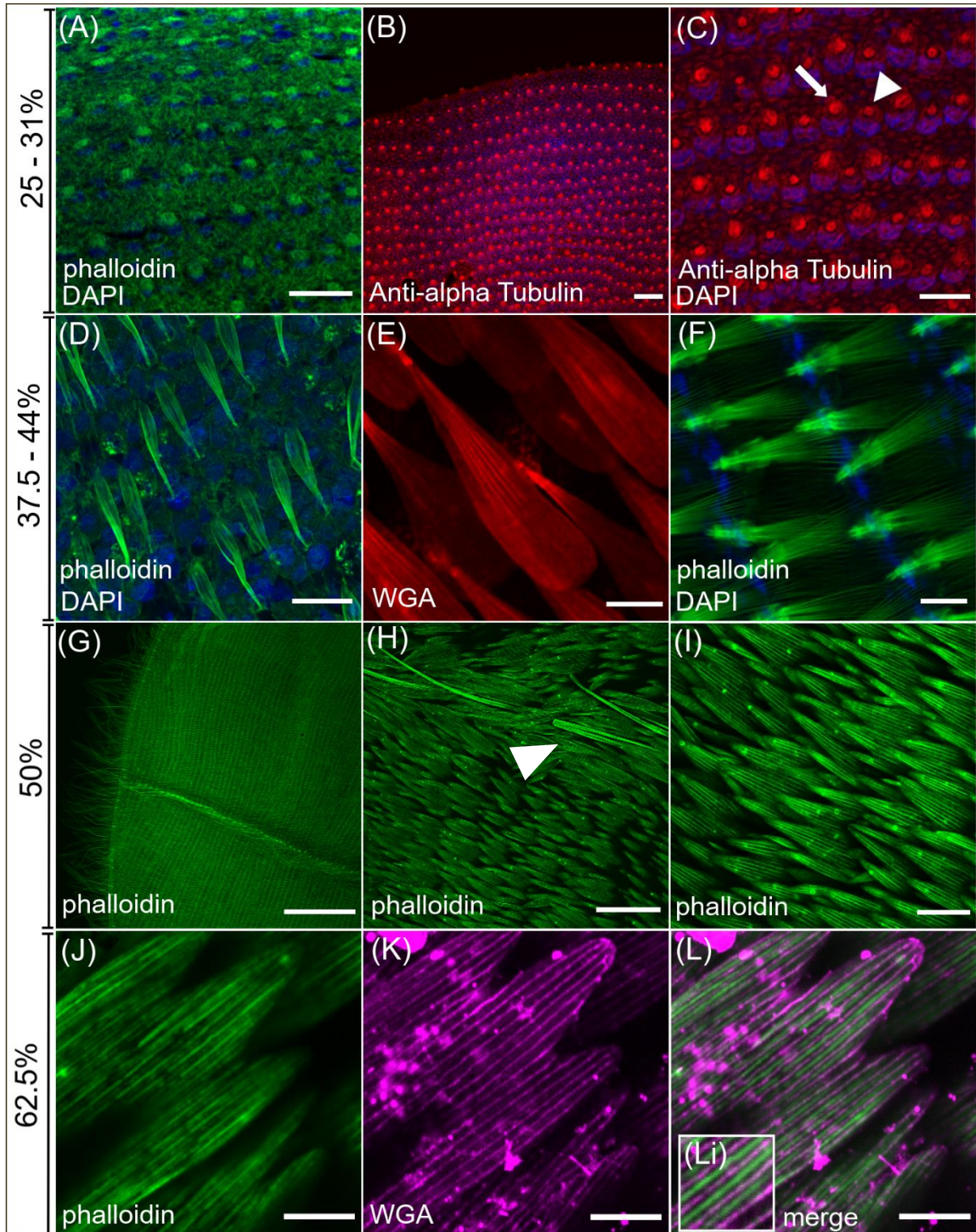


S5: All data used for SEM analyses of adult *Heliconius sara* wing scales. Each data point represents an individual scale (n = 800). Measurements of ridge spacing (μm) (A), scale area (μm^2) (B) and ridge width (μm) (C) taken from 10 cover scales and 10 ground scales in both the iridescent and non-iridescent region of 20 individuals.

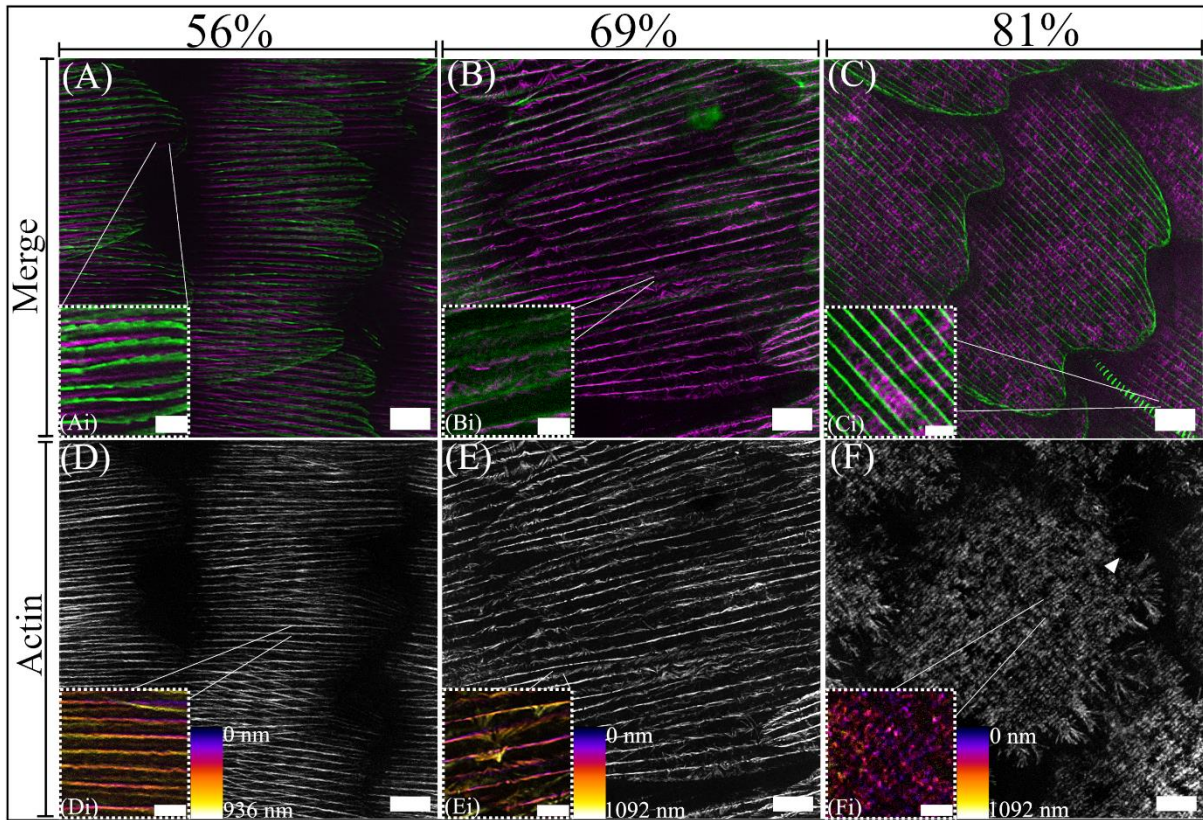


S6: Morphological analyses of adult *Heliconius erato demophoon* wing scales. (A) *H. e. demophoon* individual with wing sections taken from the proximal (blue box) and distal (grey box) forewing. These regions correspond to the iridescent and non-iridescent regions of *H. sara* (Ai). (B) SEM image of *H. e. demophoon* scales ridges, white line indicates the ridge spacing. Comparisons of cover and ground scales in the proximal and distal wing regions for (C) ridge number and scale width (μm). (D) ridge number and ridge spacing (μm). Points represent the

mean value grouped by individual, region and scale type. Shaded areas around the regression line indicate 95 % confidence intervals. Scale bar lengths: (A, Ai) = 30 μ m, (B) = 1 μ m.

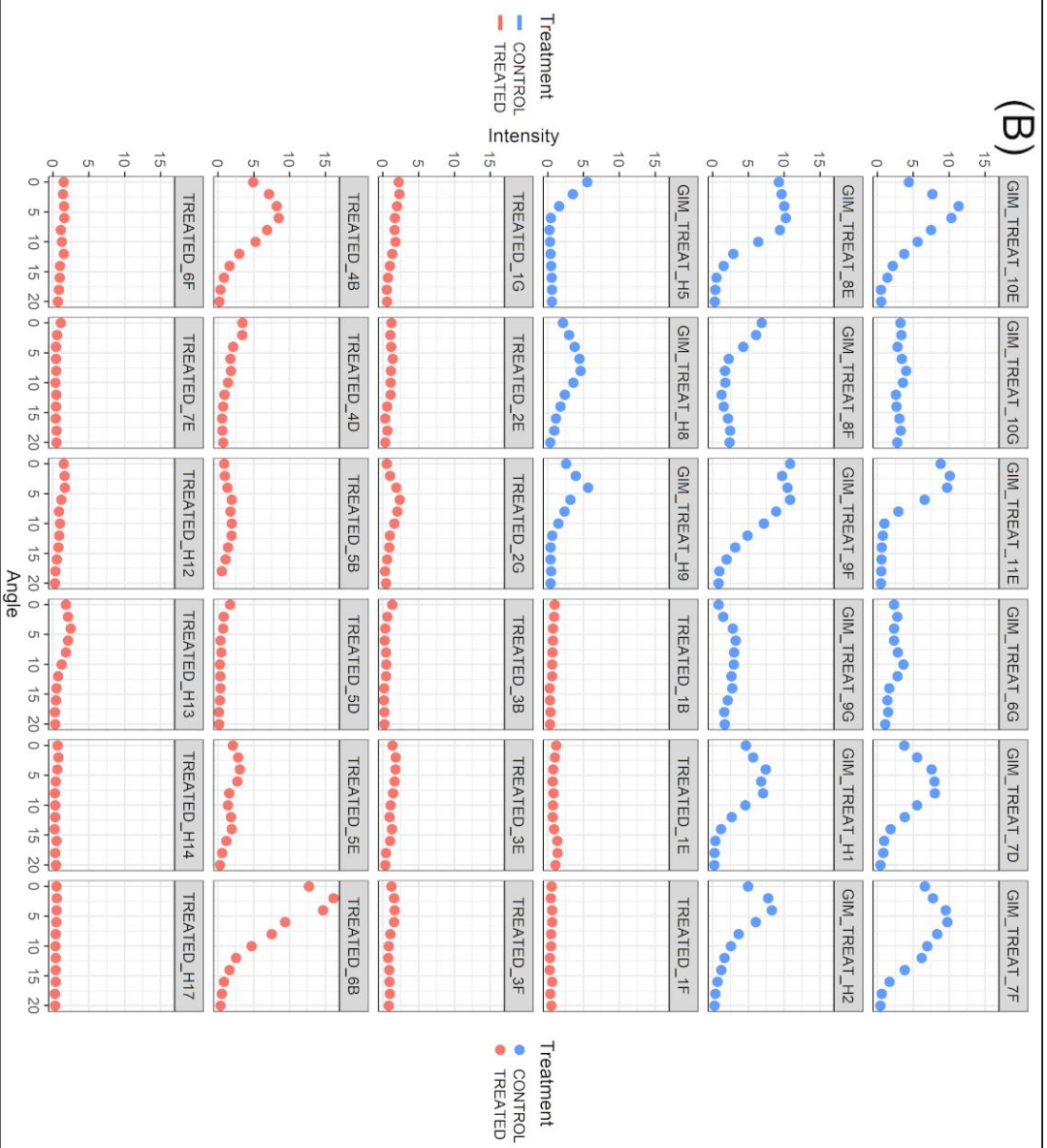
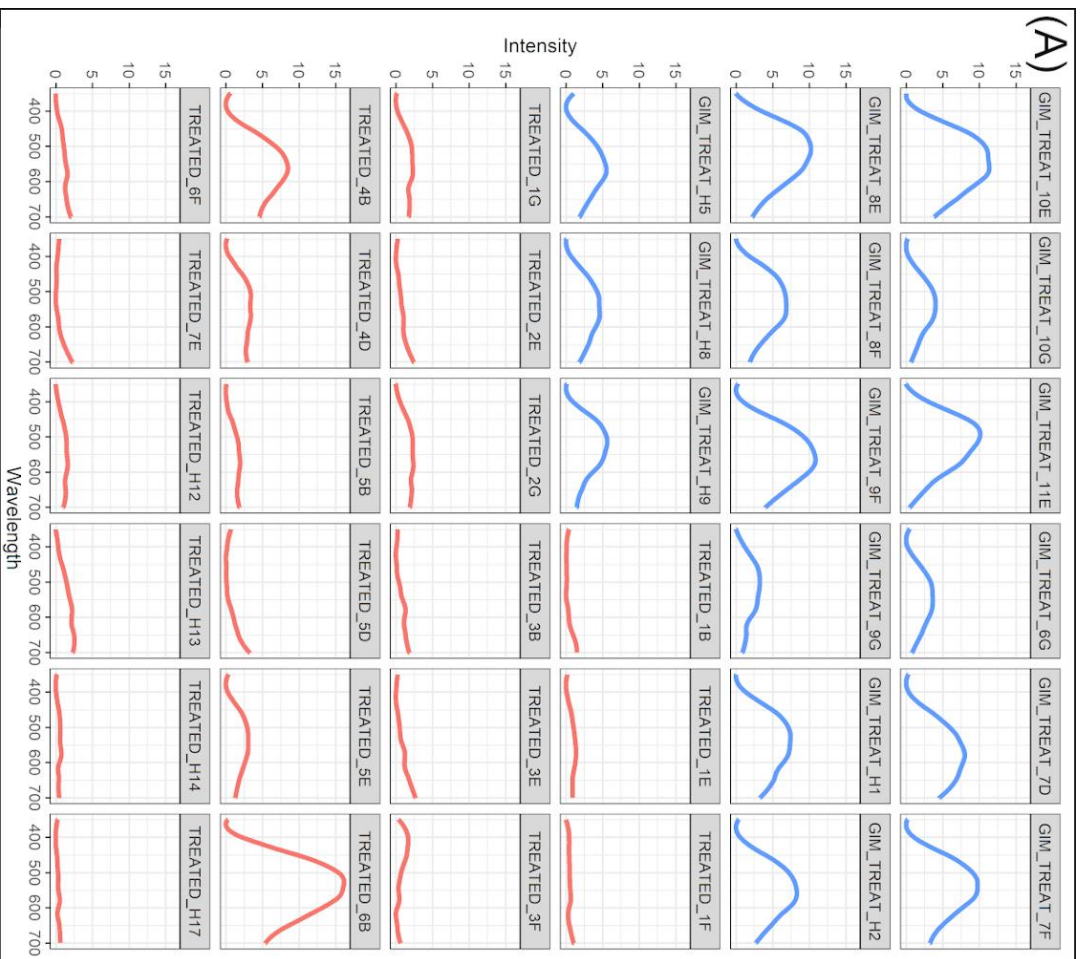


S7: Series of normal wing scale development in *H. sara*. Cell nuclei counterstained with DAPI (blue). (A – C) Early wing scale development showing cytoplasmic projections from the wing epithelium at 25%. (A) Phalloidin staining (green) of actin in the nascent scales. (B, C) Anti-alpha Tubulin immunostaining (red) reveals differing amounts of cytoplasm in developing cover (arrowhead) and ground (arrow) scales and outlines of the socket cells. (D – F) At 37.5–44% the scale cell is a sac filled with organised actin bundles (green) (D) and surrounded by a cellular membrane, highlighted by WGA staining (red) (E). Forming sockets are clearly visible (F) with the actin bundles passing directly through them. At 50%–56% (G – I) the developing scales resemble adult scales (Fig 1D). The distal forewing (G) shows hundreds of developing scales. (H) overlapping wing scales adjacent to a wing vein with actin-rich hairs protruding from the vein (arrowhead). (I) The actin (green) within the scales is highly organised at 50% and extends to the proximal portion of the scale fingers. (J – L) Final stages of scale development. (J) gaps between the phalloidin stained actin bundles (green) highlights actin sub-bundling (K) WGA (magenta) now stains the chitin being deposited extracellularly (L) Merge of actin (green) and WGA (magenta) shows the chitin being deposited between the actin bundles (Li). Scale bar lengths: (A, B, E, I) 20 μ m; (C, D, F, J, K, L) 10 μ m; (G) 300 μ m; (H) 50 μ m.

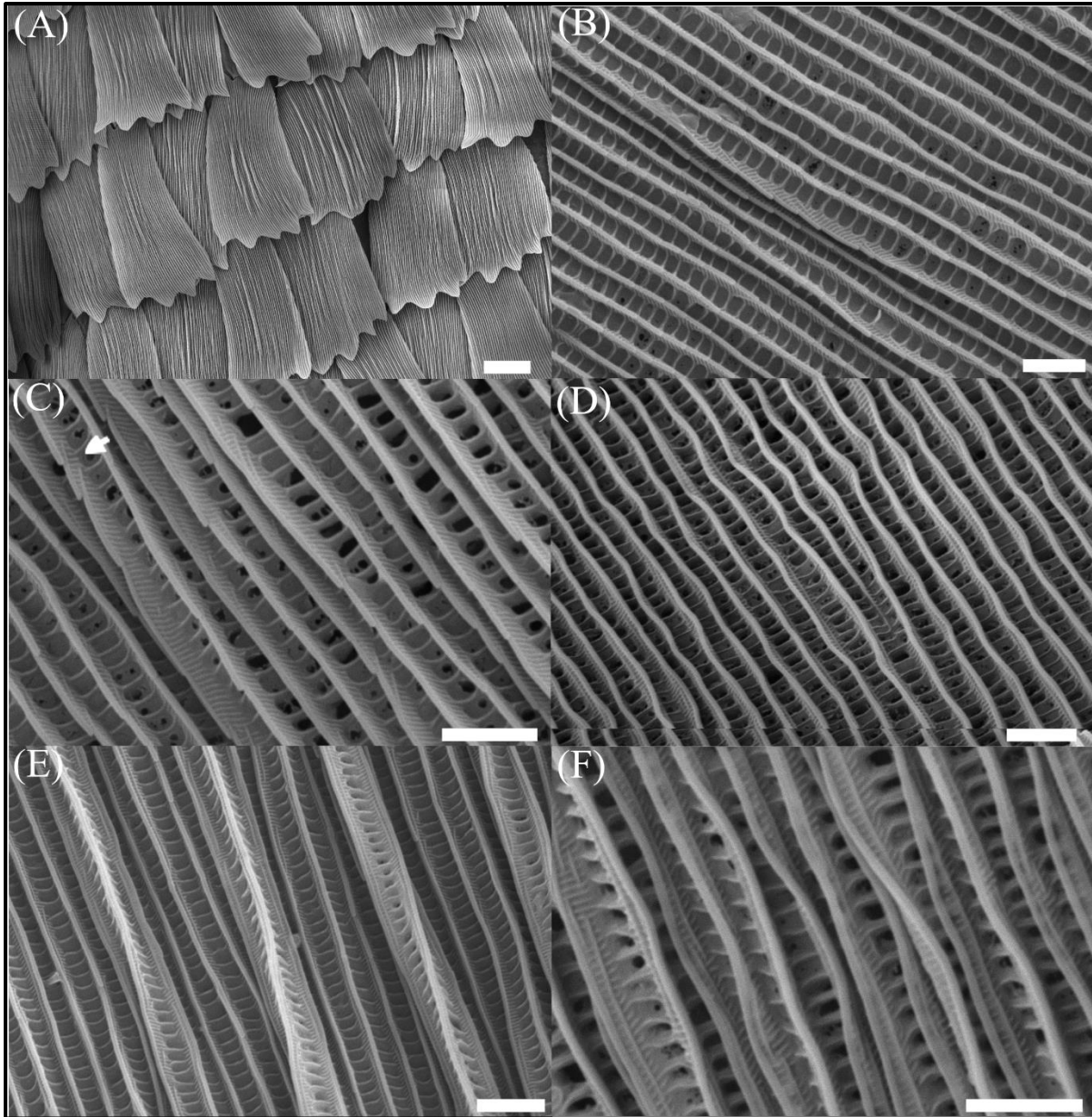


S8: Additional TauSTED images of developing *Heliconius sara* scales. (A-C) Merge of actin (magenta) and chitin (green). (A) Scale from the black region of the posterior hindwing at 56% development, with actin bundles positioned in between the chitin ridges. Individual overlapping layers of the cuticle ridges are clearly visible in the enlarged section (Ai). (B) Black scale at 69%, the large actin bundles are dissociating and rearranging. (Bi) Enlarged section showing rearrangement of the actin bundles into individual filaments which now closely associate with the individual chitin ridges. (C) Black scale from the posterior hindwing at 81%, showing the extensive deposition of cuticle and the final arrangement of the actin cytoskeleton before completion of scale development. In the enlarged section (Ci) the crossribs are clearly visible, with the actin cytoskeleton present in the future ‘window’ regions. (D-F) Grayscale images of the actin cytoskeleton in images (A-C) with the enlarged sections showing depth profiles of the actin for regions approximately shown by the white lines. (D) The actin cytoskeleton is present as large continuous bundles. (E) The actin bundles fracturing and rearranging. Enlarged section (Ei) shows the rearranged individual filaments are more ventrally

positioned than the original actin bundles. (F) Final arrangement of the actin cytoskeleton. At this stage the actin cytoskeleton is less well defined at the periphery compared to 75% (Fig 5J) and regions lacking in actin can be seen (arrowhead). Together this suggests that the actin filaments may be beginning to break down entirely. (Fi) Enlarged section indicates that the actin cytoskeleton in the central region of the scale varies little in height. Scale bars: (A, B, C, D, E, F) 5 μm ; (Ai, Bi, Ci, Di, Ei, Fi) 2 μm .

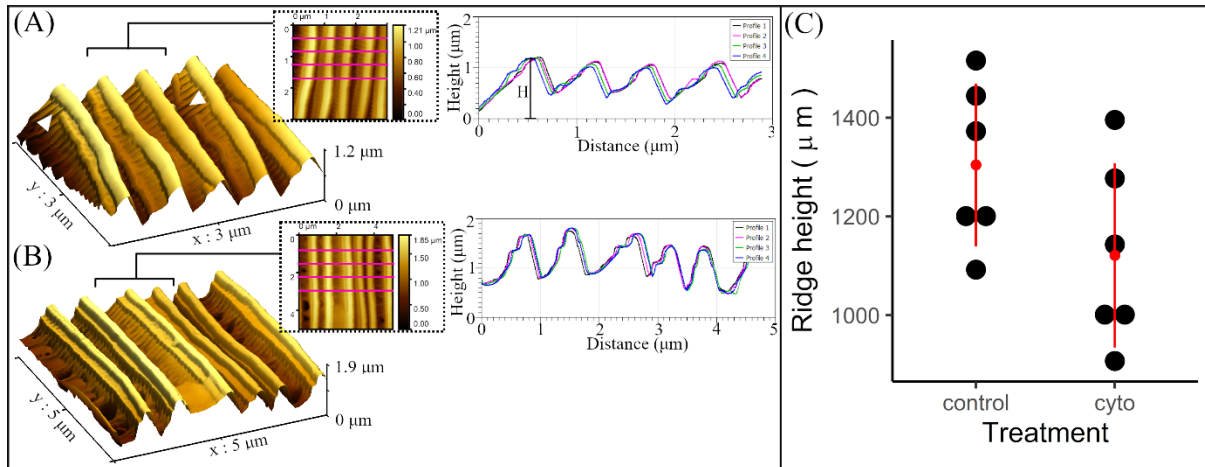


S9 (previous page): Individual reflectance spectra from all control and Cytochalasin D treated individuals. (A) Reflected intensity for measured wavelengths between 350 and 700 nm (B) Reflected intensity for each angle measured between 0° and 20°.



S10: Additional SEM images of iridescent blue scales from several butterflies treated with Cytochalasin D. (A) In some cases, defects of the whole scale were visible, with pinching of the ridges in the scale centre, coupled with deformation of the fingers creating a fanned appearance of the scale tip. (B) Some scales had windows entirely filled with chitin cuticle. (C) Uneven layering of the ridges, with some ridge layers close together (white arrow) while other layers extended some distance. (D) Acute curvature of some treated scales with a noticeable buckling of the ridges. (E) In extreme cases, combinations of defects such as filled in windows

as well as toppled ridges were seen. This was particularly the case in the ‘pinched region’ in the centre of scales shown in (A). (F) Some scales exhibited relatively normal ridge layering but the ridges had toppled over and were laying out of plane with each other. Scale bars: (A) 20 μm , (B-F) 2 μm .



S11: Atomic Force Microscopy (AFM) imaging and analysis of cytochalasin D treated and control scales. 3D AFM rendering of scale ridges in a typical cytochalasin D treated individual (A) and a control individual injected with Graces Insect Medium (B). Arrowheads in (A) indicate putative distortion of the ridge layering. Insert: AFM image of the 2D scale surface with magenta lines indicating method of selecting the four ridge profiles shown in the corresponding profile plot. Height (H) is taken as the distance from the peak of each ridge to the lowest point of the overall scale height. (C) Plot of ridge height (μm) for control and cytochalasin D treated scales. Points represent individual scales.

Chapter 4

Differential expression analysis reveals the genetic basis of iridescent structural colour in *Heliconius* butterflies

Victoria J. Lloyd¹, Melanie N. Brien², Juan Enciso-Romero³, Andrew Parnell¹ and Nicola J. Nadeau^{1*}

¹*Animal and Plant Sciences, University of Sheffield, Alfred Denny Building, Western bank, Sheffield S10 2TN, UK*

²*Institute of Biotechnology, University of Helsinki, Finland*

³*Biology Program, Faculty of Natural Sciences, Universidad del Rosario, Bogotá, Colombia*

* Corresponding author

Email: n.nadeau@sheffield.ac.uk

For published article, please see **Appendix**:

Citation for published article: Brien M, Enciso-Romero J, Lloyd V, Curran E, Parnell A, Morochz C et al. (2022) ‘The genetic basis of structural colour variation in mimetic *Heliconius* butterflies’.

Philosophical Transactions of the Royal Society B: Biological Sciences.377, (1855). doi:

10.1098/rstb.2020.0505.

Author contributions

A significant portion of this chapter is published in *Philosophical Transactions of The Royal Society B Biological Sciences*, which can be found in the Appendix. The publication consists of research presented in this Chapter together with quantitative trait locus (QTL) mapping performed by Melanie Brien and Juan Enciso-Romero.

This chapter presents the full RNAseq analysis, with further descriptions of the undertaken methods and additional analyses, including: Gene Set Enrichment Analysis, comparisons with gene expression in homologous structures and immunofluorescent staining. The research project was designed by myself and Nicola Nadeau. Collection of the RNA samples was performed by Nicola Nadeau, with library preparation and sequencing done by the Edinburgh Genomics sequencing facility. I performed all the analysis of the data. The quantitative trait locus (QTL) mapping analysis was performed by Melanie Brien. In Figure 1, the phylogenetic tree was made by Nicola Nadeau and the reflectance spectrometry plots were created by Juan Enciso-Romero. The scanning electron microscopy was performed by myself. The Atomic Force Microscopy acquisition and rendering was performed by Andrew Parnell. The QTL plots in Figure 5 A, B, G, H were made by Melanie Brien. I wrote the manuscript with feedback provided by Nicola Nadeau.

Abstract

Vivid structural colours in nature are the result of the physical interaction of light with tiny nanostructures. Butterflies display stunning examples of structural colour, which have evolved through modification of their wing scales to possess optical nanostructures. In *Heliconius* butterflies these optical nanostructures take the form of multilayer reflectors on the cuticle ridges of the upper wing scale surface. To date little is understood of genetic and developmental mechanisms underpinning structural colour formation in *Heliconius*. Here, we identify candidate genes controlling structural colouration in *Heliconius* using differential expression analyses between iridescent and non-iridescent subspecies of two co-mimetic species – *Heliconius erato* and *Heliconius melpomene*. We further narrow down these candidate genes by overlapping them with previously-identified QTL intervals controlling iridescence as well as genes involved in the formation of homologous structures in *Drosophila*. We identify several promising candidate genes, including some with roles in actin cytoskeleton organisation – a crucial cellular component hypothesised to be important in scale development. We find no evidence for convergence in the genes underpinning structural colour development in the two study species. Finally, we perform immunofluorescence of our top candidate gene to further assess its roles in optical nanostructure formation.

Keywords

Structural colour, iridescence, *Heliconius*, RNAseq, differential expression, butterfly

Introduction

Brilliant, highly-reflective structural colours are found throughout nature and are formed by the scattering of light by tiny nanostructures on the integument of animals and plants (Airoldi et al., 2019; Ingram and Parker, 2008). In contrast to pigments, which use chemicals to absorb specific wavelengths of light, structural colours are produced by periodically repeating units of biopolymers, such as keratin and chitin (Burg and Parnell, 2018; Kinoshita, 2008; Thayer et al., 2020). A diverse range of organisms (Barrows and Bartl, 2014) harness structural colours for various functional roles, including: camouflage (Kjernsmo et al., 2020), communication (Kramer et al., 2007; Waldron et al., 2017), mate choice (Kemp, 2007; Sweeney et al., 2003) and protection against irradiance (Chandler et al., 2017; Willot et al., 2016). Structural colours are frequently harnessed for visual signalling, owing to their conveyance of signals over greater distances in comparison to pigments (Denton, 1970; Douglas et al., 2007). Such optical characteristics have made structural colours a key source of technological bioinspiration (Barrows and Bartl, 2014; Saito, 2011). Therefore, an understanding of optical nanostructure formation within organisms is of broad interest from both an evolutionary and technological standpoint.

Some of the most conspicuous structural colours in nature are found within insects, such as beetles (Burg et al., 2019), flies (Shevtsova et al., 2011), moths (Kilchoer et al., 2019) and butterflies (Lloyd and Nadeau, 2021; Vukusic, 2006). In particular, the structural colours of butterflies have been subject to rich history of study, beginning with the microscopic observations of Peacock butterfly wings by Hooke, (1665). Despite occupying diverse positions on the phylogeny, butterfly structural colours originate from modifications to a general wing scale morphology (Ghiradella, 2010; Nijhout, 1991). These wing scales (<100 μm in length), are formed through cuticular extensions from a wing epidermal layer. The lower surface (lamina) is a flat featureless layer whereas the upper lamina is complex, with parallel

ridges of cuticle interconnected perpendicularly by crossribs (Figure 1 F,G,J,K)(Ghiradella, 1991; Nijhout, 1991). The generation of optical nanostructures responsible for structural colour formation results from the modification of one or more of these scale elements (Ghiradella, 2010). For example, the thickness of the lower lamina can be tuned to generate a thin-film multilayer, such as in *Junonia coenia* (Thayer et al., 2020); while the chitin ridges can be adorned with alternating layers of chitin and air forming a multilayer bragg reflector, such as in the blue *Morpho* (Kinoshita et al., 2002).

Understanding the genetic and developmental basis of structural colours in butterflies has been the focus of recent investigations. Artificial selection experiments in *Junonia coenia* (Thayer et al., 2020) and *Bicyclus anyana* (Wasik et al., 2014) were able to modify wing colour from brown to blue through tuning of lower lamina thickness. Furthermore, gene knockouts of the transcriptional regulator gene *optix* in *J. coenia* replicated the phenotypes seen in these selection experiments, by altering lower lamina thickness (Zhang et al., 2017). This suggests that *optix* may be a key regulator controlling lower lamina structural colouration in butterflies; though its position in such a regulatory network and the downstream cellular effectors remain unknown (Smith et al., 2018; Thayer et al., 2020). Interestingly, *optix* also plays a role in pigmentation and scale structure suggesting an multifaceted role of the gene in scale development (Reed et al., 2011; Zhang et al., 2017). Furthermore, gene knockout experiments have demonstrated that several other genes involved in wing patterning (McMillan et al., 2020; Peng et al., 2020) and pigment synthesis (Matsuoka and Monteiro, 2018; Peng et al., 2020) were also able to produce ultrastructural changes in scale elements; in some cases generating structural colouration. Together these studies hint at a potential interconnection in the underlying gene regulatory networks governing the generation of pigments and scale structure; including nanostructures (Smith et al., 2018).

Despite inroads into the genetic basis of structural colour, investigations have primarily focused on lower lamina nanostructures, which in optical terms represents a simplistic mechanism of structural colour production. Conversely, the formation of multilayer reflectors on the parallel ridges represents an alternative means of structural colour generation (Lloyd and Nadeau, 2021). Electron micrographs by Ghiradella suggest multilayer nanostructures form as a result of the buckling of a malleable cuticle layer, perhaps through stresses applied through an intracellular network of actin bundles (Ghiradella, 1974; Ghiradella and Radigan, 1976). Indeed, fluorescent microscopy has demonstrated key roles for the actin cytoskeleton in both overall scale development as well as a potential role in structural colour formation (Day et al., 2019; Dinwiddie et al., 2014). However, the genetic architecture underlying multilayer reflector development in butterflies is poorly understood. Gene knockouts of *optix* in species with ridge reflectors, such as *Heliconius erato*, failed to produce alterations in structural colouration; suggesting a potentially different genetic basis to that which underlies lower lamina structural colour (Zhang et al., 2017).

The butterfly genus *Heliconius* (Nymphalidae) has been extensively studied for its aposematic wing colour patterning, with the formation of mimicry rings involving the divergence of wing colour patterns amongst conspecifics as well as convergence in patterning between divergent species (Jiggins, 2017; Joron et al., 2006b; Merrill et al., 2015). The genetic basis of pigmentary colour patterns has been linked with a ‘toolkit’ of five major effect loci (Nadeau, 2016). In addition, *Heliconius* also demonstrate vivid examples of structural colouration (Parnell et al., 2018; Wilts et al., 2017a). Structural colours have evolved multiple times in the genus, with interspecific variation in intensity and hue of the colour produced (Parnell et al., 2018). Brien et al., (2018) provided initial insights into the genetic control of structural colour in *Heliconius* through phenotypic crosses of iridescent and non-iridescent subspecies of *Heliconius erato*. They demonstrated that structural colour is a quantitative trait

with no association with the previously-identified toolkit genes for colour patterning. Interestingly, a moderate effect locus was identified on the Z Chromosome suggesting potential involvement of sex-linked loci (Brien et al., 2018). Furthermore, phenotypic analysis of *Heliconius erato* as well as *Heliconius melpomene* (a sister species with which *H. erato* forms a mimicry ring with) across hybrid zones demonstrated continuous variation in iridescence; further suggesting a polygenic architecture underpinning structural colouration (Curran et al., 2020). Together these studies suggest that structural colour in *Heliconius*, produced by multilayer reflectors, is a complex trait controlled by numerous genes.

Here we use differential expression (DE) analysis of RNAseq data collected from iridescent and non-iridescent subspecies of *Heliconius erato* (*Heliconius erato cyrbia* and *Heliconius erato demophoon*, respectively) and *Heliconius melpomene* (*Heliconius melpomene cythera* and *Heliconius melpomene rosina*, respectively) to identify candidate genes underpinning structural colour development in *Heliconius*. We narrow down our list of differentially expressed genes using: Gene Set Enrichment Analysis (GSEA), comparisons with non-structurally coloured (androconial) wing regions and overlap with genes involved cuticle development and in the formation of homologous structures (bristles) in *Drosophila*. We also overlap our DE genes with previously-described QTL intervals associated with iridescence. Furthermore, we compare the set of DE genes between *H. erato* and *H. melpomene* to ascertain whether there is convergence in the genes and underlying gene regulatory pathways controlling structural colouration. Finally, we test our most promising candidate using immunofluorescence.

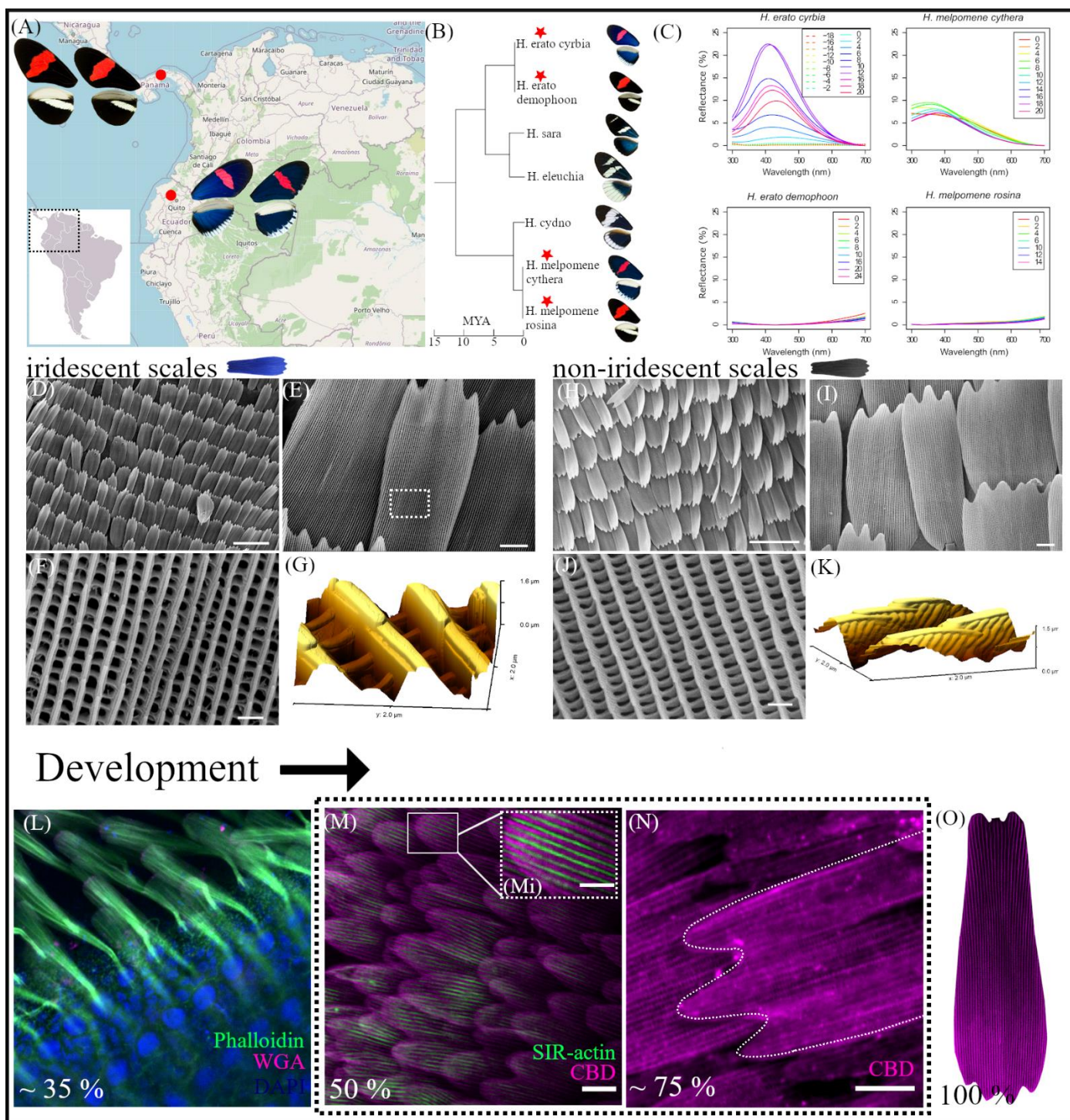


Figure 1. Structural colour in *Heliconius* butterflies. (A) The geographic location of the four *Heliconius* subspecies used in this study. Top left, non-iridescent *Heliconius melpomene rosina* (left) and *Heliconius erato demophoon* (right). Bottom right, iridescent *Heliconius melpomene cythera* (right) and *Heliconius erato cyrbia* (left). (B) Phylogenetic relationship

between *Heliconius erato* sp. (star) and *Heliconius melpomene* sp. (star). (C) Reflectance spectrometry measurements of the percentage reflectance at each wavelength (nm) of the different subspecies used in the study. (D-K) Scanning electron microscopy (SEM) and atomic force microscopy (AFM) images of progressive zooms into *Heliconius* wing scales, highlighting the general morphology of iridescent blue scales (D-G) and non-iridescent black scales (H-J) in *Heliconius* butterflies. (L-O) Time series of wing scale cell development in *Heliconius*, from the budding of the scale cell out the epithelial layer (L) to the formation an adult scale in an emerged butterfly (O). Stages of scale development used in this study approximately correspond to those highlighted in the dashed box. Actin cytoskeleton stained by phalloidin in green, cell membrane stained by Wheat Germ Agglutinin in magenta (L), chitin cuticle stained by Chitin Binding Domain (CBD) in magenta (M, N). (O) False coloured SEM image of an adult *Heliconius* scale. Scale bars: (L,M,N) = 10 μm , (Mi) = 5 μm . Coloured map image in (A) © OpenStreetMap, data made available under a CC BY-SA 2.0 license (<https://creativecommons.org/licenses/by-sa/2.0/>). Inset blank South America map obtained from Wikimedia, where it was made freely available by Vardion. Phylogenetic tree (B) and spectrometry plots (C) reproduced from Parnell et al., (2018) ,where they are made available under a CC-BY 4.0 license (<https://creativecommons.org/licenses/by/4.0/>).

Methods

Animal husbandry

Wild *Heliconius erato cyrbia* and *Heliconius melpomene cythera* butterflies (iridescent subspecies) were captured in Mashpi, Ecuador. Wild *Heliconius erato demophoon* and *Heliconius melpomene rosina* butterflies (non-iridescent subspecies) were captured in Gamboa, Panama (Figure 1A). Breeding stocks were raised from wild caught individuals at the

Arthur Willis Environment Centre, University of Sheffield. Butterflies were housed at 25 °C and fed a 10% sugar water solution with 1 gram added pollen. Caterpillars were maintained at 25 °C and fed on *Passiflora* species.

RNA extraction, library preparation and sequencing

At the required developmental stage pupae were dissected of their forewings in phosphate buffered saline (PBS) at room temperature. In total, RNA was extracted from 32 *Heliconius erato* samples (16 *H. e. demophoon*, 16 *H. e. cyrbia*) and 32 *Heliconius melpomene* samples (16 *H. m. rosina*, 16 *H. m. cythera*)(Table S1). The androconial wing region (anterior hindwing) was dissected from the rest of the wing and sampled separately. For each subspecies two developmental stages were sampled: 50 % pupation time and 70 % pupation time corresponding to day 5 and day 7 of the 10 days total pupation time of both species. For sample information see supplementary material (Table S1).

RNA was extracted using a Qiagen RNeasy kit. Paired-end sequenced data was generated from Illumina TruSeq RNA libraries (*H. melpomene* libraries created using a TruSeq Stranded mRNA-seq kit and *H. erato* libraries created using a TruSeq v2 kit) on 6 HiSeq v4 lanes (Edinburgh genomics, University of Edinburgh). The *H. melpomene* data was stranded.

Filtering, alignment and assembly

All quality control, read alignment and transcript assembly were performed on the University of Sheffield High Performance Computing (HPC) cluster (ShARC). Raw reads were downloaded from the sequencing facility in fastq format. Trimmomatic (version 0.38) was used to remove low quality reads (PHRED <33) and trim remaining Illumina adapter sequences (ILLUMINACLIP option). Read quality was inspected using FastQC (version 0.11.8) and the results aggregated and viewed using multiQC (version 1.5). Trimmed reads were aligned to the respective *Heliconius* reference genomes using HISAT2 (version 2.1.0) (Figure S1) (Kim et

al., 2015). Reference genomes: *Heliconius melpomene melpomene* [version 2.5] and *Heliconius erato demophoon* [version 1] were downloaded from Lepbase (v4) (<http://download.lepbase.org/v4/>) (Challis et al., 2016). HISAT2 was run with the ‘--known-splicesite-infile’ option to enable alignment of reads with small anchors. Exon and splice site information was extracted from the respective species gene annotation files downloaded from Lepbase (v4). Gffread was used to convert the downloaded ‘.gff’ file format into the required ‘.gtf format’. The python script ‘hisat2_extract_splice_sites.py’ was used to create the list of known splice sites to pass to HISAT2. In addition, HISAT2 was run with the -dta option to adapt the alignments for downstream programs, including StringTie. The *H. melpomene* reads were run with the –rna-strandedness RF option to account for the strandedness of the reads.

The output SAM files produced from HISAT2 were sorted and converted into .BAM files using SAMtools (version 1.9) (Li et al., 2009). The average number of reads per sample was 18.2 million for *H. erato* and 15.3 million for *H. melpomene* (Figure S1). The average overall alignment to the respective species reference genomes was 76 % for *H. erato* and 78.0 % for *H. melpomene* (Figure S1).

Transcript assembly and read quantification was performed using StringTie (version 1.3.5) (Pertea et al., 2015). The respective *H. melpomene* and *H. erato* gene annotations were provided as an input to guide read assembly. StringTie was then run in ‘merge mode’ to create a uniform set of transcripts. This non-redundant transcript set was then used to re-estimate abundance of the output alignment files from HISAT2 using the ‘-e’ option. Gene count matrices tailored to EdgeR were created separately for both species using the python script ‘prepDE.py’ provided by StringTie.

Differential expression analysis

Differential expression analysis was performed using the R/Bioconductor package EdgeR (version 3.28.1) (Robinson et al., 2009). Genes with low expression levels were filtered out from subsequent analyses using the ‘filterByExpr’ function (Chen et al., 2016). Normalisation of library size was then performed using the trimmed mean of M-values (TMM) method (Robinson and Oshlack, 2010). Samples were clustered using Multi-Dimensional Scaling (MDS) analysis on expression levels. One of the 70% development *H. m. rosina* samples (both wing regions) was removed from subsequent analysis because it clustered with the *H. m. cythera* individuals, suggesting it may have been mislabelled. For comparisons between iridescent and non-iridescent subspecies (which we term ‘subspecies comparison’) a simple design matrix was employed using ‘subspecies’ as the only treatment factor. For comparisons between the androconial (non-iridescent) wing region and iridescent wing region for iridescent species (which we term ‘wing region comparison’) ‘individual ID’ was also included in the design matrix to account for nested differences between individuals. This was included using a design matrix ‘~Individual_ID + treatment’, where treatment indicates the presence or absence of iridescence. Trended estimates of dispersion were calculated and negative binomial generalised linear models fitted using the ‘glmQLFit’ function. Testing for differential expression was undertaken using a quasi-likelihood (QL) F-test and genes were regarded as significantly differentially expressed when the FDR (False Discovery Rate) corrected P-value was less than 0.05.

Functional annotation

Differentially expressed genes between iridescent and non-iridescent subspecies were annotated using the respective species InterproScan and Blastp databases downloaded from Lepbase (<http://download.lepbase.org/>). For all other annotations genes were manually compared to the non-redundant NCBI protein database using the Blastp algorithm, as well as the FlyBase BLAST protein database (Thurmond et al., 2019).

Overlap of genes between the androconial and iridescent wing regions in iridescent species

At both 50% and 70% development DEG's between the iridescent and non-iridescent subspecies of *H. erato* and *H. melpomene* were compared to DEG's between the iridescent and non-iridescent (androconial) region of the respective iridescent subspecies (*H. erato cyrbia*, *H. melpomene cythera*). Genes which were upregulated ($\text{LogFC} > 0$) in both the 'subspecies' comparison and the 'wing region' comparison and had an $\text{FDR} < 0.2$ were labelled as 'iridescent genes'. Of these 'iridescent genes', those which had an $\text{FDR} < 0.05$ in both comparison sets were further categorised as 'significant'. Similarly, genes which were downregulated ($\text{LogFC} < 0$) in both the subspecies comparison and the wing region comparison with an $\text{FDR} < 0.2$ were labelled as 'non-iridescent genes'. Those with $\text{FDR} < 0.05$ were 'significant'.

Gene Set Enrichment Analysis (GSEA)

GO (gene ontology) enrichment analysis was performed in R (version 3.6.2) using the R/Bioconductor package topGO (version 2.38.1) (Alexa and Rahnenführer, 2021). Custom annotations were constructed using GO terms extracted from the InterproScan files downloaded from Lepbase (<http://download.lepbase.org/v4/interproscan/>). The gene universe comprised of all the genes expressed in the wings at 50% and 70% development taken from the respective species gene count matrix produced by StringTie. GO analyses were performed on the differentially expressed genes between the iridescent and non-iridescent which had an $\text{FDR} < 0.05$. A Fisher exact test was used to conduct the test using the 'weight01' algorithm. GO terms were considered significant when $P < 0.01$. GO enrichment circle plots were constructed using the package GOplot (version 1.0.2).

Overlap of differentially expressed genes with Quantitative Trait Loci (QTL)

Genomic regions associated with iridescence in *H. erato* and *H. melpomene* were identified in a previous QTL analysis (Brien, 2019; see Appendix). QTL were associated with two different aspects of structural colour: BR values (Blue-Red) for a measure blue iridescent colour and luminance for a measure of intensity. In addition, ‘Ridge spacing’ was used as a measure of scale morphology associated with reflected intensity (Brien et al., 2018). For full methods on how the QTL analysis was conducted see Brien et al., (2022) and the Appendix. For both species, all genes within the significant QTL confidence intervals on Chromosome 20 and 21 (Z Chromosome) for *H. erato* and Chromosome 3 and 7 for *H. melpomene*, were identified from the reference gene annotation files using the genomic start and stop positions. For both *H. erato* and *H. melpomene*, at 50% and 70% development, the significantly DEG’s (FDR < 0.05) were compared to the genes within the QTL confidence interval to identify overlapping genes. For *H. melpomene*, the FDR cut off was expanded to 0.2 to take into account the low number of genes within the FDR < 0.05 cut off and identify possibly candidate genes, despite these not being “significant”. In addition, we calculated the total expected number of DE genes for an equal sized genomic interval, as a rough approximation of whether our QTL intervals were enriched for DE genes (Table S14). Manhattan plots showing the FDR of genes plotted along the genome and within chromosomes were created using the R package Lattice (version 0.20-38) (Sarkar et al., 2021) and the plotting function freely available from <https://genome.sph.umich.edu/>.

Overlap of differentially expressed genes with bristle (chaeta) and cuticle development genes

FlyBase (version FB2020_04) (Thurmond et al., 2019) was used to search for gene ontology terms corresponding to macrochaeta (bristle) and cuticle development in *Drosophila*. For bristle development 82 genes and 271 associated polypeptides were identified and their sequences downloaded in fasta format. For cuticle development, 243 genes and 549 associated polypeptides were identified and downloaded. We used the ‘makeblastdb’ function from

BLAST (version 2.9.0) and blast databases were created separately for *H. erato* and *H. melpomene* using reference protein sequences downloaded from Lepbase (v4). We used the Blastp function to create tables of orthologs of the *Drosophila* sequences from the reference *H. erato* and *H. melpomene* databases. DEG's between the iridescent and non-iridescent species (FDR < 0.2) and the iridescent and non-iridescent wing regions (FDR < 0.2), at 50% and 70% development, were then compared to the bristle development ortholog tables to identify overlapping genes. Overlapping genes with an FDR < 0.05 were classed as 'significant' genes. In addition, the analysis was repeated using the DEG's between the iridescent and non-iridescent wing region of the iridescent subspecies, using the same FDR cut-offs.

Identification of convergent differentially expressed genes

BLAST (v. 2.9.0) (Altschul et al., 1990) was used to identify orthologous genes between *H. erato* and *H. melpomene*. A blast database was created using reference protein sequences for *H. melpomene* downloaded from Lepbase (v4) (Challis et al., 2016) using the 'makeblastdb' function. Then, using Blastp, protein sequences for *H. erato*, were aligned against the *H. melpomene* reference to create a table of orthologous genes between the two species. At both 50% and 70% development, genes which were differentially expressed (FDR < 0.2) between iridescent and non-iridescent subspecies in both *H. erato* and *melpomene* were identified. Genes were further filtered based on concordant expression patterns, i.e. only genes which were upregulated or downregulated in both *H. erato* and *H. melpomene* were kept. In addition, the analysis above was repeated using the DEG's between the iridescent and non-iridescent wing region of the iridescent subspecies (FDR < 0.2).

Identification of candidate genes

The frequency in which a gene occurs in our analyses was used as a metric to rank the genes in order of the most likely candidate for controlling structural colour development. This was

done separately for *H. erato* and *H. melpomene* as well as for the two development stages (50% and 70% development).

The following analyses were used as to rank genes: 1) Top 100 DE genes between iridescent and non-iridescent subspecies. 2) Top 100 DE genes between iridescent and non-iridescent wing regions of the iridescent subspecies. 3) Convergent DE genes between *H. melpomene* and *H. erato* for the iridescent vs non-iridescent subspecies comparison (FDR < 0.2). 4) Convergent DEG genes between *H. melpomene* and *H. erato* for the iridescent vs non-iridescent wing region comparison (FDR < 0.2). 5) Genes within QTL confidence intervals, with each QTL interval treated independently (*H. erato* QTL intervals: lumZ, BR_Z, RS_Z, BR_20; *H. melpomene* QTL intervals: BR_3, RS_7, Lum3) (FDR < 0.05). 6) *Drosophila* bristle development orthologs which are DE between iridescent and non-iridescent subspecies (FDR < 0.05). 7) *Drosophila* bristle development orthologs which are DE between the iridescent and non-iridescent wing region of the iridescent subspecies (FDR < 0.05). 8) *Drosophila* cuticle development orthologs which are DE between iridescent and non-iridescent subspecies (FDR < 0.05). 9) *Drosophila* cuticle development orthologs which are DE between the iridescent and non-iridescent wing region of the iridescent subspecies (FDR < 0.05). 10) DEG's which are concordantly DE in both the subspecies and wing region comparison (FDR < 0.2). In addition, genes which were DE expressed between the 'iridescent' and non-iridescent wing region of the non-iridescent species (*H. erato demophoon* and *H. melpomene rosina*) were used to filter the final list of candidate genes. This is because neither tissue in the non-iridescent subspecies contains any iridescent scales and therefore DE genes are likely play a role in other functions, such as wing region specification, rather than structural colour development.

For *H. erato*, genes which occurred in three or more of the analyses were included in the final table of candidate genes. For *H. melpomene* genes which occurred in two or more of the analyses were included in the final table of candidate genes.

Immunofluorescence

Immunofluorescent staining was performed on our top candidate gene *Trio*. An antibody for Trio (9.4A ANTI-TRIO) was obtained from the Developmental Studies Hybridoma Bank. We performed immunofluorescent staining in the related species *Heliconius sara*, which has blue iridescent forewing colour produced from the same optical nanostructures as *H. erato* and *H. melpomene* (Parnell et al., 2018). *H. sara* has both iridescent and non-iridescent scales on the same wing (forewing) which facilitates direct comparisons between two scale types in a single piece of tissue. This particularly useful for immunofluorescent staining in butterflies where there might be differences in developmental stages and staining efficiency between two separate wings. Wings of *Heliconius sara* were dissected in PBS (phosphate buffered saline) at 50% and 75% of development. Following dissection, wings were immediately fixed in 4% PFA (paraformaldehyde) in PBS for 15 minutes at room temperature. Wings were washed several times in PBSTx (1% Triton) and blocked for 2 hours using Normal Donkey Serum. Wings were incubated overnight in the primary antibody (1:1000) at 4 °C. After this, wings were again washed in PBSTx several times and then incubated in a 1:200 Donkey Anti-Mouse secondary antibody (Invitrogen, #A-31571) for 2 hours at room temperature. Wings were washed in PBS, counterstained with DAPI (1 µg/mL) and then mounted onto slides using Mowiol mounting medium and a coverslip applied.

Confocal microscopy

Imaging of developing wings was performed using a Nikon A1 Confocal (equipped with NIS elements software) and a Zeiss LSM880 AiryScan Confocal. Imaging of immunofluorescent wings was performed on a Nikon confocal A1. Images of whole wings were taken using a 10x objective using the large image acquisition function. High-magnification images of scales were

taken using a x40 oil objective lens. Z-stacks were assembled into single images using the maximum intensity projection and sum slices functions in FIJI (Schindelin et al., 2012).

Results

Differential expression

A total of 24,118 genes were expressed in the wings of *H. erato* and 30,721 in the wings of *H. melpomene*. In both *H. erato* and *H. melpomene* multidimensional scaling (MDS) analysis of expression levels revealed strong clustering by stage (dimension 1) and subspecies (dimension 2), leading to four distinct clusters (Figure 2).

Firstly, we performed differential expression between the wings (excluding the androconial region) of the iridescent and non-iridescent subspecies of *H. erato* and *H. melpomene* (termed subspecies comparison). There were 907 and 1043 genes were differentially expressed (FDR < 0.05) between *H. e. cyrbia* and *H. e. demophoon* at 50% and 70% development, respectively (Table S2; S3). In *H. melpomene*, 203 and 29 genes were differentially expressed between *H. m. cythera* and *H. m. rosina* at 50% and 70%, respectively (Table S4; S5).

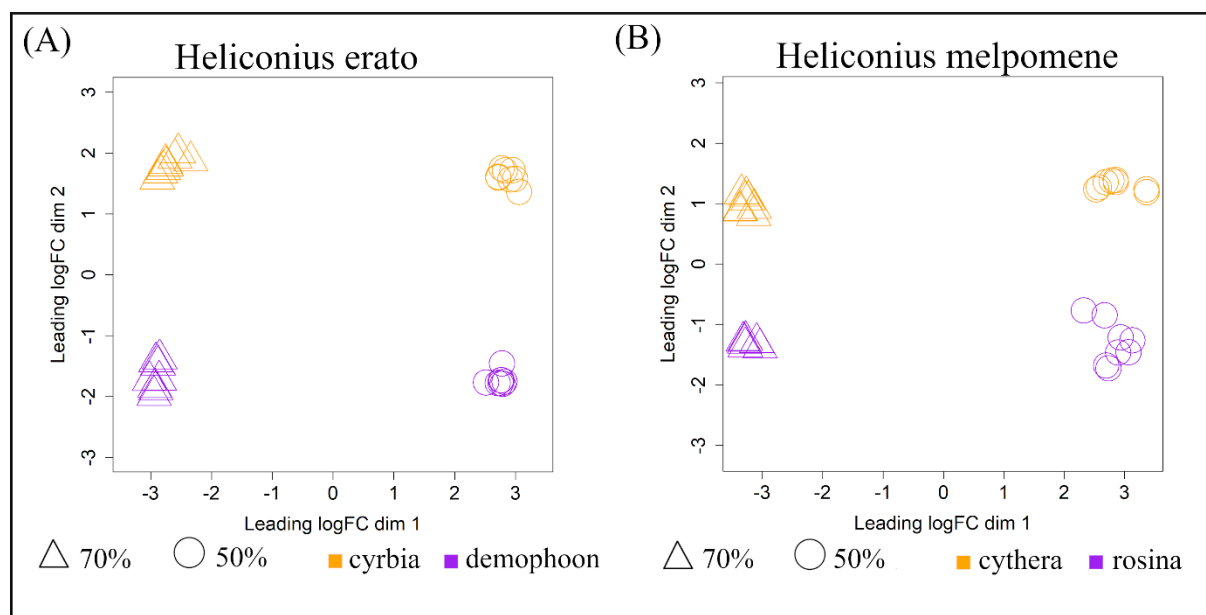


Figure 2. Multidimensional scaling of differences in expression profiles between samples of (A) *Heliconius erato* and (B) *Heliconius melpomene*. Clustering of samples is based on filtered and normalised expression levels. Point shape indicates stage and colour indicates subspecies.

Next, we assessed the differential expression between the androconial (non-iridescent) region and the iridescent region of the iridescent subspecies (termed wing region comparison). In *H. e. cyrbia* there was 1 gene at 50% and 70 genes at 70% differentially expressed (Table S6; S7). In *H. m. cythera*, there were 6 genes at 50% and 50 genes at 70% differentially expressed (Table S8; S9).

Subsequently, we overlapped these two sets of differentially expressed genes ('subspecies comparison' and 'wing region comparison') with each other to find concordantly expressed genes (Figure 3). Such genes are more likely to play a role in structural colour production rather than other unrelated population-specific differences. In particular, genes which are upregulated in both the 'subspecies' and 'wing region' comparisons are likely candidates for controlling aspects of nanostructure formation and therefore we termed these 'iridescent genes'.

In *H. erato*, at 50% development there were no significant, concordantly DE genes (Figure 3A, Table S10). However, a *doublesex-like* gene on Chromosome 8 narrowly missed the cut-off and was downregulated ($\text{LogFC} < -1.5$) in both comparisons (FDR = 0.02 between subspecies, FDR = 0.08 between wing regions). At 70% development, there were 2 genes significantly upregulated in both comparisons with an FDR < 0.05 (Figure 3B, Table S10). Interestingly, one of these was a *chitin deacetylase 1* gene, which functions in the deacetylation of chitin to chitosan and has previously described ultrastructural roles in insect cuticle development (Thurmond et al., 2019; Yu et al., 2019). The other significant gene showed similarity to the circadian clock-controlled gene *daywake*. Additionally, a *tetraspanin-9-like* gene was upregulated in both comparisons but it narrowly missed the FDR cut-off in the

subspecies comparison (FDR = 0.053 between subspecies, FDR = 0.011 between wing regions). No genes at 70% development in *H. erato* were significantly downregulated in both sets of differentially expressed genes.

At both 70% and 50% development in *H. melpomene* there was no overlap between genes that were significantly differentially expressed between subspecies and wing regions (FDR < 0.05). However, using a relaxed FDR cut-off of 0.2 revealed 1 gene upregulated at 50% as well 7 genes upregulated at 70 % development (Figure 3 C,D; Table S10).

Overall, in both *H. erato* and *H. melpomene*, the majority of genes in the two sets of differential expression analyses did not share a significant overlap in their expression patterns. This suggests that the majority of genes found to be differentially expressed are likely the result of population-specific differences rather than specifically controlling aspects of structural colouration.

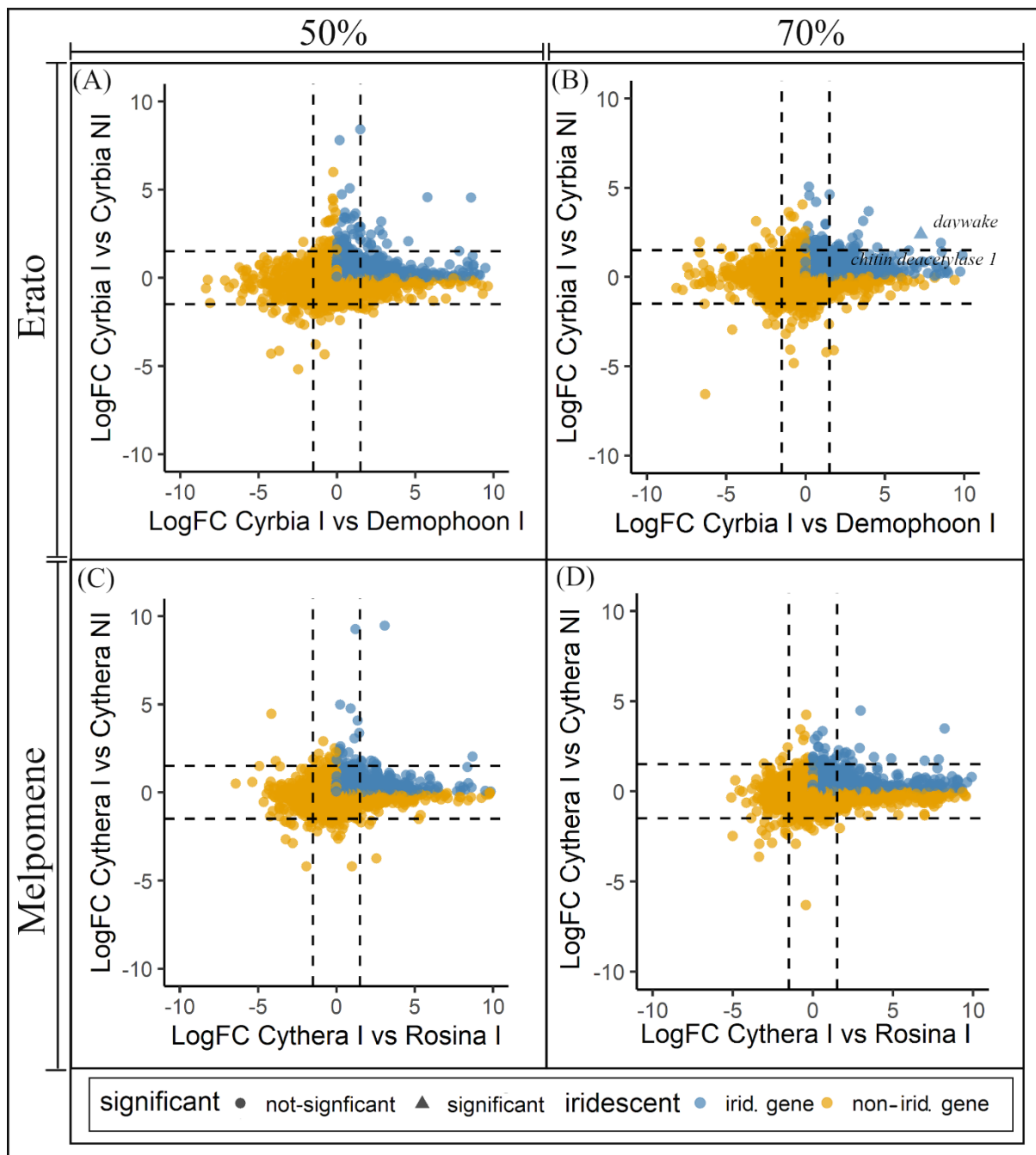


Figure 3. Overlapping expression patterns of differentially expressed genes in subspecies and wing region comparisons of *H. erato* (A-B) and *H. melpomene* (C-D) at 50% and 70% development. Genes which are upregulated ($\text{Log FC} > 0$) in both the subspecies comparison (iridescent subspecies vs non-iridescent subspecies) and the wing region comparison (iridescent region vs non-iridescent region of iridescent subspecies) are likely iridescent genes (blue points). Symbols indicate whether a gene falls within the significance level cut-off (FDR

< 0.05) for both the subspecies and wing region comparison. Dashed lines indicate $\text{LogFC} < -1.5$ and $\text{LogFC} > 1.5$ and therefore a large difference in expression.

Gene set enrichment analysis (GSEA)

GO term enrichment was performed using topGO (Alexa and Rahnenführer, 2021) to identify biologically relevant processes underpinning the DE genes in our comparisons between iridescent and non-iridescent subspecies of *H. erato* and *H. melpomene*.

In *H. erato*, at 50% development there was only 1 significant GO term (amide binding) out of the 907 differentially expressed genes between the subspecies (Figure 4). Instead, the majority of enriched GO terms occurred at 70% development, where out of the 1043 DE genes, 8 GO terms were significantly enriched across the three GO domains (4 Molecular Function, 2 Cellular Component and 2 Biological Process). Focusing on Molecular Function (Figure 4), the most enriched GO term was ‘acyl-CoA dehydrogenase activity’. Acyl-CoA dehydrogenase activity is involved in the first step of fatty acid β -oxidation; however, the specific functional role of this process is difficult to ascertain as fatty acids are required for numerous roles including: energy metabolism, precursors for eicosanoids and pheromones, synthesis of waxes and phospholipids (Arrese and Soulages, 2010). Manual Blastp search results indicate that a number of the genes annotated to the term ‘Acyl-CoA dehydrogenase activity’ are candidate enzymes in the β -oxidation step of the Lepidopteran pheromone biosynthesis pathway (Ding and Löfstedt, 2015). Indeed, many of the additional enriched GO terms could relate to pheromone biosynthesis (Figure 4), including ‘oxidoreductase activity acting on paired donors’ and ‘fatty acid beta-oxidation’. This may result from population-specific differences between the subspecies rather than colour differences.

Interestingly, the GO term ‘Voltage-gated cation channel activity’ was also significantly enriched at 70% in *H. erato*, with the majority of associated genes involved in calcium channel

activity. Intracellular Ca^{2+} (calcium) waves transmit across the developing butterfly wing and are predicted to play a role in scale development and coordinated colour pattern formation. (Ohno and Otaki, 2015).

In *H. melpomene*, there were no significantly enriched GO terms at either 50% or 70% development. This lack of enrichment is likely due to the low number of differentially expressed genes (203 genes at 50% and 78 genes at 70%). Moreover, a significant proportion of the genes in both the gene universe and DE gene list lacked GO annotation, further minimising possible gene sets which may be significant. For example, from the 30,720 genes in the *H. melpomene* gene universe, only 25.1 % have a current GO annotation of some description, compared to 30.4 % in *H. erato*.

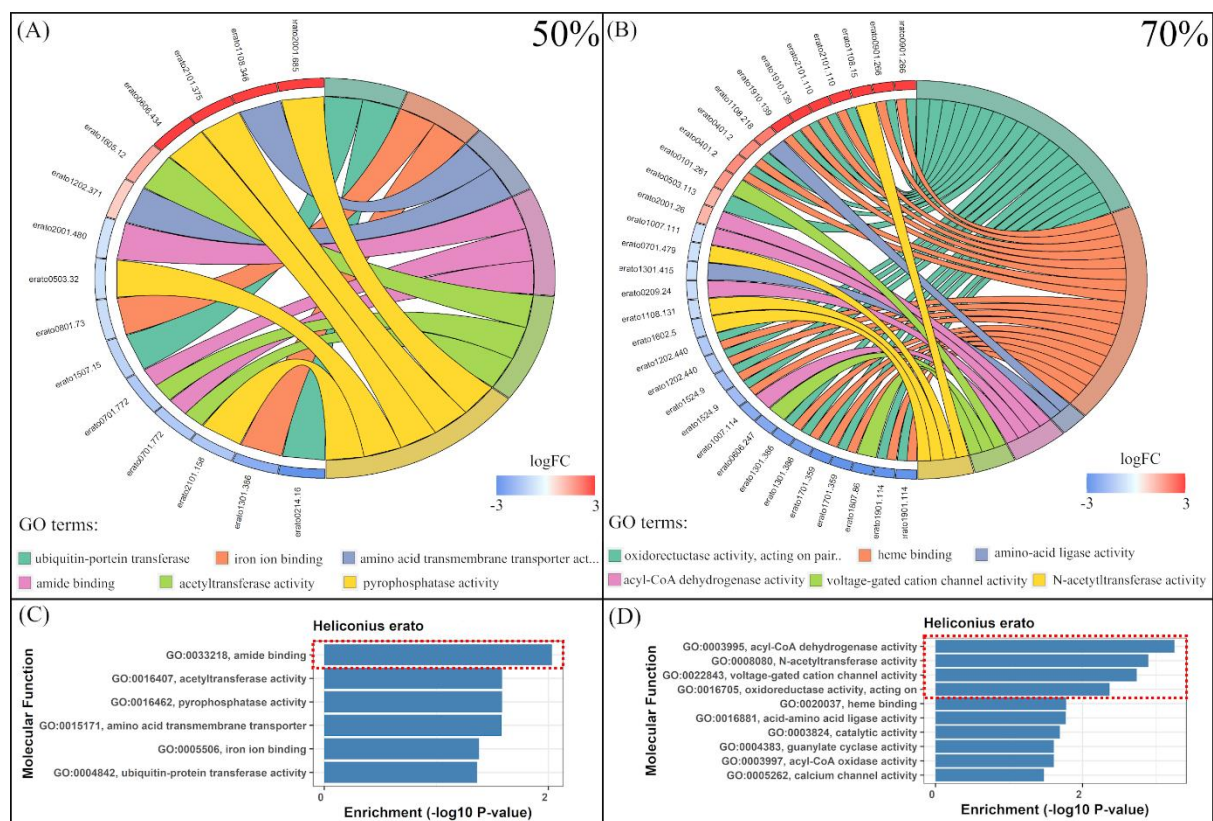


Figure 4. GSEA analysis (Molecular Function) of the differentially expressed genes between iridescent and non-iridescent subspecies of *H. erato* at 50% and 70%. (A-B) GO enrichment circle plots showing expression levels of genes belonging to the top 6 most enriched GO terms

at 50 % (A) and 70 % development (B). Genes associated with GO terms are on the left of the circle and associated GO terms are on the right. Colour scale of genes indicates amount of up/down regulation (LogFC). (C-D) Top enriched molecular function GO terms and descriptions for 50 % (C) and 70% development (D). All terms with an enrichment P-value greater than $-\log_{10}(2)$ are significant and are highlighted by a red dashed box.

Narrowing down candidate genes

Overlap of differentially expressed genes with QTL

Recently, Brien et al., (2019) used QTL mapping to explore the genetic control of iridescence in *Heliconius* (see Appendix). Using crosses between iridescent and non-iridescent subspecies of *H. erato* (*H. e. cyrbia* and *H. e. demophoon*) and *H. melpomene* (*H. m. cythera* and *H. m. rosina*) they identified genomic regions associated with different aspects of iridescent structural (the blue relative to red reflectance, hereafter “BR”, and luminance as a measure of overall brightness) as well scale morphology associated with reflective intensity (Ridge Spacing). In *H. erato*, there were two significant QTL on Chromosome 20 and the Z Chromosome (Chromosome 21) and in *H. melpomene* there were two significant QTL on Chromosome 3 and Chromosome 7 (Figure 5; S2). Through overlap of these QTL intervals with genes that we identified as being differentially expressed between the subspecies we narrow down the list of potential candidate genes.

For the subspecies comparison in *H. erato*, there were 2 and 5 significant (FDR<0.05) DE genes in the ‘BR’ interval on Chromosome 20 at 50% and 70% development, respectively (Table S11). One of the genes at 70% was *Fringe*, a boundary specific signalling molecule which modulates the Notch signalling pathway and has roles in eyespot formation and scale cell spacing in butterflies (French and Brakefield, 2004; Reed, 2004; Thurmond et al., 2019).

On the Z Chromosome, at 50% there were 27, 25, and 17 genes significantly DE (FDR<0.05) in the ‘Ridge spacing’, ‘luminance’ and ‘BR’ intervals, respectively (Table S11). Given the overlap between these intervals on the Z Chromosome, the majority of the genes were shared between the intervals, such that there were only 28 independent genes across all three intervals together. Of note, the microtubule motor protein, *dynein heavy chain 6* was within all three QTL intervals and highly-upregulated (LogFC > 3.0, FDR < 0.05) in the iridescent subspecies. Additionally, an *O-GlcNAc transferase*, with strong similarity to *Drosophila* polycomb group gene *super sex combs* was highly differentially expressed (LogFC = -9.32, FDR<0.004) and matched the exact physical location of the ‘BR’ and ‘Luminance’ marker within the genome.

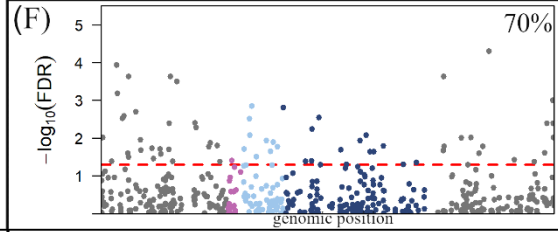
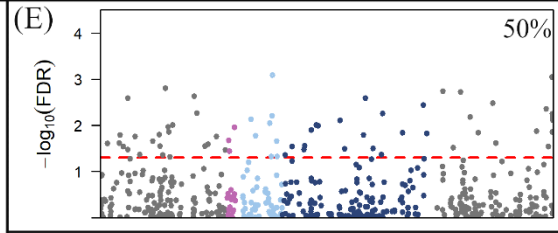
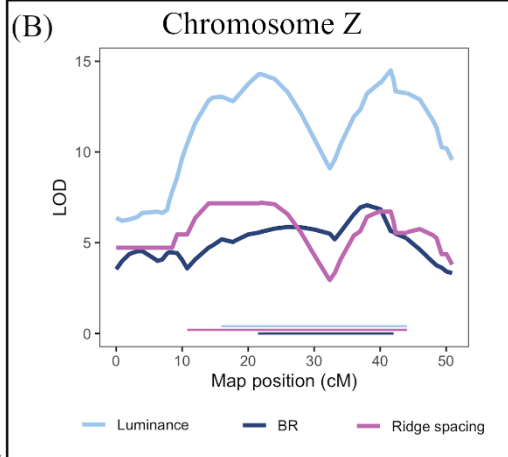
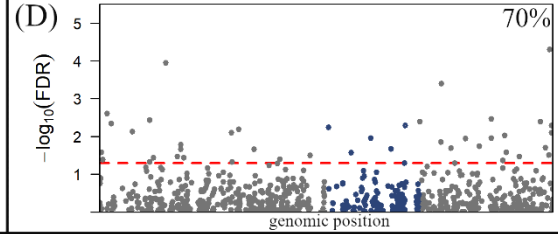
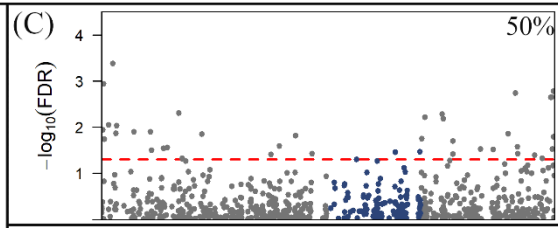
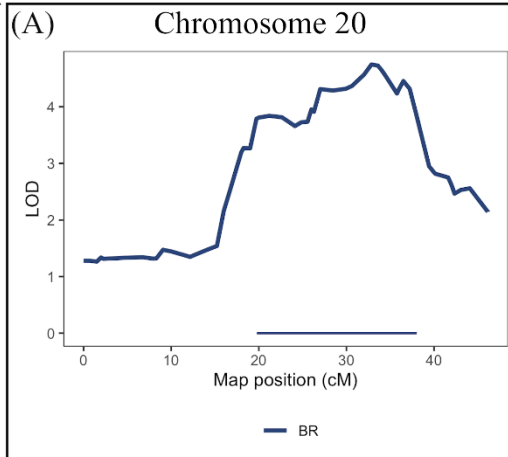
At 70%, on the Z Chromosome there were 24, 23, and 14 genes significantly DE (FDR<0.05) in the ‘Ridge spacing’, ‘luminance’ and ‘BR’ intervals, respectively (Table S11). Across all three intervals together there were 24 independent genes. The gene *trio*, which functions in actin structure regulation through activation of Rho-family GTPases (Thurmond et al., 2019), was found in all three intervals with particular proximity to the marker in the ‘Ridge Spacing’ interval. In addition to the functional role of *trio*, its high CPM and large fold change (logCPM = 7.34 , LogFC = -2.29, FDR = 0.0015) make it a particularly good candidate for a role in optical nanostructure development in *H. erato*. Additionally, an unidentified gene (MSTRG.21985) was also DE (LogFC -1.28, FDR = 0.0115) and may be related to a Rho GTPase activating protein (182 bp upstream).

In *H. melpomene*, there were no significantly DE genes (FDR<0.05) in the ‘Ridge Spacing’ interval on Chromosome 7 at either developmental stage. Using an expanded FDR cut-off of 0.2 revealed 4 DE genes within the interval at 50% and 4 DE genes at 70% (Table S12). At 70%, a notable gene of interest was *ringmaker*, which functions in microtubule organisation (Thurmond et al., 2019). On Chromosome 3, in the BR interval there was 1 novel gene

(MSTRG.3173) significantly DE expressed (FDR < 0.05) at 50% and no significant genes at 70%. Relaxing the FDR cut-off to 0.2 revealed a further 2 DE expressed genes in the BR interval at 50%, including the gene *miniature* (Table S12). In *Drosophila* hairs, *miniature* is predicted to be a component of the cuticulin envelope, functioning in interactions between the depositing cuticle, membrane and cytoskeleton (Roch et al., 2003). At 70%, there were 10 DE genes within the BR interval with an FDR < 0.2. The luminance interval had no significant genes with an FDR < 0.05 at either stage. Relaxing the cut-off to 0.2 revealed 1 further gene at 70% and 2 genes at 50%, one of these genes was *miniature*, as described above.

We also looked to see if any of the genes DE between wing regions were present in the QTL intervals. In *H. erato* there were no genes DE at either stage within any of the QTL intervals. For *H. melpomene*, there was 1 DE gene in the ‘BR’ interval (but outside the ‘luminance’ interval) on Chromosome 3 at 70% (a lactase-phlorizin hydrolase-like gene) and no DE genes at 50%. For the ‘Ridge Spacing’ interval on Chromosome 7 there was 1 DE gene at 50%, an F-actin-uncapping protein LRRC16A and 1 gene at 70%, a cuticle protein 18.6-like gene (Table S13).

Erato



Melpomene

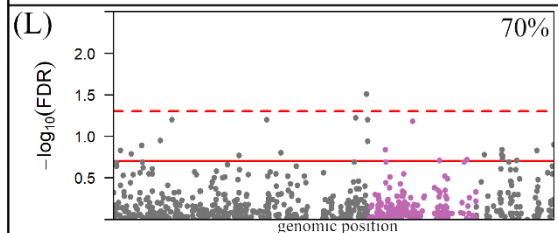
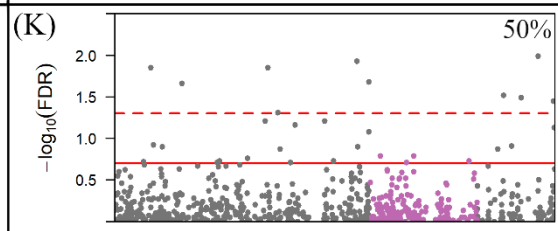
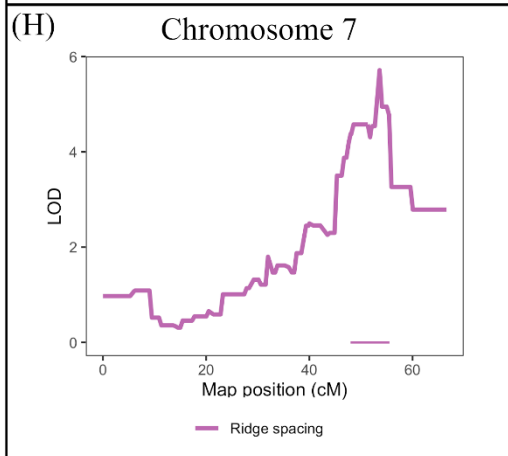
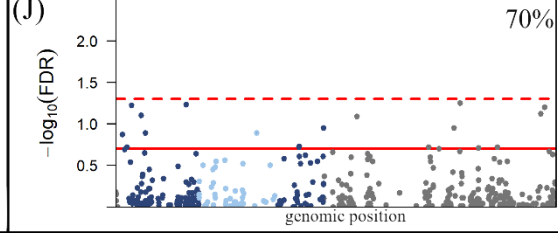
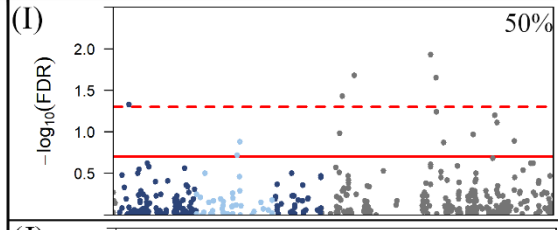
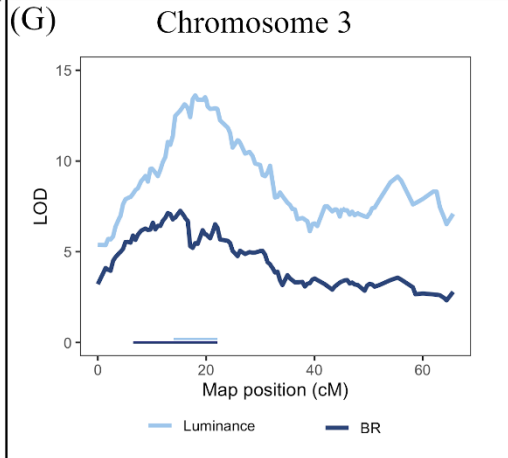


Figure 5. Differential expression of genes in the QTL in *Heliconius erato* (A-F) and *Heliconius melpomene* (G-L). Left panels: LOD scores and QTL intervals in *H. erato* (A, B) and *H. melpomene* (G, H). Right panels: $-\log_{10}$ False Discovery Rate (FDR) for differential expression at 50% and 70% development. Genes are coloured within the QTL intervals for *H. erato* (C-F) and *H. melpomene* (I-L), with colours matching those of the intervals in the panels on the left. In E and F the QTL overlap, such that all genes in the BR and ridge spacing intervals also fall within the luminance interval, see Table S6 for details. In I and J the luminance interval is within the BR interval. The dashed red line indicates FDR = 0.05 (significance), solid red line indicates FDR = 0.2.

Overlap with Drosophila bristle genes

Within our DE genes we identified genes known to play functional roles in the development of homologous structures and processes. *Drosophila* bristles (macrochaeta) represent a well-studied model system, with morphological and developmental homology to butterfly scales (Dinwiddie et al., 2014; Galant et al., 1998). In addition, cuticle development is a conserved process in invertebrates and is crucial to the formation of the optical nanostructures in butterflies (Ghiradella, 2010). Cuticle development genes have been particularly well characterised in *Drosophila* (Adler, 2017; Ostrowski et al., 2002).

For the subspecies comparison, in *H. erato* at both 50% and 70% development there was only 1 bristle gene (*NAT1*) significantly DE (50%: FDR = 0.0479; 70%: FDR = 0.0207) (Table S15). In *H. melpomene*, at 70% there were no DE bristle genes even with a relaxed significance cut off (FDR < 0.2). At 50% there were no significantly DE genes (FDR < 0.05). Using a relaxed FDR cut off (FDR < 0.2) revealed one gene (*Stim*) (FDR = 0.128) (Table S15).

For the wing region comparison, in *H. erato* at 70% development there were no significantly DE bristle genes (FDR<0.05). However, two genes narrowly missed the significance cut off, *BarH1* (FDR = 0.067) and *Rotund* (FDR = 0.088) (Table S16). At 50% development there was no significantly DE bristle genes (FDR<0.05). In *H. melpomene*, there were no bristle genes at either developmental stage significantly DE.

Overlap with cuticle development genes

For the subspecies comparison, in *H. erato*, at 70% development there were 5 cuticle genes significantly DE (FDR < 0.05) (Table S17). Of these genes, 3 were significantly upregulated in the iridescent subspecies: *Drop dead*, *Chitinase 7* and *Fringe* (also found within the QTL interval on the Z Chromosome). 2 cuticle genes were significantly downregulated, *Cytochrome P450 reductase* and *Cuticular protein 51A*. At 50% development, there were 3 significantly DE cuticle genes (FDR<0.05) (Table S17). 2 genes, *Cuticular protein 76Ba* and *Krotzkopf verkehrt (Kkv)* were significantly upregulated in the iridescent species. Interestingly, *Kkv* is a chitin synthase enzyme that patterns cuticle ridge formation in *Drosophila* bristles and together with its high expression value (LogCPM > 9) it is likely to play an important role in the developing cuticle of butterfly scales (Adler, 2019).

In *H. melpomene*, there were no significantly DE (FDR <0.05) cuticle genes at 70% development. Using the relaxed FDR cut-off of 0.2 revealed two genes, *Sec61 α subunit* and *Cytochrome P450 reductase* (Table S17). *Cytochrome P450 reductase*, which encodes the enzyme ‘NADPH--hemoprotein reductase’. At 50% development there was 1 gene (*Cytochrome P450 reductase*) significantly DE (FDR <0.05). Using a relaxed FDR cut-off of 0.2 revealed a further 2 genes, including *Miniature* (FDR = 0.19) which was also found in the QTL interval on Chromosome 3, and *Pale* (FDR = 0.19).

For the wing region comparison, in *H. erato* at 70% development there were 3 significantly DE cuticle genes (*TweedleG*, *Cuticular protein 62Ba*, *cubitus interruptus*)(Table S18). At 50% development, there were no significantly DE cuticle genes. In *H. melpomene*, at 70% development there were 4 significantly DE expressed (FDR<0.05) cuticle genes (*Larval cuticle protein 3*, *Cuticular protein 30F*, *Chitinase 5* and *Cuticular protein 62Ba*) (Table S18). At 50% development there were no significantly DE cuticle genes.

Overall, only a small number of genes involved in cuticle or bristle development were significantly DE in either species, at either developmental stage.

Convergent genes in Heliconius

Genes which are DE and show concordant expression patterns in both *H. erato* and *H. melpomene* may play a conserved role in structural colour development. We assessed DE genes in both the subspecies and wing region comparison for convergence between *H. erato* and *H. melpomene*.

For the subspecies comparison, at 70% development there were no significantly DE genes with convergent expression. However, 13 genes were found below a relaxed FDR cut-off of 0.2 (Table S19). At 50%, there were 2 concordant genes significantly DE, *Fatty acid synthase* and *Gamma-glutamylcyclotransferase* (Table S19). For the wing region comparison, at 70% there were 4 concordant genes significantly DE in both species, the homeobox gene *Invected*, *Transglutaminase*, *uncharacterized LOC113401078* and the *doublesex-like* gene (also DE between *H. erato* subspecies at 50%). There were no concordant wing region DE genes at 50% (although the *doublesex-like* gene is again DE in *H. melpomene*, Table S19).

Candidate gene identification and immunofluorescent staining

Our analyses across species, stages and tissue types revealed a large number of candidate genes. Testing large numbers of candidate genes is not practical for non-model organisms, therefore

we narrowed down candidates by identifying genes detected in multiple analyses. We ranked genes by the frequency at which they occurred in the above analyses and candidate selection was made based on the highest-ranking DE genes. Genes which occur in several analyses are more likely to be playing a role in structural colour development. In addition, we removed any genes from the final list which were significantly DE (FDR < 0.05) between the ‘iridescent’ and non-iridescent wing region of the non-iridescent subspecies. These genes are differentially expressed between non-iridescent tissues and therefore likely play no role in structural colour development but rather other functions such as wing region identity.

In *H. erato*, at 70% development there were 7 genes with occurrences in 3 or more analyses (Table 1). *Trio* was the top candidate and occurred in four analyses (top DE genes (species), and the QTL intervals: lumZ, BR_Z, RS_Z) and was significantly downregulated in the iridescent subspecies (LogFC = -2.28, FDR = 0.0015). All other genes had occurrences in 3 analyses, including the gene *Fringe*, which occurred in a QTL interval (BR_20), was a cuticle development gene and occurred in the species and wing region comparison overlap. *Fringe* was significantly upregulated in the iridescent subspecies (LogFC = 2.23, FDR < 0.027) making it a promising candidate. At 50% development there were 6 genes which occurred in 3 or more analyses (Table 1). An uncharacterized gene LOC120625954 (evm.model.Herato2101.296) was the top candidate and occurred in 4 analyses (top DE genes (species), and the QTL intervals: lumZ, BR_Z, RS_Z).

In *H. melpomene*, at 70% development there were no genes which occurred in 2 or more analyses and was significantly DE. At 50% development there were 8 genes which occurred in at least 2 analyses (Table 2). A potential candidate of interest was NADPH--cytochrome P450 reductase isoform X1, which was significantly upregulated in the iridescent subspecies (LogFC = 0.65, FDR = 0.0307) and occurred in both the top DE genes as well as being a cuticle gene.

Knockouts of this gene in *Tribolium confusum* show both cuticle and pigmentation defects (Huang et al., 2021), making it a promising candidate given the known association between butterfly wing scale pigments and cuticle structure (Matsuoka and Monteiro, 2018) .

Finally, we performed immunofluorescent staining of our most promising candidate gene, *Trio*. Immunofluorescence was performed in *Heliconius sara*, which possess iridescent blue colouration on the proximal portion of the forewing in addition to black, non-iridescent scales on the distal forewing (see Chapter 3). There was widespread expression of *Trio* at both 50% and 63% of development (Figure 6). However, there was no discernible difference in staining between the iridescent and non-iridescent regions at either stage. Closer inspection of the wing scales revealed that while staining was present in the scales (Figure 4, G-J), particularly at later developmental stages, it was also prominent within the epithelial layer (Figure 6, K). Overall, while *Trio* may play a role in wing or scale cell development, we find no evidence of a specific role in the patterning or formation of iridescent scales.

Table 1. Final candidate list of DE genes in *H. erato*. Genes were selected based on their occurrence in three or more analyses. *Trio* is highlighted in bold as the top candidate gene which was selected for immunofluorescent testing. FDR, LogFC, and LogCPM values are for the subspecies comparison.

%Development	Gene	Freq	Chr	LogFC	LogCPM	FDR	NCBI Hit	Analyses
50	Herato2101.296	4	Z	1.8458	2.6437	0.0097	uncharacterized protein LOC120625954	TopDEgenes(subspecies), lumZ QTL, BR_Z QTL, RS_Z QTL
50	Herato2101.200	3	Z	-1.137	5.2974	0.0074	sulfhydryl oxidase 1 isoform X2	TopDEgenes(subspecies), lumZ QTL, RS_Z QTL
50	Herato2101.255	3	Z	1.4654	2.898	0.0437	uncharacterized protein LOC113404158	lumZ QTL, BR_Z QTL, RS_Z QTL
50	Herato2101.263	3	Z	-0.7282	3.6591	0.029	chondroitin sulfate proteoglycan 4	lumZ QTL, BR_Z QTL, RS_Z QTL
50	Herato2101.375	3	Z	3.4585	0.1923	0.0426	dynein heavy chain 6, axonemal	lumZ QTL, BR_Z QTL, RS_Z QTL
50	Herato2101.409	3	Z	-9.3239	0.1733	0.0036	UDP-N-acetylglucosamine—peptide acetylglucosaminyltransferase 110 kDa subunit-like	N- TopDEgenes(subspecies), lumZ QTL, BR_Z QTL
70	Herato2101.253	4	Z	-2.2856	7.3362	0.0015	triple functional domain protein isoform X3	TopDEgenes(subspecies), lumZ QTL, BR_Z QTL, RS_Z QTL
70	Herato2001.420	3	20	2.2343	6.8235	0.0269	fringe	BR_20 QTL, Cuticle gene, SubSpecies & WingRegion Overlap
70	Herato2101.196	3	Z	-6.2624	-0.219	0.0083	no hit	TopDEgenes(subspecies), LumZ QTL, RS_Z QTL
70	Herato2101.200	3	Z	-1.3916	6.267	0.0014	sulfhydryl oxidase 1 isoform X2	TopDEgenes(subspecies), LumZ QTL, RS_Z QTL
70	Herato2101.284	3	Z	1.5401	0.9496	0.0394	type I inositol 3,4-bisphosphate 4-phosphatase-like	lumZ QTL, BR_Z QTL, RS_Z QTL
70	Herato2101.324	3	Z	-0.7098	4.4433	0.0489	PQ-loop repeat-containing protein 3	lumZ QTL, BR_Z QTL, RS_Z QTL
70	Herato2101.401	3	Z	-4.2198	-1.176	0.0439	mannan-binding lectin serine protease 1-like isoform X2	lumZ QTL, BR_Z QTL, RS_Z QTL

Table 2. Final candidate list of DE genes in *H. melpomene*. Genes were selected based on their occurrence in two or more analyses. FDR, LogFC, and LogCPM values are for the subspecies comparison. Convergent gene indicates genes convergent between *H. erato* and *H. melpomene* in the subspecies comparison.

%Development	Gene	Freq	Chr	LogFC	logCPM	FDR	NCBI Hit	Analyses
50	HMEL005305g	2	7	-1.6127	1.8559	0.0354	fatty acid synthase	Convergent gene, TopDEgenes(subspecies)
50	HMEL008899g	2	6	-2.1981	3.0045	0.04	leucine-rich melanocyte differentiation-associated protein-like	Convergent gene, TopDEgenes(subspecies)
50	HMEL009927g	2	13	-1.0469	3.3844	0.0414	putative pre-mRNA-splicing factor ATP-dependent RNA helicase DHX16	Convergent gene, TopDEgenes(subspecies)
50	HMEL010934	2	19	1.6169	3.283	0.0371	cytochrome P450 4C1-like	Convergent gene, TopDEgenes(subspecies)
50	HMEL017055g	2	20	1.083	4.782	0.0371	peroxisomal membrane protein 2	Convergent gene, TopDEgenes(subspecies)
50	HMEL030760g	2	10	-2.058	2.9187	0.0371	gamma-glutamylcyclotransferase-like	Convergent gene, TopDEgenes(subspecies)
50	HMEL035109g	2	20	0.6496	5.9249	0.0307	NADPH--cytochrome P450 reductase isoform X1	TopDEgenes(subspecies), Cuticle gene
50	HMEL038231g	2	9	-1.9404	4.3151	0.0113	no hit	TopDEgenes(subspecies), TopDEgenes(wing region)

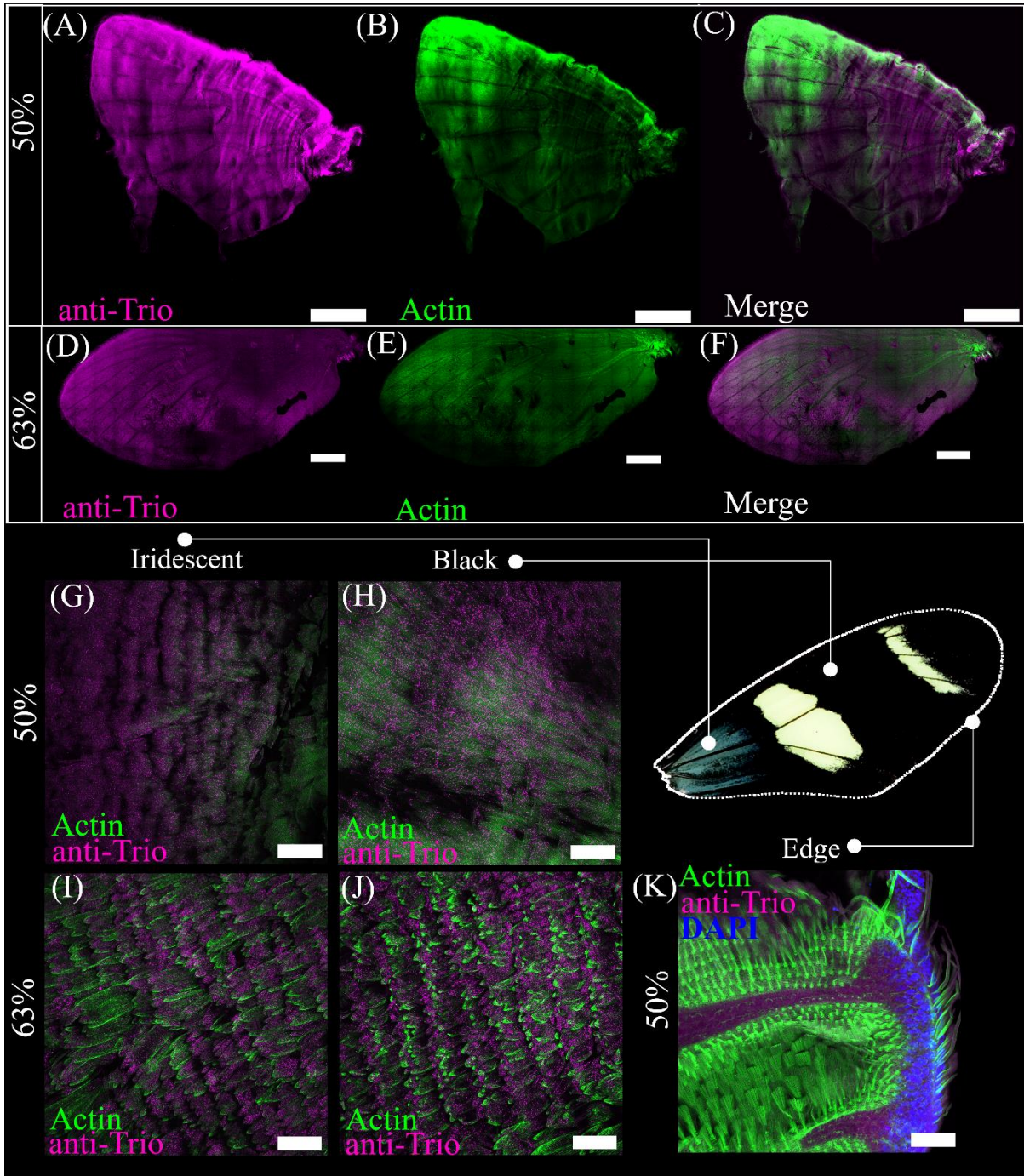


Figure 6. Immunofluorescent staining of *Trío* in *Heliconius sara* developing wings. (A-F) Whole wings of *Heliconius sara* at 50% and 70% development stained with an anti-*Trío* antibody in red and phalloidin (actin stain) in green. (G-J) Iridescent blue (G,I) and non-iridescent black (H,J) scales at 50% and 63% development. (K) Edge of the wing showing a fold in the epithelial membrane, with cell nuclei labelled with DAPI (blue). Scale bars: (A-F) 2000 μm (G-K) 50 μm .

Discussion

Heliconius butterflies possess vivid structural colours, created by multilayer ridge reflectors on their wing scales (Parnell et al., 2018). This study is one of the first to characterise the genetic and developmental basis of structural colours in *Heliconius*, by harnessing differential expression analysis of RNAseq data. Using comparative analyses between iridescent and non-iridescent subspecies and wing regions of *Heliconius erato* and *Heliconius melpomene*, we have identified several genes which may play key roles in the gene regulatory networks underpinning optical nanostructure development.

One of our most promising candidate genes was *Trio*, a Rho-GTPase activator associated with actin cytoskeleton remodelling and was DE in *H. erato* at 70% development (Seipel et al., 1999). This gene occurred repeatably in our analyses (Table 1) and was within the *H. erato* Z Chromosome QTL interval, with particular proximity to the ‘Ridge Spacing’ marker (Figure 5). Structurally coloured *Heliconius* species have reduced ridge spacing compared to non-structurally coloured species (Brien et al., 2018; Parnell et al., 2018). The spacing of cuticle ridges is determined by the actin cytoskeleton (Chapter 3), making *Trio* a promising candidate for structural colour development. Furthermore, *Trio* plays roles in the regulation of membrane ruffling as well as inducing stress fibres (Seipel et al., 1999). Both these processes may be important in chitin ridge formation, including applying the forces purportedly required for generating multilayer reflector layers (Ghiradella, 1974). Despite this, our immunofluorescence analysis of *Trio* in the closely-related *Heliconius sara* failed to detect differences in expression of *Trio* between the black and blue wing regions. It is notable, that beyond 60% development the cuticle of the wing scale forms a physically impenetrable layer to antibodies and as such differences in expression may not be detectable. Furthermore, it is also plausible that the genetic basis of structural colour in *H. sara* may be different from *H. erato* in which this gene was detected.

Several other DE genes were also found within the QTL intervals in both *H. melpomene* and *H. erato*, demonstrating how integrating such genetic approaches can be used to identify a targeted set of candidate genes (Derakhshani et al., 2020; Scolari et al., 2021). In addition, our analyses of genes across the two different stages (50% and 70%) likely highlighted two different types of underlying genetic control of structural colour. At 50% the wing scales are only partially developed, with minimal cuticle deposition (Figure 1) (Dinwiddie et al., 2014). At this stage the DE genes are likely to be upstream in the pathways underlying optical nanostructure formation and potentially playing a patterning role. The later stage, 70%, is during the period when the optical nanostructures are being deposited and we expect to find genes which are directly involved (downstream) in building the nanostructures, such as cuticle related proteins and enzymes. In agreement, our results show that in *H. erato* at 50% development, there are few cuticle-related genes in our gene list, however, at 70% we observe DE of many cuticle-related genes, such as *chitin deacetylase 1*, *cuticle protein 7-like*, *cuticle protein 1-like*, *cytochrome P450 303a1* (Table S2; S3) (Thurmond et al., 2019).

A potential shortcoming of the selected stages is that they likely omit earlier cellular events potentially important for structural colour production. For example, it is plausible that many of the genes controlling the phenotype ‘Ridge spacing’ are expressed earlier in development, when the actin filaments are cross-linked and bundled and so are not picked up by our QTL/DE overlap analysis (Day et al., 2019; Dinwiddie et al., 2014).

The number of DE genes in *H. erato* was far greater than that in *H. melpomene*, likely due to a more recent divergence of *H. melpomene* subspecies compared to *H. erato* and therefore less overall genetic difference. In agreement, our MDS analysis of gene expression indicates a closer expressional similarity between *H. melpomene* subspecies than *H. erato* (Figure 2). Population-specific differences represent an added complexity for successfully identifying only structural colour-related genes. Indeed, the gene pathways identified in our GSEA (Figure

4) highlight such a problem, with the terms identified probably related to pheromone biosynthesis and metabolism - rapidly evolving characteristics between diverging subspecies, unrelated to structural colouration (González-Rojas et al., 2020).

To circumvent this problem of population-specific genes we identified DE genes concordantly expressed between subspecies and wing regions comparisons (Figure 4). This analysis identified interesting candidates, including a *Chitin deacetylase 1* gene which was DE expressed between subspecies and wing regions in *H. erato*. Chitin is a vital component of the insect cuticle – the biopolymer from which the optical nanostructures are constructed (Moussian, 2010). Reverse genetic approaches have shown that alterations to chitin deacetylation in the locust trachea is able to induce substantial deformations in cuticle morphology, generating a ‘buckled’ cuticular architecture similar to the layered ridges present in butterfly scales (Yu et al., 2016). Further analysis using CRISPR-Cas9 gene knockouts of such genes may help decipher their specific functional role and their position within the gene regulatory networks controlling structural colour development.

We observed very little evidence for the convergence of genes controlling structural colour in *H. erato* and *H. melpomene*. While a large number of genes had shared expression in both species, very few were concordantly differentially expressed at either developmental stage. This is perhaps unsurprising given the differences in scale architecture and brightness between the species, making the probability of genetic parallelism a less likely occurrence (Parnell et al., 2018). Nevertheless, there were some potential genes of interest which may play a convergent role in structural colour development (Table S19). This includes a *Doublesex-like* gene which was DE between wing regions in both species at both stages and also between the *H. erato* subspecies at 50% development. The genomic location of this particular gene (Chromosome 7 in both *H. erato* and *H. melpomene*) does not match the primary annotated *Doublesex* on Chromosome 10; suggesting a possible duplication event. Interestingly, a novel

duplicated *Doublesex* gene is thought to play a role in UV structural colour in *Zerene cesonia* (Southern Dogface). Sex-specific isoforms of a novel *Doublesex* are able to activate and repress female- and male-type UV wing scales (Rodriguez-Caro et al., 2021). This alludes to an interesting possibility of novel *Doublesex* duplications controlling structural colouration across multiple species.

Despite the lack of evidence of convergence at the gene level, we cannot exclude the possibility of some form of parallelism in the intracellular processes governing optical nanostructure formation. Indeed, in both species we see evidence for differential expression of cuticle-related genes (Table S17; S18) as well as cytoskeleton-associated genes (Table S15; 16). It is plausible that different parts of the gene regulatory network controlling wing scale development may have been the target for selection in the evolution of optical nanostructures in *Heliconius*. Notwithstanding, our lack of evidence of convergence in DE agrees with the QTL analysis (Brien et al., 2021; Appendix), in which QTL intervals corresponding to phenotypes associated with structural colour (BR value, ridge spacing, luminance) were found on different chromosomes for *H. erato* and *H. melpomene*. The lack of evidence for convergence in our DE genes controlling structural colour contrasts to what is known about the genes underpinning pigmentary colour patterns, which repeatably harnesses several major effect loci (Joron et al., 2006a; Nadeau, 2016). However, this is perhaps unsurprising given that previous studies have shown that structural colour in *Heliconius* is a quantitative trait controlled by many small effect loci (Brien et al., 2018; Curran et al., 2020; Curran, 2018).

Overall, we have found a number of candidate genes which potentially underpin the development of structural colour in *Heliconius* butterflies. Some of these candidates include genes involved in actin cytoskeleton remodelling and cuticle formation, which are crucial intracellular processes involved in wing scale development. Other candidate genes include several previously identified to play roles in butterfly wing development, such as eyespot

formation. Future studies should perform gene knockouts to ascertain the direct role of these genes in the construction of optical nanostructures in *Heliconius*. Additionally, we found little evidence for convergence in genes underpinning structural colour development between *H. erato* and *H. melpomene*, in agreement with what is known from previous genetic analyses.

Acknowledgements

General

We thank Dr. Alan Dunbar (Department of Engineering, University of Sheffield) for use of the scanning electron microscope (machine funded via the EPSRC 4CU grant no. EP/K001329/1). We also express gratitude to Alexandre Thiery (Centre for Craniofacial & Regenerative Biology, Kings College London) for his expertise and assistance with the differential expression analysis. We also thank Darren Robinson (Light Microscope Facility, University of Sheffield) for the assistance with the Nikon A1 confocal. We also extend our thanks to Natalia Bulgakova (School of Biosciences, University of Sheffield) for her invaluable help with the immunofluorescence protocols.

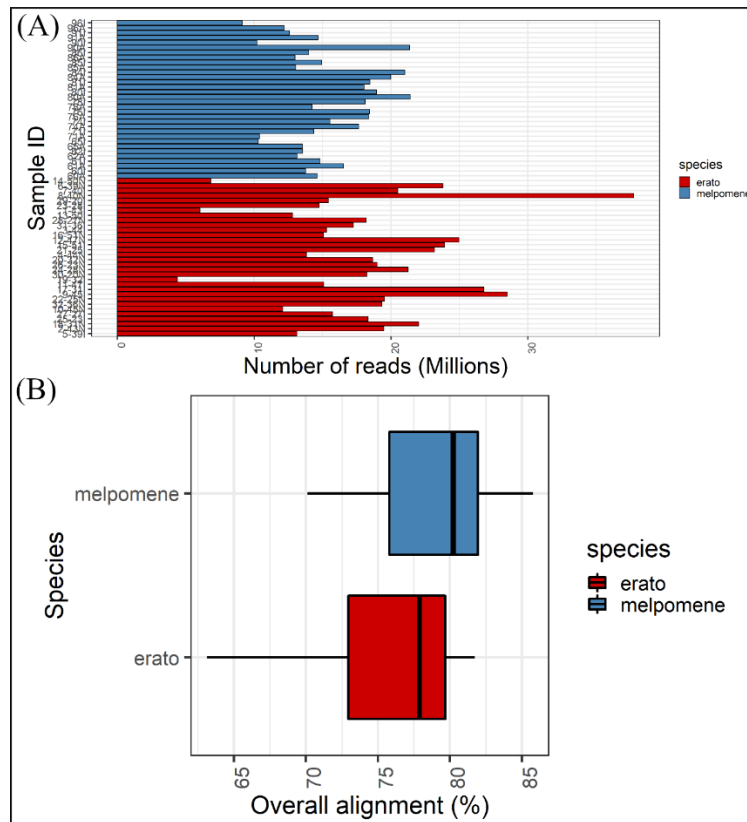
Funding

This research was supported by the following grants: Natural Environment Research Council (NERC) Fellowship to N.J.N (NE/K008498/1). This work was also funded from through a NERC doctoral training partnership (Adapting to the Challenges of a Changing Environment) (V.J.L).

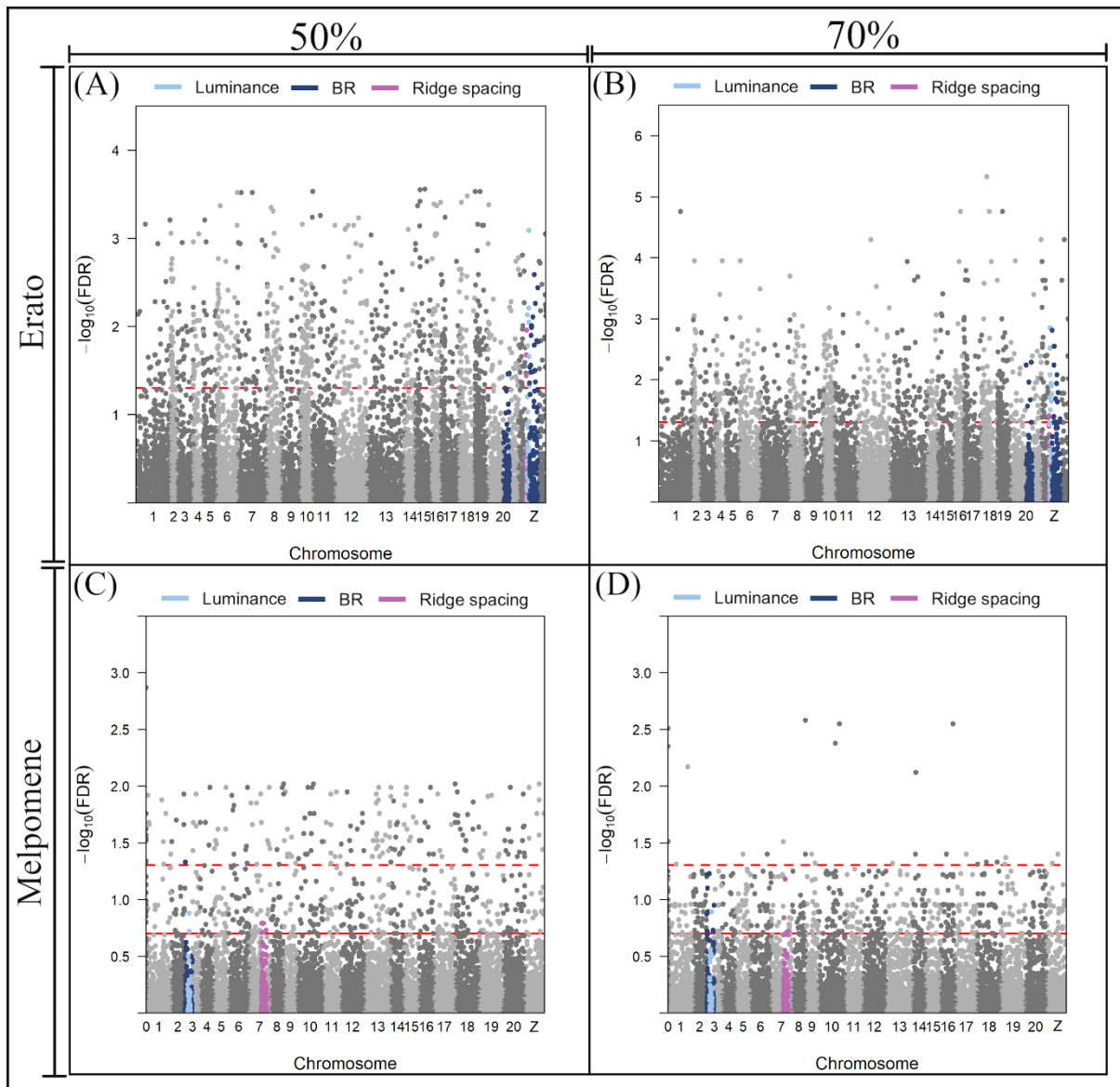
Author contributions

Specific contributions of authors are detailed at the start of the chapter.

Supplementary Information



Supplementary Figure 1. Filtering and alignment of RNAseq reads of *H. erato* and *H. melpomene*. (A) Number of raw RNA reads in the samples of *H. erato* and *H. melpomene* in millions. (B) Overall mean percentage alignment of the RNA reads with the respective species genomes using HISAT2.



Supplementary Figure 2. Genes expressed in the wings and their genomic location in *Heliconius erato* (A, B) and *Heliconius melpomene* (C, D) at the two developmental stages (50% and 70%). Genes with a $-\log_{10}(\text{FDR})$ [False Discovery Rate] greater than 1.30 (red dashed line) are significantly differentially expressed between the iridescent and non-iridescent subspecies of each species. Solid red line indicates the expanded FDR cut-off (0.02) of 0.69 used in *H. melpomene*. Coloured regions indicate previously-identified QTL intervals which are associated with iridescence in each species.

Table S1: Samples of *H. erato* and *H. melpomene* used in the RNAseq analysis.
 * indicates the *H. melpomene* sample which was removed from further DE analyses.

Sample	Subspecies	%Development	Tissue	Individual	Sex
<i>H. erato</i>					
M_23I	cyrbia	50	FW + post-HW	1	Male
M_23N	cyrbia	50	anterior-HW	1	Male
F_27I	cyrbia	50	FW + post-HW	2	Female
F_27N	cyrbia	50	anterior-HW	2	Female
F_25I	cyrbia	50	FW + post-HW	3	Female
F_25N	cyrbia	50	anterior-HW	3	Female
M_28I	cyrbia	50	FW + post-HW	4	Male
M_28N	cyrbia	50	anterior-HW	4	Male
F_31I	demophoon	50	FW + post-HW	1	Female
F_31N	demophoon	50	anterior-HW	1	Female
F_32I	demophoon	50	FW + post-HW	2	Female
F_32N	demophoon	50	anterior-HW	2	Female
F_20I	demophoon	50	FW + post-HW	3	Female
F_20N	demophoon	50	anterior-HW	3	Female
M_36I	demophoon	50	FW + post-HW	4	Male
M_36N	demophoon	50	anterior-HW	4	Male
M_43I	cyrbia	70	FW + post-HW	1	Male
M_43N	cyrbia	70	anterior-HW	1	Male
M_44I	cyrbia	70	FW + post-HW	2	Male
M_44N	cyrbia	70	anterior-HW	2	Male
M_50I	cyrbia	70	FW + post-HW	3	Male
M_50N	cyrbia	70	anterior-HW	3	Male
M_51I	cyrbia	70	FW + post-HW	4	Male
M_51N	cyrbia	70	anterior-HW	4	Male
F_39I	demophoon	70	FW + post-HW	1	Female
F_39N	demophoon	70	anterior-HW	1	Female
F_40I	demophoon	70	FW + post-HW	2	Female
F_40N	demophoon	70	anterior-HW	2	Female
M_45I	demophoon	70	FW + post-HW	3	Male
M_45N	demophoon	70	anterior-HW	3	Male
F_47I	demophoon	70	FW + post-HW	4	Female
F_47N	demophoon	70	anterior-HW	4	Female
<i>H. melpomene</i>					
S_84AF	cythera	50	anterior-HW	1	Female
S_84IF	cythera	50	FW + post-HW	1	Female
S_80AM	cythera	50	anterior-HW	2	Male
S_80IM	cythera	50	FW + post-HW	2	Male
S_91AF	cythera	50	anterior-HW	3	Female
S_91IF	cythera	50	FW + post-HW	3	Female
S_81AM	cythera	50	anterior-HW	4	Male

Sample	Subspecies	%Development	Tissue	Individual	Sex
<i>H. melpomene</i>					
S_81IM	cythera	50	FW + post-HW	4	Male
S_62AM	rosina	50	anterior-HW	1	Male
S_62IM	rosina	50	FW + post-HW	1	Male
S_76AF	rosina	50	anterior-HW	2	Female
S_76IF	rosina	50	FW + post-HW	2	Female
S_78AM	rosina	50	anterior-HW	3	Male
S_78IM	rosina	50	FW + post-HW	3	Male
S_90AF	rosina	50	anterior-HW	4	Female
S_90IF	rosina	50	FW + post-HW	4	Female
S_71AM	cythera	70	anterior-HW	1	Male
S_71IM	cythera	70	FW + post-HW	1	Male
S_96AF	cythera	70	anterior-HW	2	Female
S_96IF	cythera	70	FW + post-HW	2	Female
S_86AM	cythera	70	anterior-HW	3	Male
S_86IM	cythera	70	FW + post-HW	3	Male
S_61AF	cythera	70	anterior-HW	4	Female
S_61IF	cythera	70	FW + post-HW	4	Female
S_60AM*	rosina	70	anterior-HW	1	Male
S_60IM*	rosina	70	FW + post-HW	1	Male
S_65AM	rosina	70	anterior-HW	2	Male
S_65IM	rosina	70	FW + post-HW	2	Male
S_85AM	rosina	70	anterior-HW	3	Male
S_85IM	rosina	70	FW + post-HW	3	Male
S_74AM	rosina	70	anterior-HW	4	Male
S_74IM	rosina	70	FW + post-HW	4	Male

Table S2: Genes differentially expressed (FDR<0.2) between *H. erato cyrba* and *H. erato demophoon* at 50% development - see Excel spreadsheet (available through the online publication)

Table S3: Genes differentially expressed (FDR<0.2) between *H. erato cyrba* and *H. erato demophoon* at 70% development. - see Excel spreadsheet (available through the online publication)

Table S4: Genes differentially expressed (FDR<0.2) between *H. melpomene cythera* and *H. melpomene rosina* at 50% development - see Excel spreadsheet (available through the online publication)

Table S5: Genes differentially expressed (FDR<0.2) between *H. melpomene cythera* and *H. melpomene rosina* at 70% development - see Excel spreadsheet (available through the online publication)

Table S6: Genes differentially expressed (FDR<0.2) between wing regions in *H. erato cyrba* at 50% development - see Excel spreadsheet (available through the online publication)

Table S7: Genes differentially expressed (FDR<0.2) between wing regions in *H. erato cyrba* at 70% development. - see Excel spreadsheet (available through the online publication)

Table S8: Genes differentially expressed (FDR<0.2) between wing regions in *H. melpomene cythera* at 50% development - see Excel spreadsheet (available through the online publication)

Table S9: Genes differentially expressed (FDR<0.2) between wing regions in *H. melpomene cythera* at 70% development - see Excel spreadsheet (available through the online publication)

Table S10. Overlapping genes (FDR < 0.2) between the wing region comparison of the iridescent subspecies and the subspecies comparison. Bold indicates significant genes with an FDR < 0.05 in both comparisons.

gene	logFC .subsp ecies	logCPM .subspec ies	F.subsp ecies	FDR.su bspecies	logFC.wing _region	logCPM. wing_regi on	F.wing_ region	FDR.wi ng_regi on	Annotation	E-value
<i>Heliconius erato</i> 50%										
MSTRG.13758 evm.TU.Herato1301.635	12.664	3.502	39.655	0.020	1.280	3.995	50.369	0.179	U8-agatoxin-Ao1a-like [Vanessa tameamea]	4.00E-66
MSTRG.7192 evm.TU.Herato0801.87	-2.719	4.719	24.967	0.019	-1.839	3.853	91.115	0.080	protein doublesex-like isoform X1 [Vanessa tameamea]	2.00E-29
MSTRG.13445 evm.TU.Herato1301.472	-0.903	3.814	6.293	0.194	-0.974	3.843	47.992	0.179	transcription factor cwo isoform X4 [Vanessa tameamea]	0
70%										
MSTRG.22333	5.601	4.269	278.480	0.000	0.370	5.065	16.352	0.154	na	na
MSTRG.21653 evm.TU.Herato2101.110	3.634	3.755	160.991	0.000	0.741	4.324	28.989	0.084	probable cytochrome P450 303a1 isoform X2 [Danaus plexippus plexippus]	0
MSTRG.10205 evm.TU.Herato1007.170	4.283	7.069	90.206	0.002	0.379	7.812	14.481	0.175	carboxypeptidase N subunit 2-like [Vanessa tameamea]	0
MSTRG.18455 evm.TU.Herato1805.101 evm.TU.Herato1805.102	1.983	4.676	46.658	0.006	1.174	4.893	17.173	0.187	circadian clock-controlled protein-like [Vanessa tameamea]	7.00E-100
MSTRG.13019	6.520	-0.145	36.588	0.010	1.480	0.260	14.119	0.176	na	0

gene	logFC .subsp ecies	logCPM .subspec ies	F.subsp ecies	FDR.su bspecies	logFC.wing _region	logCPM. wing_regi on	F.wing_ region	FDR.wi ng_regi on	Annotation	E-value
MSTRG.18255 evm.TU.Herato1803.22 evm.TU.Herato1803.28	8.531	6.121	28.630	0.017	1.914	6.453	35.671	0.119	circadian clock-controlled protein-like [Vanessa tameamea]	2.00E-64
MSTRG.17035 evm.TU.Herato1701.207 evm.TU.Herato1701.208 evm.TU.Herato1701.210	1.750	4.257	27.600	0.017	0.705	4.558	17.744	0.149	TPA_inf: cytochrome P450 CYP405A4 [Heliconius erato]	0
MSTRG.21292 evm.TU.Herato2001.642	2.802	5.208	26.958	0.018	0.651	5.776	26.047	0.090	serine protease snake-like [Vanessa tameamea]	2.00E-89
MSTRG.18256*	7.243	1.525	24.987	0.021	2.406	1.762	65.210	0.024	na	na
MSTRG.20971 evm.TU.Herato2001.420	2.234	6.824	21.519	0.027	0.420	7.324	17.834	0.144	fringe [Junonia coenia]	0.00E+00
MSTRG.9120 evm.TU.Herato1003.15 evm.TU.Herato1003.17 evm.TU.Herato1003.22 evm.TU.Herato1003.23	1.194	4.395	19.771	0.031	0.396	4.704	14.415	0.175	protein MLP1 homolog isoform X2 [Aphantopus hyperantus]	0
MSTRG.3894 evm.TU.Herato0503.238	0.944	4.236	19.284	0.032	0.738	4.322	44.080	0.044	chitin deacetylase 1 [Zerene cesonia]	0.00E+00
MSTRG.681 evm.TU.Herato0101.519	0.788	4.675	18.055	0.037	0.397	4.839	18.989	0.131	chromatin complexes subunit BAP18-like [Aphantopus hyperantus]	2.00E-48
MSTRG.10736 novel_gene_126	4.930	1.026	16.283	0.045	1.236	1.592	12.718	0.190	Transposon Ty3-G Gag-Pol polyprotein [Operophtera brumata]	1.00E-170
MSTRG.2116 evm.TU.Herato0215.126	4.241	4.681	16.239	0.045	0.926	5.107	19.894	0.149	calcium/calmodulin-dependent protein kinase kinase 1 [Aphantopus hyperantus]	0.00E+00

gene	logFC .subsp ecies	logCPM .subspec ies	F.subsp ecies	FDR.su bspecies	logFC.wing _region	logCPM. wing_regi on	F.wing_ region	FDR.wi ng_regi on	Annotation	E-value
MSTRG.2111 evm.TU.Herato0215.124	4.881	2.985	14.978	0.052	1.103	3.502	20.259	0.131	uncharacterized protein LOC113404666 [Vanessa tameamea]	7.00E-32
MSTRG.17608 evm.TU.Herato1706.3	1.721	3.190	14.614	0.053	1.477	3.291	90.382	0.011	PREDICTED: tetraspanin-9- like [Papilio polytes]	4.00E-70
MSTRG.17430 evm.TU.Herato1704.13	1.546	4.868	14.176	0.057	0.569	5.158	29.804	0.083	neprilysin-4-like [Aphantopus hyperantus]	0.00E+00
MSTRG.6129 evm.TU.Herato0701.205	2.086	2.768	14.074	0.057	0.683	3.212	12.873	0.189	solute carrier family 28 member 3-like [Bicyclus anyana]	0.00E+00
MSTRG.1644 evm.TU.Herato0211.46	1.076	4.242	13.616	0.059	0.589	4.413	37.831	0.055	cell cycle control protein 50A- like isoform X2 [Vanessa tameamea]	5.00E-78
MSTRG.14815 evm.TU.Herato1411.237	0.648	4.162	12.524	0.069	0.413	4.258	14.582	0.175	pyroglutamyl-peptidase 1 [Vanessa tameamea]	7.00E-131
MSTRG.7867 evm.TU.Herato0821.114	2.116	5.488	12.238	0.073	0.348	6.047	13.712	0.179	putative phospholipase B-like 2 [Vanessa tameamea]	0.00E+00
MSTRG.12474	5.134	1.628	12.111	0.074	0.683	2.338	12.258	0.196	na	na
MSTRG.12267 evm.TU.Herato1202.501	1.625	4.813	11.141	0.083	0.483	5.209	21.059	0.117	nanos protein [Danaus plexippus plexippus]	1.00E-144
MSTRG.12213 evm.TU.Herato1202.469	0.824	7.357	10.872	0.085	0.425	7.528	16.759	0.151	Putative polypeptide N- acetylgalactosaminyltransfera se 9 [Papilio machaon]	0.00E+00
MSTRG.21139 evm.TU.Herato2001.552	0.543	5.284	10.651	0.088	0.289	5.398	13.075	0.187	selenoprotein M-like [Danaus plexippus plexippus]	2.00E-46
MSTRG.4596	1.523	-0.825	9.588	0.103	4.611	-1.120	23.398	0.099	na	na

gene	logFC .subsp ecies	logCPM .subspec ies	F.subsp ecies	FDR.su bspecies	logFC.wing _region	logCPM. wing_regi on	F.wing_ region	FDR.wi ng_regi on	Annotation	E-value
MSTRG.20663 evm.TU.Herato2001.192	0.771	2.995	9.229	0.108	0.506	3.109	14.529	0.175	BTB/POZ domain-containing adapter for CUL3-mediated RhoA degradation protein 3 [Trichoplusia ni]	0.00E+00
MSTRG.21393 evm.TU.Herato2001.698 evm.TU.Herato2001.699	0.851	3.974	7.964	0.132	0.469	4.158	14.275	0.175	acetyl-CoA carboxylase isoform X1 [Vanessa tameamea]	0.00E+00
MSTRG.9217 evm.TU.Herato1003.75	1.841	0.925	7.907	0.133	0.993	1.159	13.247	0.184	hydroxylysine kinase [Vanessa tameamea]	0.00E+00
MSTRG.875 evm.TU.Herato0101.675 evm.TU.Herato0101.677	0.516	5.310	7.848	0.134	0.328	5.393	14.497	0.175	cysteine protease ATG4B [Bicyclus anynana]	0.00E+00
MSTRG.7970 evm.TU.Herato0901.44	2.371	2.202	7.773	0.137	0.647	2.721	13.922	0.176	IDLSRF-like peptide [Bicyclus anynana]	2.00E-131
MSTRG.641 evm.TU.Herato0101.485	0.648	9.456	7.084	0.152	0.346	9.578	12.555	0.192	dopa decarboxylase [Heliconius melpomene malleti]	0.00E+00
MSTRG.20662 evm.TU.Herato2001.191	0.462	4.393	6.902	0.157	0.695	4.305	54.035	0.032	INO80 complex subunit B isoform X1 [Ostrinia furnacalis]	7.00E-168
MSTRG.18061 evm.TU.Herato1801.88	0.429	5.314	6.878	0.157	0.674	5.217	44.191	0.044	protein TANC2 isoform X2 [Vanessa tameamea]	0.00E+00
MSTRG.16897 evm.TU.Herato1701.114	0.557	8.223	6.714	0.161	0.650	8.200	21.925	0.111	flocculation protein FLO11 isoform X1 [Danaus plexippus plexippus]	0.00E+00
MSTRG.19877 evm.TU.Herato1908.46	1.716	4.514	6.406	0.172	0.821	4.810	17.792	0.155	uncharacterized protein LOC113404717 [Vanessa tameamea]	0.00E+00

gene	logFC .subsp ecies	logCPM .subspec ies	F.subsp ecies	FDR.su bspecies	logFC.wing _region	logCPM. wing_regi on	F.wing_ region	FDR.wi ng_regi on	Annotation	E-value
MSTRG.17497 evm.TU.Herato1705.21	2.474	6.833	6.075	0.182	0.643	7.310	40.304	0.050	uncharacterized protein LOC112045811 [Bicyclus anyana]	2.00E-51
MSTRG.20088 evm.TU.Herato1910.89 ev m.TU.Herato1910.91	-1.177	4.707	43.197	0.007	-0.457	4.258	15.312	0.165	transmembrane protein 136- like [Vanessa tameamea]	8.00E-128
MSTRG.21343 evm.TU.Herato2001.670_ evm.TU.Herato2001.671	-1.774	4.151	38.396	0.009	-1.032	3.623	25.269	0.098	glucose-1-phosphatase-like [Aphantopus hyperantus]	7.00E-153
MSTRG.14548 evm.TU.Herato1411.67	-1.259	3.280	31.228	0.014	-0.936	3.047	25.298	0.092	hepatocyte nuclear factor 4- gamma isoform X3 [Aphantopus hyperantus]	0.00E+00
MSTRG.5330 evm.TU.Herato0606.247	-2.400	4.490	28.716	0.017	-1.710	4.114	37.997	0.086	calcium-activated potassium channel slowpoke isoform X31 [Vanessa tameamea]	0.00E+00
MSTRG.10838 evm.TU.Herato1108.274 e vm.TU.Herato1108.275 evm.TU.Herato1 108.277	-0.788	6.332	25.518	0.019	-0.524	6.182	33.820	0.068	Multidrug resistance- associated protein 4 [Papilio machaon]	1.00E-35
MSTRG.5161 evm.TU.Herato0310.312 ev m.TU.Herato0310.313	-0.891	4.599	17.517	0.039	-0.437	4.327	16.858	0.151	no hits	na
MSTRG.12481 evm.TU.Herato1202.627	-2.595	0.616	13.765	0.059	-1.489	-0.295	13.382	0.182	condensin complex subunit 1 isoform X1 [Vanessa tameamea]	0.00E+00
MSTRG.13621 evm.TU.Herato1301.564	-0.513	6.695	12.199	0.072	-0.767	6.855	45.451	0.043	Krueppel homolog 2 [Vanessa tameamea]	2.00E-162

gene	logFC .subsp ecies	logCPM .subspec ies	F.subsp ecies	FDR.su bspecies	logFC.wing _region	logCPM. wing_regi on	F.wing_ region	FDR.wi ng_regi on	Annotation	E-value
MSTRG.1813 evm.TU.Herato0213.2	-1.752	5.625	12.050	0.075	-0.352	4.667	13.895	0.176	luciferase-like 8, partial [Heliconius erato]	0.00E+00
MSTRG.15493 evm.TU.Herato1507.212	-0.974	4.880	9.197	0.109	-0.374	4.510	13.676	0.179	hypothetical protein evm_013227 [Chilo suppressalis]	8.00E-70
MSTRG.4075 evm.TU.Herato0508.49	-0.811	5.537	8.785	0.115	-0.520	5.385	32.559	0.073	hypothetical protein RR46_04746 [Papilio xuthus]	0.00E+00
MSTRG.604 evm.TU.Herato0101.456	-0.714	5.993	8.591	0.119	-0.604	5.935	15.093	0.175	uncharacterized protein LOC112050048 [Bicyclus anyana]	0.00E+00
MSTRG.11531 evm.TU.Herato1202.83 ev m.TU.Herato1202.84	-0.796	3.092	6.519	0.167	-0.529	2.939	12.675	0.190	PREDICTED: histone H2B [Plutella xylostella]	6.00E-82
MSTRG.12897 evm.TU.Herato1301.53	-0.712	5.143	6.253	0.175	-0.553	5.059	18.032	0.143	protein espinas isoform X3 [Vanessa tameamea]	0.00E+00
MSTRG.14849 evm.TU.Herato1501.1	-2.660	4.687	6.024	0.184	-0.839	3.238	28.371	0.086	chaoptin-like [Danaus plexippus plexippus]	0.00E+00
MSTRG.6831 evm.TU.Herato0701.670	-2.363	1.531	5.793	0.192	-1.505	0.654	12.125	0.198	cysteine and histidine-rich protein 1-like [Vanessa tameamea]	0.00E+00
<i>Heliconius melpomene</i> 50%										
MSTRG.18872 HMEL003022g1	1.494	2.443	17.566	0.107	0.877	2.619	52.117	0.158	LOW QUALITY PROTEIN: xanthine dehydrogenase 1-like [Bicyclus anyana]	0
70%										

gene	logFC .subsp ecies	logCPM .subspec ies	F.subsp ecies	FDR.su bspecies	logFC.wing _region	logCPM. wing_regi on	F.wing_ region	FDR.wi ng_regi on	Annotation	E-value
MSTRG.14267 HMEL031592g1	1.747	2.525	46.347	0.057	0.819	2.749	18.494	0.195	uncharacterized protein LOC113397890 [Vanessa tameamea]	4.00E-87
MSTRG.8396 HMEL013392g1 HMEL03 7724g1	0.815	3.116	16.497	0.146	0.544	3.218	21.269	0.151	drebrin-like protein B [Vanessa tameamea]	1.00E-177
MSTRG.8785 HMEL002509g1	0.808	3.784	15.115	0.160	0.657	3.840	23.923	0.131	hemicentin-1-like isoform X1 [Vanessa tameamea]	0
MSTRG.2699 HMEL002124g1	1.398	6.822	14.991	0.161	0.718	7.016	21.448	0.173	probable fatty acid-binding protein [Danaus plexippus plexippus]	9.00E-66
MSTRG.4246 HMEL036361g1	1.578	2.876	14.618	0.166	1.219	2.937	27.330	0.120	cuticle protein 8-like [Bicyclus anynana]	2.00E-72
MSTRG.18497 HMEL012022g1	2.982	1.492	14.528	0.167	4.471	1.288	106.926	0.004	brachyurin-like [Aphantopus hyperantus]	1.00E-109
MSTRG.18976 HMEL008071g1 HMEL0 08071g2	1.182	1.740	14.134	0.170	1.494	1.656	35.183	0.054	tetra-peptide repeat homeobox protein 1-like [Vanessa tameamea]	4.00E-37
MSTRG.20941 HMEL034284g1	-4.999	2.881	21.651	0.113	-2.481	0.775	23.140	0.143	circadian clock-controlled protein-like [Vanessa tameamea]	5.00E-27

Table S11. Genes differentially expressed (FDR<0.05) between *H. erato cyrbia* and *H. erato demophoon* within the QTL intervals. In cases where there were several transcripts expressed for each gene, the position of the first transcript is given.

Phenotype	Stage	gene id	annotated gene	logFC	logCPM	FDR	scaffold id	start	stop	protein hit (FlyBase)	comment
Chr 20											
BR	50%	MSTRG.211 20		-1.365	3.047	0.034	Herato 2001	13665388	13667572	tho2	immediately before (392bp) tho2 (Herato2001: 13,667,964-13,668,985) , poor hit (E value > 1)
BR		MSTRG.210 53	evm.TU.Herato2001.480	-0.738	6.529	0.035	Herato 2001	12606947	12613794	Acyl-CoA binding protein 1	na
BR	70%	MSTRG.211 08	evm.TU.Herato2001.529	1.914	4.091	0.005	Herato 2001	13118144	13142065	Dmel\CG11318	na
BR		MSTRG.209 35		8.806	-0.216	0.006	Herato 2001	9817864	9818213	Dmel\CG10904	large distance from genomic feature, downstream of Dmel\CG10904 (Herato2001: 9,835,885-9,839,014)
BR		MSTRG.210 07		3.730	1.757	0.011	Herato 2001	11641700	11643873	no hit	exact match
BR		MSTRG.210 45	evm.TU.Herato2001.474	-8.527	-0.402	0.022	Herato 2001	12513101	12535184	Tetraspanin 26A	na
BR		MSTRG.209 71	evm.TU.Herato2001.420	2.234	6.824	0.027	Herato 2001	10786686	10804234	fringe	na
Chr Z											
BR, LUM, RS	50%	MSTRG.219 95		-9.396	0.264	0.003	Herato 2101	10209394	10209747	ATPase 8B	nearest gene 709 bp upstream
BR, LUM, RS		MSTRG.220 90	evm.TU.Herato2101.409	-9.324	0.173	0.004	Herato 2101	12435747	12453213	super sex combs	na
BR, LUM, RS		MSTRG.220 36		-1.129	4.704	0.006	Herato 2101	10864412	10867976	wacky	wacky (Herato2101: 10,868,052-10,881,937) ; Dynein heavy chain at 16F (Herato2101: 10,853,504-10,864,142)
BR, LUM, RS		MSTRG.219 47		-2.230	2.952	0.008	Herato 2101	9228419	9229979	dunce	downstream dunce Herato2101: 9,232,569-9,323,532)
BR, LUM, RS		MSTRG.219 22	evm.TU.Herato2101.296	1.846	2.644	0.010	Herato 2101	8312400	8313137	no hit	na

Phenotype	Stage	gene id	annotated gene	logFC	logCPM	FDR	scaffold	start	stop	protein hit (FlyBase)	comment
RS		MSTRG.21759	evm.TU.Herato2101.179	-1.896	3.495	0.011	Herato2101	5162891	5181891	Polypeptide N-acetylgalactosaminyltransferase 35A	na
BR, LUM, RS		MSTRG.21925		-2.405	1.881	0.010	Herato2101	8391373	8393792	Dmel\CG7888	exact match
BR, LUM, RS		MSTRG.21910		-1.088	3.331	0.013	Herato2101	8128295	8129254	moleskin	upstream of moleskin (Herato2101: 8,116,509-8,124,979)
BR, LUM, RS		MSTRG.22060		1.523	3.241	0.015	Herato2101	11644379	11647064	Dmel\CG18659	upstream of Herato2101: 11,595,296-11,638,782
BR, LUM		MSTRG.22097		-4.799	-1.420	0.015	Herato2101	12536727	12612327	Glutamate receptor IA	very large transcript, end overlaps with Glutamate receptor IA(Herato2101: 12,610,251-12,656,299)
BR, LUM, RS		MSTRG.21992		-2.784	0.752	0.016	Herato2101	10124805	10127463	IGF-II mRNA-binding protein	large distance from genomic feature, closest to IGF-II mRNA-binding protein (Herato2101: 10,133,734-10,191,778)
BR, LUM, RS		MSTRG.21899		-3.067	0.732	0.028	Herato2101	7873746	7874214	Dmel\CG42269	large distance from genomic feature, closest to Dmel\CG42269 (Herato2101: 7,882,762-7,884,480)
BR, LUM, RS		MSTRG.21877	evm.TU.Herato2101.263	-0.728	3.659	0.029	Herato2101	7365009	7386279	kon-tiki	na
BR, LUM, RS		MSTRG.22022		1.106	2.683	0.031	Herato2101	10495531	10524827	CG3739-PB	large transcript, includes CG3739-PB but E-value > 0.90
BR, LUM, RS		MSTRG.21959		2.954	-0.441	0.032	Herato2101	9404792	9405280	Dmel\CG13293	overlap with two genes, chose largest gene for blast (Dmel\CG13293 Herato2101: 9,339,580-9,409,387)

Phenotype	Stage	gene id	annotated gene	logFC	logCPM	FDR	scaffold	start	stop	protein hit (FlyBase)	comment
BR, LUM, RS		MSTRG.218 97		-2.592	-0.391	0.033	Herato 2101	7853355	7853655	Transient receptor potential cation channel A1	exact match
RS		MSTRG.217 43		-1.217	2.834	0.037	Herato 2101	4973958	4975233	Site-1 protease	291 bp downstream of Site-1 protease (Herato2101: 4,975,524-4,997,675)
BR, LUM, RS		MSTRG.220 35	evm.TU.Herato2101.375	3.459	0.192	0.043	Herato 2101	10815026	10848055	Dynein heavy chain at 16F	na
BR, LUM, RS		MSTRG.218 67	evm.TU.Herato2101.255	1.465	2.898	0.044	Herato 2101	7114906	7119901	Dmel\CG5541	na
LUM, RS		MSTRG.218 43		3.250	2.182	0.001	Herato 2101	6628831	6630351	Dmel\CG41520	exact match
LUM, RS		MSTRG.218 39		-1.741	3.493	0.006	Herato 2101	6605080	6607246	no hit	large distance from genomic feature, downstream of Herato2101: 6,614,966- 6,621,785
LUM, RS		MSTRG.217 93	evm.TU.Herato2101.200	-1.137	5.297	0.007	Herato 2101	5793288	5802200	Quiescin sulfhydryl oxidase 1	na
LUM, RS		MSTRG.218 32		-1.331	3.298	0.009	Herato 2101	6516431	6525230	Autophagy- related 9	downstream (1491bp) Autophagy-related 9 (Herato2101: 6,526,721- 6,538,967)
LUM, RS		MSTRG.218 03		-5.262	0.125	0.017	Herato 2101	5980907	5981143	biniou	large distance from genomic feature, downstream to biniou (Herato2101: 5,991,068- 6,012,882)
LUM, RS		MSTRG.218 51		-5.381	-0.146	0.022	Herato 2101	6795954	6797473	Phosphogluconate dehydrogenase	downstream (2666bp) Phosphogluconate dehydrogenase (Herato2101: 6,800,139-6,808,101)
LUM, RS		MSTRG.218 53	evm.TU.Herato2101.242	3.305	0.251	0.047	Herato 2101	6811074	6814359	CG42674	na

Phenotype	Stage	gene id	annotated gene	logFC	logCPM	FDR	scaffold	start	stop	protein hit (FlyBase)	comment
LUM, RS		MSTRG.21837		-1.041	3.300	0.047	Herato2101	6585420	6585932	Ubiquitin carboxy-terminal hydrolase L5	upstream 5515bp of Ubiquitin carboxy-terminal hydrolase L5 (Herato2101: 6,580,417-6,584,825)
BR, LUM, RS	70%	MSTRG.21863	evm.TU.Herato2101.252, evm.TU.Herato2101.253	-2.286	7.336	0.002	Herato2101	7007539	7033173	trio	na
BR, LUM, RS		MSTRG.21925		-2.255	1.924	0.003	Herato2101	8391373	8393792	Dmel\CG7888	exact match
BR, LUM, RS		MSTRG.21910		-1.260	3.781	0.006	Herato2101	8128295	8129254	moleskin	upstream of moleskin (Herato2101: 8,116,509-8,124,979)
BR, LUM, RS		MSTRG.21995		-8.767	-0.195	0.008	Herato2101	10209394	10209747	ATPase 8B	nearest gene 709 bp upstream
BR, LUM, RS		MSTRG.21985		-1.279	3.797	0.012	Herato2101	9964577	9969000	Rho GTPase activating protein at 68F	immediately before (<200bp) Rho GTPase activating protein at 68F (Herato2101: 9,969,182-9,976,893)
BR, LUM, RS		MSTRG.22036		-0.817	4.101	0.016	Herato2101	10864412	10867976	wacky	wacky (Herato2101: 10,868,052-10,881,937) ; Dynein heavy chain at 16F (Herato2101: 10,853,504-10,864,142)
BR, LUM, RS		MSTRG.21947		-1.615	2.054	0.020	Herato2101	9228419	9229979	dunce	slightly downstream of dunce Herato2101: 9,232,569-9,323,532)
RS		MSTRG.21742	evm.TU.Herato2101.164	-2.354	-0.332	0.021	Herato2101	4946459	4952457	Dmel\CG31717	poor hit , E value > 1
BR, LUM, RS		MSTRG.22001		3.915	-0.094	0.023	Herato2101	10356441	10357252	procollagen lysyl hydroxylase	in between two genes, downstream from procollagen lysyl hydroxylase (Herato2101: 10,359,604-10,392,288)
BR, LUM, RS		MSTRG.22022		1.028	4.202	0.023	Herato2101	10495531	10524827	CG3739-PB	large transcript, includes CG3739-PB but E-value > 0.90

Phenotype	Stage	gene id	annotated gene	logFC	logCPM	FDR	scaffold	start	stop	protein hit (FlyBase)	comment
BR, LUM, RS		MSTRG.21907	evm.TU.Herato2101.284	1.540	0.950	0.039	Herato2101	8100167	8115041	Dmel\CG42271	na
BR, LUM, RS		MSTRG.21899		-3.326	0.461	0.041	Herato2101	7873746	7874214	Dmel\CG42269	large distance from genomic feature, closest to Dmel\CG42269 (Herato2101: 7,882,762-7,884,480)
BR, LUM, RS		MSTRG.22076	evm.TU.Herato2101.401	-4.220	-1.176	0.044	Herato2101	12146767	12154685	Dmel\CG32260	na
BR, LUM, RS		MSTRG.21964	evm.TU.Herato2101.324	-0.710	4.443	0.049	Herato2101	9445555	9471870	Dmel\CG1265	na
BR, LUM, RS		MSTRG.22060		2.058	3.282	0.049	Herato2101	11644379	11647064	Dmel\CG18659	quite a bit upstream of Herato2101: 11,595,296-11,638,782
LUM, RS		MSTRG.21793	evm.TU.Herato2101.200	-1.392	6.267	0.001	Herato2101	5793288	5802200	Quiescin sulfhydryl oxidase 1	na
LUM, RS		MSTRG.21786		-1.957	1.858	0.003	Herato2101	5711007	5714276	Kip1 ubiquitination-promoting complex subunit 1	large distance from any genomic feature, upstream of Kip1 ubiquitination-promoting complex subunit 1 (Herato2101: 5,693,521-5,707,165)
LUM, RS		MSTRG.21787	evm.TU.Herato2101.196	-6.262	-0.219	0.008	Herato2101	5718097	5742135	miles to go	poor hit , E value > 1
LUM, RS		MSTRG.21822		-2.732	1.040	0.011	Herato2101	6356559	6359488	Dmel\CG12531	exact match
LUM, RS		MSTRG.21843		3.750	3.131	0.013	Herato2101	6628831	6630351	Dmel\CG41520	exact match
LUM, RS		MSTRG.21851		-5.617	0.274	0.017	Herato2101	6795954	6797473	Phosphogluconate dehydrogenase	downstream (2666bp) Phosphogluconate dehydrogenase (Herato2101: 6,800,139-6,808,101)
LUM, RS		MSTRG.21774		-1.734	2.303	0.019	Herato2101	5508065	5508627	period	immediately downstream (72bp) of period (Herato2101: 5,508,699-5,543,290)

Phenotype	Stage	gene id	annotated gene	logFC	logCPM	FDR	scaffold	start	stop	protein hit (FlyBase)	comment
LUM, RS		MSTRG.21832		-1.935	5.821	0.022	Herato2101	6516431	6525230	Autophagy-related 9	downstream (1491bp) Autophagy-related 9 (Herato2101: 6,526,721-6,538,967)
LUM, RS		MSTRG.21803		-2.551	-0.259	0.031	Herato2101	5980907	5981143	biniou	large distance from genomic feature, downstream to biniou (Herato2101: 5,991,068-6,012,882)
RS		MSTRG.21751	evm.TU.Herato2101.170	-1.258	1.600	0.039	Herato2101	5033858	5036106	cricketlet	na

Table S12. Genes differentially expressed (FDR<0.2) between *H. melpomene cythera* and *H. melpomene rosina* within the QTL intervals. In cases where there were several transcripts expressed for each gene, the position of the first transcript is given.

Phenotype	Stage	gene id	annotated gene	logFC	logCPM	FDR	scaffold	start	stop	protein hit (FlyBase)	novel transcript comment
Chr 3											
BR	50%	MSTRG.3173		11.518	6.073	0.047	Hmel203003o	380684	383247	SIFamide receptor	downstream 653bp of SIFamide receptor (Hmel203003o: 383,900-384,613)
BR, LUM		MSTRG.3408	HMEL007690g2,HMEL013806g1	-1.825	2.127	0.131	Hmel203003o	3012068	3023317	Heterochromatin Protein 1c	na
BR, LUM		MSTRG.3403	HMEL036038g1	1.600	1.836	0.192	Hmel203003o	2924821	3004843	miniature	na
BR	70%	MSTRG.3297	HMEL016174g1	1.168	3.895	0.060	Hmel203003o	1674761	1679707	Dmel\CG5377	na
BR		MSTRG.3173		11.052	4.856	0.061	Hmel203003o	380684	383247	SIFamide receptor	downstream 653bp of SIFamide receptor (Hmel203003o: 383,900-384,613)
BR		MSTRG.3196	HMEL015572g1	1.721	2.951	0.079	Hmel203003o	599479	612509	Saccheropin dehydrogenase 1	na
BR		MSTRG.3531	HMEL036114g1	-1.491	1.009	0.113	Hmel203003o	4947102	4949039	pitchoune	na
BR, LUM		MSTRG.3421		6.803	-1.539	0.128	Hmel203003o	3355012	3355456	Sol1	in region of no genomic features, equal distance between genes, upstreamstream 8822 bp of Hmel203003o: 3,332,639-3,346,190
BR		MSTRG.3214	HMEL008058g1	1.352	2.344	0.130	Hmel203003o	709863	710876	Dmel\Daao1	na
BR		MSTRG.3151	HMEL021694g1,HMEL021694g2	1.348	3.405	0.134	Hmel203003o	159359	167643	Dmel\CG9701	na
BR		MSTRG.3485		6.643	-1.663	0.186	Hmel203003o	4365102	4365486	Dmel\CG30413	immediately downstream 436 bp of Dmel\CG30413 (Hmel203003o: 4,365,922-4,366,814)
BR		MSTRG.3484		7.491	-0.957	0.190	Hmel203003o	4363434	4364216	Dmel\CG30413	downstream 2488 bp of Dmel\CG30413 (Hmel203003o:

Phenotype	Stage	gene id	annotated gene	logFC	logCPM	FDR	scaffold	start	stop	protein hit (FlyBase)	novel transcript comment
											4,365,922-4,366,814), before MSTRG.3485
BR		MSTRG.3159	HMEL036008g1	1.256	1.020	0.191	Hmel203003o	269089	271724	Ubiquitin conjugating enzyme 84D	poor hit, E value 2.56
Chr 7											
RS	50%	MSTRG.8012	HMEL013683g1	0.642	3.345	0.162	Hmel207001o	8627421	8630143	Gemin 3	na
RS		MSTRG.8188	HMEL037634g1	-0.737	1.789	0.162	Hmel207001o	9711504	9713128	RNA polymerase III subunit G	na
RS		MSTRG.8324	HMEL012321g1	0.694	5.347	0.186	Hmel207001o	11485564	11535901	ADP ribosylation factor-like 4	na
RS		MSTRG.8164	HMEL013901g1	0.656	6.590	0.194	Hmel207001o	9458675	9505412	Phosphoinositide-dependent kinase 1	na
RS	70%	MSTRG.8186	HMEL002406g2,HMEL037635g1	1.084	3.409	0.066	Hmel207001o	9708171	9719190	Dmel\CG32681	poor hit E Value = 9.44
RS		MSTRG.8049	HMEL007780g1	-1.426	1.081	0.144	Hmel207001o	8824630	8833804	ringmaker	na
RS		MSTRG.8321		-4.665	-0.081	0.192	Hmel207001o	11474783	11476066	inaF-D	poor hit , E value 9.86, in region of no genomic features, downstream 9293 bp of Hmel207001o: 11,485,359-11,485,712
RS		MSTRG.8258	HMEL037660g1	0.480	3.766	0.196	Hmel207001o	10575157	10595319	Dmel\CG8243	na

Table S13. Genes differentially expressed (FDR<0.05) between *H. melpomene cythera* wing regions within the QTL intervals. In cases where there were several transcripts expressed for each gene, the position of the first transcript is given.

Phenotype	Stage	gene id	annotated gene	logFC	logCPM	FDR	scaffold	start	stop	Protein hit (Flybase)	NCBI blastp hit
Chr 3											
BR	70%	MSTRG.3151	HMEL021694g1,HMEL021694g2	-0.793	4.336	0.025	Hmel203003o	159359	167643	Dmel\CG9701	PREDICTED: lactase-phlorizin hydrolase-like [Papilio machaon]
BR		MSTRG.3338	HMEL021575g1	-0.530	6.252	0.091	Hmel203003o	1912342	1917684	tracheal-prostasin	trypsin-1-like [Vanessa tameamea]
Chr 7											
RS	50%	MSTRG.8196	HMEL015765g1	-1.024	5.557	0.024	Hmel207001o	9752688	9775897	Leucine-rich repeat	F-actin-uncapping protein LRRC16A isoform X2 [Pararge aegeria]
RS	70%	MSTRG.8135	HMEL021853g1	0.702	6.947	0.020	Hmel207001o	9318579	9319970	Dmel\CG18294 (poor hit)	cuticle protein 18.6-like [Bicyclus anynana]
RS		MSTRG.8147	HMEL003671g1	0.438	8.687	0.174	Hmel207001o	9391192	9391719	Dmel\CG13063 (poor hit)	cuticular protein hypothetical 9 precursor [Bombyx mori]

Table S14. Expected numbers of differentially expressed genes in the QTL intervals, based on their relative size, assuming random distribution of DE genes.

<i>H. erato</i>			Expected numbers of DE genes in QTL based on numbers of DE genes in each comparison			
QTL	QTL size (bp)	Size as proportion of genome	Subsp. comparison 50% development (907 DE genes)	Subsp. comparison 70% development (1043 DE genes)	Wing region comparison 50% (1 DE gene)	Wing region comparison 70% (70 DE genes)
BR Z	5669050	0.0148	13.43	15.44	0.01	1.04
BR 20	4005369	0.0105	9.49	10.91	0.01	0.73
lum Z	7278729	0.0190	17.24	19.83	0.02	1.33
RS Z	7618121	0.0199	18.05	20.75	0.02	1.39
overlap (BR/lum/RS) Z	2726386	0.0071	6.46	7.43	0.01	0.50
<i>H. melpomene</i>						
QTL	QTL size (bp)	Size as proportion of genome	Subsp. comparison 50% development (203 DE genes)	Subsp. comparison 70% development (29 DE genes)	Wing region comparison 50% (6 DE genes)	Wing region comparison 70% (50 DE genes)
BR 3	4831878	0.0176	15.92	18.31	0.02	1.23
lum 3	1811304	0.0066	5.97	6.86	0.01	0.46
rs 7	3466364	0.0126	11.42	13.14	0.01	0.88
overlap (BR/lum) 3	1811304	0.0066	5.97	6.86	0.01	0.46

Table S15. Overlapping genes (FDR < 0.2) between the iridescent subspecies comparison and *Drosophila* bristle development genes. Bold indicates significant genes with an FDR < 0.05.

Species	%development	identity	logFC	logCP	F	PValu	FDR	%iden	expect	gene_name
				M		e		t		e
Erato	50	evm.model.Herato1701.	0.7697	5.9722	15.684	0.0033	0.0479	41.200	1.1E-	NAT1-PB
		7			0			0	51	
	50	evm.model.Herato1708.3	0.5704	5.4388	7.8525	0.0207	0.1475	76.733	7.9E-	msi-PE
		7						0	110	
	50	evm.model.Herato1108.1	-	4.1361	11.300	0.0084	0.0857	27.959	2.9E-60	dally-PB
		13	0.7384		4			0		
	70	evm.model.Herato1701.	0.8041	4.9092	24.670	0.0009	0.0207	41.200	1.1E-	NAT1-PB
		7			0			0	51	
	70	evm.model.Herato0301.3	0.4831	5.4301	10.992	0.0096	0.0836	90.187	9.9E-	Rab11-PA
		2			6			0	145	
	70	evm.model.Herato1901.6	0.4097	6.4317	9.2075	0.0149	0.1086	91.643	0.0E+0	CtBP-PA
		2						0	0	
	70	evm.model.Herato1701.3	0.9862	4.8878	6.3500	0.0342	0.1728	67.602	0.0E+0	Ten-m-
		6						0	0	PD
	70	evm.model.Herato0101.3	0.7313	6.2924	5.7291	0.0415	0.1928	83.164	0.0E+0	ck-PA
		28						0	0	

Species	%development	identity	logFC	logCP M	F	PValu e	FDR	%iden t	expect	gene_nam e
	70	evm.model.Herato1108.1 61	- 0.6666	4.6337	14.776 6	0.0043	0.0517	49.254 0	3.0E-02	kto-PB
	70	evm.model.Herato0606.9 6	- 0.8081	4.4184	14.392 1	0.0046	0.0539	27.164 0	5.9E-28	spn-F-PA
	70	evm.model.Herato1005.5 6	- 0.5378	6.3889	11.971 5	0.0077	0.0741	58.664 0	0.0E+0 0	capt-PB
	70	evm.model.Herato1108.2 27	- 0.4131	5.9887	10.145 1	0.0117	0.0946	88.828 0	0.0E+0 0	ebi-PA
	70	evm.model.Herato2101.5 30	- 1.0017	8.1077	9.1800	0.0150	0.1088	76.166 0	2.4E- 106	Fkbp14- PE
Melpomen e	50	HMEL032216g1	- 0.9901	4.6835	15.402 8	0.0042	0.1281	67.990 0	0.0E+0 0	Stim-PD

Table S16. Overlapping genes (FDR < 0.2) between the wing region comparison and *Drosophila* bristle development genes. Bold indicates significant genes with an FDR < 0.05.

Species	%development	identity	logFC	logCPM	F	PValue	FDR	ident	expect	gene_name
Erato	70	evm.model.Herato0901.100	0.3310	8.4258	12.6861	0.0079	0.1904	52.5500	0.0E+00	DI-PA
	70	evm.model.Herato1108.424	-1.1527	2.8997	34.4172	0.0004	0.0669	69.4810	4.3E-59	B-H1-PA
	70	evm.model.Herato1807.66	-0.5386	5.4652	27.5341	0.0009	0.0879	65.6830	1.9E-111	rn-PC
	70	evm.model.Herato1705.75	-0.4049	5.5380	16.7513	0.0038	0.1513	74.1940	7.1E-167	Chi-PB
	70	evm.model.Herato1202.113	-0.6288	4.8212	14.3005	0.0064	0.1765	38.0680	3.3E-48	Sox15-PA
	70	evm.model.Herato0701.643	-0.4031	4.8176	13.4441	0.0069	0.1819	69.6630	8.4E-40	emc-PA
	70	evm.model.Herato1701.148	-1.1865	2.0806	13.5425	0.0070	0.1828	38.6500	6.2E-21	ac-PA

Table S17. Overlapping genes (FDR < 0.05 *H. erato*; FDR <0.2 *H. melpomene*) between the iridescent subspecies comparison and *Drosophila* cuticle development genes.

Species	%development	identity	logFC	logCPM	F	PValue	FDR	%ident	expect	gene_name
Erato	50	evm.model.Herato0101.493	0.9456	9.2496	21.1055	0.0013	0.0265	69.6280	0.0E+00	kkv-PD
	50	evm.model.Herato1301.141	2.3628	7.2450	15.8116	0.0033	0.0474	57.4710	9.0E-28	Cpr76Ba-PA
	50	evm.model.Herato1901.66	-2.3211	-0.0821	17.8512	0.0022	0.0373	48.1310	0.0E+00	e-PA
	70	evm.model.Herato1703.5	0.6910	4.7221	22.8039	0.0011	0.0234	37.2200	7.6E-147	drd-PA
	70	evm.model.Herato2001.420	2.2343	6.8235	21.5191	0.0014	0.0269	61.1890	1.6E-128	fng-PA
	70	evm.model.Herato1505.48	0.6159	7.4112	16.6562	0.0030	0.0425	71.9210	0.0E+00	Cht7-PA
	70	evm.model.Herato2001.242	-1.1760	6.8885	23.7778	0.0010	0.0220	66.6670	0.0E+00	Cpr-PC
70	evm.model.Herato1301.179	-2.9633	4.5552	21.2006	0.0015	0.0282	29.5650	1.7E-06	Cpr51A-PA	
Melpomene	50	HMEL035109g1	0.6496	5.9249	34.7007	0.0003	0.0307	66.8140	0.0E+00	Cpr-PC
	50	HMEL036038g1	1.6000	1.8358	11.6765	0.0087	0.1920	87.9430	0.0E+00	m-PA
	50	HMEL009822g1	-1.5221	5.0155	11.7471	0.0087	0.1920	72.1520	0.0E+00	ple-PA
	70	HMEL035109g1	0.6279	6.1607	16.3640	0.0042	0.1467	66.8140	0.0E+00	Cpr-PC
	70	HMEL021905g1	-0.7881	7.3089	20.2128	0.0023	0.1135	94.5380	0.0E+00	Sec61alpha-PA

Table S18. Overlapping genes (FDR < 0.05 *H. erato*; FDR <0.2 *H. melpomene*) between the wing region comparison and *Drosophila* cuticle development genes.

Species	%development	identity	logFC	logCPM	F	PValue	FDR	%ident	expect	gene_name
Erato	70	evm.model.Herato2101.139	1.8687	4.7540	154.0256	0.0000	0.0046	51.9230	3.8E-19	Twd1G-PB
	70	evm.model.Herato0101.707	1.1287	4.5570	43.1617	0.0003	0.0486	36.3640	5.7E-08	Cpr62Ba-PC
	70	evm.model.Herato1807.12	-2.3276	2.4375	62.2058	0.0001	0.0275	55.1910	1.5E-107	ci-PA
Melpomene	70	HMEL031931g1	2.8428	1.8369	143.4593	0.0000	0.0015	38.0950	2.1E-15	Lcp3-PB
	70	HMEL036362g1	1.7435	3.3193	107.1630	0.0000	0.0037	59.8040	8.1E-32	Cpr30F-PA
	70	HMEL014632g1	0.8886	9.4323	66.9731	0.0000	0.0123	59.4830	0.0E+00	Cht5-PA
	70	HMEL032535g1	1.0188	6.2640	45.5957	0.0001	0.0382	31.7460	3.2E-09	Cpr62Ba-PC
	70	HMEL005738g1	-1.1391	7.6303	41.1502	0.0003	0.0625	54.0150	8.2E-40	CG34461-PB
	70	HMEL008086g1	-0.4683	9.0117	22.2491	0.0011	0.1422	81.1760	4.0E-41	Cpr66D-PA
	70	HMEL008807g1	-0.5657	5.2641	19.9439	0.0016	0.1677	44.6150	2.7E-107	t-PB

Table S19: Concordantly expressed genes between *H. erato* and *H. melpomene* with an FDR < 0.2. Bold indicates genes which are significantly DE expressed (FDR < 0.05) in both species.

erato.gene	logFC.erato	logCPM.erato	FDR.erato	mel.gene	identity(%)	expect	logFC.mel	logCPM	FDR.mel	NCBI Blastp Annotation	E-value
Subspecies comparison											
50%											
evm.model.Herato0606.92	2.312	1.730	0.061	HMEL016763g1	95.639	0	1.099	3.282	0.066	putative carbonic anhydrase 3 [Aphantopus hyperantus]	0
evm.model.Herato2001.729	0.783	4.304	0.087	HMEL004468g1	96.468	0	0.830	4.670	0.111	glucose-6-phosphate exchanger SLC37A2 isoform X1 [Vanessa tameamea]	0
evm.model.Herato1805.232	0.650	5.655	0.119	HMEL006054g1	96.678	0	0.634	5.469	0.081	solute carrier family 12 member 9 isoform X2 [Aphantopus hyperantus]	0
evm.model.Herato2001.75	0.618	5.295	0.125	HMEL017055g1	97.297	7.08E-134	1.083	4.782	0.037	peroxisomal membrane protein 2 [Bicyclus anynana]	3.00E-122
evm.model.Herato1901.116_ evm.model.Herato1901.120	1.085	3.358	0.147	HMEL010934	94.375	0	1.617	3.283	0.037	cytochrome P450 4C1-like [Danaus plexippus plexippus]	9.00E-157
evm.model.Herato0503.162	1.450	2.221	0.150	HMEL008925g1	93.986	0	2.697	0.757	0.097	pickpocket protein 28 [Vanessa tameamea]	0
evm.model.Herato0701.776	-7.725	1.805	0.003	HMEL037763g1	86.275	2.12E-08	-1.282	1.421	0.075	reticulon-4-interacting protein 1, mitochondrial [Bombyx mori]	1.00E-32
evm.model.Herato1805.48	-0.884	3.619	0.011	HMEL003070g1	97.035	0	-0.544	3.552	0.162	threonine aspartase 1 [Vanessa tameamea]	0
evm.model.Herato0801.233	-1.429	2.805	0.017	HMEL038031g1	92.492	0	-1.067	2.867	0.072	mitochondrial amidoxime-reducing component 1 isoform X2 [Manduca sexta]	0
evm.model.Herato1004.1	-0.977	3.717	0.026	HMEL030760g1	95.021	1.26E-174	-2.058	2.919	0.037	Gamma-glutamyl cyclotransferase-like venom protein isoform 1, partial	4.00E-108

erato.gene	logFC.erato	logCPM.erato	FDR.erato	mel.gene	identity(%)	expect	logFC.mel	logCPM	FDR.mel	NCBI Blastp Annotation [Operophtera brumata]	E-value
evm.model.Herato0701.772	-1.454	2.037	0.029	HMEL005305g3	94.811	0	-1.613	1.856	0.035	Fatty acid synthase [Danaus plexippus plexippus]	0
evm.model.Herato1901.44	-2.216	3.225	0.058	HMEL034227g1	62.048	0	-2.664	1.676	0.129	PREDICTED: uncharacterized protein LOC106710892 [Papilio machaon]	0
evm.model.Herato1301.53	-0.928	5.189	0.084	HMEL031781g1	99.315	0	-0.601	4.465	0.172	protein espinas isoform X3 [Vanessa tameamea]	0
evm.model.Herato1005.109	-0.646	3.735	0.142	HMEL013306g1	83.571	1.07E-76	-0.735	3.875	0.135	PREDICTED: E3 ubiquitin-protein ligase RNF4-like [Papilio polytes]	2.00E-39
evm.model.Herato1005.218	-0.791	4.931	0.145	HMEL030866g1	96.407	0	-1.158	2.614	0.120	myrosinase 1-like [Vanessa tameamea]	0
evm.model.Herato1301.541	-0.719	3.126	0.164	HMEL009927g1	68.487	0	-1.047	3.384	0.041	putative pre-mRNA- splicing factor ATP- dependent RNA helicase DHX16 [Vanessa tameamea]	1.00E-64
evm.model.Herato0606.27	-0.746	2.997	0.192	HMEL008899g1	95.299	4.87E-168	-2.198	3.004	0.040	leucine-rich melanocyte differentiation- associated protein-like [Vanessa tameamea]	5.00E-136
50%											
evm.model.Herato0701.610	1.238	1.873	0.153	HMEL037635g1	92.13	0	1.084	3.409	0.066	sperm-associated antigen 6-like [Ostrinia furnacalis]	0
evm.model.Herato1004.1	-1.675	4.087	0.004	HMEL030760g1	95.021	0	-1.333	2.991	0.060	Gamma-glutamyl cyclotransferase-like venom protein isoform 1, partial [Operophtera brumata]	0
evm.model.Herato0701.716	-1.399	2.279	0.019	HMEL037725g1	65.987	0	-1.276	2.659	0.172	protein ZDS1-like [Vanessa tameamea]	0

erato.gene	logFC.erato	logCPM.erato	FDR.erato	mel.gene	identity(%)	expect	logFC.mel	logCPM	FDR.mel	NCBI Blastp Annotation	E-value
evm.model.Herato0204.6	-2.914	1.107	0.019	HMEL022589g1	97.268	0	-3.063	1.582	0.060	TWiK family of potassium channels protein 12 [Aphantopus hyperantus]	0
evm.model.Herato0419.55	-2.078	5.269	0.022	HMEL013922g1	70.292	0	-0.523	3.641	0.189	ATP-dependent Clp protease ATP-binding subunit clpX-like, mitochondrial isoform X1 [Vanessa tameamea]	0
evm.model.Herato0214.16	-4.442	4.578	0.026	HMEL014358g1	81.265	0	-0.615	6.778	0.113	E3 ubiquitin-protein ligase SIAH1-like isoform X3 [Bicyclus anynana]	0
evm.model.Herato1108.426	-0.713	7.556	0.078	HMEL009792g1	98.282	0	-0.575	7.463	0.117	dynamamin isoform X10 [Aphantopus hyperantus]	0
evm.model.Herato0801.322	-0.954	4.645	0.091	HMEL010036g1	98.131	0	-0.770	2.715	0.152	28S ribosomal protein S5, mitochondrial [Aphantopus hyperantus]	0
evm.model.Herato2101.87	-0.434	6.700	0.133	HMEL013502g1	98.688	0	-1.433	6.768	0.090	zinc-type alcohol dehydrogenase-like protein C1773.06c [Manduca sexta]	0
evm.model.Herato0205.2	-3.573	2.130	0.147	HMEL033207g1	80.782	0	-2.253	2.086	0.082	uncharacterized protein LOC112049287 [Bicyclus anynana]	0
evm.model.Herato1805.220	-1.434	3.752	0.149	HMEL003246g1	95.722	0	-1.578	1.672	0.198	organic cation transporter protein-like [Vanessa tameamea]	0
evm.model.Herato0211.81	-0.585	3.613	0.154	HMEL015454g1	95.873	0	-0.766	2.478	0.170	transcription initiation protein SPT3 homolog [Vanessa tameamea]	0
evm.model.Herato1005.61	-1.642	0.595	0.167	HMEL005932	95.519	0	-2.696	2.571	0.063	cytochrome P450 4C1-like [Aphantopus hyperantus]	0
Wing region comparison											
50%											

erato.gene	logFC.erato	logCPM.erato	FDR.erato	mel.gene	identity(%)	expect	logFC.mel	logCPM	FDR.mel	NCBI Blastp Annotation	E-value
evm.model.Herato1001.152	3.334	0.505	0.149	HMEL002901	99.296	0	2.338	1.044	0.041	paired box protein [Vanessa tameamea]	0
evm.model.Herato0801.87	-1.839	3.853	0.080	HMEL037907g1	100	0	-1.807	3.979	0.044	protein doublesex-like isoform X1 [Vanessa tameamea]	0
70%											
evm.model.Herato0701.190	1.949	11.511	0.032	HMEL007136g1	93.377	0	1.404	9.371	0.163	cuticle protein 1-like [Danaus plexippus plexippus]	0
evm.model.Herato0701.220	1.906	2.423	0.034	HMEL009343g2	98.638	0	1.702	2.967	0.023	homeobox protein invected-like isoform X1 [Vanessa tameamea]	0
evm.model.Herato2101.383	1.192	2.494	0.060	HMEL008471g6	99.407	0	1.575	2.236	0.032	homeobox protein araucan-like isoform X2 [Vanessa tameamea]	0
evm.model.Herato1003.176	0.573	7.077	0.074	HMEL030728g1	99.643	0	0.925	7.318	0.003	protein limb expression 1 homolog isoform X1 [Vanessa tameamea]	0
evm.model.Herato0208.10	1.296	1.458	0.075	HMEL017792g5	94.187	0	0.616	3.141	0.168	uncharacterized protein LOC117985176 [Aphantopus hyperantus]	0
evm.model.Herato0901.76	1.364	2.272	0.082	HMEL008230g1	99.552	0	1.159	1.348	0.163	uncharacterized protein LOC113401684 isoform X1 [Vanessa tameamea]	0
evm.model.Herato1704.13	0.569	5.158	0.083	HMEL017687g1	80.077	0	0.583	5.852	0.053	nepriylsin-4-like [Aphantopus hyperantus]	0
evm.model.Herato0211.105	0.442	6.843	0.088	HMEL002124g1	93.617	0	0.718	7.016	0.173	probable fatty acid-binding protein [Danaus plexippus plexippus]	0
evm.model.Herato0701.563	0.718	7.387	0.093	HMEL021853g1	98.413	0	0.702	6.947	0.020	cuticle protein 18.6-like [Bicyclus anynana]	0
evm.model.Herato1301.179	0.984	2.057	0.097	HMEL007991g4	99.471	0	0.865	3.134	0.166	cuticle protein 7-like [Vanessa tameamea]	0

erato.gene	logFC.erato	logCPM.erato	FDR.erato	mel.gene	identity(%)	expect	logFC.mel	logCPM	FDR.mel	NCBI Blastp Annotation	E-value
evm.model.Herato1301.115	0.846	2.279	0.108	HMEL015354g1	99.568	0	0.838	1.964	0.186	GATA-binding factor C-like isoform X2 [Vanessa tameamea]	0
evm.model.Herato0101.722	0.425	6.064	0.128	HMEL011421g3	92.096	0	1.539	3.113	0.007	tubulin glycyclase 3A-like isoform X1 [Vanessa tameamea]	0
evm.model.Herato0901.205	0.462	9.382	0.131	HMEL014632g1	95.028	0	0.889	9.432	0.012	endochitinase [Vanessa tameamea]	0
evm.model.Herato1001.42	0.536	9.577	0.132	HMEL017377g1	96.727	0	0.431	8.496	0.139	chymotrypsin-1-like [Vanessa tameamea]	0
evm.model.Herato1301.86	-1.127	3.618	0.020	HMEL031805g1	98.2	0	-0.467	5.026	0.121	facilitated trehalose transporter Tret1-like isoform X1 [Vanessa tameamea]	0
evm.model.Herato1411.170	-0.738	8.444	0.027	HMEL005529g1	98.582	0	-0.762	9.122	0.005	hemocyte protein-glutamine gamma-glutamyltransferase-like [Vanessa tameamea]	0
evm.model.Herato1007.62	-1.216	7.046	0.027	HMEL015975g1	93.103	0	-0.795	3.002	0.047	uncharacterized protein LOC117993154 [Aphantopus hyperantus]	0
evm.model.Herato0101.17	-0.740	9.229	0.037	HMEL022617g1	94.937	0	-0.444	9.207	0.112	GATA zinc finger domain-containing protein 14-like [Aphantopus hyperantus]	0
evm.model.Herato0801.87	-0.884	3.032	0.049	HMEL037907g1	100	0	-1.676	4.105	0.006	protein doublesex-like isoform X1 [Vanessa tameamea]	0
evm.model.Herato0601.10	-0.536	7.260	0.084	HMEL012144g1	99.099	0	-0.428	6.486	0.151	zinc finger protein Noc [Vanessa tameamea]	0
evm.model.Herato2101.123	-0.633	5.067	0.144	HMEL008807g1	84.559	0	-0.566	5.264	0.168	tan [Heliconius melpomene malleti]	0

erato.gene	logFC.erato	logCPM.erato	FDR.erato	mel.gene	identity(%)	expect	logFC.mel	logCPM	FDR.mel	NCBI Blastp Annotation	E- value
evm.model.Herato1301.434	-0.434	8.426	0.151	HMEL008086g1	98.131	0	-0.468	9.012	0.142	cuticle protein 19.8 isoform X1 [Vanessa tameamea]	0

Chapter 5

Impact of dietary stress on the development of structural colour in the butterfly *Heliconius sara*

Victoria J. Lloyd^{1*}, Molly Vokes^{2*}, Stephanie L. Burg³, Nicola J. Nadeau^{1*} and Andrew J. Parnell^{2*}

¹*Ecology and Evolutionary Biology, School of Biosciences, University of Sheffield, Alfred Denny Building, Western bank, Sheffield S10 2TN, UK*

²*Department of Physics and Astronomy, University of Sheffield, Hicks Building, Hounsfield Road, Sheffield S3 7RH, UK*

[†]*These authors contributed equally to this work*

* Corresponding authors

Email: n.nadeau@sheffield.ac.uk;

a.j.parnell@sheffield.ac.uk

Author contributions

This chapter is written in manuscript format for future submission. Myself, Nicola Nadeau and Andrew Parnell designed the research project. The dietary stress experiment was performed by myself. Elemental analysis of the leaves was performed by Molly Vokes and Andrew Parnell. Collection of the digital images and reflectance spectrometry measurements of the iridescent blue wing region was performed by Molly Vokes. I collected the reflectance spectrometry measurements of the yellow wing bar. I analysed all the developmental and spectrometry data. I collected and analysed the scanning electron microscopy data. Atomic Force Microscopy in

Figure 5 was performed by Andrew Parnell and Molly Vokes. Transmission Electron Microscopy was performed at the Electron Microscopy Facility, University of Sheffield by Chris Hill with assistance from Frane Babarović. I performed the optical modelling with the tmm simulation Python script written by Stephanie Burg. All authors contributed to data interpretation. I wrote the manuscript with feedback from Nicola Nadeau, Melanie Brien and Andrew Parnell.

Abstract

Striking displays of colour in butterfly wings originate from tiny wing scales which can selectively absorb light using pigments or reflect light using sophisticated photonic nanostructures. *Heliconius* butterflies harness the flexibility of these colour producing mechanisms to generate conspicuous displays of colour. These serve as warning signals and also intraspecific mating cues. In many taxa, including butterflies, brightly coloured traits are often condition dependent and serve as honest indicators of individual quality. However, the condition dependence of *Heliconius* colouration remains poorly studied. In particular, the iridescent, structural colour produced from the multilayer reflectors may be especially sensitive to individual condition, owing to the precision of optical nanostructure formation. While *Heliconius* nanostructures have been previously characterised, their response to environmental stressors is unknown. Here, we subject larval stages of *Heliconius sara* to dietary stress using a diet of nutrient-poor, old leaves. We use reflectance spectrometry to measure the effect of dietary stress on the blue iridescent and yellow pigmentary colour. Our results indicate a condition dependent and sexual dimorphic effect of dietary stress on the iridescent blue colour, with a decrease in brightness and hue. Electron microscopy indicates that dietary stress causes a disruption in multilayer reflector layering. Together with simulated models of *Heliconius* ridge multilayers we characterised the optical response of *Heliconius sara* to these architectural deviations resulting from dietary stress.

Keywords

Structural colour, condition dependence, iridescence, *Heliconius*, optical modelling

Introduction

The natural world is a rich tapestry of colours and complex patterns. Apart from bioluminescence, all colour production mechanisms originate from the illumination of light (Doucet and Meadows, 2009; Sun et al., 2013). Chemical pigments selectively absorb specific wavelengths of light to produce a colour (Berthier, 2007). Structural colours are instead produced by the interaction of light with nanostructures that have length scales comparable to the wavelength of visible light, resulting in optical phenomena such as diffraction and interference (Barrows and Bartl, 2014; Burg and Parnell, 2018; Ingram and Parker, 2008). Both these mechanisms are found in diverse taxa and often in combination, to create salient and multifaceted visual signals (Airoldi et al., 2019; Kinoshita, 2008; Onelli et al., 2017; Sun et al., 2013). As well as crucial physiological roles (i.e., thermoregulation (Krishna et al., 2020; Shi et al., 2015)), colouration also provides a fundamental communication channel between organisms, which can modulate fitness through roles such as sexual advertisement (Hawkes et al., 2019; Kemp, 2007), predator deterrence (Waldron et al., 2017) and camouflage (Kjernsmo et al., 2020; Wilts et al., 2012). Such a variety of adaptive roles make colouration a model system for understanding the developmental and evolutionary mechanisms responsible for generating diversity.

Natural selection underpins many aspects of colour evolution in nature. For example, *Heliconius* butterflies possess aposematic colours which advertise their toxicity to predators and warning colours have converged amongst species in mimicry rings (Brown, 1981; Jiggins, 2017; Joron et al., 2006b; Kronforst and Papa, 2015). Conversely, sexual selection may act as an opposing force to natural selection by driving the elaboration of traits if they convey reliable

information about an individual's quality (Johnstone et al., 2009). Evolutionary theory predicts that traits will be selected for if they are costly to produce such that only individuals of the highest quality may realise the trait maxima (i.e., they are honest signals of quality) (Andersson and Iwasa, 1996; Kemp and Rutowski, 2007; Morehouse, 2014). The choosier sex (usually females) will use these traits to directly assess the direct and/or indirect benefits ('good genes') that may be accrued from mating (Andersson, 1986; Andersson and Iwasa, 1996). A well cited example is carotenoid colouration in birds (Weaver et al., 2018; White, 2020). Redder ornamentation is associated with increased survival (Fernández-Eslava et al., 2022), mitochondrial efficiency (Hill et al., 2019), immune function (McGraw et al., 2002), parasite resistance (Weaver et al., 2018) and oxidative stress resistance (Rodríguez et al., 2020). Such traits can serve as honest indicators of mate quality and the expression is driven by sexual selection through mate choice (Andersson and Iwasa, 1996; White, 2020).

Sexually selected traits typically demonstrate enhanced levels of condition dependence, whereby trait expression varies depending on an individual's ability to withstand environmental challenges (Cotton et al., 2006; Hill, 2011). Typically, the relationship between condition and trait expression is positive and is often demonstrated by generating stressful conditions and measuring trait expression (Morehouse, 2014). Condition dependence of colour traits has been demonstrated in numerous taxa, including insects (Kemp and Rutowski, 2007; White et al., 2021), birds (Surmacki et al., 2015), and fish (Trigo et al., 2020).

Butterfly wing colour originates from tiny overlapping wing scales which act as pointillistic origins of colour, similar to pixels on a computer screen (Hanly, 2017; Nijhout, 1991; Vukusic, 2006). The conspicuous colouration of butterfly wings offers an ideal system to explore condition dependence and the link between trait expression and the underlying mechanistic processes governing their production (Morehouse, 2014).

Several studies have demonstrated phenotypic effects on pigmentary colouration due to environmental stressors, such as larval food stress (Johnson et al., 2014; Pegram et al., 2013; Talloen et al., 2004) and thermal stress (Piszter et al., 2019). In many cases, environmental stressors can trigger adaptive plasticity in butterfly pigmentary colours. Temperature decrease can increase wing melanisation (Kingsolver and Wiernasz, 1991), which can enhance thermal absorption (Schmitz, 1994) and ultimately effect flight performance (Goulson, 1994) and developmental rate (Roland, 1982) in Lepidoptera. Thermal stress in *Bicyclus anyana* alters eyespot size, resulting in a more camouflaged appearance (Bhardwaj et al., 2020). Adaptive plasticity implies several optimal phenotypes depending on the environment and is the basis for seasonal polymorphism (Gotthard and Nylin, 1995). However, the response of butterfly wing colouration is not necessarily always adaptive. Often the response to an environmental stress is condition dependent, such that there is a single optimal phenotype, but under suboptimal conditions certain individuals are not able to produce that phenotype, or will trade it off against allocation of resources to other fitness-related traits. For example, dietary restriction decreases the chroma of the orange spots on *Battus philenor* hindwings, creating variation in the warning colouration, which potentially impacts predation level (Pegram et al., 2013).

Less emphasis has been placed on the plasticity and condition dependence of structural colour in butterflies, though it has been studied in other taxa (Lim and Li, 2007; McGraw et al., 2002; Meadows et al., 2012; Siefferman and Hill, 2007; White et al., 2021). The most extensive work has been performed in the sexually dimorphic *Colias eurytheme*, with males possessing UV dorsal colouration, due to multi-layered reflectors in their wing scales. Thermal and dietary stress experiments led to a decrease in UV brightness (Kemp et al., 2006; Kemp and Rutowski, 2007), a trait known to function in mate choice (Kemp, 2007). Dietary stress caused direct morphological changes to the multilayer reflector (Kemp, 2008; Kemp and

Rutowski, 2007). More recently, Fenner et al., (2019), performed dietary stress experiments in *Zerene* butterflies, a sister genus to *Colias*, whose UV structural colours is also controlled by multi-layered reflectors. Unlike *Colias eurytheme*, dietary stress in *Zerene cesonia* caused a reduction in UV wing scale density, suggesting the response to dietary stress can vary between species (Fenner et al., 2019). Dietary stress likely affects the allocation of limited resources between scale building and other essential metabolic functions (Kemp and Rutowski, 2007). Further characterisation of the effect of dietary stress on structural colours in diverse butterfly species and families is warranted.

In this study we investigate the effects of dietary stress in the butterfly *Heliconius sara* (*H. sara*) (Nymphalidae). *H. sara* inhabits forest edges in the neotropics of South and Central America. Multiple females lay eggs together in a large clutch on its *Passiflora* host species. Larvae exhibit gregarious group feeding behaviour, often completely defoliating food plants, therefore dietary stress is likely a common, ecologically-relevant stressor during development (Jiggins, 2017). *H. sara* possesses iridescent blue structural colour in the proximal forewing and hindwing, produced from multilayer reflectors on the ridges which run parallel along the scale surface (Parnell et al., 2018). Additionally, *H. sara* also possess a yellow pigmented forewing band. The yellow colour is the result of the chemical pigment 3-hydroxykynurenine (3-OHK), which reflects UV light (Wilts et al., 2017a). In addition to its role in predator deterrence, wing colour patterns in *Heliconius* serve as visual signals used for mate choice and species recognition (Finkbeiner et al., 2014; Jiggins, 2017; Jiggins et al., 2004, 2001; Merrill et al., 2014). However, the role of structural colours in mate choice for *Heliconius* is unknown, though light polarisation is utilised in female mate preference (Sweeney et al., 2003). Understanding the condition dependent nature of *Heliconius* structural colours in response to stressors, such as dietary stress, will lay the foundations for future studies on the roles such colours may play in mate choice.

Here, we use an experimental set-up consisting of larvae split between two diets, one of young, ‘fresh’ leaves and the other of mature, ‘old’ leaves. We infer the fresh diet of younger leaves to be better-quality, which we empirically demonstrate with elemental leaf analysis as well as measurements of key life history variables such as wing size and developmental rate. We then quantify the effects of dietary stress on colour production in adult *H. sara*. We aim to determine the effect of dietary stress on the reflective properties (hue, chroma, brightness) of iridescent, blue structural colour, and pigmentary yellow colouration on the forewing and whether the impact of dietary stress on colour differs between sexes. Additionally, we aim to characterise how dietary stress directly affects optical nanostructure formation. Using Scanning electron microscopy, we assess the underlying structural changes to the optical nanostructures in response to dietary stress. We then use optical models to simulate the multilayer nanostructure of *H. sara*, to assess how the scale nanostructure changes in response to dietary stress and its impact on the resultant structural colour, including reflectance and hue.

Materials and Methods

Butterfly Husbandry

A breeding stock of *Heliconius sara* butterflies were maintained in temperature-controlled greenhouses at the Arthur Willis Environment Centre, University of Sheffield. Butterflies were maintained at 25°C and 75% humidity with a 12-hour light and dark cycle. A 10% sugar water solution with 1 gram of added pollen substitute was used for feeding. *Passiflora auriculata* shoots were provided for egg laying. Larvae were maintained at 24 °C and 75% humidity and fed *Passiflora biflora*.

Diet manipulation

Two days post-hatching larvae were divided into separate tanks corresponding to the two diet treatments. One tank was fed entirely on a diet of ‘fresh’ shoots (Figure 1A), which comprised of the youngest growing branches of *Passiflora biflora*. The second tank was fed ‘old’ shoots (Figure 1B), which were tougher, mature branches of the plant. Both treatments were fed *ad libitum* to prevent any confounding impacts of starvation. After emergence butterflies were allowed to dry for several hours before being humanely culled. 95 individual butterflies emerged (n = 49 fresh; n = 46 old), split across two experimental batches (n = 43 batch 1; n = 52 batch 2). Experimental batches were performed approximately 6 months apart (Batch 1: October 2020; batch 2: April 2021). Larval development time was taken as the time from hatching to pupation in days, and pupation time was pupal case formation to the emergence of adult butterflies in days.

Developmental times were analysed in R using Generalised Linear Models (GLM). In all cases, model fits were assessed for normality and heteroscedasticity of residuals using the ‘DHARMA’ package (version 0.4.5) (Florian Harting, 2017). The effect of diet on larval developmental time was analysed using a GLM with a Gamma family distribution and the canonical inverse link function. The model included diet, wing area to represent body size (wing area and body size are correlated in butterflies (Chai and Srygley, 1990)), sex and batch as fixed effect variables. Collinearity was assessed between explanatory variables using the package ‘Performance’(v. 0.8.0) (Lüdecke et al., 2021). Pupation time was analysed with a GLM with a negative binomial distribution and a log link function. Here, the negative binomial distribution was used, due to a better fit of the model in relation to the residual dispersion and outliers compared to a Gamma distribution. Diet, batch and sex were fitted as fixed effect variables. In all models Likelihood ratio tests using the *anova* function were performed to calculate significance levels.

Leaf chemistry

Elemental analysis was performed to quantify the nutrient status of the diet treatments. Leaves were sampled from the collection of *Passiflora biflora* maintained in greenhouses at the Arthur Willis Environment Centre, University of Sheffield. Plants were watered three times per week and regularly supplemented with plant food. Three leaves per diet category (fresh versus old) were selected from five separate *Passiflora biflora* plants of similar age and size. Leaves were ground using a mortar and pestle and 10-50 mg of each sample were used to determine Carbon (C) and Nitrogen (N) content. Measurements were conducted on an elemental analyser (Vario max MACRO cube (Elementar)) using CN mode. Percentages of C and N and the C:N ratio were analysed in R (version 4.1.2) using paired sample T-tests.

Digital imaging

To measure the overall wing size as well as the proportion of colour on the wings, we performed photography of the adult butterfly wings. Butterfly forewings and hindwings were individually removed and positioned flat against a white background under standardised lighting conditions. Imaging was performed using a fix-mount Nikon DSLR camera, equipped with a 40 mm f/2.8 lens and an aperture of f/10, shutter speed of 1/60 and ISO 100. Overhead lights were maintained at a distance of 22 cm and positioned at a 45° angle to highlight the iridescent region. An X-rite colour checker standard was included in all images for colour standardisation.

Wing area analysis

Wing area analysis was performed in FIJI (Version 1.53n) (Schindelin et al., 2012). Digital images were converted to 8-bit, cropped of the colour standard and thresholded using the ‘make binary’ and ‘fill holes’ functions. The area of individual wings was calculated using the ‘Analyse Particles’ function. The above processes were summarised into a macro to automate the analysis. Only butterflies with undamaged wings were measured (total n = 92; fresh n = 49,

old $n = 43$). Data was analysed in R and a multiple linear regression approach was used to determine the effect of diet, sex and batch on wing area. Diet, sex and batch were fitted as fixed effect variables, with an interaction term between sex and diet and batch and diet.

Colour area analysis

Images of 48 fresh diet wings (female $n = 25$; male $n = 23$) and 39 old diet wings (female $n = 16$; male $n = 23$) (total $n = 87$) were imported into GNU image manipulation program (GIMP) (version 2.10.14) and the colour corrected using the ‘curves’ function. The white background was removed using a transparent alpha channel. Remaining background around the wing margins was manually removed using the ‘fuzzy select’ tool. Images were imported into R using the ‘colordistance’ package (Weller and Westneat, 2019). For each image, pixels were binned using a k-means clustering method, implemented in the ‘getKMeanColors’ function. Single bins were used to cluster the black wing region and yellow wing bars as well as two bins to encompass the angle-dependent variation in hue from green to dark blue within the iridescent region. The ‘extractClusters’ function was run to produce a dataframe containing RGB values and proportion values of each of the four bins for each image. Percentage area of the black region, yellow wing bars and iridescent region were calculated from these proportions with the iridescent region being the sum of the blue and green bins. To ascertain the colour similarities between images a colour distance matrix was calculated using the ‘colordistance’ metric implemented in the ‘getcolourDistanceMatrix’ function. This metric harnesses the Euclidean distance in colour space between pairs of clusters to analyse the colour similarity between samples (Weller and Westneat, 2019).

For each wing colour, Generalised linear models were fitted using a Gamma family distribution with the inverse function. Diet, sex and batch were fitted as fixed effect variables

with an interaction term between ‘sex and diet’ and ‘batch and diet’. Likelihood ratio tests were performed on the models to determine effect of diet, sex and batch on % colour area.

Reflectance spectrometry

To measure the reflectance of the separate colour regions on the dorsal forewings we performed reflectance spectrometry. This allows a more accurate and standardised method of measuring reflective properties (hue, chroma and brightness) than the digital photography images. Forewings were mounted onto a rotating optical stage and reflectance measurements taken using an Ocean Optics USB2000+ Spectrometer coupled with a PX-2 xenon light source and fibre optic probe. A Polytetrafluoroethylene (PTFE) diffuse white standard (Labsphere) was used as the reflectance standard. For the iridescent region, 48 fresh diet samples (female n = 25; male n = 23) and 39 old diet samples (female n = 16; male n = 23) were measured. The probe was mounted 5 mm from the rotating stage and reflectance measurements were taken across a 20° angular range, with 2° intervals, beginning at 0° in which the wing was at normal incidence to the probe. Spectra Suite (Ocean Optics) software was used to acquire measurements with the integration time set to 350 ns, 5 scans to average and a boxcar width of 3 nm.

Spectral data was analysed in R using the package Pavo (version 2.7.1)(Maia et al., 2013). Smoothing and peak extraction of spectra (350 – 700 nm) was performed using the ‘Prospec’ and ‘Peakshape’ function, respectively. Colourimetric variables were extracted using the ‘summary’ function. Seven Colourimetric variables were chosen to evaluate the brightness (B1, B3), Chroma (S1G; S1B; S8), Contrast (S6) and Hue (H1), described in Table 1 (Montgomerie, 2006). For information on their implementation see Pavo manual (Maia et al., 2013).

Table 1. The seven colourimetric variables implemented in the analyses of spectral data.

Descriptions are directly taken from (Montgomerie, 2006).

Colourimetric variables	
Total Brightness (B1)	Sum of relative reflectance over the entire spectral range (area under the curve).
Intensity (B3)	Maximum relative reflectance (Reflectance percentage at the wavelength of maximum reflectance).
Blue Chroma (S1B)	Relative contribution of the spectral range between 400 – 510 nm (Blue) to the total brightness (B1).
Green Chroma (S1G)	Relative contribution of the spectral range between 510 – 605 nm (Green) to the total brightness (B1).
Contrast (S6)	Maximum reflectance subtracted by the minimum reflectance.
Chroma (S8)	Value of the maximum reflectance subtracted by the minimum divided by the mean brightness.
Hue (H1)	Wavelength at maximum reflectance.

Reflectance of the yellow bar followed the methods above. Two measurements were taken at 0° and 2° in the upper and lower portion of the yellow wing region, separated by the forewing cell vein and averages were fitted. Reflectance values were taken from 23 fresh diet males, 25 old diet males, 26 fresh diet females and 19 old diet females. The yellow hue was calculated following the method of (Kemp, 2008) by plotting the mean reflectance for each diet and then calculating the inflection point using the R package Inflection (Christopoulos, 2019). Colourimetric variables assessed were B1, B3, S8, S6 (Table 1).

For both iridescent and yellow bar reflectance colourimetric and spectral data was analysed using multiple linear regression models with sex, experimental batch and diet fitted as explanatory variables. Models also encompassed two interaction terms, sex and diet and batch and diet.

Atomic Force Microscopy (AFM)

To gain a three-dimensional insight into the effects of diet on ridge architecture we performed AFM. AFM was performed in tapping mode on individual scales using a Dimension 3100 AFM equipped with a Nanoscope 3A controller following the methods of (Parnell et al., 2018). Individual scales from the iridescent region were transferred onto glass slides and the scanning tip directed above them. Image reconstruction and measurements were performed in the freely available software Gwyddion (Nečas and Klapetek, 2012). Images were levelled, corrected for horizontal line artefacts and the height scaled to zero.

Transmission Electron Microscopy (TEM)

TEM was performed to gain accurate measurements of chitin layer and air thickness in the multilayer reflector. A single *H. sara* butterfly was randomly selected from the breeding population. Ventral wing scales were removed by lifting away the scales with sticky tape. A few mm of iridescent wing surface was cut using scissors. TEM preparation followed the protocol of Shawkey et al., (2003). Samples were washed with 0.25M sodium hydroxide with 0.1% Tween for 30 minutes. Then wing samples were transferred to a 2:3 solution of formic acid to ethanol for 2.5 hours before dehydration using two washes of 100% ethanol for 30 minutes. Samples were infiltrated with Epon epoxy resin using progressive washes of 15%, 50%, 70% and 100% Epon in propylene oxide, each step lasted 24 hours. Then samples were cut and placed in resin molds and baked for 24 hours in a 60 °C oven until the resin cured. A Leica ultramicrotome was used to cut thin sections of the sample (70-100nm) and these were placed on a copper grid. Samples were stained using Uranyl acetone for 10 minutes before being washed twice with distilled water for 5 minutes. Further staining was performed using a solution of Lead nitrate, sodium citrate and 1M sodium hydroxide, followed by two washes in

distilled water. Imaging was performed using a Phillips CM100 Transmission electron microscope at an accelerating voltage of 100 kv.

Scanning Electron Microscopy (SEM)

SEM was performed to measure the ridge architecture features associated with structural colour production. Five individuals from the fresh diet and five individuals from the old diet were selected for scanning electron microscopy. A portion of the iridescent region in the proximal section of the dorsal forewing was removed and placed on 9 mm carbon tabs (Agar scientific) mounted onto 9 mm aluminium stubs (Agar scientific). Mounted samples were sputter coated with several nanometres of gold to provide conductivity. Scanning electron microscopy was performed on a JEOL JSM-6010LA SEM. The accelerating voltage was varied between 5 kv and 20 kv depending on the required magnification.

Structural analysis

SEM images of ten scales (including both cover and ground scales) were taken from five fresh diet and five old diet individuals. Measurements of scale features (scale size, ridge spacing, ridge width) were performed in FIJI following the methods outlined in Chapter 3 (scale size and ridge spacing). Scale size was taken as the length of the scale multiplied by the width of the scale at the midpoint of the length. Ridge spacing was calculated as an average, with the number of ridges divided by the scale width at the midpoint of the length, using the PeakFinder tool (Vischer, 2011). Ridge width was measured using the line draw tool and measure function in FIJI.

Statistical analyses were performed in R. For each individual the mean ridge spacing and mean ridge width was calculated and individuals from each diet treatment compared using Welch Two Sample T-tests. For scale size, measurements were grouped by scale type (cover and ground) before a Welch Two Sample T-test was performed. In addition, high-

magnification images of the ridges were taken of ten scales for each of the five fresh and five old diet individuals, with the exception of sample 44d, from which nine scales were measured. The number of ridge termination points (where the upper ridge layer ends) was calculated for four ridges per scale. If two or more ridges per scale contained ridge termination points the scale was classified as a ‘tilted’ scale. The proportion of ‘tilted’ scales to normal scales between the fresh and old diets was compared using a Chi-squared test.

Optical Modelling

Simulations of optical properties were performed using the freely available Python package ‘tmm’ (version 0.1.8) (Byrnes, 2021). The nanostructure in *H. sara* was assumed to be stack of alternating planar layers of chitin and air (for details of the underlying optical principles and calculations see Supplementary information). Chitin and air layer thickness were calculated from TEM images, five ridges were selected which were the most perpendicularly sectioned across the scale. Images were imported into FIJI and the contrast and brightness manually adjusted. The line tool and measure function were used to measure the distance of two chitin layers and the corresponding air spacing. Mean thickness values (mean chitin thickness \pm SD = 87 ± 9.10 nm, mean air spacing \pm SD = 122 ± 16.9 nm) were used as input parameters. Refractive indices were taken from the literature; chitin ($n = 1.56$) and air (1.0) (Vukusic et al., 1999). A normal incidence and an ‘s’ polarisation of light (electric field orientation normal to the plane) were used for all simulations.

In order for the simulated spectra produced from the model to be compared to (and plotted against) the spectra collected from the diet treatments (measured spectra) we performed scaling of the measured spectra. This is because the simulated model is based on a single, perfect ridge with no interfacial roughness and a total recovery of the reflected light. In contrast, our measured spectra were collected using a probe (which has inherent inefficiencies such that not

all reflected light is recovered) over an area covering hundreds of scales which include lots of additional interfaces which scatter light as well pigments. This means that the actual nanostructure of interest is actually a relatively small proportion of the material in the path of the light. Therefore, the percent reflectance, which is experimentally determined as the ratio between the reflectance of the white standard and the butterfly wing, is not directly comparable to the simulated values for the maximum theoretical reflectance of an ideal multilayer. However, both the simulated and measured spectra have a peak in the reflectance which corresponds to the most common wavelength reflected by the optical nanostructure. Therefore, to make the spectra more comparable we multiplied all of our diet treatment measurements with a scaling factor (below) based on the peak reflectance of the simulation of a 2 chitin layer model (which we assume from our TEM measurements is the optical nanostructure). This does not change the peak shape of the observations because we assume all the differences between observed and simulated data are due to consistent measurement bias (i.e. the probe consistently measures a lower reflectance than the 'real' one, at the same rate for all wavelengths).

$$scale\ factor = \frac{\% \text{ fresh reflectance}_{max}}{\% \text{ simulated reflectance}_{max}}$$

The equivalent drop in reflectance from the measured fresh diet to the old diet was modelled using an ideal, 2 chitin layer model with a chitin backing and incorporating a weighted percentage of an ideal 1 chitin layer model with a chitin backing. This was performed to understand the how losing a layer (equivalent to gaps in the multilayer reflector) would lead to a (relative) drop in reflectance similar to the diet treatment.

Reflectance spectra under D65 illumination and the corresponding plots were created using the Python package 'Pypvcell' (version 0.2.0) (Lee et al., 2017). The package harnesses the Python package 'tmm' and a modified version of 'ColorPy' (version 0.1.0) available at

<https://github.com/kanhua/ColorPy>. The script ‘color_of_surface_tmm_2.ipynb’, available at <https://github.com/kanhua/pypvcell> was modified using values of chitin refractive index and thicknesses. Conversions of the physical properties of light into RGB values was performed using ‘ColorPy’. Chroma was extracted using the ‘chroma_from_irgb’ function and the hue extracted using the ‘hue_from_irgb’ function.

Results

Diet manipulation and leaf chemistry

All nutrients required for wing development are acquired during the larval stage, through consumption of plant material. Firstly, we sought to quantify whether the diet treatments were correlated with apparent differences in nutrient composition of the leaves, focusing on the %Carbon and %Nitrogen.

Elemental analysis revealed there was no significant difference in Carbon content between fresh and old leaves (Paired t-test, $t = 0.78$, $df = 4$, $p = 0.48$; mean %C \pm SE: fresh = $37.89\% \pm 2.24$; old = $35.67\% \pm 2.41$) (Fig 1D). However, there was a significance difference in Nitrogen content, with fresh leaves having almost twice the Nitrogen content compared to old leaves (Paired t-test, $t = 4.44$, $df = 4$, $p = 0.01$; mean %N \pm SE: fresh = $4.47\% \pm 0.58$; old = $2.73\% \pm 0.32$) (Fig 1E). The %Nitrogen of the fresh leaves were within the typical ranges for *Passiflora* leaves of between 4 – 5%, however the old diet had significantly less Nitrogen suggesting a loss or dilution of Nitrogen from mature leaves (Menzel et al., 1993).

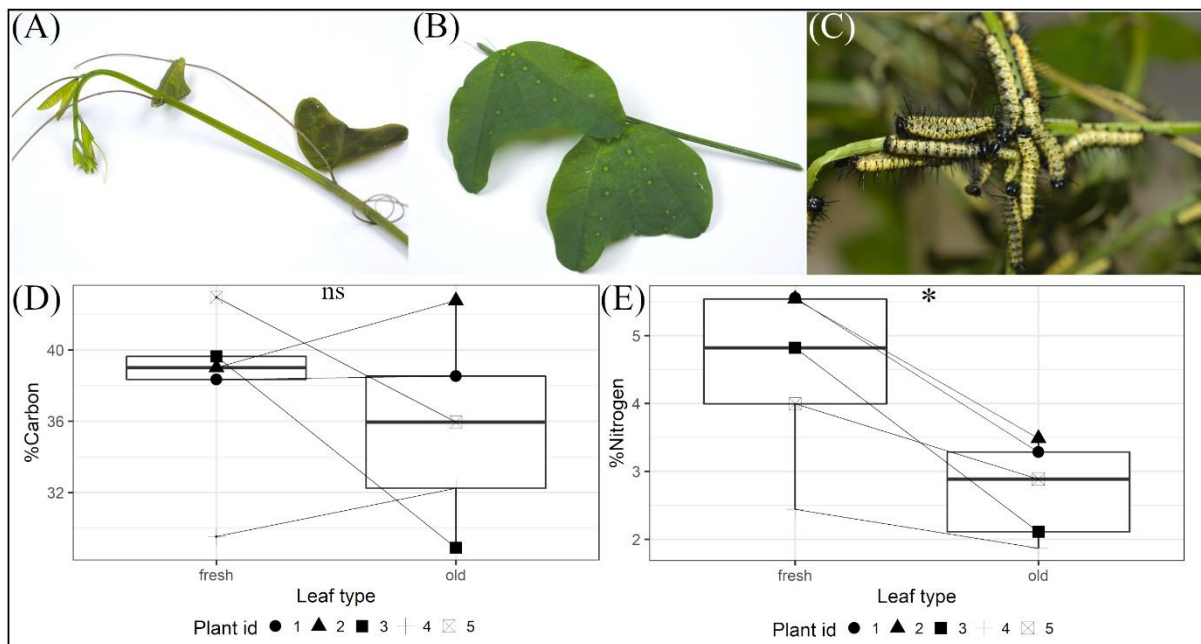


Figure 1. Diet manipulation and leaf chemistry. (A) An example of a typical ‘fresh’ shoot, which is the newest re-growth of the plant. Both the leaves and the stem are soft and flexible, with tendrils extending out of the axillary buds along the growing branch. (B) An example of a typical ‘old’ shoot in which the leaves have reached maturation and attained maximal size. Both the stem and the leaves are tough, indicative of being highly lignified. (C) Gregarious larvae of *H. sara* exhibiting group feeding behaviour. All parts of the host plant are consumed, including the stem. Elemental analysis of %Carbon (D) and %Nitrogen (E) in fresh and old leaves.

Impacts of dietary stress on development and size

Next, we assessed the impact of diet on key developmental and fitness-related variables, including developmental rate and wing area as a proxy for body size.

Both male and female butterflies were smaller in wing area when fed the old diet compared to the fresh diet (mean \pm SE total wing area, fresh diet (female, male) = 1153 mm² \pm 31, 1138 mm² \pm 30; old diet (female, male) = 1023 mm² \pm 35, 1019 mm² \pm 32; (F= 17.4; df = 1, 86; p <

0.001) (Figure 2A). However, there was no difference in wing area between males and females for either diet treatment ($F = 0.16$; $df = 1, 86$; $p = 0.69$). There was a significant difference in wing area between fresh and old diet individuals within the first experimental batch (Tukey multiple comparison test; $P < 0.001$) but not the second experimental batch (Tukey multiple comparison test; $P = 0.53$).

Larvae took longer to develop when raised on the old diet (mean \pm SE larval days, fresh diet = 14.9 ± 0.14 days; old diet = 17.8 ± 0.27 days; $\chi^2 = 0.66$; $df = 1, 84$; $p < 0.001$) (Figure 2B). There was also a significant effect of experimental batch on larval development time ($\chi^2 = 0.18$; $df = 1, 82$; $p < 0.001$) and an interaction between experimental batch and diet ($\chi^2 = 0.03$; $df = 1, 79$; $p < 0.01$). There was no significant difference in larval developmental time between experimental batches fed the fresh diet ($p = 0.12$); however, larvae fed the old diet took significantly longer to develop in the first experimental batch compared to the second ($p < 0.001$).

The batch effect in both wing size and larval development time suggests either population differences between batches or, more likely, slight differences in treatment application between batches. The first batch likely received a lower-quality old diet than the second batch resulting in an exaggerated stress response corresponding to longer development times and smaller wing size. Diet had no effect on pupal development time with almost all pupae taking 9 days to emerge (mean \pm SE pupal days, fresh diet = 9.00 ± 0.00 days; old diet = 8.92 ± 0.06 days; $\chi^2 = 0.014$; $df = 1, 68$; $p = 0.90$) (Figure 2C).

Overall, dietary stress resulted in a substantial impact on life-history traits. Larvae took longer to develop; but this extended feeding time did not compensate for the nutritional deficits and the emerging butterflies of both sexes were smaller.

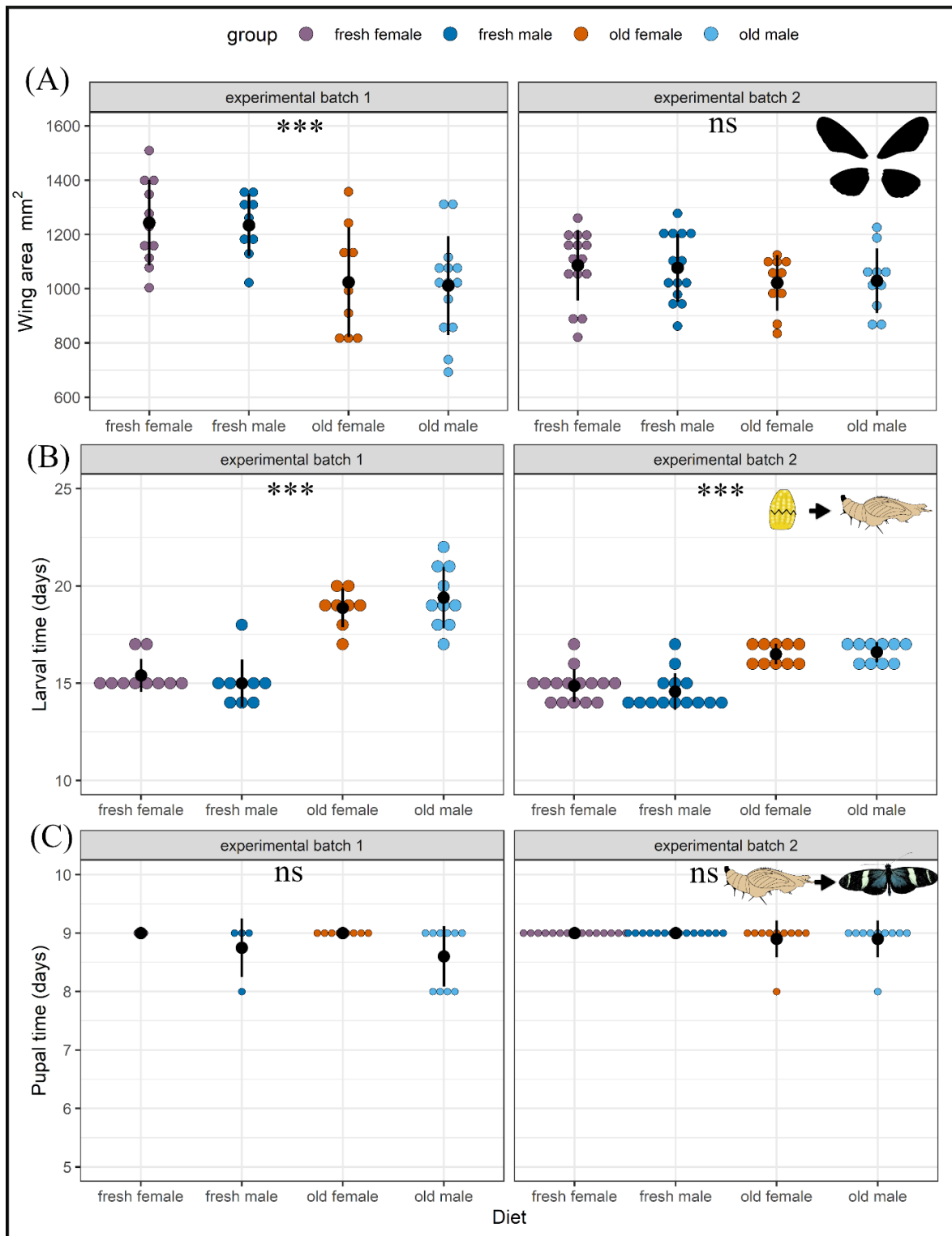


Figure 2. Effect of larval dietary stress on development. (A) Total wing area (mm²) (B) larval development time (days) (C) pupation time (days) for male and female butterflies fed the fresh and old diet for the two experimental batches. Black dot indicates the mean and lines indicate the standard deviation of the mean for each group.

Impacts of dietary stress on wing colouration

Next, we investigated the impact of dietary stress on the production of the iridescent structural colour, and yellow pigmentary colour on the dorsal forewing of *H. sara*.

Iridescent area

Dietary stress had no impact on the area of the iridescent signal. The percentage area of blue on the forewing did not differ between the fresh and old diet ($\chi^2 = 0.004$; $df = 1, 85$; $p = 0.72$) (Supplementary Figure 1, 2; Supplementary Table 1). While there was an effect of experimental batch on iridescent area ($\chi^2 = 2.72$; $df = 1, 84$; $p < 0.001$), there was no interaction between experimental batch and diet ($p = 0.26$); with dietary stress leading to no significant change in % blue in either batch (Supplementary Figure 1; Supplementary Table 2). On inspection of the raw images, it was determined that the lighting conditions had fractionally changed between the experimental batches leading to reduction in iridescent region being visible in batch 2 and an increase in black. The batch effect did not change the conclusion that iridescent area does not change as a result of dietary stress.

Reflectance of iridescent blue

The reflectance of the iridescent blue was significantly affected by dietary stress. There was an observable reduction in the peak reflectance spectra in both males and females fed the old diet (Figure 3A). This corresponded to a significant decrease in overall brightness as well as a significant reduction in the chroma and contrast (Table 2). Dietary stress caused a greater decrease in reflectance in males than females. There was a 14.6 % decrease in brightness in males fed the old diet compared to the fresh diet (Tukey multiple comparison test; $p < 0.05$). However, there was only a 9.4 % decrease in brightness of females fed the old diet (Tukey multiple comparison test; $p = 0.61$) (Figure 3A, Supplementary table 2). There was an effect of batch on brightness ($F = 15.6$; $df = 1, 81$; $p < 0.001$). The decrease in brightness between the

fresh and old diet in batch 1 was not significant (Tukey multiple comparison test; $p = 0.61$, Supplementary Table 2), potentially due to the low sample size ($n = 41$).

The hue of the reflected colour was also significantly affected by diet with both male and female butterflies fed the old diet undergoing a blue shift towards shorter wavelengths (Figure 3A; Table 1). The reduction in hue in males was significant ($t = 2.91$, $df = 81$, $p < 0.05$) but in females it was not significant ($t = 1.63$, $df = 81$, $p = 0.56$; Supplementary Table 2).

Table 2. Mean \pm SE values and statistical results of the selected Colourimetric variables at angle of maximum reflectance describing various aspects of reflected iridescent blue colour in the fresh and old diet treatments.

Colourimetric variable	Mean \pm SE 'fresh'	Mean \pm SE 'old'	F	df	p-value
B1 (Total brightness)	2231 \pm 80	1955 \pm 81	6.75	1, 81	0.011
B3 (Intensity)	10.7 \pm 0.371	9.41 \pm 0.37	6.73	1, 81	0.011
S1B (Blue Chroma)	0.406 \pm 0.0079	0.437 \pm 0.0076	7.67	1, 81	0.0070
S1G (green Chroma)	0.399 \pm 0.0047	0.379 \pm 0.0052	8.5	1, 81	0.0046
S6 (Contrast)	10.7 \pm 0.371	9.40 \pm 0.370	6.73	1, 81	0.0112
S8 (Chroma)	1.68 \pm 0.0071	1.69 \pm 0.012	1.34	1, 81	0.25
H1 (Hue)	510 \pm 3.47	496 \pm 2.83	9.47	1,81	0.0028

Angular variation

There was no effect of dietary stress on the angle of maximum reflectance (mean \pm SE angle maximum reflectance, fresh diet = $5.5 \pm 0.46^\circ$; old diet = $5.2 \pm 0.45^\circ$; $F = 0.120$; $df = 1, 81$; $p = 0.66$, Figure 3B). However, across the majority of the angular range the old diet individuals had a significantly decreased reflectance and hue compared to the fresh diet (Supplementary Table 3, 4). Furthermore, we observed sexual dimorphism in iridescence properties, with the male peak reflectance angle ($5.9 \pm 0.54^\circ$) significantly greater than the female peak reflectance

angle ($4.7 \pm 0.36^\circ$) ($F = 4.09$; $df = 1, 81$; $p < 0.05$). In addition, across the angular range the greatest difference in hue between the fresh and old diet was observed in males (Figure 3E-F).

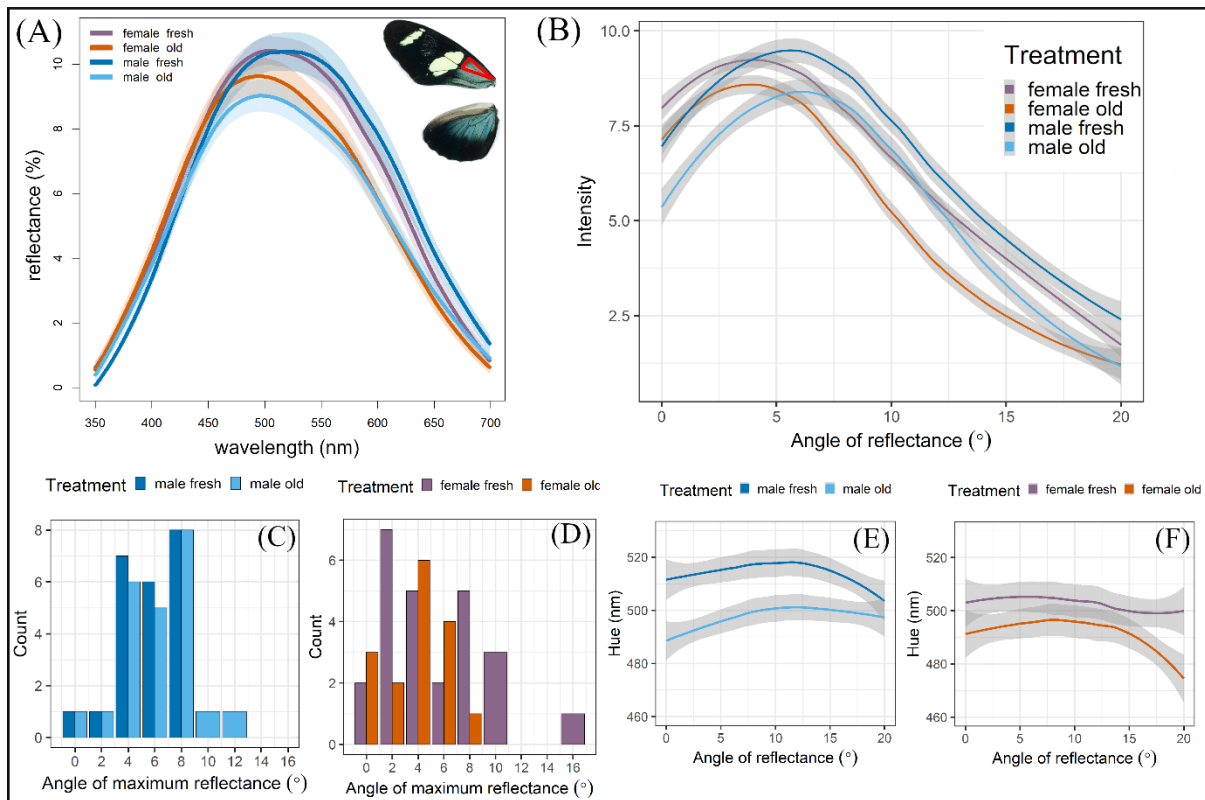


Figure 3. Impact of dietary stress on the structural colour of *Heliconius sara*. (A) Mean percentage reflectance at angle of maximum reflectance for male and female *H. sara* fed an old and fresh diet. (B) Angular dependent change in reflected intensity of males and females in the old and fresh diets. (C) Angle of maximum reflectance of males (D) and females (D) in the different diets. Angle dependent change in reflected hue in males (E) and females (F) for the fresh and old diets. Shaded areas in all plots represent the standard error.

Impact of diet on pigmentary colouration

Reflectance spectra obtained from the yellow bar (Figure 4A) were typical of *Heliconius*, in which the yellow colouration is produced by the chemical pigment 3-hydroxy-dl-kynurenine (3-OHK) (Wilts et al., 2017a). There was a characteristic peak within the UV range (300 – 400 nm) before a rapid increase in reflectance between 425 – 500 nm and a relative plateau at the longer wavelengths (500 – 700 nm). There was negligible angle-dependence of the colour, with little change in intensity across the measured angular range (Figure 4D). Yellow pigment hue has been previously defined by Kemp (2008) as the ‘midpoint of the inflection between low midwave and high longwave reflectance’ and varies from whitish-yellow to orange-yellow (Kemp, 2008). For both fresh and old diets, the mean inflection midpoint was 456 nm (Figure 4A), indicating no difference in the hue of the yellow region.

Diet had no impact on brightness, chroma or saturation of the yellow colour (Table 3). We note there was slight decrease in brightness between fresh and old diet males but post-hoc Tukey analyses revealed this was not significant ($p = 0.210$) (Figure 4B). Furthermore, there was no correlation between the brightness of iridescent blue and the brightness of the yellow bar (Pearson product-moment, $r = -0.019$, $t = -0.18$, $df = 85$, $p = 0.861$) (Figure 4C).

Inspection of longwave reflectance from 500 – 700nm (Figure 4B) revealed significant sexual dimorphism, with males having a greater peak reflectance followed by a decrease in reflectance towards the longest wavelengths. In contrast, female reflectance peaked lower but increased towards the near-infrared values. In accord, we found a significant difference in total brightness between sexes within the 500 - 700nm region (mean \pm SE brightness (B1), female fresh diet = 6761 ± 169 ; female old diet = 6769 ± 125 ; male fresh diet = 7331 ± 102 ; male old diet = 6938 ± 186 ; $F = 6.52$; $df = 1, 87$; $p = 0.012$).

Overall, we demonstrate that pigimentary colour in *Heliconius sara* has a sexually dimorphic component, but it is robust to dietary stress.

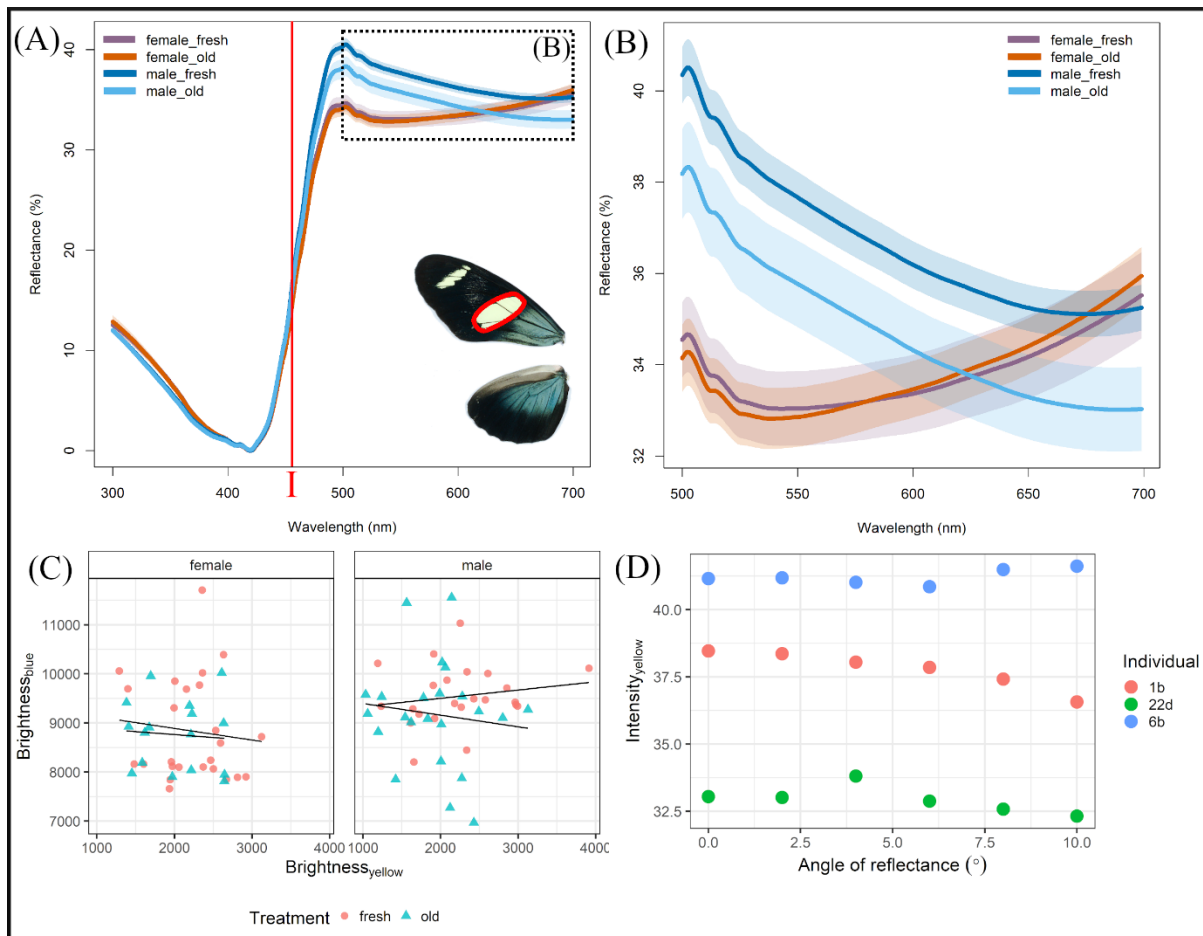


Figure 4. Effect of dietary stress on the yellow pigimentary colour of *Heliconius sara*. (A) Reflectance spectra of males and females for the fresh and old diet. Red line (I) indicates the inflection point corresponding to the yellow hue. Inset image shows the region of yellow bar measured on the wing. (B) Enlarged view of the longer wavelength region (500 – 700nm) in (A). (C) Correlation between brightness (B1) of the blue iridescent region and yellow bar for each individual measured. (D) Intensity (B3) of the yellow region across the measured angular range from 0 to 10° for 3 randomly chosen individuals.

Table 3. Mean \pm SE values and statistical results of the selected Colourimetric variables describing various aspects of the yellow pigmentary colour in the fresh and old diet treatments.

Colourimetric variable	Mean \pm SE 'fresh'	Mean \pm SE 'old'	F	df	p-value
B1 (Total brightness)	9179 \pm 131	8970 \pm 144	1.34	1, 87	0.251
B3 (Intensity)	38.4 \pm 0.616	37.4 \pm 0.646	1.39	1, 87	0.241
S6 (Contrast)	38.4 \pm 0.616	37.4 \pm 0.646	1.39	1, 87	0.241
S8 (Chroma)	1.67 \pm 0.0071	1.67 \pm 0.0056	0.0759	1, 87	0.784
H3 (Hue)	457 \pm 2.66	456 \pm 3.65	0.0546	1, 87	0.8157

Structural analysis

To investigate the impact of dietary stress on the optical nanostructures responsible for the structural colour, we interrogated the iridescent wing scales in a subset of fresh diet and old diet individuals using scanning electron microscopy.

There was no significant difference in the overall size of either the cover (mean \pm SE scale size, fresh diet = 2963 \pm 119 μm^2 ; old diet = 3044 \pm 182 μm^2 ; $t = -0.31$, $df = 5.95$, $p\text{-value} = 0.77$) or ground scales (mean \pm SE scale size, fresh diet = 3832 \pm 182 μm^2 ; old diet = 3952 \pm 172 μm^2 ; $t = -0.48$, $df = 7.97$, $p = 0.643$) between diet treatments (Figure 5K). Furthermore, there was no difference in ridge spacing between diet treatments (mean \pm SE ridge spacing, fresh diet = 716 \pm 11 nm; old diet = 734 \pm 30 nm; $t = -0.57$, $df = 5.10$, $p = 0.60$; Figure 5I). However, there was a significant reduction in ridge width in the old diet compared to the fresh diet (mean \pm SE ridge width, fresh diet = 186 \pm 5 nm; old diet = 167 \pm 6 nm; $t = 2.47$, $df = 7.80$, $p < 0.05$; Figure 5J). While we saw no observable difference in scale density; this was not quantified (Figure 5A, B).

Closer inspection of the scale ridges further revealed numerous discontinuities in the ridge layering of dietary stressed individuals (Figure 5A-D; Supplementary Figure 8). Scales in the fresh diet had a continuous arrangement of ridge layers (Figure 5G), whereas dietary stressed scales often had gaps in the ridge layering as well as angular deviations in the layers away from parallel (Figure 5H). In some cases, dietary stressed individuals had extreme tilting of the ridges resulting in numerous termination points along the uppermost ridge layer (Figure 5F; Supplementary Figure 8H). Such scales, which we termed ‘tilted scales’, more closely resemble the non-iridescent scale types found in *Heliconius* (Parnell et al., 2018) . However, in some individuals in the old diet they were found throughout the entire iridescent region and the proportion of tilted scales was significantly greater than in the fresh diet ($\chi^2 = 13.27$, $df = 1$, $p < 0.001$).

Overall, reduction of reflectance of the blue structurally coloured in the old diet is likely attributed to interruption of the layering process through narrowing of the scale ridges, loss of ridge layers and/or tilting of the layers away from parallel.

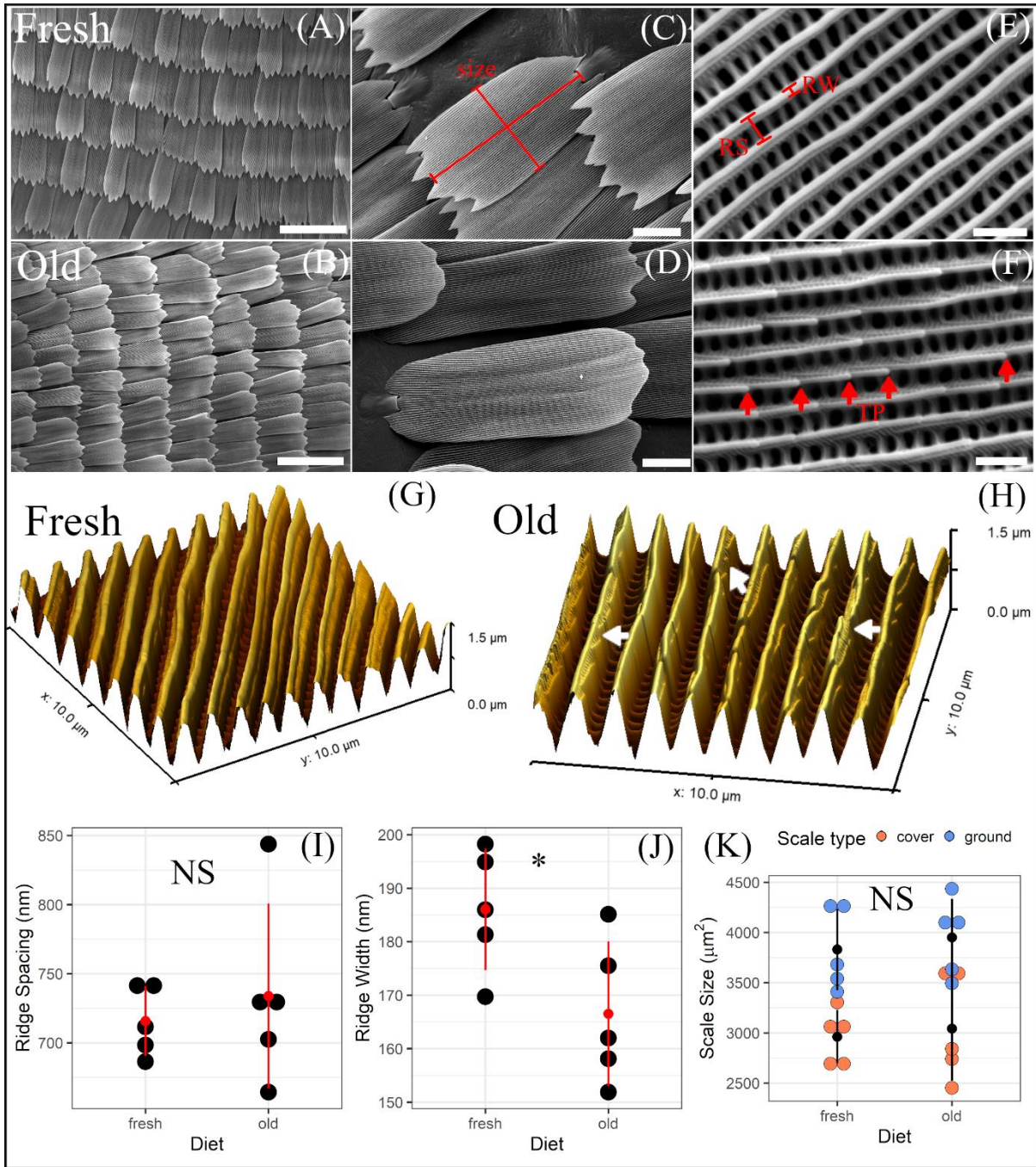


Figure 5. Structural analysis of *H. sara* scales in the fresh and old diet. (A, B) scale density of an individual from the fresh (A) and old (B) diet. (C, D) Overall morphology of the scales was similar between fresh (C) and old diet (D) individuals. Red line indicates the measurement of scale size, taken as the scale width multiplied by the length. (E, F) High-magnification images of the scale ridges. Ridges in the fresh diet (E) were uniform with a continuous patterning of the ridge layers. Red lines indicate measurements of ridge width (RW) and ridge

spacing (RS). (F) Old diet ridges frequently showed discontinuities in the ridge layering including, numerous ridge termination points (TP) as highlighted by the red arrows. (G) Atomic force microscopy images of typical scales from the fresh diet (G) and old diet (H). White arrows in (H) highlight disruption to the ridge layers (gaps). (I – K) Mean ridge spacing (I), ridge width (J), and scale size (K) for each individual measured from the fresh and old diet. Red point indicates overall mean for each diet and the standard deviation. Scale bars: A, B = 100 μm , C, D = 20 μm , E, F = 1 μm .

Optical modelling

To gain insight into how the diet affects the optical properties of the nanostructures responsible for the blue structural colour we performed optical modelling.

We first modelled the reflectance properties of an ideal *H. sara* multilayer (Supplementary Figure 13). Reflectors between one and ten layers were simulated between 350 nm and 700 nm (Figure 6A). The resulting model showed a sharp increase in reflectance as the number of layers increased. The most substantial increase in reflectance occurred between 1 and 3 layers before a plateau around 9 layers where the modelled reflectance matched the intensity of incident light. Additionally, the peak of reflectance narrowed as the number of layers increased, enhancing the chroma of the reflected colour.

We next compared the simulated spectra to our measured spectra of the fresh and old diets. Our TEM and SEM analyses indicated that *H. sara* predominantly possess two chitin layers in its multilayer stack (though occasionally three layers were visible) (Supplementary Figure 13). We note the discrepancy in simulated and measured percentage reflectance, with a peak measured reflectance of 10.4% compared to a simulated peak reflectance of 64.5%. This difference in reflectance is due to the simplistic assumptions of the tmm model which uses a single reflective ridge, which is entirely uniform and planar. In contrast the diet measurements

were taken across an area of the wings containing hundreds of scales using a probe which has inherent signal detection inefficiencies. In addition, the scales themselves have a punctuated nature of reflective ridges on their surface. Overall, these factors mean the reflection is stronger in the model compared to reality. To account for the disparity in percentage reflectance of the simulated and measured spectra and to compare the model to our measured values of reflectance we performed scaling of the measured values based on the peak reflectance of the simulated 2 chitin layer ideal system.

Inspection of the resulting distributions (Figure 6B) showed the measured (scaled) reflectance values were comparable to the 2 chitin layer simulation with a peak wavelength of reflection of 506 nm for the fresh diet compared to 516 nm for the simulated spectra. Interestingly, the peak of the measured (scaled) reflectance was narrower than the 2 chitin layer simulation, suggesting *H. sara* has more chromatic colour than predicted. This may be due to several reasons: (i) The presence of some three-layer ridges in the scales. (ii) Melanin within the ridges increasing the refractive index contrast. (iii) A degree of thin-film reflectance from the lower lamina enhancing spectral purity, as seen in *Morpho* (Giraldo and Stavenga, 2016). Thin-film calculations using measurements of the lower lamina thickness from our TEM images indicates a peak reflectance wavelength at 490 nm; comparable to the peak of the multilayer stack.

Next, we investigated how aspects of ridge architecture may influence the peak reflectance and shape of the modelled spectra (Supplementary Figure 9). Incorporating a chitin backing into the simulation increased peak reflectance by 21.9 % compared to an air backing and narrowed the peak spectra. This could partly explain the function of the thicker, lower part of the ridge which is densely filled with chitin. Additionally, to better represent a real ridge architecture we incorporated a degree of disorder into the system by varying chitin and air thickness by the standard deviation of the mean layer thicknesses from our TEM

measurements. The model was run for 500 simulations (Supplementary Figure 9C) and the statistical average of the resulting matrix was compared to the ideal reflector (Supplementary Figure 9D). Disorder in the system resulted in variation of the peak position but the mean spectra closely matched the ideal system, suggesting the structure is robust in response to minor deviations in layer thicknesses (Supplementary Figure 9D).

Next, we used our model to gain an understanding of how the old diet affected the optical properties of the nanostructure. For simplification, we address the reduction in reflectance and shift in hue observed in the old diet separately.

Reduction in reflectance

If the tilting of the ridges was the primary cause of the reduction in reflectance, we would expect to observe a deviation in the peak angle of reflectance for the old diet. However, both the fresh and the old diet have a closely matched maximum angle of reflectance (Figure 3B). This suggests that the reduction in the number of ridge layers, typically observed as frequent gaps along the second ridge layer (Supplementary Figure 8), is the predominant cause of the reduction in reflectance. Indeed, the plot of the scaled reflectance spectra of the old and fresh diet (Figure 6B) suggests that old diet has somewhere between one and two layers in the reflector. Assuming the fresh diet is an ideal 2 chitin layer system with a chitin backing, the equivalent decrease in the peak reflectance in the measured old diet of 10.4 % (males and females combined) was achieved using a simulation which incorporated a weighted average of 22.5 % one chitin layer to 77.47 % two chitin layers in the reflector. The simulated spectra also maintained the same peak shape despite a lower percentage for 2 chitin layers, similar to what was observed in the measured (scaled) spectra of the fresh and old diet (Figure 6B).

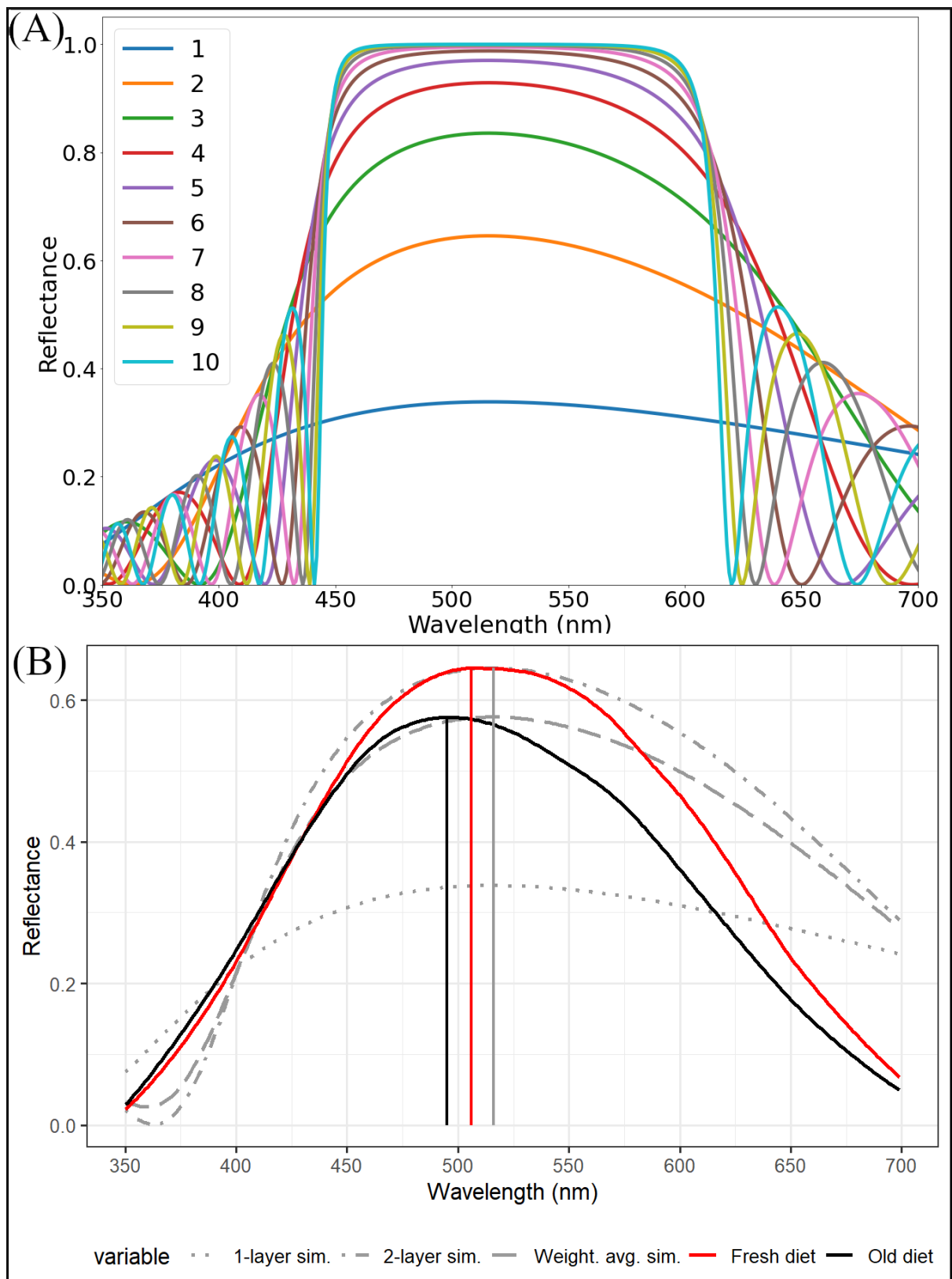


Figure 6. Optical modelling of *H. sara*. Simulated reflectance spectra of a *H. sara* optical multilayer with a stack of alternating 87 nm chitin layers and 122 nm air layers. (A) Reflectance

spectra produced from varying the number of simulated chitin layers between one and ten. (B) Reflectance spectra of the fresh diet (red) and the old diet (black) with the values of % reflectance scaled to the simulated reflectance maximum of two chitin layers (grey, dot-dash line). The grey dotted line shows a simulated one chitin layer. The grey dashed line shows the simulated reflectance spectra of a weighted average of a 77% two chitin layer and 23 % one chitin layer model, replicating the relative decrease in percentage reflectance observed from the old diet treatment. Vertical solid lines indicate the wavelength at maximum reflectance for the fresh diet (red), old diet (black) and all simulated spectra (grey).

Shift in hue to shorter wavelengths

In addition to the reduction in percentage reflectance there was a shift in hue of the old diet towards the shorter, bluer wavelengths (Figure 3A, 6B). Using our ideal 2 chitin layer model we found this reduction in peak wavelength in the old diet can be achieved by decreasing the chitin layer or air layer thickness (or both) (Figure 7; Table 4). This is consistent with the assumption that a poor-quality diet decreases the amount of material available to build the ridges.

To quantify the amount of layer thickness reduction required to produce observable changes in visible colour we simulated the reflected spectrum of an ideal 2 chitin layer multilayer under daylight conditions (D65 illuminant) (Figure 7A). This illumination matched the light source used with the spectrometer to acquire reflectance measurements of the wings. Independently varying the air and chitin thicknesses resulted in significant variation in the peak wavelength and corresponding reflected colour (Table 1). A chitin thickness reduction of just 5 nm was able to replicate the decrease in peak reflectance seen between the measured fresh diet (516 nm) and old diet (496 nm) and produced an observable change in reflected colour.

Simulated chroma levels for the 2 chitin layer ideal model suggest that reduction in chitin and air thicknesses could actually enhance the chroma of the reflected colour (Figure 7B). This corresponds to what we observe in the old diet as the butterflies generally become more ‘bluer’ on the whole and lose the ‘greeny-yellow’ tinge visible in some fresh diet individuals. Inspection of the hue map (Figure 7C) suggests the modelled colour of the *H. sara* would require minimal increase in either air and/or chitin to shift hue towards greeny-yellow. Indeed, in our stock population we often observed the occasional entirely green individual (V.J.L, pers. obs.).

Overall, our optical modelling suggests a relatively small decrease in the number of layers is able to explain the reduction in reflectance for a *H. sara* scale. This agrees with our SEM observations, where frequent gaps are seen in the ridge layers of the old diet individuals. In addition, a shift in hue of the old diet individuals towards bluer wavelengths can be achieved by relatively minor decreases in the chitin or air layer thickness.

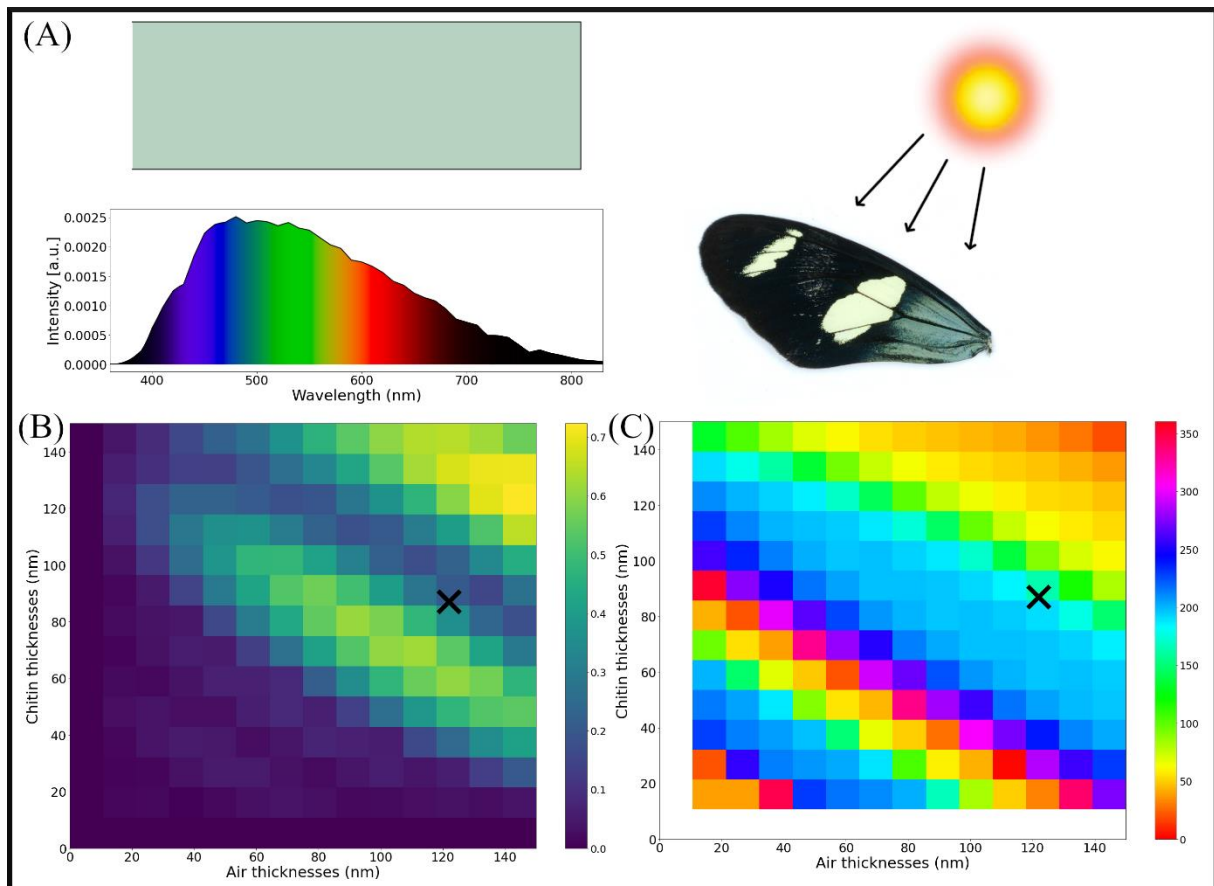











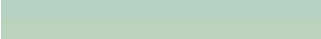





Figure 7. Reflected colour of a simulated *H. sara* multilayer under D65 illuminant (natural sunlight) conditions. (A) Simulated reflected spectrum under D65 illumination. Colour underneath the curve indicates the contribution of each wavelength in the spectra to the overall colour. The brightness of the colours depicted show the degree of sensitivity to the human visual system. Chroma (B) and hue (C) map for the simulated *H. sara* multilayer with varying thicknesses of the chitin layer (y-axis) and air layer (x-axis). In (B) brighter colours indicate greater chroma levels. The black marker on the plots indicates the chitin and air layer thickness measured from the TEM measurements of a stock *H. sara* individual.

Table 4. Peak wavelength (nm) of the simulated reflectance spectra of the 2 chitin layer and 1 chitin layer tmm model when the air and chitin layer thicknesses were varied. Top line (bold) indicates measured values of air and chitin layer thickness from the TEM measurements. The corresponding reflected colour shows the simulated reflectance spectrum as a human-perceived RGB colour under a D65 illuminant.

air spacing (nm)	chitin thickness (nm)	1-layer wavelength (nm)	2-layer wavelength (nm)	Reflected spectra (D65)
122	87	516	516	
122	70	463	463	
122	75	478	478	
122	80	494	494	
122	85	510	509	
122	90	526	525	
122	95	542	541	
122	100	559	557	
105	87	484	483	
110	87	493	492	
115	87	503	502	
120	87	512	512	
125	87	522	522	
130	87	532	531	
135	87	541	541	

Discussion

Here we use dietary stress in larval stages to show that iridescent, structural colour in *Heliconius sara* is a condition dependent trait. The ‘old’ diet resulted in a decrease of the available nitrogen which can be accrued by the larval stages (Figure 1). Nitrogen is a crucial element for protein synthesis and is a limiting resource during insect development (Huberty and Denno, 2006; Mattson, 1980). Crucially, nitrogen is a component of the biopolymer chitin, a major constituent of the insect cuticle, which is harnessed in the production of optical nanostructures (Moussian, 2010).

An extended larval period and decrease in wing (body) size in the old diet implies some level of dietary stress (Figure 2) in the old diet. The old diet resulted in a decrease in brightness

and chroma as well as a shift in hue of the iridescent blue structural colouration, towards shorter bluer wavelengths (Figure 3). Our results indicate the potential of structural colour in *H. sara* to serve as an honest indicator of condition in response to the accumulation of larval food resources. Decreases in hue and brightness of structural colour have been demonstrated in previous dietary stress experiments in *Colias* and *Eurema* butterflies (Fenner et al., 2019; Kemp et al., 2006; Kemp, 2008). In particular, we have shown that males have a greater reduction of brightness and hue compared to females in response to dietary stress, although females showed a slightly bluer colour to begin with.

The sex-dependent response to dietary stress may be the result of selection pressure differences. Female *Heliconius* generally mate soon after emergence, receiving a nutritious spermatophore from males (Jiggins, 2017). If *H. sara* females are the choosier sex, they may use brightness and hue of the iridescent region to select males which will provide the most nutritious spermatophore (Kemp and Rutowski, 2007; Rutowski, 1985). Alternatively, iridescence may be correlated with underlying genetic superiority, with brighter coloured individuals able to withstand environmental stressors, such as reduced host plant availability (White, 2020). This would require a genotype x environment interaction, which could be tested by conducting controlled breeding experiments and tests for heritability (Kemp and Rutowski, 2007).

Sexual dimorphism in peak angle of reflection could support the prediction that iridescence functions in sexual signalling (Figure 3). Sex differences in peak angle may correspond to the angle at which males approach females during courtship. Nevertheless, we cannot disregard the possibility of iridescence being utilised in male-male competition displays, such as in Damselflies (Guillermo-Ferreira et al., 2019). *H. sara* exhibit pupal guarding behaviours (Hernández and Benson, 1998) and in our *H. sara* population we observed guarding males on pupae flash their wings to approaching competitors (V.J.L, pers. obs.). Mate choice

experiments are warranted to decipher whether there is a sexual signalling role of iridescence in *Heliconius*.

Iridescence is a multi-dimensional signal, with colour and intensity being dependent not only on the underlying precise nanostructure but also on the incident light angle and viewing angle. Therefore, iridescence may represent an advantageous signal for conveying information as it can be readily manipulated by the bearer (Doucet and Meadows, 2009; White, 2020). This may be particularly prudent for *Heliconius*, in which aposematic displays are crucial for defending against predators, with selection for mimics to converge on the same visual signal to assist predator learning (Arias et al., 2020; Finkbeiner et al., 2014; Jiggins, 2017). Therefore, iridescence may serve as a multifunctional and controllable visual signal in *Heliconius*, with a potential sexually-selected component, as well as functioning as a warning signal. This controllable aspect of iridescence is seen in other butterfly species. *Hypolimnas bolina* males have forewing UV colour patches and during courtship they position themselves relative to females in such a way which maximises signal transmission. During non-sexual behaviour, such as foraging and travel, the UV signal is less obvious to avian predators (White et al., 2015).

Pigmentary yellow colouration of *H. sara* was robust to dietary stress. Yellow bar hue was not affected by dietary stress, and brightness decreased only in males, but this was not significant. Brightness, but not hue, of the yellow colour was sexually dimorphic, with males having a greater brightness than females at wavelengths above 500 nm (Figure 4). Behaviour experiments in *Heliconius erato* have shown that 3-OHK in the yellow hindwing bar was important for intraspecific signalling (Finkbeiner et al., 2017; Finkbeiner and Briscoe, 2021). Visual modelling suggests the yellow bar may function as a private communication channel, with *H. erato* females able to distinguish yellow colours potentially beyond the perception of avian predators (Dell'Aglio et al., 2018; Finkbeiner and Briscoe, 2021). Together with our

results, this could suggest the yellow wing bar may be used in sexual signalling in *H. sara*. In addition, there was no correlation between the brightness of iridescent colour and yellow pigmentary colour, suggesting these two signalling mechanisms may act independently of each other (Figure 4C). The role of both yellow pigmentary colour and structural blue on sexual signalling presents an interesting future question.

Pigments synthesised *de novo* are predicted to show heightened condition dependence (McGraw and Hill, 2000; Weaver et al., 2018) and so the finding that structural colour was more affected by dietary stress than pigmentary colour was unexpected. 3-OHK pigment is synthesised in fat bodies before transport to wing scales in the late stages of their development (Reed et al, 2008). The pigment constituents are attained entirely from diet and are converted through biochemical pathways before being able to produce their signal. Selective forces are therefore able to efficiently link diet, metabolic processes and signal strength (White, 2020). This mechanistic link has been well documented in the red carotenoid colouration of birds (Simons et al., 2012; Weaver et al., 2018). Conversely, the ordered, periodic nanostructures underlying *H. sara* structural colour are hypothesised to form through self-organising processes such as cuticle buckling in response to actin generated forces (Ghiradella, 1974). Therefore, we would expect structural colour to be more dependent on other developmental conditions, such as temperature during pupation, rather than larval diet.

A potential explanation for the heightened sensitivity of *H. sara* structural colour to dietary stress relates to the precise nature of optical nanostructure formation. Iridescence is produced by highly-ordered, coherent photonic systems (Burg and Parnell, 2018; Prum et al., 2006). The level of spatial organisation is greater than that of other photonic regimes such as quasi-ordered systems and disordered photonic systems (incoherent scattering) (Doucet and Meadows, 2009; Mouchet et al., 2020; Prum et al., 2006). Therefore, signal expression may be particularly sensitive to trade-offs which occur at the physiological level, small perturbations / alterations

in the optical parameters, such as ridge layering distance, would generate discernible optical differences in the macro-level signal expression. This sets up the premise for such signals to indicate genetic quality if there is heritable variation in the ability to achieve the higher-level ordering, through behaviour-mediated attainment of developmental stability as well as physiological constraints (White, 2020). Indeed, a meta-analysis by White et al., (2020) found stronger condition dependence amongst iridescent structural colours than non-iridescent structural colours.

Hill (2011) emphasised the importance of moving beyond defining a trait as condition dependent based simply on a positive association between expression and a measured quality. Instead, emphasis should be placed on understanding the mechanistic link between underlying cellular process and developmental pathways and trait expression (Hill, 2011). Our interrogation of the wing scales using electron microscopy permitted quantification of the impact of dietary stress on reflective properties. Dietary stress resulted in alteration of the ridge layering process, with loss of ridge layers observed in the old diet (Supplementary Figure 8). In addition, we noted that for some old diet individuals the scales had tilted ridge layers, creating numerous ridge termination points (Figure 5). Increased ridge termination following dietary stress was also observed in dietary stressed *Colias eurytheme* butterflies, whose UV structural colour is also produced by ridge multilayers (Kemp, 2008). This suggests that dietary stress effects a conserved developmental process during ridge multilayer production in both species. Whether this is due to an upstream effect of scale specification or a direct effect on the actual process of layer formation (e.g., chitin synthase localisation) remains unknown.

Optical modelling was used to link the microscopic observations of scale nanostructure alterations with the underlying optical physics which governs structural colour production. The observed gaps in the ridge layers effectively reduced the number of layers in the multilayer reflector. Simulated models of this had a notable decrease in reflectance, consistent with our

reflectance spectrometry measurements (Figure 6). The reduction in hue between the old and fresh diet was simulated through a decrease in the chitin layer thickness of around 5 nm (Figure 7). This demonstrates how even small deviations in microstructural organisation can have profound consequences on macro-level expression; lending support to the idea that iridescence may function as an indicator of individual quality, based on the underlying precision required to attain the maximal signal (White, 2020). Further TEM images of individuals from the old and fresh diet are needed to understand whether there is reduction in air or chitin layer thickness, or indeed both, as a result of dietary stress. Interestingly, similar decreases in hue towards shorter wavelengths in response to diet manipulation occur in other butterflies which possess multilayer reflectors (Fenner et al., 2019) as well as in thin-film nanostructures (Pegram et al., 2013). This could suggest that a common response to dietary stress across all butterfly nanostructure types is to reduce the chitin layer thickness, perhaps as a result of an underlying resource trade-off between building larger nanostructures and other crucial physiological functions.

To conclude, dietary stress in *Heliconius sara* resulted in a decrease in the percentage reflectance as well as a shift in hue of the blue iridescent colour, showing that the development of these colours is sensitive to the resources accumulated during the larval stage. Conversely, there was minimal effect of dietary stress on the pigmentary yellow colouration. The condition dependence and sexual dimorphism of iridescence hints at a potential role of iridescence as a sexually-selected signal in *Heliconius*. Determining this requires further behavioural experiments looking at mate preference for wings which vary in aspects of their reflected colour, namely hue, brightness and chroma.

Acknowledgements

General

We extend our thanks to Alan Dunbar (Department of Chemical Engineering, University of Sheffield) for access to the scanning electron microscope (machine funded via the EPSRC 4CU grant no. EP/K001329/1). We also thank Frane Babarović (School of Biosciences, University of Sheffield) and Chris Hill (Electron Microscopy Facility, University of Sheffield) for performing the TEM on the butterfly wings. I also thank Patricio A. Salazar Carrión (School of Biosciences, University of Sheffield) for his assistance in the statistical modelling. Finally, I thank Melanie Brien (Department of Biological & Environmental Sciences, University of Helsinki) for her comments on the manuscript.

Funding

This research was supported by the following grants: Natural Environment Research Council (NERC) Fellowship to N.J.N (NE/K008498/1). This work was also funded from through a NERC doctoral training partnership (Adapting to the Challenges of a Changing Environment) (V.J.L).

Author contributions

Specific contributions of authors are detailed at the start of the chapter.

Supplementary Tables, Figures and Information

Supplementary Table 1. Mean \pm SE percentage area of blue, black and yellow on the forewing of *H. sara* fed an old and a fresh diet. All individuals and the two separate experimental batches are shown.

	Colour element	Mean % \pm SE 'fresh'	Mean % \pm SE 'old'	χ^2	df	p-value
all individuals	blue	9.64 \pm 0.37	9.78 \pm 0.41	0.00477	1, 85	0.718
	black	77.43 \pm 0.48	76.60 \pm 0.52	0.00248	1, 85	0.159
	yellow	12.93 \pm 0.16	13.62 \pm 0.19	0.05736	1, 85	0.003
batch 1	blue	11.54 \pm 0.58	11.52 \pm 0.45	0.00005	1, 39	0.972
	black	75.28 \pm 0.80	74.89 \pm 0.62	0.00028	1, 39	0.695
	yellow	13.18 \pm 0.26	13.60 \pm 0.24	0.00991	1, 39	0.221
batch 2	blue	8.33 \pm 0.31	7.82 \pm 0.30	0.04275	1, 44	0.264
	black	78.00 \pm 0.43	78.64 \pm 0.53	0.00022	1, 44	0.599
	yellow	12.67 \pm 0.19	13.53 \pm 0.31	0.04734	1, 44	0.009

Supplementary Table 2. Mean \pm SE values and statistical results of the selected colourimetric variables describing the iridescent properties of the fresh and old diet treatments at angle of maximum reflectance, separated by sex and experimental batch.

	Colourimetric variable	Mean \pm SE 'fresh'	Mean \pm SE 'old'	t-ratio	df	p-value
Females	B1	2220 \pm 95	2011 \pm 118	1.22	81	0.614
	B3	10.7 \pm 0.44	9.78 \pm 0.55	1.19	81	0.638
	S1B	0.418 \pm 0.012	0.444 \pm 0.012	-1.62	81	0.376
	S1G	0.393 \pm 0.008	0.376 \pm 0.009	-1.63	81	0.366
	S6	10.7 \pm 0.438	9.77 \pm 0.548	1.184	81	0.6388
	S8	1.69 \pm 0.011	1.71 \pm 0.022	-0.88	81	0.815
	H1	505 \pm 4.88	494 \pm 4.62	1.63	81	0.366
Males	B1	2244 \pm 133	1916 \pm 112	2.88	81	0.026
	B3	10.6 \pm 0.622	9.15 \pm 0.500	2.88	81	0.025
	S1B	0.392 \pm 0.010	0.431 \pm 0.010	-2.56	81	0.059
	S1G	0.406 \pm 0.004	0.380 \pm 0.006	-2.71	81	0.040
	S6	10.6 \pm 0.622	9.14 \pm 0.500	2.886	81	0.0252
	S8	1.66 \pm 0.008	1.68 \pm 0.013	-1.08	81	0.702
	H1	516 \pm 4.80	497 \pm 3.63	2.91	81	0.024
batch 1	B1	2423 \pm 112	2199 \pm 96.400	1.24	81	0.607
	B3	11.6 \pm 0.519	10.5 \pm 0.437	1.26	81	0.591
	S1B	0.402 \pm 0.012	0.435 \pm 0.010	-2.22	81	0.126
	S1G	0.406 \pm 0.006	0.379 \pm 0.007	-2.69	81	0.042
	S6	11.6 \pm 0.519	10.5 \pm 0.436	1.264	81	0.5882
	S8	1.68 \pm 0.0109	1.68 \pm 0.0171	-0.39	81	0.981
	H1	512 \pm 5.49	496 \pm 3.74	2.52	81	0.065

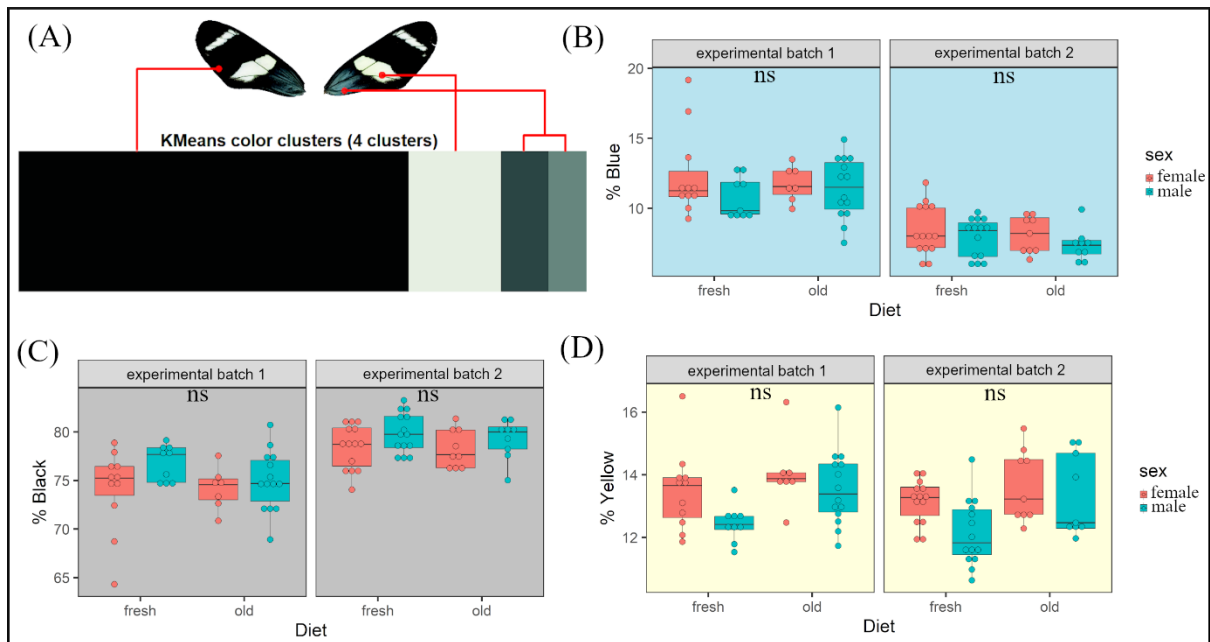
Colourimetric						
	variable	Mean±SE 'fresh'	Mean±SE 'old'	t-ratio	df	p-value
batch 2	B1	2095 ± 105	1670 ± 101	2.85	81	0.028
	B3	9.99 ± 0.484	8.09 ± 0.460	2.79	81	0.033
	S1B	0.408 ± 0.011	0.438 ± 0.012	-1.91	81	0.233
	S1G	0.395 ± 0.007	0.379 ± 0.008	-1.58	81	0.394
	S6	9.98 ± 0.484	8.08 ± 0.460	2.784	81	0.0332
	S8	1.67 ± 0.009	1.70 ± 0.016	-1.60	81	0.384
	H1	509 ± 4.55	496 ± 4.41	1.96	81	0.210

Supplementary Table 3. Mean ±SE reflected intensity for the iridescent region of fresh and old diets across the entire range of angles measured.

Angle (°)	Mean Intensity ±SE 'fresh'	Mean Intensity ±SE 'old'	F	df	p-value
0	7.49 ± 0.404	6.16 ± 0.509	4.38	1, 84	0.039
2	8.64 ± 0.395	7.33 ± 0.455	4.95	1, 84	0.029
4	9.32 ± 0.368	8.29 ± 0.402	3.59	1, 84	0.062
6	9.17 ± 0.366	8.29 ± 0.399	2.66	1, 84	0.107
8	8.55 ± 0.391	7.76 ± 0.406	2.06	1, 84	0.155
10	6.97 ± 0.384	6.09 ± 0.367	2.84	1, 84	0.095
12	5.75 ± 0.412	4.61 ± 0.354	4.28	1, 84	0.042
14	4.76± 0.422	3.53 ± 0.367	4.64	1, 84	0.034
16	3.85± 0.417	2.52 ± 0.313	6.03	1, 84	0.016
18	2.86± 0.369	1.76 ± 0.261	5.42	1, 84	0.022
20	2.04± 0.291	1.18 ± 0.170	5.84	1, 8	0.018

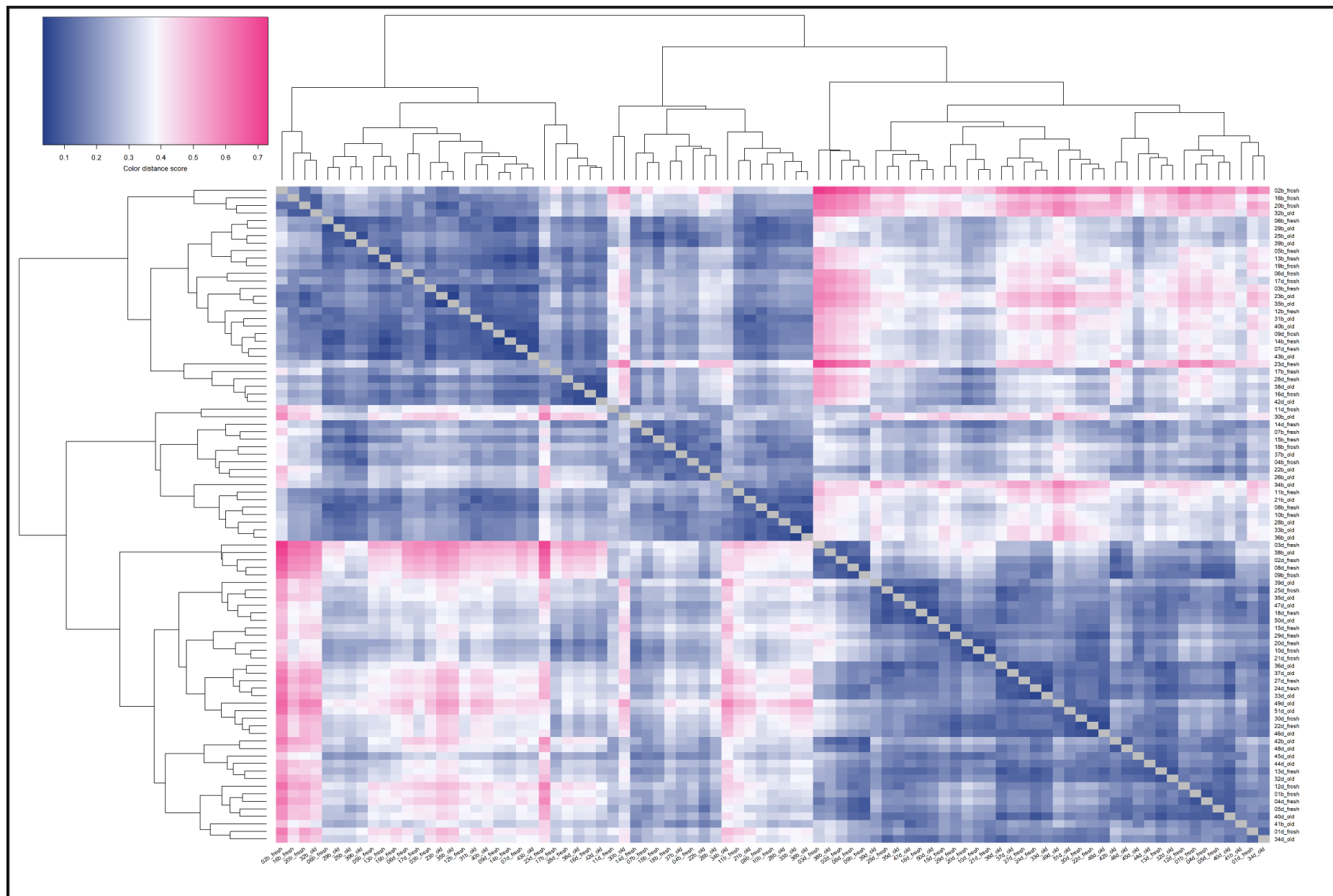
Supplementary Table 4. Mean ±SE reflected hue for the iridescent region of fresh and old diets across the entire range of angles measured.

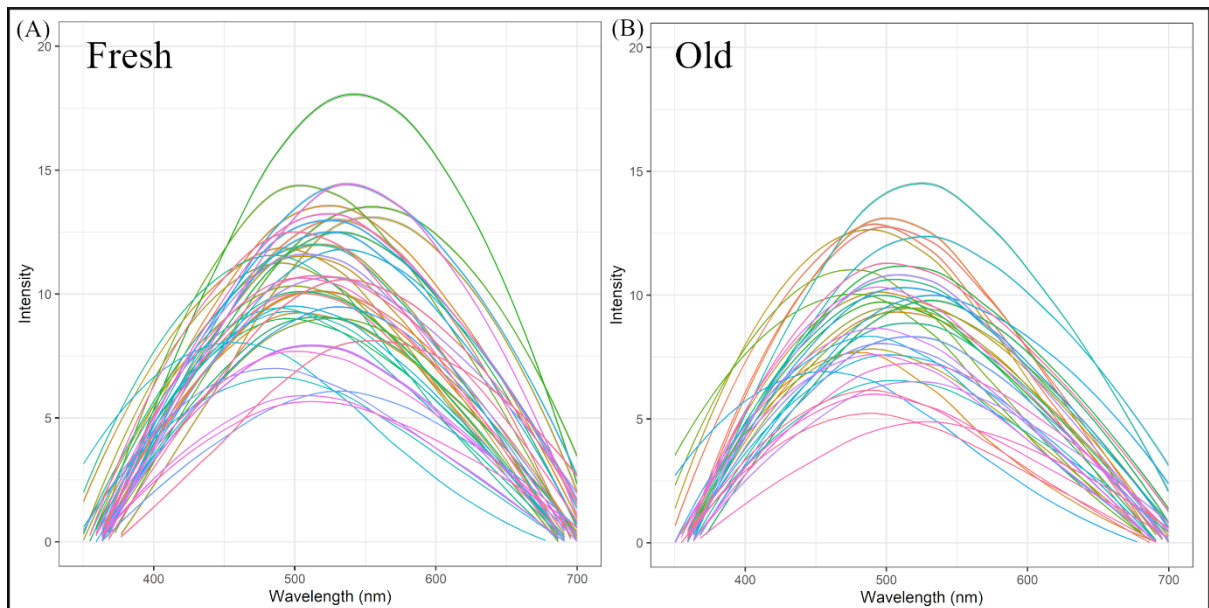
Angle (°)	Mean Hue ±SE 'fresh'	Mean Hue ±SE 'old'	F	df	p-value
0	507 ± 4	490 ± 3	12.66	1, 84	0.001
2	508 ± 4	492 ± 3	11.86	1, 84	0.001
4	510 ± 4	494 ± 3	11.31	1, 84	0.001
6	511 ± 4	496 ± 3	9.54	1, 84	0.003
8	510 ± 3	499 ± 3	7.00	1, 84	0.010
10	512 ± 3	499 ± 3	7.17	1, 84	0.009
12	509 ± 3	499 ± 3	6.27	1, 84	0.014
14	509 ± 3	497 ± 3	7.62	1, 84	0.007
16	507 ± 3	498 ± 4	3.78	1, 84	0.055
18	499 ± 4	490 ± 3	3.34	1, 84	0.071
20	504 ± 4	488 ± 6	4.38	1, 84	0.039



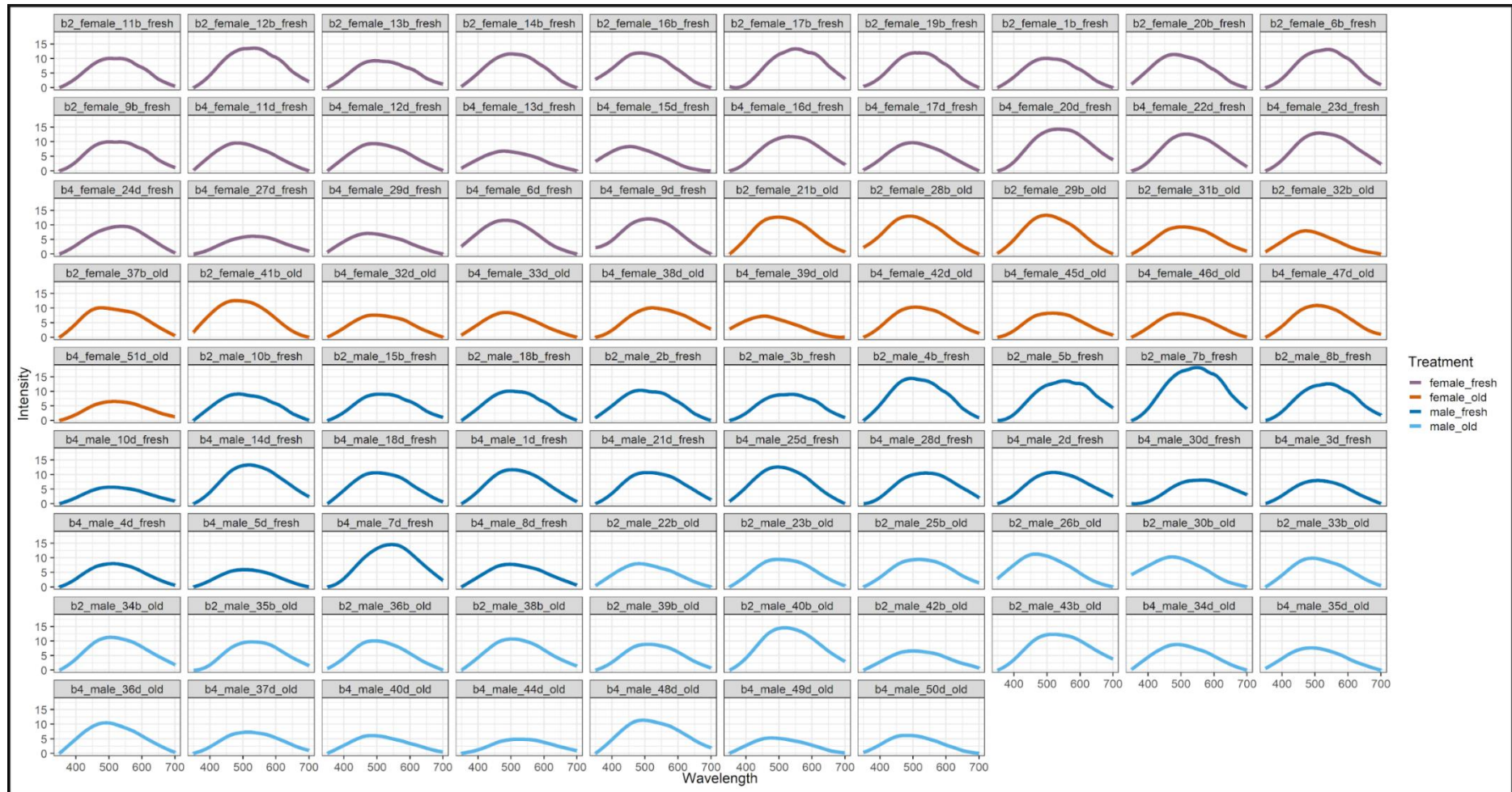
Supplementary Figure 1. Percentage area of black, blue and yellow on old diet and fresh diet adult wings. (A) K-means clustering of colour pixels on the wings of *Heliconius sara*. The two green/blue bins were combined to give an overall representation of total blue (iridescent) area. Percentage of blue (B), black (C) and yellow (D) on wings for the different diets and sexes, separated by experimental batch.

Supplementary Figure 2 (next page). Heatmap of colour distances between all individuals in the both the fresh and the old diet. Overall individuals do not cluster entirely based on their diet.

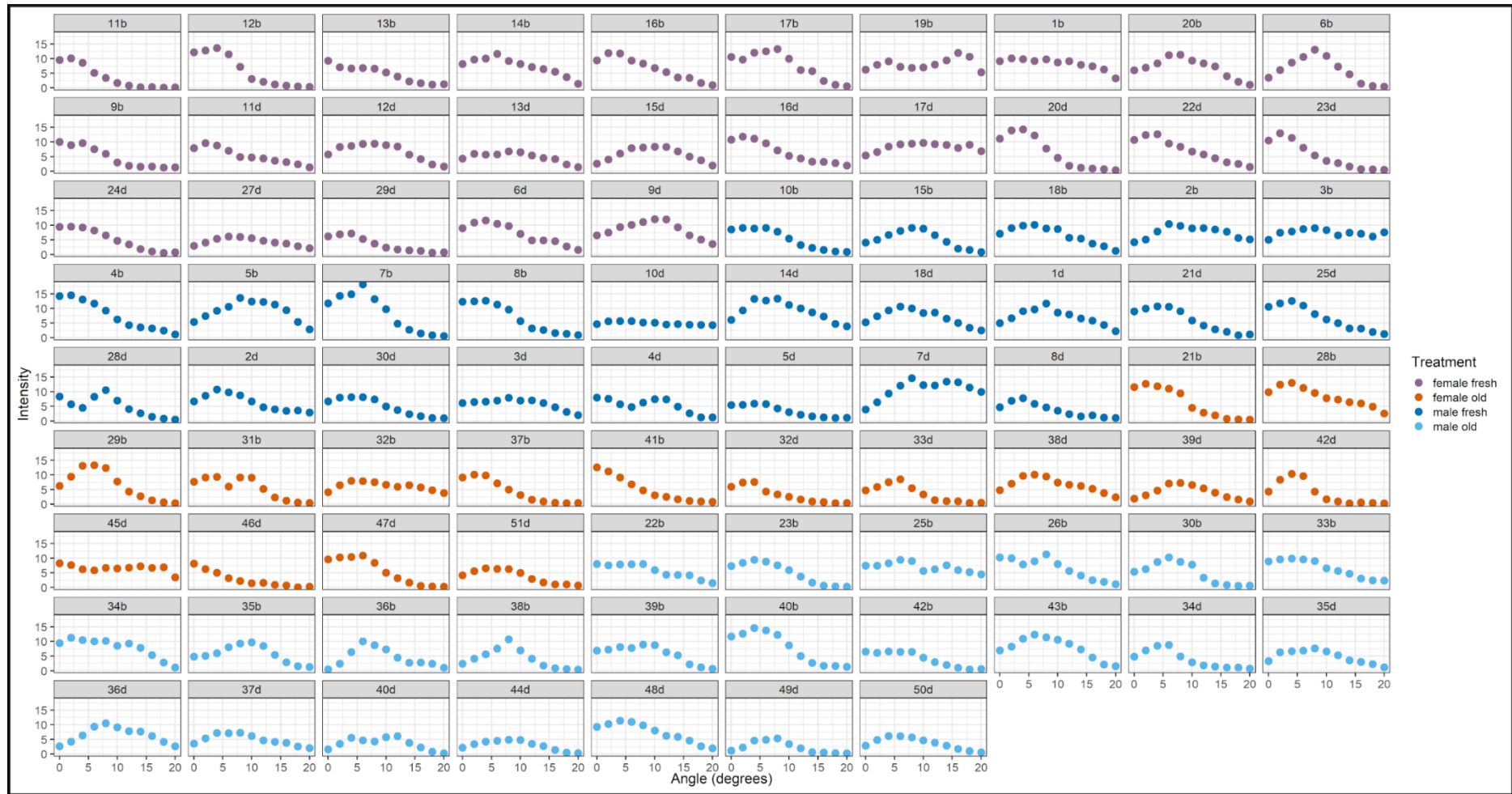




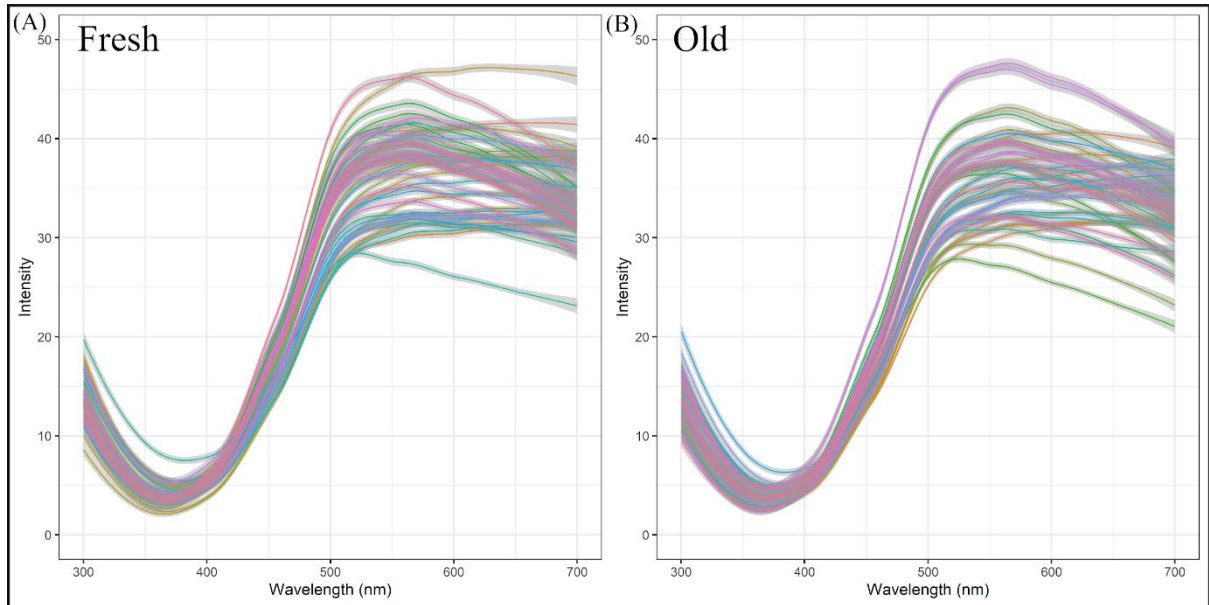
Supplementary Figure 3. Intensity at the angle of peak reflection (B3) for the iridescent blue region between 350 nm and 700 nm, for all individuals fed the fresh diet (A) and old diet (B).



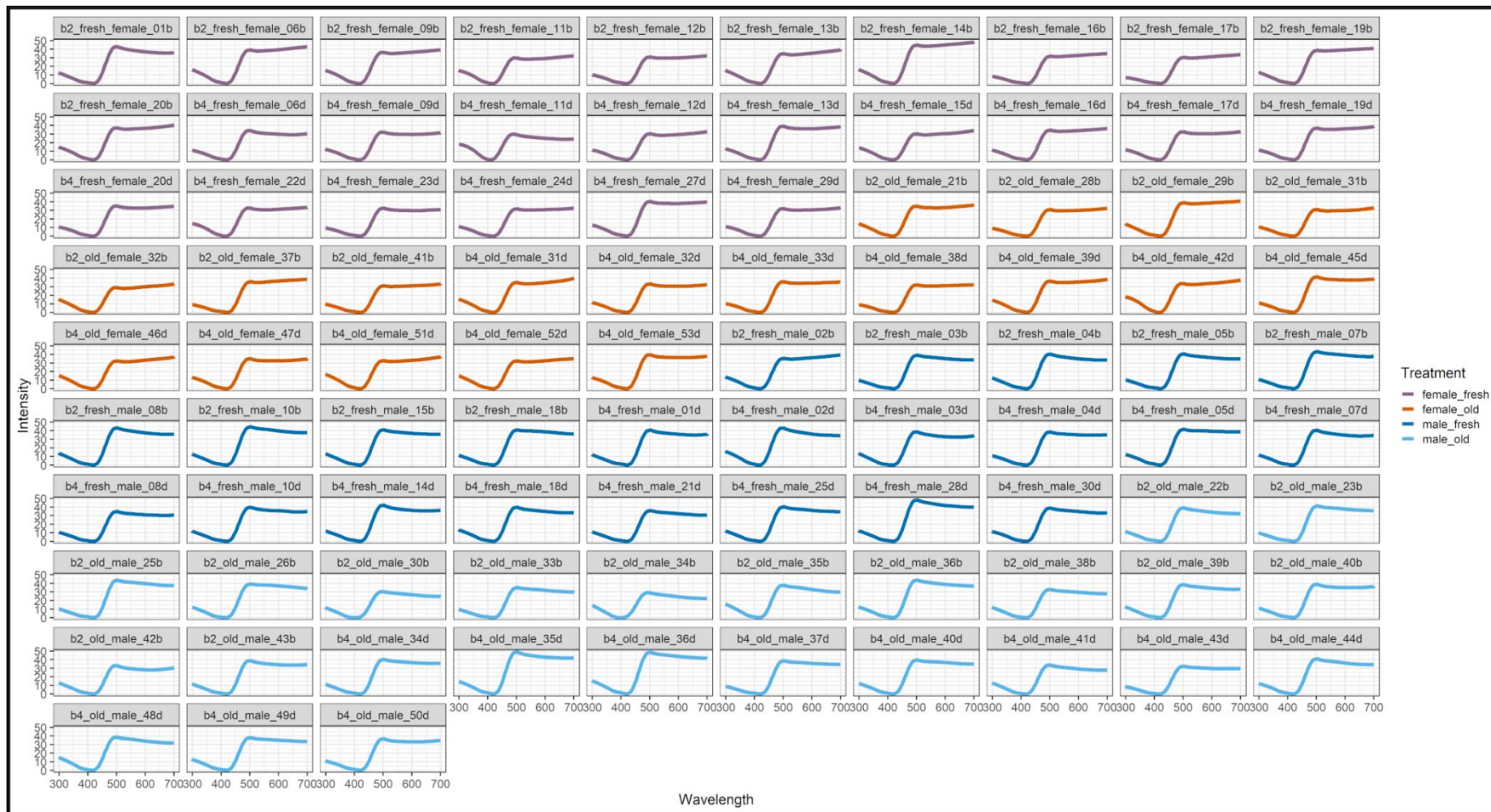
Supplementary Figure 4. Reflected intensity [a.u.] and wavelength (nm) of the blue iridescent region for all individuals measured in the experiment. Colour indicates grouping based on sex and diet.



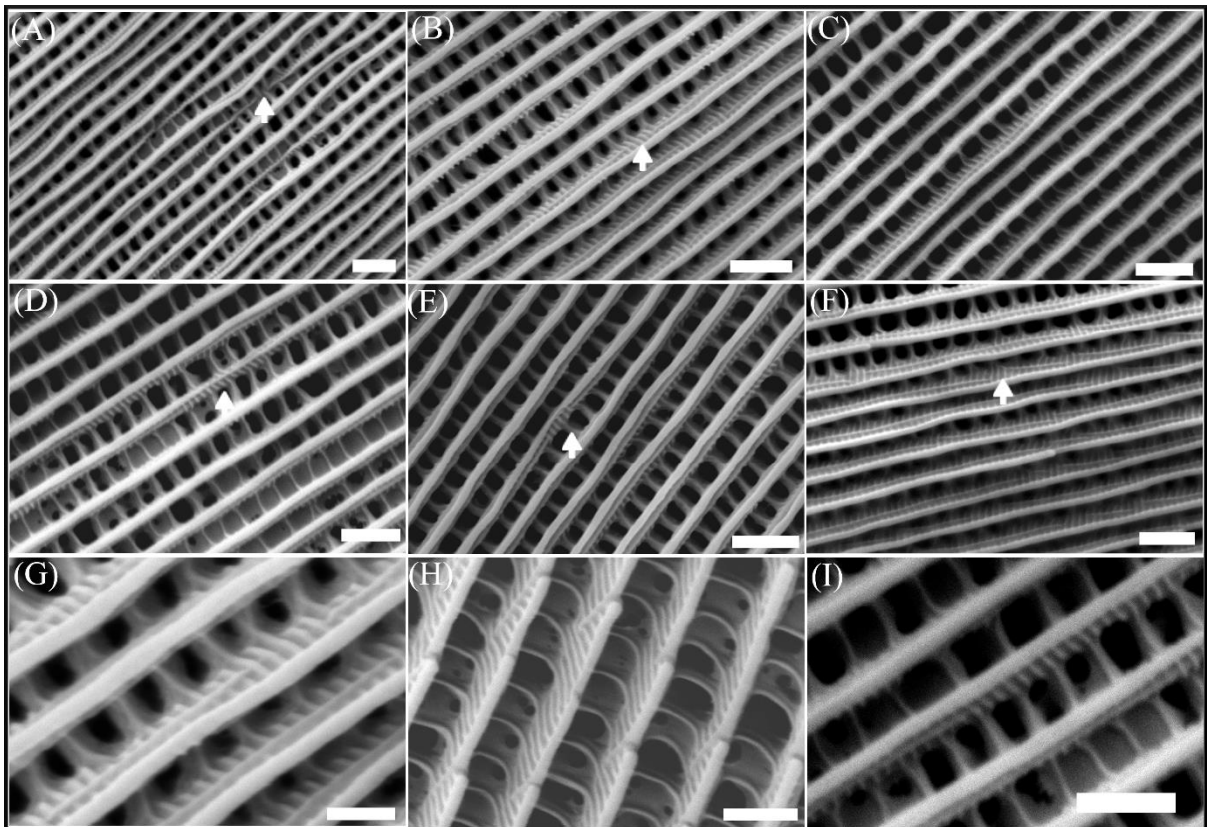
Supplementary Figure 5. Reflected intensity [a.u.] of the blue iridescent region at each of the measured angles, between 0 and 20 degrees, for all individuals measured in the experiment. Colour indicates grouping based on sex and diet.



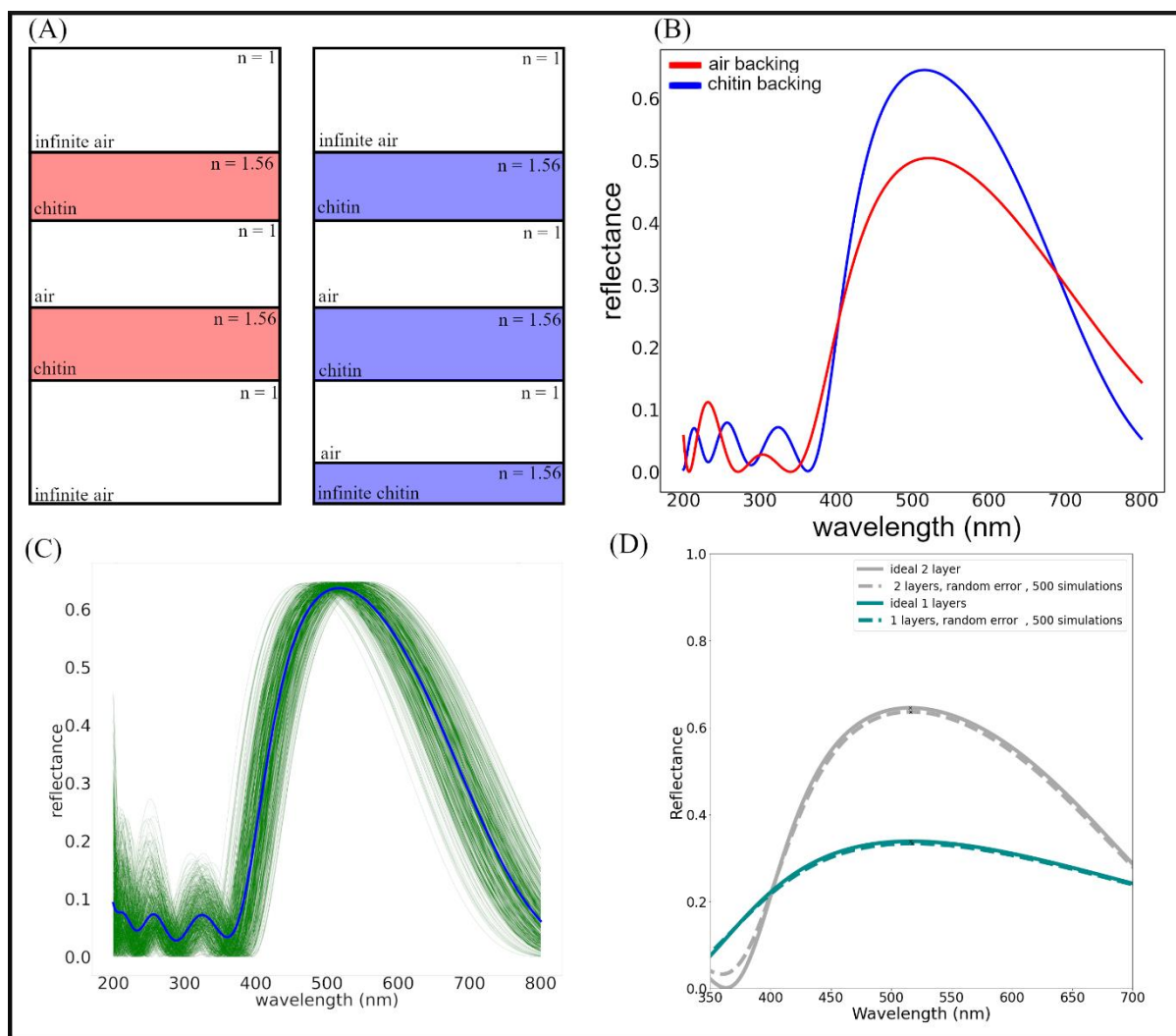
Supplementary Figure 6. Intensity at the angle of peak reflection (B3) for the yellow wing bar between 300 nm and 700 nm, for all individuals fed the fresh diet (A) and old diet (B).



Supplementary Figure 7. Reflected intensity [a.u.] at peak angle of the reflection (B3) for the yellow wing bar between 300 and 700 nm for all individuals measured in the experiment. Colour indicates grouping of sex and diet.



Supplementary figure 8. Examples of the various disruptions to ridge layering observed in specimens fed the old diet. (A) Complete loss of large portions of the ridge (white arrow), this was more frequently observed in the scales of the individuals fed the old diet. (B) The most common disruption to the ridges in the old diet were gaps in the second ridge layer (white arrow). The uppermost ridge layer and ridge height remained unaffected despite the loss of this second layer. (C) Narrowing and non-uniformity of the uppermost ridge layer. (D) More extreme example of ridge gaps, with large portions of the second layer missing for numerous ridges. In some cases, the uppermost layer has also been disrupted (white arrow). (E) Gap in the ridge layering which has been filled by the enlargement of the microribs (white arrow). (F) Numerous small gaps in the second layer are accompanied by deviation of the layer away from the parallel plane. (G) Enlarged view of a ridge gap along the second ridge layer. (H) The second ridge layer is completely absent from all the ridges in the scale. The uppermost layer is curved creating numerous termination points along the ridge. (G) Enlarged view of a larger ridge gap, the actual ridge height remains unaffected. Scale bars = 1 μm .



Supplementary Figure 9. Refining the tmm model. (A) Two possible models of a 2 chitin layer *H. sara* multilayer reflector. Red model (left) represents the most-simplified model with an infinite air backing (floating nanostructure). Blue model (right) incorporates a chitin infinite backing onto the nanostructure to represent the lower-most section of the ridge and underlying scale features. (B) Simulated reflectance spectra between 200 – 800 nm of the simplified, air-backed (red) and chitin-backed (blue) models described in (A). (C) Simulated reflectance spectra of a 2 chitin layer model (with chitin backing) which incorporates a degree of disorder into the system by varying d_a and d_b by the standard deviation of the mean, calculated from the TEM analysis. Green lines indicate simulation runs; blue line is the calculated average of all the simulations. (D) Modelled reflectance of the ideal multilayer (solid lines) with 2- (green) and 1- (grey) layers and calculated average of the simulated disordered multilayers (dashed lines) from (C).

Supplementary information: Thin-film interference, multilayers and simulating the optical properties of *Heliconius sara*.

The prevalence of thin-films as a means of structural colour production in nature is due to their relative simplicity of construction, requiring a thin layer surrounded by two media with contrasting refractive indices (Burg, 2018; Thayer et al., 2020). Thin-films create the optical phenomenon known as thin-film interference and this is demonstrated schematically in Supplementary figure 10. Incident light waves (black arrows) hit the thin film layer (red), of thickness d , at the angle θ_a . At the top interface of the thin film there is a partial reflection and refraction of light. A portion of light is refracted at angle θ_b and continues to propagate through the material before hitting the lowermost interface where it is refracted and reflected. The refracted light leaves the structure and is of no further consideration. However, the portion of light reflected will travel back towards the top interface, where again it is refracted and reflected. As the refracted portion of light exits the top layer it can encounter the first reflected wave and interfere through superposition (Burg, 2018; Burg and Parnell, 2018; Sun et al., 2013).

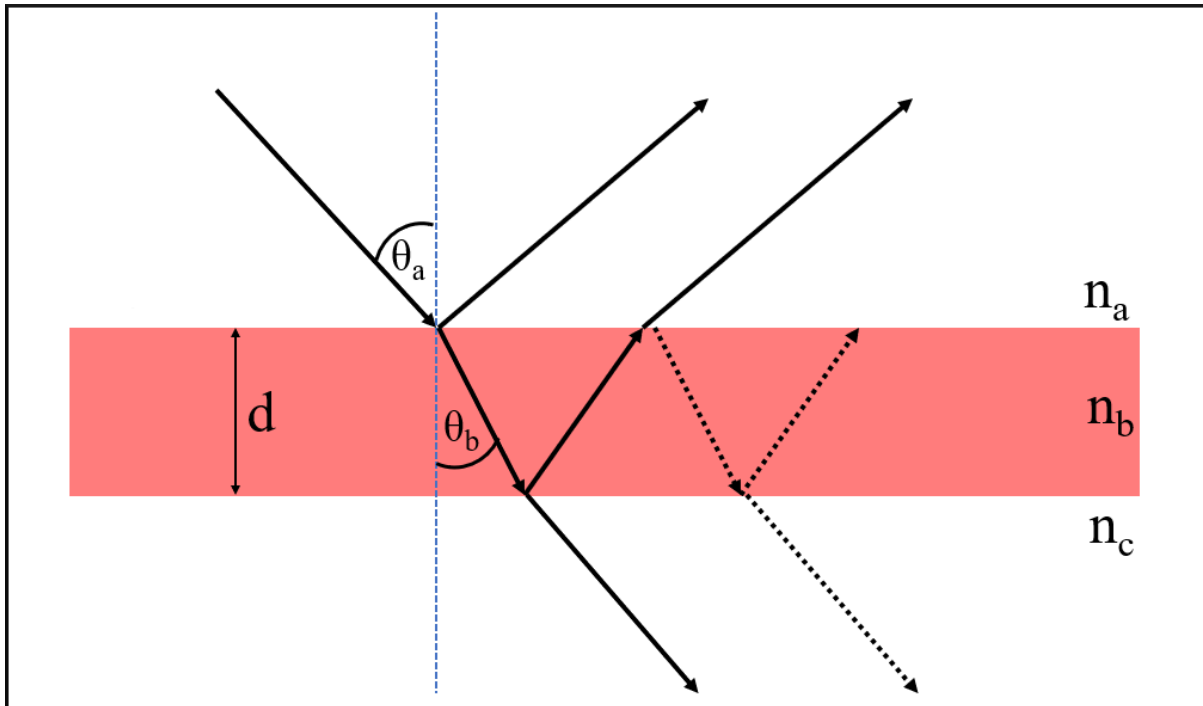
The light wave will gain an optical path difference (OPD) during its propagation through the film, relating to the film thickness (d), refractive index n_b , and the angle of internal reflection θ_b . The OPD between the first and second reflected wave from the top layer of the film is given by Equation S1 (equations from (Burg, 2018)).

$$OPD = 2n_b d \cos\theta_b \quad (S1)$$

$$2n_b d \cos\theta_b = \left(m - \frac{1}{2}\right)\lambda \quad (S2)$$

$$2n_b d \cos\theta_b = m\lambda \quad (S3)$$

$$m = 0, 1, 2, 3 \dots \text{ (integer value)}$$

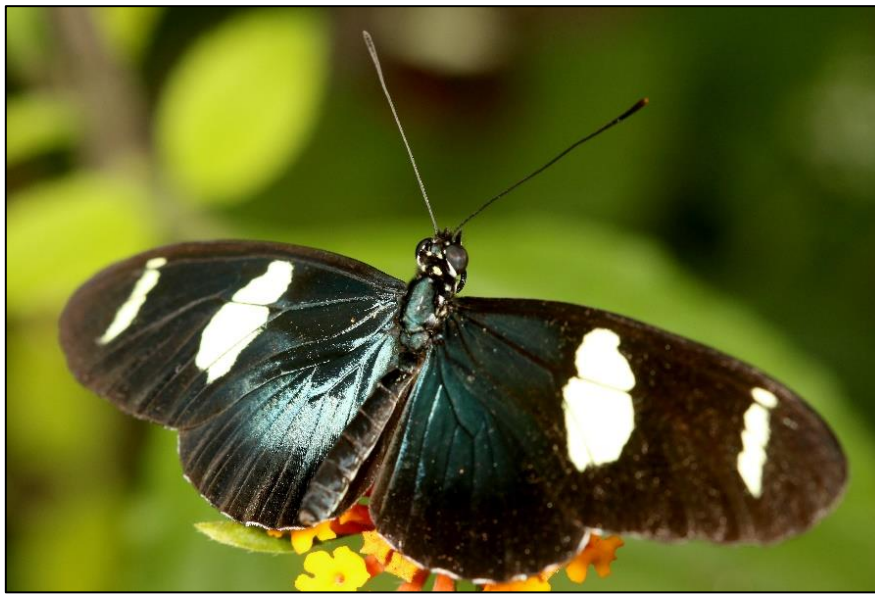


Supplementary Figure 10. Schematic showing the principles of thin-film interference.

Light waves (black arrows) undergoing reflection and refraction at the interfaces with different refractive indices (n_a and n_b). The reflected light at the different interfaces result in an interference pattern and a peak in the reflectance pattern which is effected by layer thickness, refractive index contrast and number of layers. Redrawn from Sun et al., (2013) and Burg, (2018).

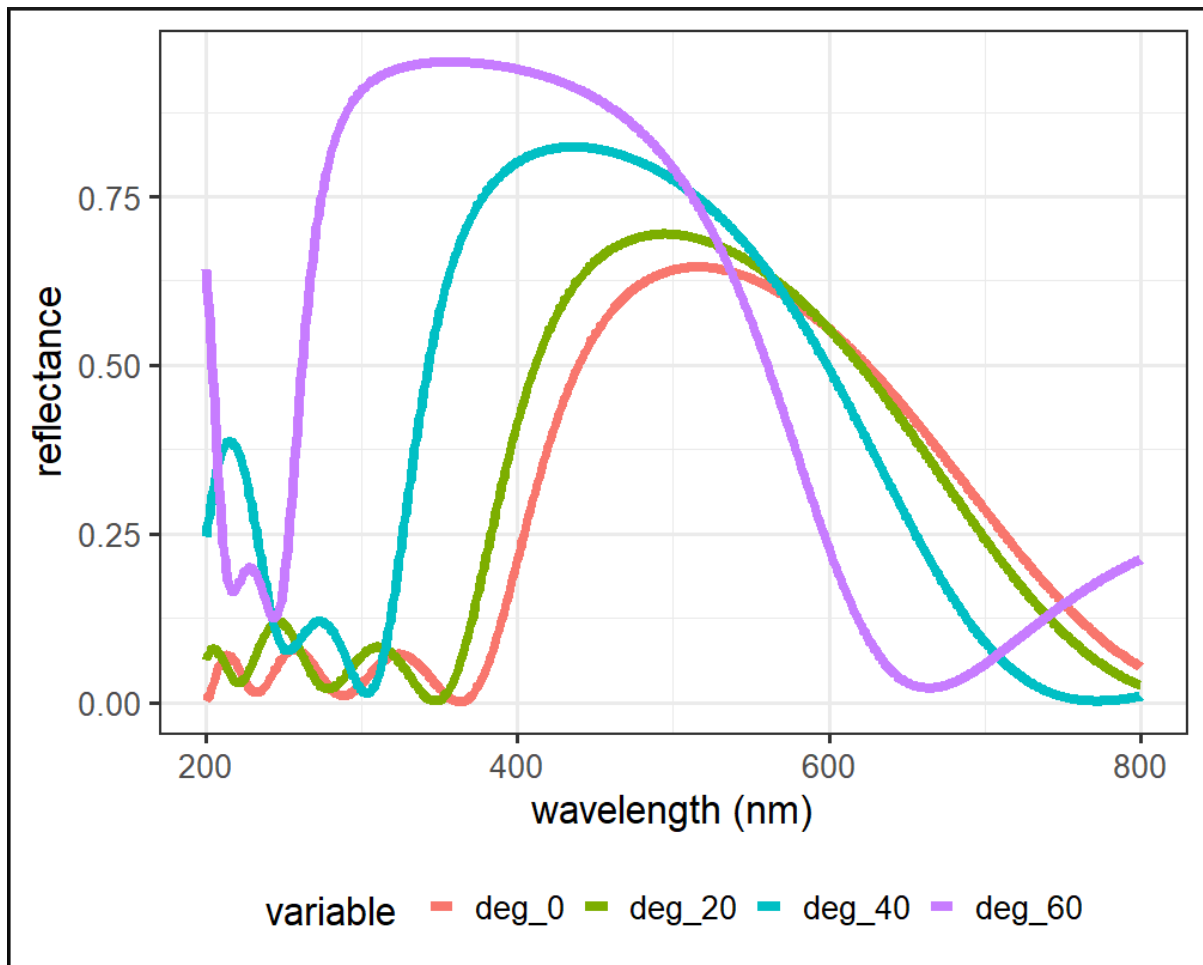
For constructive interference to occur the OPD must be comparable to some integer number multiplied by the wavelength of incident light. The integer is typically given by m . When the refractive index the final layer below the film is smaller than that of the film ($n_c < n_b$), so that there is no phase shift, then constructive interference can occur if the conditions of Equation (S2) are satisfied (Burg, 2018; Kinoshita, 2008). Conversely, if the refractive index is lower in the final layer than the second layer so that ($n_c > n_b$), then there is overall no phase shift, so that constructive interference will occur if Equation 3 is satisfied (Burg, 2018; Kinoshita, 2008; Mouchet and Vukusic, 2018).

A notable aspect of thin film interference is that the reflection is wavelength dependent, and varies with incident angle of the light (and observation angle) (Mouchet and Vukusic, 2018; Prum et al., 2006). Such a property is known as iridescence and is observed in *H. sara* as a dark blue/green colour of the wing at increasing angles away from the normal (Supplementary Figure 11) (Kinoshita, 2008). Simulations of how incident angle shifts the reflected hue of *H. sara* towards the blue wavelengths are shown in Supplementary Figure 12.



Supplementary Figure 11. Female *H. sara* feeding from a Lantana flower. Iridescent properties of the wings are visible as variations in the reflected intensity depending on the angle of the wing region to the overhead light source. Photo credit: Paul Richards.

Selection forces can drive enhancement of visual signals if it confers a reproductive or survival advantage to the bearers (Andersson and Iwasa, 1996; Doucet and Meadows, 2009). In terms of structural colours, an enhanced signal can be achieved by an increase in the total reflectance. This can be generated by increasing the refractive index contrast between the alternating layers (Burg, 2018). However, natural systems are limited by the available biopolymers to construct their optical nanostructures (typically cellulose, chitin, keratin).



Supplementary Figure 12. Plotted reflectance spectra for a 2 chitin layer *H. sara* multilayer as the angle of incidence is varied between 0 and 60 degrees. Redrawn from (Burg, 2018).

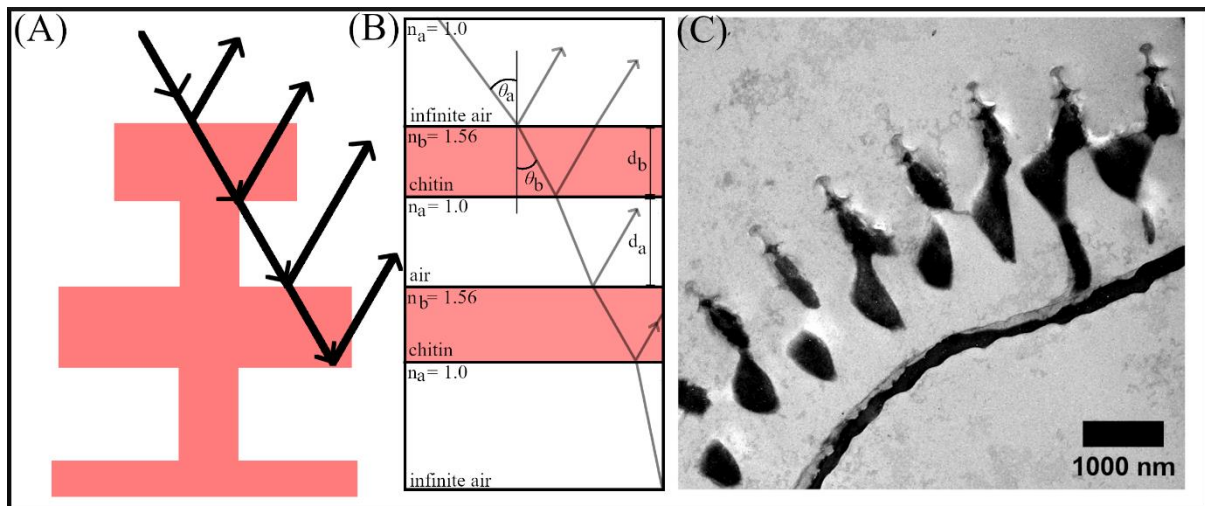
In the case of Lepidoptera, as in all insects, this material is chitin which has a refractive index of 1.56 (Kinoshita, 2008). Therefore, to increase the reflectance thin-films can be stacked on top of each other to create a series of alternating layers, termed a multilayer reflector, and if certain conditions of interference are met they can be deemed a Bragg mirror (Burg, 2018). The multilayer reflector extends the physical principles described above for thin-films.

Supplementary Figure 13B shows a schematic representation of the multilayer found in *H. sara*, consisting of alternating layers of chitin (thickness d_b) and air (thickness d_a). The reflector is essentially floating in space with infinite air layers found at the entry and exit points of light.

The total reflectance of the nanostructure can be understood from the interfering light waves from the top layer of chitin. In this case the OPD is the sum of the OPD from each reflecting layer and constructive interference will occur when the conditions of Equation S4 are satisfied. Equations from (Burg, 2018).

$$2(2n_a d_a \cos\theta_a + 2n_b d_b \cos\theta_b) = m\lambda \quad (\text{S4})$$

$$m = 0, 1, 2, 3 \dots (\text{integer})$$



Supplementary Figure 13. Tmm modelling of the multilayer reflector in *H. sara*. (A) A schematic representation of a *H. sara* multilayer reflector with two chitin layers. At the interface of each boundary of air and chitin the incident light is partially reflected and refracted. The resulting interference effect of the reflected light waves is responsible for the structural colour and iridescence. (B) The most simplified model of the nanostructure in (A) represents an ideal multilayer system. Black arrows denote the path of a light wave as it propagates through the structure with a chitin layer thickness (d_b) and air layer thickness (d_a). The refractive indices of air (n_a) and chitin (n_b) are shown in the plot. (C) TEM image of a transverse

section through an iridescent scale from a wildtype *H. sara*. The layers of the optical nanostructure are visible on the ridges.

Mathematical complexity arises due to the many reflections/refractions of light at each interface in the structure, in addition to the numerous layers which some butterfly optical nanostructures can possess (e.g. *Morpho* (Kinoshita et al., 2002)) (Burg, 2018; Byrnes, 2021; Kinoshita, 2008). Numerous software programs have been developed to overcome this complexity. In all our examples we use the ‘tmm’ Python package (written by Steven Byrnes) which implements the transfer matrix method to simulate the optical properties of stacks. Deriving the equations harnessed in this package is beyond the scope of this section, for full calculations see (Byrnes, 2021). Briefly, the package harnesses Fresnel’s equations for the reflection and transmission of light as well as formulations of the transfer matrix method to overcome the complexity of the multiple interfaces, whilst also taking into account the polarisation of light. In all cases, we performed the simulations using the coherent transfer matrix method, with a ‘s’ light polarisation (electric field orientation normal to the plane). The angle of incident light was maintained at normal (0 degrees). An assumption of flat planar surfaces which are laterally infinite can be achieved by treating the ‘Christmas tree’ nanostructures of *H. sara* as a series of rectangular slabs. This ignores some aspects of the real nanostructure, particularly the central supporting column of chitin and the microribs, which align vertically between the layers, and any surface roughness. However, it allows a complex three-dimensional structure to be optically understood from relatively few mathematical equations.

Chapter 6

General discussion

Research summary

Striking displays of structural colours in butterflies originate from sub-micron photonic nanostructures within the wing scales (Ingram and Parker, 2008; Lloyd and Nadeau, 2021). Blue iridescent structural colour has convergently evolved in numerous species of *Heliconius*, through folding of the scale cuticle ridges into multilayer reflectors (Parnell et al., 2018; Wilts et al., 2017a). The development of butterfly wing scales remains relatively unexplored and the formation of optical nanostructures even less so. Recent fluorescent microscopy observations have definitively shown that the actin cytoskeleton controls wing scale cell shape, cuticle ridge positioning and may also contribute to lower lamina optical nanostructure formation (Day et al., 2019; Dinwiddie et al., 2014). However, studies are lacking in species which contain multilayer reflectors, such as *Heliconius*. To date much of what we know about multilayer reflector development still comes from pioneering TEM observations conducted by Ghiradella over 40 years ago (Ghiradella, 1974).

In order to understand the role the actin cytoskeleton plays in structural colour development we compared the development of iridescent blue and non-iridescent black scales in *Heliconius sara* (Chapter 3). Firstly, we demonstrated that an increase in actin bundle number in developing iridescent scale cells enables a denser packing of cuticle ridges, thereby increasing the reflective surface area in adult iridescent scales. We then harness TauSTED super-resolution microscopy to gain unparalleled insights into the nano-level cellular workings of the scale cells. We observe a previously undescribed network of branched actin filaments in developing scale cells that exists around the time of nanostructure formation. In contrast to

previous studies which show a breakdown of the large actin bundles into the constituent actin monomers, we instead show a rearrangement of the actin bundles into a dynamic, branched actin network (Dinwiddie et al., 2014). This branched actin network likely stabilises the cuticle as it is deposited, starting from the external ridges towards the internal structures, such as the trabeculae. Indeed, our subsequent chemical perturbation of actin in developing iridescent scale cells resulted in collapse and buckling of the ridges, culminating in near total structural colour loss. Branched actin networks are ubiquitous in animal cells, providing the compressive forces necessary to generate membrane protrusions from the leading edge of cells (Bisi et al., 2013; Fletcher and Mullins, 2010; Li et al., 2022). Such mechanisms may also contribute to generation of the multilayer ridge reflectors. Our AFM and SEM images of actin-inhibited scales reveals architectural defects to the ridge layers themselves, suggesting that actin has additional, more direct roles in producing these cuticle layers. The exact details of this role remain unknown, but it may entail a force-generating interaction with Myosin motor proteins, as seen in the homologous *Drosophila* bristle (Wu et al., 2016), or through interaction with chitin synthase enzymes, such as in the generation of cuticle folds in the insect trabeculae (Öztürk-Çolak et al., 2016).

Underlying the cellular processes governing structural colour production is a gene regulatory network (GRN). Recent genetic analyses have shown that genes such as *optix*, *doublesex* and *bric a brac* (*bab*) control structural colour development in various butterfly species (Ficarrotta et al., 2022; Rodriguez-Caro et al., 2021; Thayer et al., 2020; Zhang et al., 2017). However, their position in the scale development GRN is likely upstream of the cellular mechanisms which directly build optical nanostructures (Smith et al., 2018). To date, the genetic basis of structural colour production in *Heliconius* butterflies remains relatively obscure. Previous phenotypic analyses have alluded to a quantitative genetic basis of structural colour, in contrast

to pigmentary colour in *Heliconius*, which is controlled by a few, major effect genes (Brien et al., 2018; Curran et al., 2020; Jiggins et al., 2017; Nadeau, 2016).

We performed differential expression analyses in two species, *Heliconius erato* and *Heliconius melpomene*, which have closely-related iridescent and non-iridescent subspecies (Chapter 4) (Parnell et al., 2018). Our analyses indicate that genes such as *Chitin deacetylase 1* may be crucial to structural colour development. Furthermore, our candidate genes include actin and microtubule cytoskeleton genes, further reinforcing the potential importance of these intracellular networks in governing optical nanostructure formation. We found little evidence of a shared genetic basis of structural colour in *H. erato* and *H. melpomene*. While this contrasts to the genetic basis of pigmentary colours it agrees with QTL analyses (see Appendix) showing different chromosomes are responsible for structural colour in these species (Nadeau, 2016).

Finally, we determine the condition dependent effects of external environmental factors on the development of structural colouration (Chapter 5). Such analyses provide insights into the optical nanostructure formation processes by revealing the requirements for proper structure formation. In addition, our analyses lay the groundwork for future studies on the adaptive function of structural colouration in *Heliconius*, including a potential role in sexual signalling. We use dietary stress to demonstrate that iridescent structural colour in *Heliconius sara* is a condition dependent trait. A diet of old, nutrient-deficient leaves results in a reduction in the optical reflectance and causes a shift in hue towards the bluer wavelengths. This effect was particularly prominent in males, which also show sexual dimorphism in the angle of maximum reflectance of blue iridescent colour. In contrast, while aspects of the yellow pigmentary colour were sexually dimorphic (brightness), there was no evidence that dietary stress results in a condition dependent response. Subsequent SEM and optical modelling of iridescent scales demonstrated that the phenotypic response to dietary stress at the level of the nanostructure caused gaps in the ridge layers (multilayer reflector) resulting in a decrease in the overall

reflectance. In addition, a small reduction in thickness of chitin or air layers of the multilayer reflector is all that is necessary to generate the measured shift in hue. The precise development of optical nanostructures is therefore subject to external factors, including diet. The cellular processes underlying optical nanostructure development likely require the correct input of constituent molecules in order to produce the most ordered reflective nanostructures.

A broader insight into optical nanostructure development

Our understanding of the development of optical nanostructures in nature remains limited. In Lepidoptera, various wing scale elements can be modified to form nanostructures, from lower lamina thin films to complex three-dimensional internal gyroids as well as ridge multilayers (Parnell et al., 2018; Thayer et al., 2020; Wilts et al., 2017b). Uniting these morphologies is a tweaking of a more general and widely conserved process of wing scale development (Ghiradella and Butler, 2009). Indeed, all butterfly optical nanostructures harness the biopolymer chitin (a material universal in insect morphological structures) to generate refractive index contrast and enable optical scattering (Burg and Parnell, 2018; Ghiradella, 2010; Thayer et al., 2020). Optical nanostructures result from the patterned deposition of cuticle into spatially precise configurations which can generate optical phenomena (diffraction effects) resulting in structural colouration (Burg and Parnell, 2018; Ghiradella and Butler, 2009; Prum et al., 2006).

The cellular processes underlying the development of optical nanostructures are highly dynamic and involve interactions with numerous intracellular components (Ghiradella, 2010, 1974; Saranathan et al., 2010). One of the most important findings of this thesis was the additional roles of the actin cytoskeleton in structural colour development in *Heliconius*. Previously the actin cytoskeleton was thought to be a relatively stable structure in butterfly

scale cells, forming thick bundles which drive cell elongation and guide cuticle ridge positioning (Day et al., 2019; Dinwiddie et al., 2014). After these patterning functions it was assumed that the actin filaments breakdown (Dinwiddie et al., 2014). However, we have instead shown that the actin cytoskeleton also has a dynamic branched component in addition to stable actin bundles. A branched network appears concurrently with larger actin bundle break down. The most energetically efficient predication is that the actin bundles lose their cross-linking and the actin filaments become reused within a branched network, likely through interactions with the Arp2/3 complex (Pollitt and Insall, 2009). Knockouts of *Arp3* (part of the Actin Related Protein 2/3 complex) in *Drosophila* bristles results in the loss of non-bundled F-actin (termed snarls) and excess actin bundles attached to the membrane, supporting our prediction (Frank et al., 2006).

Proteomic analyses in wing scales of *Bombyx mori* has previously shown that actin is one of the most abundant proteins in the wing scales during late development (60-80% development) together with cuticle components (Liu et al., 2021). This suggests that the remodelling of actin we observe is likely a conserved process in Lepidoptera scales and highlights the potential for cuticle and actin cytoskeleton interactions. Such interactions are likely crucial in the formation of nanostructures, such as ridge multilayers, and are supported by our actin perturbation experiments where the iridescent scales had ridge cuticle deformities, including ridge layer loss and other deleterious architectural alterations. Gene expression studies of butterfly wings, including the one in this thesis, have also highlighted a role of actin-related proteins. For example, *Rho1* (a key regulator of actin dynamics), is one of the most differentially expressed genes in RNAseq analyses of wing development in *Vanessa cardui* (Connahs et al., 2016; Thurmond et al., 2019). In addition, *optix* knockouts resulting in structural colour formation in *J. coenia*, are associated with the downregulation of actin-related genes (Smith et al., 2018; Zhang et al., 2017). This further supports the important function the

actin network plays at a broader level of scale cell development. Taken together we predict that the actin network has a multifunctional role in butterfly scales, including mediating some process of the precise and stable deposition of cuticle into optical nanostructures. Future studies should seek to elucidate the role of this branched actin network and its intracellular interactions, particularly in scales which contain optical nanostructures.

In addition to the actin cytoskeleton, our differential expression analysis also highlighted numerous other intracellular components which may play a role in structural colour development, including membrane proteins and microtubules. This further points to a complex and dynamic network of cellular interactions required to build *Heliconius* optical nanostructures. Such complexity may also apply at the broader level of optical nanostructure development. For example, the internal photonic crystals of Lycaenids and Papilionids form through folding of the membrane and smooth endoplasmic reticulum, together with deposition of cuticle into a complex, three-dimensional gyroid structure (Ghiradella, 1989; Saranathan et al., 2010; Wilts et al., 2017b). Whether such internal nanostructures are entirely self-assembled, resulting from phase transitions and membrane energetics, or incorporate some level of growth process remains understudied (Wilts et al., 2019, 2017b). Several recent studies have shown that microtubules interact with, as well as guide, the distribution of the smooth endoplasmic reticulum within cells (Gurel et al., 2014; Terasaki et al., 1986; Tikhomirova et al., 2022). This suggests microtubules could contribute to the folding of the internal membranes into gyroid structures. Interestingly, plant cells also harness a microtubule network to pattern the cellulose multilayer reflectors found in fruits (Airoldi et al., 2019). Overall, at a broader level this suggests that across the diversity of life structural colour producing cells likely harness the dynamic and multifunctional activity of internal protein networks (actin and microtubules) to precisely pattern optical nanostructures.

Convergence in structural colour formation

Perhaps the most surprising finding of this thesis was the lack of convergent genes controlling structural colour development in *H. erato* and *H. melpomene*. Since the advent of next-generation Omic technologies many studies have sought to understand the genetic basis of convergent phenotypic evolution (Sackton and Clark, 2019; Stern, 2013). A frequent observation has been that species with phenotypic convergence display higher levels of genetic convergence than would otherwise be predicted from null models (Sackton and Clark, 2019). Genetic convergence occurs at different levels. For example, the same gene can undergo identical amino acid substitutions in different species, as observed in the evolution of Cyclodiene resistance in numerous insect species. In such species, resistance evolves through an Adenine to Serine substitution at the GABA receptor (French-Constant, 1994; Stern, 2013). In other cases, convergent evolution involves the same gene but different sites of mutation. The light, blached colour of both Fence and Whiptail lizards in White Sands New Mexico, is an adaptation to match the white gypsum substrate (Rosenblum, 2006). The recent evolution of lighter pigmentation involves mutations at different sites in the *Mclr* gene (Manceau et al., 2010). Heightened convergence at the genetic level is often explained through constraints at the developmental and genetic level (pleiotropy), mutational biases and sharing of genetic variation (Sackton and Clark, 2019; Stern, 2013). The latter of which is exemplified in the convergent evolution of colour patterns in some species of co-mimicing *Heliconius* through hybridisation and subsequent exchange of colour pattern genes (*Heliconius* Genome Consortium, 2012).

Given the precise nature of optical nanostructure formation it can first appear incongruous that different genes are involved in the development of structural colour in related species. However, a potential explanation may come from the principles of cellular developmental mechanisms that underpin structural colour. The development of the optical nanostructures

(and the scale cell as a whole) can be understood as a process of ‘self-organisation’. Here, an emergence of order and form (in time and space) occurs from a network of interacting components (Wedlich-Söldner and Betz, 2018). Many cellular and subcellular features adhere to the principles of self-organisation, such as the nucleus and Golgi body (Misteli, 2001). Such systems are dynamic, invariably complex, and with many physical and biochemical reactions and feedback mechanisms that ultimately determine their form and function (Misteli, 2001; Wedlich-Söldner and Betz, 2018). Importantly though, self-organising systems typically demonstrate robustness and adaptability, where modification to the components leads to a shift to a new steady state rather than a breakdown as would be imposed by a rigid developmental framework. Therefore, in such systems there is a greater opportunity for the interacting components to be readily modified to produce a range of different structures and architectures (Misteli, 2001; Wedlich-Söldner and Betz, 2018).

Flexibility in the developmental process of scale cells means that there may be many developmental (and ultimately evolutionary) routes to producing the same phenotype, meaning genetic convergence may be unlikely. While the exact cellular mechanisms controlling the multilayer reflector formation remain unknown in *Heliconius*, different parts of the self-organising system can be targeted, for example through various different protein interactions with the actin and microtubule cytoskeleton. Indeed, we found some evidence that similar cellular pathways exist but that different genes were differentially expressed in *H. erato* and *H. melpomene*. Such principles may also apply at the broader level of optical nanostructure evolution. Future studies should continue to address the genetic basis of structural colour development and the convergence of optical nanostructures. *Heliconius* offers the ideal system for understanding convergent phenotypic evolution, with multiple recent origins of structural colour in closely-related species as well as more divergent species (the iridescent specialists) possessing similar phenotypes (McMillan et al., 2020; Parnell et al., 2018).

Future directions and challenges

The present study harnesses a range of developmental imaging and genetic techniques to characterise the development of structural colour in *Heliconius* butterflies. Our results highlight the complex nature of optical nanostructure formation at the genetic and cellular level and serves as a useful reference point for future studies on scale cell development and optical nanostructure formation in *Heliconius* and beyond.

The study of structural colour development straddles the disciplines of material science, optics, cellular development and genetics (Ingram and Parker, 2008). A deeper understanding of the formation of optical nanostructures *in vivo* will involve future cross-disciplinary collaborations between these diverse fields. As such, future project directions may follow many different trajectories of scientific enquiry starting from several findings of this thesis.

The breaking of the light diffraction barrier through super-resolution techniques, such as STED and SIM (Structured Illumination Microscopy), has been important for the recent discovery of many sub-cellular morphologies, such as nuclear pores (Hell et al., 2015; Szymborska et al., 2013; Wegel et al., 2016). In our study the use of TauSTED microscopy proved invaluable in revealing the nano-level complexities of the actin cytoskeleton in developing scale cells. While such studies have been difficult in the past, due to bleaching of samples using the STED laser, new fluorescent molecules specially designed for super-resolution microscopy are now available across multiple wavelengths, meaning the technique is considerably more accessible (Kwon et al., 2022). We predict future advances will come from harnessing these techniques to study a wide range of optical nanostructures, from luminal photonic crystals to multilayer reflectors.

One of the major challenges of developmental imaging of butterfly scale cells is the deposition of the cuticle layer around 50% of development. The cuticle forms an impermeable

and rigid layer which prevents diffusion of larger fluorescent molecules, such as antibodies, into the intracellular region of the scale cell. This hinders imaging at later stages when cuticular architectures are being constructed. Chemical dissolution of the constituent chitin may be feasible but in many cases, such as studying optical nanostructure formation, the morphology of interest is the cuticle layer itself (Xie et al., 2006). Such properties also make techniques such as expansion microscopy difficult in these systems (though protocols for expanding cuticle in *C. elegans* have been recently developed (Yu et al., 2020)). A new technology which may circumvent the problem of the cuticle layer, are Affimers (Tiede et al., 2017). These small protein molecules present an effective, super-resolution compatible alternative to antibodies, with stable and targeted binding to molecules at the nanolevel. Such molecules may be able to penetrate the cuticle in a way similar to other small molecules, such as Phalloidin, and they are worthy of future investigation.

Our developmental imaging focused on fixed tissues at various stages of optical nanostructure formation. This provided a broad overview of the developmental basis of scale cells, from the early budding of a scale cell out of the epithelial layer to formation of the final adult scale morphology, including the cuticle structures such as crossribs. However, many dynamic intracellular processes, such as microtubule trafficking and actin cytoskeleton rearrangement, cannot be fully appreciated from fixed snapshots of development (McDougal et al., 2021; Wilts et al., 2019). Live cell imaging presents an exciting future avenue of research into the formation of optical nanostructures, particularly if such approaches can be combined with super-resolution microscopy to acquire detailed *in vivo* imaging of nanostructure formation (Wilts et al., 2019). Recently, *in vivo* imaging techniques have been developed in butterflies, with Speckle-correlation phase microscopy used to characterise developing scale morphology formation in *Vanessa cardui* (McDougal et al., 2021). In addition, detailed

protocols for live cell imaging techniques have also been published for *Drosophila* pupae, with videos of dissections and staining readily available online (Zitserman and Roegiers, 2011).

Live cell imaging would also provide an avenue for more complex analytical methods, such as laser ablation to understand actin cytoskeleton dynamics (Fischer et al., 2014) as well as probes to quantify the membrane surface tension (Colom et al., 2018). Quantitative measurements from such experimental manipulations can directly feed into simulations of the forces and physical processes required to form the optical nanostructures (McDougal et al., 2021; Wilts et al., 2019). Methods such as these will be able to directly address the hypothesis that multilayer reflectors form as a result of actin-mediated elastic buckling of the cuticle layer (Ghiradella, 1974). Many challenges are still to be overcome to fully utilise such techniques, including maintaining the pupae during the addition of cytotoxic chemicals and laser imaging without disrupting or distorting the formation of the optical nanostructure.

At the genetic level, new insights will inevitably come from genomic technologies such as CRISPR-Cas9. Recent studies of colour pattern genetics in *Heliconius* have been greatly advanced through knockouts of colour pattern genes such as *cortex* (Livraghi et al., 2021; McMillan et al., 2020), *optix* (Zhang et al., 2017) and *WntA* (Mazo-Vargas et al., 2017). Previously, characterisation of genetic function has been challenging in non-model organisms, such as butterflies. Not only are transgenic lines (which are commonplace in organisms such as *Drosophila*) unavailable, but gene-knockout methods such as RNA interference are fraught with difficulties in Lepidoptera (Terenius et al., 2011). Our differential expression analysis revealed several key genes which warrant further investigation in *Heliconius*, including *chitin deacetylase 1* and actin-related proteins such as *Trio*. Given the dynamic and complex network which likely underlies scale cell and optical nanostructure development, a particular challenge may be deciphering the interactions and key nodes within the GRN in *Heliconius* and other butterfly species (Smith et al., 2018). In such cases, single-cell RNA sequencing may provide

an avenue for understanding the scale development GRN. Through comparisons of structurally coloured and non-structurally coloured scale types, single-cell RNA seq may uncover genes related specifically to optical nanostructure development. Protocols for obtaining scale cells from butterfly wing tissues for single-cell sequencing have been recently published (Prakash and Monteiro, 2020).

Our dietary stress experiments demonstrate that scale structure is subject to environmental factors. Different environmental factors likely affect different aspects of the cellular mechanisms which underpin scale cell and optical nanostructure development. For example, in our dietary stress experiments, there was no effect on ridge spacing and overall scale shape, suggesting that the actin cytoskeleton is largely robust to diet. Likely this network is more dependent on thermodynamic influences on the scale cell (such as temperature) and requires further investigation. Instead, we noted a loss of cuticle ridge layers in our stressed samples, suggesting that some developmental process of chitin formation and/or deposition is hindered potentially through lack of available resources to form sufficient cuticle. Application of different stressors on various development stages will present further avenues for understanding the external influences on optical nanostructure formation.

Our results showing condition dependence of iridescent, blue colour in *H. sara* also presents an interesting further question on whether there is a sexually selected component to structural colour in *Heliconius*, as has been demonstrated in *Colias eurytheme* (Kemp and Rutowski, 2007). Mate choice experiments present an obvious further study to determining whether such colours are sexually selected. Within these experiments, different components of the colour (hue, brightness, chroma) can be manipulated to elucidate their contributions to the overall signal, in terms of mate preference. A particular challenge will be manipulating the iridescent colour of the wing to use as models for such experiments. Recent advances in the artificial fabrication of iridescent butterfly wings could present an interesting route to generating

artificial *Heliconius* wings which can be used as models (Zhang and Chen, 2015). Another potential challenge concerns the complexities of the mating system of *Heliconius* butterflies. *H. sara* is an obvious model to use for behavioural experiments in *Heliconius*; it is gregarious and can be maintained in the lab at high densities (Jiggins, 2017). Nonetheless, these butterflies exhibit complex mating strategies including pupal mating, which seemingly precludes female mate choice (Jiggins, 2017). In addition, male *H. sara* employ different mating strategies depending on size, which may be impeded in the artificial environment of the lab (Hernández and Benson, 1998). Nevertheless, such mate choice experiments have been successfully undertaken in the past in *Heliconius*, one example being to demonstrate mating preference for polarised light (Merrill et al., 2014; Sweeney et al., 2003). Ultimately, the evolution of structural colour in *Heliconius* cannot be fully appreciated without an insight into its adaptive function.

Conclusion

The vivid structural colours of butterflies are some of the most eye-catching spectacles in nature. The visually impressive displays are matched by an equally impressive developmental origin, whereby single cells are controlled through a network of genetic code that is able to generate complex biopolymer architectures capable of manipulating light. Although the developmental process still remains relatively unexplored, the field is entering an exciting period with advances in super-resolution microscopy and gene-editing techniques. Being able to visualise the *in vivo* formation of optical nanostructures whilst also being able to decode the gene networks underpinning these processes is certainly a very real prospect. Undoubtedly, *Heliconius* butterflies will remain a key model organism for understanding optical nanostructure evolution and development. Above all, the study of structural colour will

continue to be a rich fusion of research from many branches of science, including physics, material science and biology. Though the ultimate goals of such fields may vary, be it nanofabrication of new technologies or an understanding of the evolution of phenotypic diversity, butterfly structural colours will continue to provide inspiration for centuries to come.

References

- Adler, P.N., 2017. Gene expression and morphogenesis during the deposition of *Drosophila* wing cuticle. *Fly (Austin)*. 11, 194–199.
- Adler, P.N., 2019. The localization of chitin synthase mediates the patterned deposition of chitin in developing *Drosophila* bristles. *bioRxiv*.
- Airoldi, C.A., Ferria, J., Glover, B.J., 2019. The cellular and genetic basis of structural colour in plants. *Curr. Opin. Plant Biol.* 47, 81–87.
- Alexa, A., Rahnenführer, J., 2021. Gene set enrichment analysis with topGO. R Packag. version 2.48.0.
- Alvarez, L.A.J., Schwarz, U., Friedrich, L., Foelling, J., Hecht, F., Roberti, M.J., 2021. TauSTED : pushing STED beyond its limits with lifetime (Application note). *Nat. Methods*.
- Anderson, T.F., Richards, A.G., 1942. An electron microscope study of some structural colors of insects. *J. Appl. Phys.* 13, 748–758.
- Andersson, M., 1986. Evolution of condition-dependent sex ornaments and mating preferences: sexual selection based on viability differences. *Evolution (N. Y.)*. 40, 804–816.
- Andersson, M., Iwasa, Y., 1996. Sexual selection. *Trends Ecol. Evol.* 11, 53–58.
- Antoniou Kourouniotti, R.L., Band, L.R., Fozard, J.A., Hampstead, A., Lovrics, A., Moyroud, E., Vignolini, S., King, J.R., Jensen, O.E., Glover, B.J., 2013. Buckling as an origin of ordered cuticular patterns in flower petals. *J. R. Soc. Interface* 10, 20120847. <http://dx.doi.org/10.1098/rsif.2012.0847>.
- Arias, M., Davey, J.W., Martin, S., Jiggins, C., Nadeau, N., Joron, M., Llaurens, V., 2020. How do predators generalize warning signals in simple and complex prey communities? Insights from a videogame. *Proc. R. Soc. B Biol. Sci.* 287, 20200014. <http://dx.doi.org/10.1098/rspb.2020.0014>.
- Arrese, E.L., Soulages, J.L., 2010. Insect fat body: Energy, Metabolism and Regulation. *Annu. Rev. Entomol.* 207–225.
- Bagnara, J.T., Fernandez, P.J., Fujii, R., 2007. On the blue coloration of vertebrates. *Pigment Cell Res.* 20, 14–26.
- Barrows, F.P., Bartl, M.H., 2014. Photonic Structures in Biology: A Possible Blueprint for Nanotechnology. *Nanomater. Nanotechnol.* 4, doi: 10.5772/58289.
- Bates, D., Mächler, M., Bolker, B.M., Walker, S.C., 2015. Fitting Linear Mixed-Effects Models Using lme4. *J. Stat. Softw.* 67, 10.18637/jss.v067.i01.
- Bates, H.W., 1862. Contributions to an Insect Fauna of the Amazon Valley. *Lepidoptera: Heliconinae*. *Trans. Linn. Soc. London* 23, 495–566.
- Berthier, S., 2007. Pigments and Pigmentary Colors. In: *Iridescences - The Physical Colours of Insects*. Springer, pp. 127–134.
- Bhardwaj, S., Jolander, L.S.H., Wenk, M.R., Oliver, J.C., Frederik Nijhout, H., Monteiro, A.,

2020. Origin of the mechanism of phenotypic plasticity in satyrid butterfly eyespots. *Elife* 9, e49544.
- Bisi, S., Disanza, A., Malinverno, C., Frittoli, E., Palamidessi, A., Scita, G., 2013. Membrane and actin dynamics interplay at lamellipodia leading edge. *Curr. Opin. Cell Biol.* 25, 565–573.
- Blochlinger, K., Jan, L.Y., Jan, Y.N., 1991. Transformation of sensory organ identity by ectopic expression of *Cut* in *Drosophila*. *Genes Dev.* 5, 1124–1135.
- Brien, M.N., 2019. The genetics and evolution of iridescent structural colour in *Heliconius* butterflies. University of Sheffield.
- Brien, M.N., Enciso-Romero, J., Lloyd, V.J., Curran, E. V., Parnell, A.J., Morochz, C., Salazar, P.A., Rastas, P., Zinn, T., Nadeau, N.J., 2022. The genetic basis of structural colour variation in mimetic *Heliconius* butterflies. *Philos. Trans. R. Soc. B Biol. Sci.* 377, 20200505.
- Brien, M.N., Enciso-romero, J., Parnell, A.J., Bainbridge, H.E., Salazar, P.A., Morochz, C., Chala, D., Zinn, T., Curran, E. V, Nadeau, N.J., Sheffield, S., Brien, M.N., Nadeau, N.J., 2018. Phenotypic variation in *Heliconius erato* crosses shows that iridescent structural colour is sex-linked and controlled by multiple genes. *Interface Focus* 9, <http://dx.doi.org/10.1098/rsfs.2018.0047>.
- Briscoe, A.D., Bybee, S.M., Bernard, G.D., Yuan, F., Sison-Mangus, M.P., Reed, R.D., Warren, A.D., Llorente-Bousquets, J., Chiao, C.C., 2010. Positive selection of a duplicated UV-sensitive visual pigment coincides with wing pigment evolution in *Heliconius* butterflies. *Proc. Natl. Acad. Sci. U. S. A.* 107, 3628–3633.
- Brown, K.S., 1981. The Biology of *Heliconius* and Related Genera. *Annu. Rev. Entomol.* 26, 427–457.
- Brown, K.S., Benson, W.W., 1974. Adaptive Polymorphism Associated with Multiple Müllerian Mimicry in *Heliconius numata* (Lepid. Nymph.). *Assoc. Trop. Biol. Conserv.* 6, 205–228.
- Burg, S.L., 2018. Biological structural whites and synthetic routes to mimic these structures. University of Sheffield.
- Burg, S.L., Parnell, A.J., 2018. Self-assembling structural colour in nature. *J. Phys. Condens. Matter* 30, 413001.
- Burg, S.L., Washington, A., Coles, D.M., Bianco, A., Mcloughlin, D., Mykhaylyk, O.O., Villanova, J., Dennison, A.J.C., Hill, C.J., Vukusic, P., Doak, S., Martin, S.J., Hutchings, M., Parnell, S.R., Vasilev, C., Clarke, N., Ryan, A.J., Furnass, W., Croucher, M., Dalgliesh, R.M., Prevost, S., Dattani, R., Parker, A., Jones, R.A.L., Fairclough, J.P.A., Parnell, A.J., 2019. Liquid-liquid phase separation morphologies in ultra-white beetle scales and a synthetic equivalent. *Commun. Chem.* 2:100, 10.1038/s42004-019-0202-8.
- Bybee, S.M., Yuan, F., Ramstetter, M.D., Llorente-Bousquets, J., Reed, R.D., Osorio, D., Briscoe, A.D., 2012. UV photoreceptors and UV-yellow wing pigments in *heliconius* butterflies allow a color signal to serve both mimicry and intraspecific communication. *Am. Nat.* 179, 38–51.
- Byrnes, S.J., 2021. Multilayer optical calculations. arXiv.

- Cardoso, M.Z., Gilbert, L.E., 2013. Pollen feeding, resource allocation and the evolution of chemical defence in passion vine butterflies. *J. Evol. Biol.* 26, 1254–1260.
- Chai, P., Srygley, R.B., 1990. Predation and the Flight, Morphology, and Temperature of Neotropical Rain-Forest Butterflies. *Am. Nat.* 135, 748–765.
- Challis, R.J., Kumar, S., Dasmahapatra, K.K., Jiggins, C.D., Blaxter, M., 2016. Lepbase: the Lepidopteran genome database. *BioRxiv*.
- Chandler, C.J., Wilts, B.D., Brodie, J., Vignolini, S., 2017. Structural Color in Marine Algae. *Adv. Opt. Mater.* 5, 1600646.
- Chen, F., Huang, Y., Li, R., Zhang, S., Wang, B., Zhang, W., Wu, X., Jiang, Q., Wang, F., Zhang, R., 2021. Bio-inspired structural colors and their applications. *Chem. Commun.* 57, 13448–13464.
- Chen, G., Cong, Q., Feng, Y., Ren, L., 2004. Study on the wettability and self-cleaning of butterfly wing surfaces. In: Brebbia, M.W., Collins, C.A. (Eds.), *Design and Nature II*, WIT Press, Boston, USA, pp. 245–251.
- Chen, Y., Gu, J., Zhang, D., Zhu, S., Su, H., Hu, X., Feng, C., Zhang, W., Liu, Q., Parker, A.R., 2011a. Tunable three-dimensional ZrO₂ photonic crystals replicated from single butterfly wing scales. *J. Mater. Chem.* 21, 15237–15243.
- Chen, Y., Lun, A.T.L., Smyth, G.K., 2016. From reads to genes to pathways: Differential expression analysis of RNA-Seq experiments using Rsubread and the edgeR quasi-likelihood pipeline. *F1000Research* 5, 1–51.
- Chen, Y., Zang, X., Gu, J., Zhu, S., Su, H., Zhang, D., Hu, X., Liu, Q., Zhang, W., Liu, D., 2011b. ZnO single butterfly wing scales: Synthesis and spatial optical anisotropy. *J. Mater. Chem.* 21, 6140–6143.
- Chouvardas, P., Kollias, G., Nikolaou, C., 2016. Inferring active regulatory networks from gene expression data using a combination of prior knowledge and enrichment analysis. *BMC Bioinformatics* 17:181, doi: 10.1186/s12859-016-1040-7.
- Christopoulos, D.T., 2019. inflection: Finds the inflection point of a curve. R Package version 1.3.5.
- Clark, A.G., Wartlick, O., Salbreux, G., Paluch, E.K., 2014. Stresses at the cell surface during animal cell morphogenesis. *Curr. Biol.* 24, R484–R494.
- Colom, A., Derivery, E., Soleimanpour, S., Tomba, C., Molin, M.D., Sakai, N., González-Gaitán, M., Matile, S., Roux, A., 2018. A fluorescent membrane tension probe. *Nat. Chem.* 10, 1118–1125.
- Concha, C., Wallbank, R.W.R., Hanly, J.J., Fenner, J., Livraghi, L., Rivera, E.S., Paulo, D.F., Arias, C., Vargas, M., Sanjeev, M., Morrison, C., Tian, D., Aguirre, P., Ferrara, S., Foley, J., Pardo-Diaz, C., Salazar, C., Linares, M., Massardo, D., Counterman, B.A., Scott, M.J., Jiggins, C.D., Papa, R., Martin, A., McMillan, W.O., 2019. Interplay between Developmental Flexibility and Determinism in the Evolution of Mimetic *Heliconius* Wing Patterns. *Curr. Biol.* 29, 3996–4009.
- Connahs, H., Rhen, T., Simmons, R.B., 2016. Transcriptome analysis of the painted lady butterfly, *Vanessa cardui* during wing color pattern development. *BMC Genomics* 17:270, 10.1186/s12864-016-2586-5.

- Connahs, H., Tlili, S., van Creijl, J., Loo, T.Y.J., Banerjee, T. Das, Saunders, T.E., Monteiro, A., 2019. Activation of butterfly eyespots by Distal-less is consistent with a reaction-diffusion process. *Development* 146, dev169367.
- Cotton, S., Small, J., Pomiankowski, A., 2006. Sexual Selection and Condition-Dependent Mate Preferences. *Curr. Biol.* 16, 755–765.
- Curran, E. V., Stankowski, S., Pardo-Diaz, C., Salazar, C., Linares, M., Nadeau, N.J., 2020. Müllerian mimicry of a quantitative trait despite contrasting levels of genomic divergence and selection. *Mol. Ecol.* 29, 2016–2030.
- Curran, E. V., 2018. An exploration of the parallel evolution of iridescent structural colour in *Heliconius* butterflies. University of Sheffield.
- Day, C.R., Hanly, J.J., Ren, A., Martin, A., 2019. Sub-micrometer insights into the cytoskeletal dynamics and ultrastructural diversity of butterfly wing scales. *Dev. Dyn.* 248, 657–670.
- Dell’Aglia, D.D., Troscianko, J., McMillan, W.O., Stevens, M., Jiggins, C.D., 2018. The appearance of mimetic *Heliconius* butterflies to predators and conspecifics. *Evolution* (N. Y). 72, 2156–2166.
- Denton, E.J., 1970. On the organisation of reflecting surfaces in some marine animals. *Philos. Trans. R. Soc. B Biol. Sci.* 258, 285–313.
- Derakhshani, B., Jafary, H., Zanjani, B.M., Hasanpur, K., Mishina, K., Tanaka, T., Kawahara, Y., Oono, Y., 2020. Combined QTL mapping and RNA-Seq profiling reveals candidate genes associated with cadmium tolerance in barley. *PLoS One* 15, e0230820.
- Ding, B.J., Löfstedt, C., 2015. Analysis of the *agrotis segetum* pheromone gland transcriptome in the light of Sex pheromone biosynthesis. *BMC Genomics* 16:711, 10.1186/s12864-015-1909-2.
- Dinwiddie, A., Null, R., Pizzano, M., Chuong, L., Leigh Krup, A., Ee Tan, H., Patel, N.H., 2014. Dynamics of F-actin prefigure the structure of butterfly wing scales. *Dev. Biol.* 392, 404–418.
- Doucet, S.M., Meadows, M.G., 2009. Iridescence: A functional perspective. *J. R. Soc. Interface* 6, S115–S132.
- Douglas, J.M., Cronin, T.W., Chiou, T.H., Dominy, N.J., 2007. Light habitats and the role of polarized iridescence in the sensory ecology of neotropical nymphalid butterflies (Lepidoptera: Nymphalidae). *J. Exp. Biol.* 210, 788–799.
- Emmert-Streib, F., Dehmer, M., Haibe-Kains, B., 2014. Gene regulatory networks and their applications: Understanding biological and medical problems in terms of networks. *Front. Cell Dev. Biol.* 2, 10.3389/fcell.2014.00038.
- Espeland, M., Breinholt, J., Willmott, K.R., Warren, A.D., Vila, R., Toussaint, E.F.A., Maunsell, S.C., Aduse-Poku, K., Talavera, G., Eastwood, R., Jarzyna, M.A., Guralnick, R., Lohman, D.J., Pierce, N.E., Kawahara, A.Y., 2018. A Comprehensive and Dated Phylogenomic Analysis of Butterflies. *Curr. Biol.* 28, 770–778.
- Fei, X., He, B., Adler, P.N., 2002. The growth of *Drosophila* bristles and laterals is not restricted to the tip or base. *J. Cell Sci.* 115, 3797–3806.

- Fenner, J., Benson, C., Rodriguez-Caro, L., Ren, A., Papa, R., Martin, A., Hoffmann, F., Range, R., Counterman, B.A., 2020. Wnt Genes in Wing Pattern Development of Coliadinae Butterflies. *Front. Ecol. Evol.* 8, <https://doi.org/10.3389/fevo.2020.00197>.
- Fenner, J., Rodriguez-Caro, L., Counterman, B., 2019. Plasticity and divergence in ultraviolet reflecting structures on Dogface butterfly wings. *Arthropod Struct. Dev.* 51, 14–22.
- Fernández-Eslava, B., Alonso, D., Galicia, D., Arizaga, J., 2022. Strong evidence supporting a relationship between colour pattern and apparent survival in common crossbills. *J. Ornithol.* 163, 243–249.
- Fernandez-Valverde, S.L., Aguilera, F., Ramos-Díaz, R.A., 2018. Inference of developmental gene regulatory networks beyond classical model systems: New approaches in the post-genomic era. *Integr. Comp. Biol.* 58, 640–653.
- French-Constant, R.H., 1994. The molecular and population genetics of cyclodiene insecticide resistance. *Insect Biochem. Mol. Biol.* 24, 335–345.
- Ficarrotta, V., Hanly, J.J., Loh, L.S., Francescutti, C.M., Ren, A., Tunström, K., Wheat, C.W., Porter, A.H., Counterman, B.A., Martin, A., 2022. A genetic switch for male UV iridescence in an incipient species pair of sulphur butterflies. *Proc. Natl. Acad. Sci. U. S. A.* 119, e2109255118.
- Finkbeiner, S.D., Briscoe, A.D., 2021. True UV color vision in a female butterfly with two UV opsins. *J. Exp. Biol.* 224, doi:10.1242/jeb.242802.
- Finkbeiner, S.D., Briscoe, A.D., Reed, R.D., 2014. Warning signals are seductive: Relative contributions of color and pattern to predator avoidance and mate attraction in *Heliconius* butterflies. *Evolution (N. Y.)* 68, 3410–3420.
- Finkbeiner, S.D., Fishman, D.A., Osorio, D., Briscoe, A.D., 2017. Ultraviolet and yellow reflectance but not fluorescence is important for visual discrimination of conspecifics by *Heliconius erato*. *J. Exp. Biol.* 220, 1267–1276.
- Fischer, S.C., Blanchard, G.B., Duque, J., Adams, R.J., Arias, A.M., Guest, S.D., Gorfinkiel, N., 2014. Contractile and mechanical properties of epithelia with perturbed actomyosin dynamics. *PLoS One* 9, e95695.
- Fletcher, D.A., Mullins, R.D., 2010. Cell mechanics and the cytoskeleton. *Nature* 463, 485–492.
- Florian Harting, 2017. DHARMA: ResidualDiagnostics for Hierarchical (Multi-Level/ Mixed) Regression Models. R package version 0.1.5. R package version 0.1.5.
- Frank, Deborah J., Hopmann, R., Lenartowska, M., Miller, K.G., 2006. Capping Protein and the Arp2/3 Complex Regulate Nonbundle Actin Filament Assembly to Indirectly Control Actin Bundle Positioning during *Drosophila melanogaster* Bristle Development. *Mol. Biol. Cell* 17, 3930–3939.
- French, V., Brakefield, P.M., 2004. Pattern formation: A focus on notch in butterfly eyespots. *Curr. Biol.* 14, 663–665.
- Galant, R., Skeath, J.B., Paddock, S., Lewis, D.L., Carroll, S.B., 1998. Expression pattern of a butterfly achaete-scute homolog reveals the homology of butterfly wing scales and insect sensory bristles. *Curr. Biol.* 8, 807–813.

- Gallant, J.R., Imhoff, V.E., Martin, A., Savage, W.K., Chamberlain, N.L., Pote, B.L., Peterson, C., Smith, G.E., Evans, B., Reed, R.D., Kronforst, M.R., Mullen, S.P., 2014. Ancient homology underlies adaptive mimetic diversity across butterflies. *Nat. Commun.* 5, 4817. doi: <https://doi.org/10.1038/ncomms5817>.
- Ghiradella, H., 1974. Development of ultraviolet-reflecting butterfly scales: How to make an interference filter. *J. Morphol.* 142, 395–409.
- Ghiradella, H., 1989. Structure and Development of Iridescent Butterfly Scales: Lattices and Laminae. *J. Morphol.* 202, 69–88.
- Ghiradella, H., 1991. Light and color on the wing: structural colors in butterflies and moths. *Appl. Opt.* 30, 3492–3500.
- Ghiradella, H., 2010. Insect Cuticular Surface Modifications: Scales and Other Structural Formations. In: *Advances in Insect Physiology*. Elsevier Ltd., pp. 135–180.
- Ghiradella, H., Aneshansley, D., Eisner, T., Silberglied, R.E., Hinton, H.E., 1972. Ultraviolet Reflection of a Male Butterfly: Interference Color Caused by Thin-Layer Elaboration of Wing Scales. *Science* (80-.). 178, 1214–1217.
- Ghiradella, H., Radigan, W., 1976. Development of Butterfly Scales II. STRUTS, LATTICES AND SURFACE TENSION. *J. Morphol.* 150, 279–297.
- Ghiradella, H.T., Butler, M.W., 2009. Many variations on a few themes: A broader look at development of iridescent scales (and feathers). *J. R. Soc. Interface* 6, S243–S251.
- Gilbert, L.E., 1972. Pollen Feeding and Reproductive Biology of Heliconius Butterflies . *Proc. Natl. Acad. Sci.* 69, 1403–1407.
- Giraldo, M.A., Stavenga, D.G., 2016. Brilliant iridescence of Morpho butterfly wing scales is due to both a thin film lower lamina and a multilayered upper lamina. *J. Comp. Physiol. A* 202, 381–388.
- González-Rojas, M.F., Darragh, K., Robles, J., Linares, M., Schulz, S., McMillan, W.O., Jiggins, C.D., Pardo-Díaz, C., Salazar, C., 2020. Chemical signals act as the main reproductive barrier between sister and mimetic Heliconius butterflies. *Proc. R. Soc. B Biol. Sci.* 287, 20200587.
- Gotthard, K., Nylin, S., 1995. Adaptive Plasticity and Plasticity as an Adaptation : A Selective Review of Plasticity in Animal Morphology and Life History. *Oikos* 74, 3–17.
- Goulson, D., 1994. Determination of larval melanization in the moth, *Mamestra brassicae*, and the role of melanin in thermoregulation. *Heredity (Edinb.)* 73, 471–479.
- Guild, G.M., Connelly, P.S., Ruggiero, L., Vranich, K.A., Tilney, L.G., 2005. Actin Filament Bundles in Drosophila Wing Hairs: Hairs and Bristles Use Different Strategies for Assembly. *Mol. Biol. Cell* 16, 3620–3631.
- Guild, G.M., Connelly, P.S., Vranich, K.A., Shaw, M.K., Tilney, L.G., 2002. Actin filament turnover removes bundles from Drosophila bristle cells. *J. Cell Sci.* 115, 641–653.
- Guillermo-Ferreira, R., Bispo, P.C., Appel, E., Kovalev, A., Gorb, S.N., 2019. Structural coloration predicts the outcome of male contests in the Amazonian damselfly *Chalcopteryx scintillans* (Odonata: Polythoridae). *Arthropod Struct. Dev.* 53, 100884.
- Gurel, P.S., Hatch, A.L., Higgs, H.N., 2014. Connecting the cytoskeleton to the endoplasmic

- reticulum and Golgi. *Curr. Biol.* 24, 660–672.
- Hanly, J.J., 2017. Developmental basis of wing pattern diversity in *Heliconius* butterflies. University of Cambridge.
- Hanly, J.J., Wallbank, R.W.R., McMillan, W.O., Jiggins, C.D., 2019. Conservation and flexibility in the gene regulatory landscape of heliconiine butterfly wings. *Evodevo* 10:15, <https://doi.org/10.1186/s13227-019-0127-4>.
- Hawkes, M.F., Duffy, E., Joag, R., Skeats, A., Radwan, J., Wedell, N., Sharma, M.D., Hosken, D.J., Troscianko, J., 2019. Sexual selection drives the evolution of male wing interference patterns. *Proc. R. Soc. B Biol. Sci.* 286, 20182850.
- Heliconius Genome Consortium, 2012. Butterfly genome reveals promiscuous exchange of mimicry adaptations among species. *Nature* 487, 94–98.
- Hell, S.W., Sahl, S.J., Bates, M., Zhuang, X., Heintzmann, R., Booth, M.J., Bewersdorf, J., Shtengel, G., Hess, H., Tinnefeld, P., Honigsmann, A., Jakobs, S., Testa, I., Cognet, L., Lounis, B., Ewers, H., Davis, S.J., Eggeling, C., Klenerman, D., Willig, K.I., Vicidomini, G., Castello, M., Diaspro, A., Cordes, T., 2015. The 2015 super-resolution microscopy roadmap. *J. Phys. D. Appl. Phys.* 48, 443001.
- Hernández, M.I.M., Benson, W.W., 1998. Small-male advantage in the territorial tropical butterfly *Heliconius sara* (Nymphalidae): A paradoxical strategy? *Anim. Behav.* 56, 533–540.
- Hill, G.E., 2011. Condition-dependent traits as signals of the functionality of vital cellular processes. *Ecol. Lett.* 14, 625–634.
- Hill, G.E., Hood, W.R., Ge, Z., Grinter, R., Greening, C., Johnson, J.D., Park, N.R., Taylor, H.A., Andreasen, V.A., Powers, M.J., Justyn, N.M., Parry, H.A., Kavazis, A.N., Zhang, Y., 2019. Plumage redness signals mitochondrial function in the house finch. *Proc. R. Soc. B Biol. Sci.* 286, 20191354.
- Hof, A.E.V. t., Campagne, P., Rigden, D.J., Yung, C.J., Lingley, J., Quail, M.A., Hall, N., Darby, A.C., Saccheri, I.J., 2016. The industrial melanism mutation in British peppered moths is a transposable element. *Nature* 534, 102–105.
- Hooke, R., 1665. *Micrographia* : or, Some physiological descriptions of minute bodies made by magnifying glasses. With observations and inquiries thereupon. Royal Society, London.
- Hopmann, R., Cooper, J.A., Miller, K.G., 1996. Actin Organization, Bristle Morphology, and Viability Are Affected by Actin Capping Protein Mutations in *Drosophila*. *J. Cell Biol.* 133, 1293–1305.
- Hopmann, R., Miller, K.G., 2003. A Balance of Capping Protein and Profilin Functions Is Required to Regulate Actin Polymerization in *Drosophila* Bristle. *Mol. Biol. Cell* 14, 118–128.
- Huang, Y., Shi, S., Wu, H.L., Yue, S.L., Liao, M., Cao, H.Q., 2021. CYP4G7 and CYP4G14 mediate cuticle formation and pigmentation in *Tribolium confusum*. *J. Stored Prod. Res.* 94, 101881.
- Huberty, A.F., Denno, R.F., 2006. Consequences of nitrogen and phosphorus limitation for the performance of two planthoppers with divergent life-history strategies. *Oecologia*

149, 444–455.

- Ingram, A.L., Parker, A.R., 2008. A review of the diversity and evolution of photonic structures in butterflies, incorporating the work of John Huxley (The Natural History Museum, London from 1961 to 1990). *Philos. Trans. R. Soc. B Biol. Sci.* 363, 2465–2480.
- Jenner, R.A., Wills, M.A., 2007. Opinion: The choice of model organisms in evo-devo. *Nat. Rev. Genet.* 8, 311–319.
- Jiggins, C.D., 2017. *The ecology and evolution of Heliconius butterflies*. Oxford University Press, Oxford.
- Jiggins, C.D., Estrada, C., Rodrigues, A., 2004. Mimicry and the evolution of premating isolation in *Heliconius melpomene* Linnaeus. *J. Evol. Biol.* 17, 680–691.
- Jiggins, C.D., Mcmillan, W.O., Mallet, J., 1997. Host plant adaptation has not played a role in the recent speciation of *Heliconius himera* and *Heliconius erato*. *Ecol. Entomol.* 22, 361–365.
- Jiggins, C.D., Naisbit, R.E., Coe, R.L., Mallet, J., 2001. Reproductive isolation caused by colour pattern mimicry. *Nature* 411, 302–305.
- Jiggins, C.D., Wallbank, R.W.R., Hanly, J.J., 2017. Waiting in the wings: What can we learn about gene co-option from the diversification of butterfly wing patterns? *Philos. Trans. R. Soc. B Biol. Sci.* 372, 20150485.
- Johnson, H., Solensky, M.J., Satterfield, D.A., Davis, A.K., 2014. Does skipping a meal matter to a butterfly's appearance? Effects of larval food stress on wing morphology and color in monarch butterflies. *PLoS One* 9, e93492.
- Johnstone, R.A., Rands, S.A., Evans, M.R., 2009. Sexual selection and condition-dependence. *J. Evol. Biol.* 22, 2387–2394.
- Joron, M., Jiggins, C.D., Papanicolaou, A., McMillan, W.O., 2006a. *Heliconius* wing patterns: An evo-devo model for understanding phenotypic diversity. *Heredity (Edinb.)* 97, 157–167.
- Joron, M., Papa, R., Beltrán, M., Chamberlain, N., Mavárez, J., Baxter, S., Abanto, M., Bermingham, E., Humphray, S.J., Rogers, J., Beasley, H., Barlow, K., Ffrench-Constant, R.H., Mallet, J., McMillan, W.O., Jiggins, C.D., 2006b. A conserved supergene locus controls colour pattern diversity in *Heliconius* butterflies. *PLoS Biol.* 4, 1831–1840.
- Kazama, M., Ichinei, M., Endo, S., Iwata, M., Hino, A., Otaki, J.M., 2017. Species-dependent microarchitectural traits of iridescent scales in the triad taxa of Ornithoptera birdwing butterflies. *Entomol. Sci.* 20, 255–269.
- Kemp, A.D.J., Vukusic, P., Rutowski, R.L., 2006. Stress-Mediated Covariance between Nano-Structural Architecture and Ultraviolet Butterfly Coloration 20, 282–289.
- Kemp, D.J., 2007. Female butterflies prefer males bearing bright iridescent ornamentation. *Proc. R. Soc. B Biol. Sci.* 274, 1043–1047.
- Kemp, D.J., 2008. Resource-mediated condition dependence in sexually dichromatic butterfly wing coloration 62, 2346–2358.
- Kemp, D.J., Rutowski, R.L., 2007. Condition dependence, quantitative genetics, and the

- potential signal content of iridescent ultraviolet butterfly coloration. *Evolution* (N. Y.) 61, 168–183.
- Kilchoer, C., Steiner, U., Wilts, B.D., 2019. Thin-film structural coloration from simple fused scales in moths. *Interface Focus* 9, 20180044.
- Kim, D., Langmead, B., Salzberg, S.L., 2015. HISAT: A fast spliced aligner with low memory requirements. *Nat. Methods* 12, 357–360.
- Kingsolver, J.G., Wiernasz, D.C., 1991. Seasonal Polyphenism in Wing-Melanin Pattern and Thermoregulatory Adaptation in *Pieris* Butterflies. *Am. Nat.* 137, 816–830.
- Kinoshita, S., 2008. Structural colors in the realm of nature, *Structural Colors in the Realm of Nature*. World Scientific Publishing.
- Kinoshita, S., Yoshioka, S., Fujii, Y., Okamoto, N., 2002. Photophysics of structural color in the *Morpho* butterflies. *Forma* 17, 103–121.
- Kinoshita, S., Yoshioka, S., Miyazaki, J., 2008. Physics of structural colors. *Reports Prog. Phys.* 71, 076401.
- Kjernsmo, K., Whitney, H.M., Scott-Samuel, N.E., Hall, J.R., Knowles, H., Talas, L., Cuthill, I.C., 2020. Iridescence as Camouflage. *Curr. Biol.* 30, 551-555.e3.
- Koch, N., Dharmalingam, E., Westermann, M., Qualmann, B., Thomas, U., Kessels, M.M., 2012. Abp1 utilizes the Arp2 / 3 complex activator Scar / WAVE in bristle development. *J. Cell Sci.* 125, 3578–3589.
- Kozak, K.M., Wahlberg, N., Neild, A.F.E., Dasmahapatra, K.K., Mallet, J., Jiggins, C.D., 2015. Multilocus species trees show the recent adaptive radiation of the mimetic heliconius butterflies. *Syst. Biol.* 64, 505–524.
- Kramer, R.M., Crookes-Goodson, W.J., Naik, R.R., 2007. The self-organizing properties of squid reflectin protein. *Nat. Mater.* 6, 533–538.
- Krishna, A., Nie, X., Warren, A.D., Llorente-Bousquets, J.E., Briscoe, A.D., Lee, J., 2020. Infrared optical and thermal properties of microstructures in butterfly wings. *Proc. Natl. Acad. Sci. U. S. A.* 117, 1566–1572.
- Kronforst, M.R., Papa, R., 2015. The functional basis of wing patterning in *Heliconius* butterflies: The molecules behind mimicry. *Genetics* 200, doi: 10.1534/genetics.114.172387.
- Kwon, J., Elgawish, M.S., Shim, S.H., 2022. Bleaching-Resistant Super-Resolution Fluorescence Microscopy. *Adv. Sci.* 9, 2101817.
- Lee, K.-H., Araki, K., Elleuch, O., Kojima, N., Yamaguchi, M., 2017. Pypvcell: An Open-Source Solar Cell Modeling Library in Python. 2017 IEEE 44th Photovolt. Spec. Conf. 359–362.
- Lenth, R., Singmann, H., Love, J., Buerkner, P., Herve, M., 2018. emmeans: Estimated Marginal Means, aka LeastSquares Means. <https://CRAN.R-project.org/Packag>.
- Li, H., Handsaker, B., Wysoker, A., Fennell, T., Ruan, J., Homer, N., Marth, G., Abecasis, G., Durbin, R., 2009. The Sequence Alignment/Map format and SAMtools. *Bioinformatics* 25, 2078–2079.

- Li, T.-D., Bieling, P., Weichsel, J., Mullins, R.D., Fletcher, D.A., 2022. The molecular mechanism of load adaptation by branched actin networks. *Elife* 11, e73145.
- Lim, M.L.M., Li, D., 2007. Effects of age and feeding history on structure-based UV ornaments of a jumping spider (Araneae: Salticidae). *Proc. R. Soc. B Biol. Sci.* 274, 569–575.
- Liu, E., Li, L., Cheng, L., 2019. Gene regulatory network review. In: *Encyclopedia of Bioinformatics and Computational Biology: ABC of Bioinformatics*. Elsevier, pp. 155–164.
- Liu, J., Chen, Z., Xiao, Y., Asano, T., Li, S., Peng, L., Chen, E., Zhang, J., Li, W., Zhang, Y., Tong, X., Kadono-Okuda, K., Zhao, P., He, N., Arunkumar, K.P., Gopinathan, K.P., Xia, Q., Willis, J.H., Goldsmith, M.R., Mita, K., 2021. Lepidopteran wing scales contain abundant cross-linked film-forming histidine-rich cuticular proteins. *Commun. Biol.* 4:491, <https://doi.org/10.1038/s42003-021-01996-4>.
- Livraghi, L., Hanly, J.J., Van Bellghem, S.M., Montejo-Kovacevich, G., van der Heijden, E.S.M., Loh, L.S., Ren, A., Warren, I.A., Lewis, J.J., Concha, C., Hebberecht, L., Wright, C.J., Walker, J.M., Foley, J., Goldberg, Z.H., Arenas-Castro, H., Salazar, C., Perry, M.W., Papa, R., Martin, A., McMillan, W.O., Jiggins, C.D., 2021. Cortex cis-regulatory switches establish scale colour identity and pattern diversity in *Heliconius*. *Elife* 10, e68549.
- Lloyd, V.J., Nadeau, N.J., 2021. The evolution of structural colour in butterflies. *Curr. Opin. Genet. Dev.* 69, 28–34.
- Locke, B., 1958. The Formation of Tracheae and Tracheoles in *Rhodnius prolixus*. *Q. J. Microsc. Sci.* 99, 29–46.
- Lüdecke, D., Ben-Shachar, M., Patil, I., Waggoner, P., Makowski, D., 2021. performance: An R Package for Assessment, Comparison and Testing of Statistical Models. *J. Open Source Softw.* 6, 3139.
- Maia, R., Eliason, C.M., Bitton, P.P., Doucet, S.M., Shawkey, M.D., 2013. pavo: An R package for the analysis, visualization and organization of spectral data. *Methods Ecol. Evol.* 4, 906–913.
- Mallet, J., Barton, N.H., 1989. Strong natural selection in a warning-color hybrid zone. *Evolution (N. Y.)* 43, 421–431.
- Mallet, J., Gilbert, L.E., 1995. Why are there so many mimicry rings? Correlations between habitat, behaviour and mimicry in *Heliconius* butterflies. *Biol. J. Linn. Soc.* 55, 159–180.
- Manceau, M., Domingues, V.S., Linnen, C.R., Rosenblum, E.B., Hoekstra, H.E., 2010. Convergence in pigmentation at multiple levels: Mutations, genes and function. *Philos. Trans. R. Soc. B Biol. Sci.* 365, 2439–2450.
- Martin, A., McCulloch, K.J., Patel, N.H., Briscoe, A.D., Gilbert, L.E., Reed, R.D., 2014. Multiple recent co-options of *Optix* associated with novel traits in adaptive butterfly wing radiations. *Evodevo* 5, doi: 10.1186/2041-9139-5-7.
- Mary, H., Brouhard, G.J., 2019. Kappa (κ): Analysis of Curvature in Biological Image Data using B-splines. *bioRxiv*.

- Matsuoka, Y., Monteiro, A., 2018. Melanin Pathway Genes Regulate Color and Morphology of Butterfly Wing Scales. *Cell Rep.* 24, 56–65.
- Mattson, W.J., 1980. Herbivory in Relation to Plant Nitrogen Content. *Annu. Rev. Ecol. Syst.* 11, 119–161.
- Mazo-Vargas, A., Concha, C., Livraghi, L., Massardo, D., Wallbank, R.W.R., Zhang, L., Papador, J.D., Martinez-Najera, D., Jiggins, C.D., Kronforst, M.R., Breuker, C.J., Reed, R.D., Patel, N.H., McMillan, W.O., Martin, A., 2017. Macroevolutionary shifts of *WntA* function potentiate butterfly wing-pattern diversity. *Proc. Natl. Acad. Sci.* 2, 201708149.
- McCulloch, K.J., Osorio, D., Briscoe, A.D., 2016. Sexual dimorphism in the compound eye of *Heliconius erato*: A nymphalid butterfly with at least five spectral classes of photoreceptor. *J. Exp. Biol.* 219, 2377–2387.
- McDougal, A.D., Kang, S., Yaqoob, Z., So, P.T.C., Kolle, M., 2021. In vivo visualization of butterfly scale cell morphogenesis in *Vanessa cardui*. *Proc. Natl. Acad. Sci. U. S. A.* 118, e2112009118.
- McGraw, K.J., Hill, G.E., 2000. Differential effects of endoparasitism on the expression of carotenoid- and melanin-based ornamental coloration. *Proc. R. Soc. B Biol. Sci.* 267, 1525–1531.
- McGraw, K.J., Mackillop, E.A., Dale, J., Hauber, M.E., 2002. Different colors reveal different information: How nutritional stress affects the expression of melanin- and structurally based ornamental plumage. *J. Exp. Biol.* 205, 3747–3755.
- McMillan, W.O., Livraghi, L., Concha, C., Hanly, J.J., 2020. From Patterning Genes to Process: Unraveling the Gene Regulatory Networks That Pattern *Heliconius* Wings. *Front. Ecol. Evol.* 8:221, doi: 10.3389/fevo.2020.00221.
- Meadows, M.G., Roudybush, T.E., McGraw, K.J., 2012. Dietary protein level affects iridescent coloration in Anna’s hummingbirds, *Calypte anna*. *J. Exp. Biol.* 215, 2742–2750.
- Menzel, C.M., Haydon, G.F., Doogan, V.J., Simpson, D.R., 1993. New standard leaf nutrient concentrations for passionfruit based on seasonal phenology and leaf composition. *J. Hortic. Sci.* 68, 215–229.
- Merrill, R.M., Chia, A., Nadeau, N.J., 2014. Divergent warning patterns contribute to assortative mating between incipient *Heliconius* species. *Ecol. Evol.* 4, 911–917.
- Merrill, R.M., Dasmahapatra, K.K., Davey, J.W., Dell’Aglia, D.D., Hanly, J.J., Huber, B., Jiggins, C.D., Joron, M., Kozak, K.M., Llaurens, V., Martin, S.H., Montgomery, S.H., Morris, J., Nadeau, N.J., Pinharanda, A.L., Rosser, N., Thompson, M.J., Vanjari, S., Wallbank, R.W.R., Yu, Q., 2015. The diversification of *Heliconius* butterflies: What have we learned in 150 years? *J. Evol. Biol.* 28, 1417–1438.
- Michielsen, K., Stavenga, D.G., 2008. Gyroid cuticular structures in butterfly wing scales: Biological photonic crystals. *J. R. Soc. Interface* 5, 85–94.
- Misteli, T., 2001. The concept of self-organization in cellular architecture. *J. Cell Biol.* 155, 181–185.
- Montgomerie, R., 2006. Analyzing colors In: In Hill, G.E and McGraw, K.J. *Bird Coloration Volume 1 Mechanisms and measurements*. In: *Bird Coloration*. Harvard University

Press, Cambridge, Massachusetts:

- Morehouse, N.I., 2014. Condition-dependent ornaments, life histories, and the evolving architecture of resource-use. *Integr. Comp. Biol.* 54, 591–600.
- Mouchet, S.R., Luke, S., McDonald, L.T., Vukusic, P., 2020. Optical costs and benefits of disorder in biological photonic crystals. *Faraday Discuss.* 223, 9–48.
- Mouchet, S.R., Vukusic, P., 2018. Structural Colours in Lepidopteran Scales, *Advances in Insect Physiology*.
- Moussian, B., 2010. Recent advances in understanding mechanisms of insect cuticle differentiation. *Insect Biochem. Mol. Biol.* 40, 363–375.
- Nadeau, N.J., 2016. Genes controlling mimetic colour pattern variation in butterflies. *Curr. Opin. Insect Sci.* 17, 24–31.
- Nagaraj, R., Adler, P.N., 2012. Dusky-like functions as a Rab11 effector for the deposition of cuticle during *Drosophila* bristle development. *Development* 139, 906–916.
- Nečas, D., Klapetek, P., 2012. Gwyddion: An open-source software for SPM data analysis. *Cent. Eur. J. Phys.* 10, 181–188.
- Nijhout, H., 1984. Colour pattern modification by coldshock in Lepidoptera. *J Embryol Exp Morphol* 81, 287–305.
- Nijhout, H.F., 1991. The development and evolution of butterfly wing patterns. Smithsonian Institution, Washington and London.
- Nunes, M.D.S., Arif, S., Schlötterer, C., McGregor, A.P., 2013. A perspective on micro-evo-devo: Progress and potential. *Genetics* 195, 625–634.
- Ohno, Y., Otaki, J.M., 2015. Spontaneous long-range calcium waves in developing butterfly wings. *BMC Dev. Biol.* 15:17, doi: 10.1186/s12861-015-0067-8.
- Onelli, O.D., Kamp, T. Van De, Skepper, J.N., Powell, J., Rolo, T.D.S., Baumbach, T., Vignolini, S., 2017. Development of structural colour in leaf beetles. *Sci. Rep.* 7, <https://doi.org/10.1038/s41598-017-01496-8>.
- Ostrowski, S., Dierick, H.A., Bejsovec, A., 2002. Genetic control of cuticle formation during embryonic development of *Drosophila melanogaster*. *Genetics* 161, 171–182.
- Overton, J., 1966. Microtubules and microfibrils in morphogenesis of the scale cells of *Ephestia kühniella*. *J. Cell Biol.* 29, 293–305.
- Öztürk-Çolak, A., Moussian, B., Araújo, S.J., Casanova, J., 2016. A feedback mechanism converts individual cell features into a supracellular ECM structure in *drosophila* trachea. *Elife* 5, :e09373 <https://doi.org/10.7554/eLife.09373.001>.
- Parker, A.R., 2000. 515 Million Years of Structural Colour. *J. Opt. A Pure Appl. Opt.* 2, R15–R28.
- Parnell, A.J., Bradford, J.E., Curran, E. V., Washington, A.L., Adams, G., Brien, M.N., Burg, S.L., Morochz, C., Fairclough, J.P.A., Vukusic, P., Martin, S.J., Doak, S., Nadeau, N.J., 2018. Wing scale ultrastructure underlying convergent and divergent iridescent colours in mimetic *Heliconius* butterflies. *J. R. Soc. Interface* 15, 20170948. <http://dx.doi.org/10.1098/rsif.2017.0948>.

- Pegram, K. V, Nahm, A.C., Rutowski, R.L., 2013. Warning color changes in response to food deprivation in the pipevine swallowtail butterfly, *Battus philenor* Kimberly. *J. Insect Sci.* 13, 1536–2442.
- Peng, C.L., Mazo-Vargas, A., Brack, B.J., Reed, R.D., 2020. Multiple roles for laccase2 in butterfly wing pigmentation, scale development, and cuticle tanning. *Evol. Dev.* 22, 336–341.
- Pertea, M., Pertea, G.M., Antonescu, C.M., Chang, T.C., Mendell, J.T., Salzberg, S.L., 2015. StringTie enables improved reconstruction of a transcriptome from RNA-seq reads. *Nat. Biotechnol.* 33, 290–295.
- Piszter, G., Kertész, K., Horváth, Z.E., Bálint, Z., Biró, L., 2019. Reproducible phenotype alteration due to prolonged cooling of the pupae of *Polyommatus icarus* butterflies. *PLoS One* 14, e0225388.
- Pollard, T.D., Cooper, J.A., Pollard, T.D., Cooper, J.A., 2009. Actin , a Central Player in Cell Shape and Movement. *Science* (80-.). 326, 1208–1212.
- Pollitt, A.Y., Insall, R.H., 2009. WASP and SCAR/WAVE proteins: the drivers of actin assembly. *J. Cell Sci.* 122, 2575–2578.
- Potyrailo, R.A., Bonam, R.K., Hartley, J.G., Starkey, T.A., Vukusic, P., Vasudev, M., Bunning, T., Naik, R.R., Tang, Z., Palacios, M.A., Larsen, M., Le Tarte, L.A., Grande, J.C., Zhong, S., Deng, T., 2015. Towards outperforming conventional sensor arrays with fabricated individual photonic vapour sensors inspired by *Morpho* butterflies. *Nat. Commun.* 6, <https://doi.org/10.1038/ncomms8959>.
- Prakash, A., Finet, C., Banerjee, T. Das, Saranathan, V., Monteiro, A., 2022. Antennapedia and optix regulate metallic silver wing scale development and cell shape in *Bicyclus anynana* butterflies. *Cell Rep.* 40, 111052.
- Prakash, A., Monteiro, A., 2020. Cell dissociation from butterfly pupal wing tissues for single-cell RNA sequencing. *Methods Protoc.* 3, doi:10.3390/mps3040072.
- Prum, R.O., Quinn, T., Torres, R.H., 2006. Anatomically diverse butterfly scales all produce structural colours by coherent scattering. *J. Exp. Biol.* 209, 748–765.
- R Core team, 2018. R: A language and environment for statistical computing. R Foundation for Statistical Computing.
- Reed, R.D., 2004. Evidence for Notch-mediated lateral inhibition in organizing butterfly wing scales. *Dev. Genes Evol.* 214, 43–46.
- Reed, R.D., Papa, R., Martin, A., Hines, H.M., Counterman, B.A., Pardo-Diaz, C., Jiggins, C.D., Chamberlain, N.L., Kronforst, M.R., Chen, R., Halder, G., Nijhout, H.F., Mcmillan, W.O., 2011. optix Drives the Repeated Convergent Evolution of Butterfly Wing Pattern Mimicry Robert. *Science* (80-.). 333, 1137–1141.
- Ren, A., Day, C.R., Hanly, J.J., Counterman, B.A., Morehouse, N.I., Martin, A., 2020. Convergent Evolution of Broadband Reflectors Underlies Metallic Coloration in Butterflies. *Front. Ecol. Evol.* 8, doi: 10.3389/fevo.2020.00206.
- Robinson, M.D., McCarthy, D.J., Smyth, G.K., 2009. edgeR: A Bioconductor package for differential expression analysis of digital gene expression data. *Bioinformatics* 26, 139–140.

- Robinson, M.D., Oshlack, A., 2010. A scaling normalization method for differential expression analysis of RNA-seq data. *Genome Biol.* 11:R25, <http://genomebiology.com/2010/11/3/R25>.
- Roch, F., Alonso, C.R., Akam, M., 2003. *Drosophila* miniature and dusky encode ZP proteins required for cytoskeletal reorganisation during wing morphogenesis. *J. Cell Sci.* 116, 1199–1207.
- Rodriguez-Caro, F., Fenner, J., Bhardwaj, S., Cole, J., Benson, C., Colombara, A.M., Papa, R., Brown, M.W., Martin, A., Range, R.C., Counterman, B.A., 2021. Novel Doublesex Duplication Associated with Sexually Dimorphic Development of Dogface Butterfly Wings. *Mol. Biol. Evol.* 38, 5021–5033.
- Rodríguez, A., Mundy, N.I., Ibáñez, R., Pröhl, H., 2020. Being red, blue and green: The genetic basis of coloration differences in the strawberry poison frog (*Oophaga pumilio*). *BMC Genomics* 21:301, doi: <https://doi.org/10.1186/s12864-020-6719-5>.
- Roland, J., 1982. Melanism and diel activity of alpine *Colias* (Lepidoptera: Pieridae). *Oecologia* 53, 214–221.
- Rosenblum, E.B., 2006. Convergent evolution and divergent selection: Lizards at the white sands ecotone. *Am. Nat.* 167, doi: 10.1086/498397.
- Rutowski, R.L., 1985. Evidence for Mate Choice in a Sulphur Butterfly (*Colias eurytheme*). *Z. Tierpsychol.* 70, 103–114.
- Sackton, T.B., Clark, N., 2019. Convergent evolution in the genomics era: New insights and directions. *Philos. Trans. R. Soc. B Biol. Sci.* 374, 24–27.
- Sadier, A., Santana, S.E., Sears, K.E., 2020. The Role of Core and Variable Gene Regulatory Network Modules in Tooth Development and Evolution. *Integr. Comp. Biol.* doi: <https://doi.org/10.1093/icb/icaa116>.
- Saito, A., 2011. Material design and structural color inspired by biomimetic approach. *Sci. Technol. Adv. Mater.* 12, 064709.
- Saranathan, V., Osuji, C.O., Mochrie, S.G.J., Noh, H., Narayanan, S., 2010. Crystals in Butterfly Wing Scales. *Proc. Natl. Acad. Sci. U. S. A.* 107, 11676–11681.
- Sarkar, D., Andrews, F., Klepeis, N., Larsson, J., Murrell, P., 2021. Package ‘lattice’ R package version 0.20-44.
- Schindelin, J., Arganda-Carrera, I., Frise, E., Verena, K., Mark, L., Tobias, P., Stephan, P., Curtis, R., Stephan, S., Benjamin, S., Jean-Yves, T., Daniel, J.W., Volker, H., Kevin, E., Pavel, T., Albert, C., 2012. Fiji: an open-source platform for biological-image analysis. *Nat. Methods* 9, 676–682.
- Schmitz, H., 1994. Thermal characterization of butterfly wings-1. Absorption in relation to different color, surface structure and basking type. *J. Therm. Biol.* 19, 403–412.
- Schneider, C.A., Rasband, W.S., Eliceiri, K.W., 2012. NIH Image to ImageJ : 25 years of Image Analysis. *Nat. Mater.* 9, 671–675.
- Scolari, L.M., Hancock, R.D., Hedley, P.E., Morris, J., Smith, K., Graham, J., 2021. Combining qtl mapping and gene expression analysis to elucidate the genetic control of ‘crumbly’ fruit in red raspberry (*Rubus idaeus* l.). *Agronomy* 11, doi: <https://>

doi.org/10.3390/agronomy11040794 Cel.

- Seago, A.E., Oberprieler, R., Saranathan, V.K., 2019. Evolution of insect iridescence: Origins of three-dimensional photonic crystals in weevils (Coleoptera: Curculionoidea). *Integr. Comp. Biol.* 59, 1664–1672.
- Seipel, K., Medley, Q.G., Kedersha, N.L., Zhang, X.A., O'Brien, S.P., Serra-Pages, C., Hemler, M.E., Streuli, M., 1999. Trio amino-terminal guanine nucleotide exchange factor domain expression promotes actin cytoskeleton reorganization, cell migration and anchorage-independent cell growth. *J. Cell Sci.* 112, 1825–1834.
- Shapira, S., Bakhrat, A., Bitan, A., Abdu, U., 2011. The *Drosophila* javelin Gene Encodes a Novel Actin-Associated Protein Required for Actin Assembly in the Bristle. *Mol. Cell. Biol.* 31, 4582–4592.
- Shawkey, M.D., Estes, A.M., Siefferman, L.M., Hill, G.E., 2003. Nanostructure predicts intraspecific variation in ultraviolet-blue plumage colour. *Proc. R. Soc. B Biol. Sci.* 270, 1455–1460.
- Shevtsova, E., Hansson, C., Janzen, D.H., Kjærandsen, J., 2011. Stable structural color patterns displayed on transparent insect wings. *Proc. Natl. Acad. Sci. U. S. A.* 108, 668–673.
- Shi, N.N., Tsai, C.C., Camino, F., Bernard, G.D., Yu, N., Wehner, R., 2015. Keeping cool: Enhanced optical reflection and radiative heat dissipation in Saharan silver ants. *Science* (80-.). 349, 298–301.
- Siddique, R.H., Donie, Y.J., Gomard, G., Yalamanchili, S., Merdzhanova, T., Lemmer, U., Hölscher, H., 2017. Bioinspired phase-separated disordered nanostructures for thin photovoltaic absorbers. *Sci. Adv.* 3, e1700232.
- Siddique, R.H., Vignolini, S., Bartels, C., Wacker, I., Hölscher, H., 2016. Colour formation on the wings of the butterfly *Hypolimnys salmactis* by scale stacking. *Sci. Rep.* 6, <https://doi.org/10.1038/srep3620410>.
- Siefferman, L., Hill, G.E., 2007. The effect of rearing environment on blue structural coloration of eastern bluebirds (*Sialia sialis*). *Behav. Ecol. Sociobiol.* 61, 1839–1846.
- Silberglied, R.E., 1984. Visual Communication and Sexual Selection. *Biol. Butterflies. Symp. R. Entomol. Soc. London*, No. 11 207–223.
- Silberglied, R.E., Taylor, O.R., 1973. Ultraviolet Differences between the Sulphur Butterflies, *Colias eurytheme* and *C. philodice*, and a Possible Isolating Mechanism. *Nature* 241, 406–408.
- Simons, M.J.P., Cohen, A.A., Verhulst, S., 2012. What does carotenoid-dependent coloration tell? Plasma carotenoid level signals immunocompetence and oxidative stress state in birds—a meta-analysis. *PLoS One* 7, e43088.
- Slegers, N., Heilman, M., Cranford, J., Lang, A., Yoder, J., Habegger, M.L., 2017. Beneficial aerodynamic effect of wing scales on the climbing flight of butterflies. *Bioinspiration and Biomimetics* 12, 016013.
- Smith, S.J., Rebeiz, M., Davidson, L., 2018. From pattern to process: studies at the interface of gene regulatory networks, morphogenesis, and evolution. *Curr. Opin. Genet. Dev.* 51, 103–110.

- Sommer, R.J., 2009. The future of evo–devo: model systems and evolutionary theory Ralf. *Nat. Rev. Genet.* 10, 416–422.
- Stavenga, D.G., Leertouwer, H.L., Wilts, B.D., 2014. Coloration principles of nymphaline butterflies - thin films, melanin, ommochromes and wing scale stacking. *J. Exp. Biol.* 217, 2171–2180.
- Steger, C., 1998. An unbiased detector of curvilinear structures. *IEEE Trans. Pattern Anal. Mach. Intell.* 20, 113–125.
- Stern, D.L., 2013. The genetic causes of convergent evolution. *Nat. Rev. Genet.* 14, 751–764.
- Strobl, G.R., Schneider, M., 1980. Direct Evaluation of the Electron Density Correlation Function of Partially Crystalline Polymers. *J. Polym. Sci.* 18, 1343–1359.
- Sun, J., Bhushan, B., Tong, J., 2013. Structural coloration in nature. *RSC Adv.* 3, 14862–14889.
- Surmacki, A., Stępniewski, J., Stępniewska, M., 2015. Juvenile sexual dimorphism, dichromatism and condition- dependent signaling in a bird species with early pair bonds. *J. Ornithol.* 156, 65–73.
- Sweeney, A., Jiggins, C., Johnsen, S., 2003. Polarized light as a butterfly mating signal. *Nature* 423, 31–32.
- Szymborska, A., Marco, A. De, Daigle, N., Cordes, V.C., Briggs, J.A.G., Ellenberg, J., 2013. Nuclear Pore Scaffold Structure Analyzed by Super-Resolution Microscopy and Particle Averaging. *Science* (80-.). 341, 655–659.
- Talloon, W., Van Dyck, H., Lens, L., 2004. The cost of melanization: Butterfly wing coloration under environmental stress. *Evolution* (N. Y). 58, 360–366.
- Tendolkar, A., Pomerantz, A.F., Heryanto, C., Shirk, P.D., Patel, N.H., Martin, A., 2021. Ultrabithorax Is a Micromanager of Hindwing Identity in Butterflies and Moths. *Front. Ecol. Evol.* 9:643661., doi: 10.3389/fevo.2021.643661.
- Terasaki, M., Chen, L.B., Fujiwara, K., 1986. Microtubules and the endoplasmic reticulum are highly interdependent structures. *J. Cell Biol.* 103, 1557–1568.
- Terenius, O., Papanicolaou, A., Garbutt, J.S., Eleftherianos, I., Huvenne, H., Kanginakudru, S., Albrechtsen, M., An, C., Aymeric, J.L., Barthel, A., Bebas, P., Bitra, K., Bravo, A., Chevalier, F., Collinge, D.P., Crava, C.M., de Maagd, R.A., Duvic, B., Erlandson, M., Faye, I., Felföldi, G., Fujiwara, H., Futahashi, R., Gandhe, A.S., Gatehouse, H.S., Gatehouse, L.N., Giebultowicz, J.M., Gómez, I., Grimmlikhuijzen, C.J.P., Groot, A.T., Hauser, F., Heckel, D.G., Hegedus, D.D., Hrycaj, S., Huang, L., Hull, J.J., Iatrou, K., Iga, M., Kanost, M.R., Kotwica, J., Li, C., Li, J., Liu, J., Lundmark, M., Matsumoto, S., Meyering-Vos, M., Millichap, P.J., Monteiro, A., Mrinal, N., Niimi, T., Nowara, D., Ohnishi, A., Oostra, V., Ozaki, K., Papakonstantinou, M., Popadic, A., Rajam, M. V., Saenko, S., Simpson, R.M., Soberón, M., Strand, M.R., Tomita, S., Toprak, U., Wang, P., Wee, C.W., Whyard, S., Zhang, W., Nagaraju, J., French-Constant, R.H., Herrero, S., Gordon, K., Swevers, L., Smagghe, G., 2011. RNA interference in Lepidoptera: An overview of successful and unsuccessful studies and implications for experimental design. *J. Insect Physiol.* 57, 231–245.
- Thayer, R.C., Allen, F.I., Patel, N.H., 2020. Structural color in *Junonia* butterflies evolves by tuning scale lamina thickness. *Elife* 9, :e52187. doi: <https://doi.org/10.7554/eLife.52187>.

The Gimp Development Team, 2014. GIMP.

Thurmond, J., Goodman, J.L., Strelets, V.B., Attrill, H., Gramates, L.S., Marygold, S.J., Matthews, B.B., Millburn, G., Antonazzo, G., Trovisco, V., Kaufman, T.C., Calvi, B.R., Perrimon, N., Gelbart, S.R., Agapite, J., Broll, K., Crosby, L., Dos Santos, G., Emmert, D., Falls, K., Jenkins, V., Sutherland, C., Tabone, C., Zhou, P., Zytkevich, M., Brown, N., Garapati, P., Holmes, A., Larkin, A., Pilgrim, C., Urbano, P., Czoch, B., Cripps, R., Baker, P., 2019. FlyBase 2.0: The next generation. *Nucleic Acids Res.* 47, D759–D765.

Tiede, C., Bedford, R., Heseltine, S.J., Smith, G., Wijetunga, I., Ross, R., Alqallaf, D., Roberts, A.P.E., Balls, A., Curd, A., Hughes, R.E., Martin, H., Needham, S.R., Zanetti-Domingues, L.C., Sadigh, Y., Peacock, T.P., Tang, A.A., Gibson, N., Kyle, H., Platt, G.W., Ingram, N., Taylor, T., Coletta, L.P., Manfield, I., Knowles, M., Bell, S., Esteves, F., Maqbool, A., Prasad, R.K., Drinkhill, M., Bon, R.S., Patel, V., Goodchild, S.A., Martin-Fernandez, M., Owens, R.J., Nettleship, J.E., Webb, M.E., Harrison, M., Lippiat, J.D., Ponnambalam, S., Peckham, M., Smith, A., Ferrigno, P.K., Johnson, M., McPherson, M.J., Tomlinson, D.C., 2017. Affimer proteins are versatile and renewable affinity reagents. *Elife* 6, e24903.

Tikhomirova, M.S., Kadosh, A., Saukko-Paavola, A.J., Shemesh, T., Klemm, R.W., 2022. A role for endoplasmic reticulum dynamics in the cellular distribution of microtubules. *Proc. Natl. Acad. Sci. U. S. A.* 119, e2104309119.

Tilney, L.G., Connelly, P., Smith, S., Guild, G.M., 1996. F-Actin Bundles in *Drosophila* Bristles Are Assembled from Modules Composed of Short Filaments. *J. Cell Biol.* 135, 1291–1308.

Tilney, L.G., Connelly, P.S., Ruggiero, L., Vranich, K.A., Guild, G.M., Stocks, D., 2003. Actin Filament Turnover Regulated by Cross-linking Accounts for the Size, Shape, Location, and Number of Actin Bundles in *Drosophila* Bristles 14, 3953–3966.

Tilney, L.G., Connelly, P.S., Vranich, K.A., Shaw, M.K., Guild, G.M., 1998. Why Are Two Different Cross-linkers Necessary for Actin Bundle Formation In Vivo and What Does Each Cross-link Contribute? 143, 121–133.

Tilney, L.G., Connelly, P.S., Vranich, K.A., Shaw, M.K., Guild, G.M., 2000a. Actin filaments and microtubules play different roles during bristle elongation in *Drosophila* 1265, 1255–1265.

Tilney, L.G., Connelly, P.S., Vranich, K.A., Shaw, M.K., Guild, G.M., Stocks, D., 2000b. Regulation of Actin Filament Cross-linking and Bundle Shape in *Drosophila* Bristles. *J. Cell Biol.* 148, 87–99.

Tilney, L.G., DeRosier, D.J., 2005. How to make a curved *Drosophila* bristle using straight actin bundles. *Pnas* 102, 18785–18792.

Tilney, L.G., Tilney, M.S., Guild, G.M., 1995. F Actin Bundles in *Drosophila* Bristles I. Two Filament Cross-links Are Involved in Bundling. *J. Cell Biol.* 130, 629–638.

Trigo, S., Gomes, A.C.R., Cardoso, S.C., Teixeira, M., Cardoso, G.C., Soares, M.C., 2020. Cleaner blues: Condition-dependent colour and cleaner fish service quality. *Behav. Processes* 181, 104246.

Trzeciak, T.M., Vukusic, P., 2009. Photonic crystal fiber in the polychaete worm *Pherusa* sp. *Phys. Rev. E* 80, <https://doi.org/10.1103/PhysRevE.80.061908>.

- Trzeciak, T.M., Wilts, B.D., Stavenga, D.G., Vukusic, P., 2012. Variable multilayer reflection together with long-pass filtering pigment determines the wing coloration of papilionid butterflies of the nireus group. *Opt. Express* 20, 8877.
- Uv, A., Moussian, B., 2010. The apical plasma membrane of *Drosophila* embryonic epithelia. *Eur. J. Cell Biol.* 89, 208–211.
- Van Belleghem, S.M., Lewis, J.J., Rivera, E.S., Papa, R., 2021. Heliconius butterflies: a window into the evolution and development of diversity. *Curr. Opin. Genet. Dev.* 69, 72–81.
- Vischer, N., 2011. PeakFinder Tool.
- Vukusic, P., 2006. Structural colour in Lepidoptera. *Curr. Biol.* 16, 621–623.
- Vukusic, P., Sambles, J.R., Lawrence, C.R., Wootton, R.J., 1999. Quantified interference and diffraction in single Morpho butterfly scales. *Proc. R. Soc. B Biol. Sci.* 266, 1403–1411.
- Waldron, S.J., Endler, J.A., Valkonen, J.K., Honma, A., Dobler, S., Mappes, J., 2017. Experimental evidence suggests that specular reflectance and glossy appearance help amplify warning signals. *Sci. Rep.* 7, <https://doi.org/10.1038/s41598-017-00217-5>.
- Wasik, B.R., Liew, S.F., Lilien, D.A., Dinwiddie, A.J., Noh, H., Cao, H., Monteiro, A., 2014. Artificial selection for structural color on butterfly wings and comparison with natural evolution. *Proc. Natl. Acad. Sci.* 111, 12109–12114.
- Weaver, R.J., Santos, E.S.A., Tucker, A.M., Wilson, A.E., Hill, G.E., 2018. Carotenoid metabolism strengthens the link between feather coloration and individual quality. *Nat. Commun.* 9:73, doi: 10.1038/s41467-017-02649-z.
- Wedlich-Söldner, R., Betz, T., 2018. Self-organization: The fundament of cell biology. *Philos. Trans. R. Soc. B Biol. Sci.* 373, 20170103.
- Wee, J.L.Q., Das Banerjee, T., Prakash, A., Seah, K.S., Monteiro, A., 2022. Distal-less and spalt are distal organisers of pierid wing patterns. *Evodevo* 13:12, doi: <https://doi.org/10.1186/s13227-022-00197-2>.
- Wegel, E., Göhler, A., Lagerholm, B.C., Wainman, A., Uphoff, S., Kaufmann, R., Dobbie, I.M., 2016. Imaging cellular structures in super-resolution with SIM, STED and Localisation Microscopy: A practical comparison. *Sci. Rep.* 6, 27290.
- Weller, H.I., Westneat, M.W., 2019. Quantitative color profiling of digital images with earth mover's distance using the R package colordistance. *PeerJ* 7:e6398, doi: 10.7717/peerj.6398.
- Westerman, E.L., VanKuren, N.W., Massardo, D., Tenger-Trolander, A., Zhang, W., Hill, R.I., Perry, M., Bayala, E., Barr, K., Chamberlain, N., Douglas, T.E., Buerkle, N., Palmer, S.E., Kronforst, M.R., 2018. Aristaless Controls Butterfly Wing Color Variation Used in Mimicry and Mate Choice. *Curr. Biol.* 28, 3469–3474.
- White, T.E., 2020. Structural colours reflect individual quality: A meta-analysis. *Biol. Lett.* 16, 20200001. <http://dx.doi.org/10.1098/rsbl.2020.0001>.
- White, T.E., Locke, A., Latty, T., 2021. Heightened condition dependent expression of structural coloration in the faces, but not wings, of male and female flies. *Curr. Zool.* 1–8, <https://doi.org/10.1093/cz/zoab087>.

- White, T.E., Zeil, J., Kemp, D.J., 2015. Signal design and courtship presentation coincide for highly biased delivery of an iridescent butterfly mating signal. *Evolution* (N. Y). 69, 14–25.
- Wickham, H., 2016. *ggplot2: Elegant Graphics for Data Analysis*.
- Wickham, S., Large, M.C.J., Poladian, L., Jermiin, L.S., 2006. Exaggeration and suppression of iridescence: The evolution of two-dimensional butterfly structural colours. *J. R. Soc. Interface* 3, 99–108.
- Willot, Q., Simonis, P., Vigneron, J.P., Aron, S., 2016. Total internal reflection accounts for the bright color of the saharan silver ant. *PLoS One* 11, e0152325. doi:10.1371/journal.pone.0152325.
- Wilts, B.D., Clode, P.L., Patel, N.H., Schröder-Turk, G.E., 2019. Nature’s functional nanomaterials: Growth or self-assembly? *MRS Bull.* 44, 119–123.
- Wilts, B.D., Ijbema, N., Stavenga, D.G., 2014. Pigmentary and photonic coloration mechanisms reveal taxonomic relationships of the Cattlehearts (Lepidoptera: Papilionidae: Parides). *BMC Evol. Biol.* 14, <http://www.biomedcentral.com/1471-2148/14/160>.
- Wilts, B.D., Michielsen, K., Kuipers, J., Raedt, H. De, Stavenga, D.G., 2012. Brilliant camouflage : photonic crystals in the diamond weevil , *Entimus imperialis*. *Proc. R. Soc. B Biol. Sci.* 279, 2524–2530.
- Wilts, B.D., Vey, A.J.M., Briscoe, A.D., Stavenga, D.G., 2017a. Longwing (*Heliconius*) butterflies combine a restricted set of pigmentary and structural coloration mechanisms. *BMC Evol. Biol.* 17:226, doi: 10.1186/s12862-017-1073-1.
- Wilts, B.D., Zubiri, B.A., Klatt, M.A., Butz, B., Fischer, M.G., Kelly, S.T., Spiecker, E., Steiner, U., Schröder-Turk, G.E., 2017b. Butterfly gyroid nanostructures as a time-frozen glimpse of intracellular membrane development. *Sci. Adv.* 3, e1603119.
- Woronik, A., Tunström, K., Perry, M.W., Neethiraj, R., Stefanescu, C., Celorio-Mancera, M. de la P., Brattström, O., Hill, J., Lehmann, P., Käkälä, R., Wheat, C.W., 2019. A transposable element insertion is associated with an alternative life history strategy. *Nat. Commun.* 10:5757, <https://doi.org/10.1038/s41467-019-13596-2>.
- Wu, J., Wang, H., Guo, X., Chen, J., 2016. Cofilin-mediated actin dynamics promotes actin bundle formation during *Drosophila* bristle development. *Mol. Biol. Cell* 27, 2554–2564.
- Xie, H., Zhang, S., Li, S., 2006. Chitin and chitosan dissolved in ionic liquids as reversible sorbents of CO₂. *Green Chem.* 8, 630–633.
- Young, F.J., Montgomery, S.H., 2020. Pollen feeding in *Heliconius* butterflies: The singular evolution of an adaptive suite: Pollen feeding in *Heliconius* butterflies. *Proc. R. Soc. B Biol. Sci.* 287, 20201304. doi: <http://dx.doi.org/10.1098/rspb.2020>.
- Yu, C.C., Barry, N.C., Wassie, A.T., Sinha, A., Bhattacharya, A., Asano, S., Zhang, C., Chen, F., Hobert, O., Goodman, M.B., Haspel, G., Boyden, E.S., 2020. Expansion microscopy of *c. Elegans*. *Elife* 9, e46249.
- Yu, R., Liu, W., Li, D., Zhao, X., Ding, G., Zhang, M., Ma, E., Zhu, K.Y., Li, S., Moussian, B., Zhang, J., 2016. Helicoidal organization of chitin in the cuticle of the migratory

- locust requires the function of the chitin deacetylase2 enzyme (LmCDA2). *J. Biol. Chem.* 291, 24352–24363.
- Yu, R.R., Liu, W.M., Zhao, X.M., Zhang, M., Li, D.Q., Zuber, R., Ma, E.B., Zhu, K.Y., Moussian, B., Zhang, J.Z., 2019. LmCDA1 organizes the cuticle by chitin deacetylation in *Locusta migratoria*. *Insect Mol. Biol.* 28, 301–312.
- Zhang, D., Zhang, W., Gu, J., Fan, T., Liu, Q., Su, H., Zhu, S., 2015. Inspiration from butterfly and moth wing scales: Characterization, modeling, and fabrication. *Prog. Mater. Sci.* 68, 67–96.
- Zhang, L., Mazo-Vargas, A., Reed, R.D., 2017. Single master regulatory gene coordinates the evolution and development of butterfly color and iridescence. *Proc. Natl. Acad. Sci.* 114, 10707–10712.
- Zhang, Q., Mey, W., Ansoerge, J., Starkey, T.A., McDonald, L.T., McNamara, M.E., Jarzembowski, E.A., Wichard, W., Kelly, R., Ren, X., Chen, J., Zhang, H., Wang, B., 2018. Fossil scales illuminate the early evolution of lepidopterans and structural colors. *Sci. Adv.* 4, e1700988.
- Zhang, S., Chen, Y., 2015. Nanofabrication and coloration study of artificial *Morpho* butterfly wings with aligned lamellae layers. *Sci. Rep.* 5:16637, doi: 10.1038/srep16637.
- Zhang, W., Zhang, D., Fan, T., Ding, J., Gu, J., Guo, Q., Ogawa, H., 2006. Biomimetic zinc oxide replica with structural color using butterfly (*Ideopsis similis*) wings as templates. *Bioinspiration and Biomimetics* 1, 89–95.
- Zhou, Q., Yu, L., Shen, X., Li, Y., Xu, W., Yi, Y., Zhang, Z., 2009. Homology of dipteran bristles and lepidopteran scales: Requirement for the *Bombyx mori* achaete-scute homologue ASH2. *Genetics* 183, 619–627.
- Zhu, Y., Hao, J., Li, W., Yang, J., Dong, E., 2019. A new robotic tactile sensor with biomimetic structural colour inspired by *Morpho* butterflies. *Bioinspiration and Biomimetics* 14, 056010.
- Zitserman, D., Roegiers, F., 2011. Live-cell imaging of sensory organ precursor cells in intact *Drosophila* pupae. *J. Vis. Exp.* e2706, doi:10.3791/2706.

Appendix

Abbreviations

3-OHK	3-hydroxy-DL-kynurenine (pigment)
AFM	Atomic force microscopy
AF	Alexa Fluor (dye)
Blast	Basic Local Alignment Search Tool
BR (values)	Blue-red values
CBD	Chitin Binding Domain
Cyto-D	Cytochalasin D
CRISPR-Cas9	Clustered regularly interspaced short palindromic repeats - CRISPR-associated protein 9 (gene editing)
DAPI	4',6-diamidino-2-phenylindole
DE(G)	Differentially expressed (gene)
DMSO	Dimethyl sulfoxide
EdgeR	Empirical Analysis of Digital Gene Expression Data in R (Robinson et al., 2009)
F-actin	Filamentous actin
FDR	False discovery rate
FW	Forewing
GIM	Graces insect medium
GO	Gene ontology
GRN	Gene Regulatory Network
GSEA	Gene Set Enrichment Analysis (Alexa and Rahnenführer, 2021)
HISAT	Hierarchical indexing for spliced alignment of transcripts
HW	Hindwing
(L)FC	(Log) fold change
LOD (score)	Logarithm of the odds (score)
PBS(T)	Phosphate buffered saline (with Triton)
PFA	Paraformaldehyde
QTL	Quantitative Trait Loci
SEM	Scanning electron microscopy
SIM	Structured Illumination Microscopy
SiR (dye)	Silicon-rhodamine (dye)
STED	Stimulated emission depletion (microscopy)
TMM	Trimmed mean of M values (package EdgeR: (Robinson et al., 2009)
tmm	Transfer-matrix method (optics)
WGA	Wheat germ agglutinin

Research



Cite this article: Brien MN *et al.* 2022

The genetic basis of structural colour variation in mimetic *Heliconius* butterflies. *Phil. Trans. R. Soc. B* **377**: 20200505.

<https://doi.org/10.1098/rstb.2020.0505>

Received: 7 October 2021

Accepted: 18 December 2021

One contribution of 11 to a theme issue 'Genetic basis of adaptation and speciation: from loci to causative mutations'.

Subject Areas:

genetics, evolution, biophysics

Keywords:

structural colour, iridescence, gene expression, *Heliconius*, QTL, convergence

Author for correspondence:

Nicola J. Nadeau

e-mail: n.nadeau@sheffield.ac.uk

[†]These authors contributed equally to this study.

Electronic supplementary material is available online at <https://doi.org/10.6084/m9.figshare.c.5958667>.

The genetic basis of structural colour variation in mimetic *Heliconius* butterflies

Melanie N. Brien^{1,†}, Juan Enciso-Romero^{1,2,†}, Victoria J. Lloyd^{1,†}, Emma V. Curran¹, Andrew J. Parnell³, Carlos Morochz⁴, Patricio A. Salazar¹, Pasi Rastas⁵, Thomas Zinn⁶ and Nicola J. Nadeau¹

¹Ecology and Evolutionary Biology, School of Biosciences, The University of Sheffield, Alfred Denny Building, Western Bank, Sheffield S10 2TN, UK

²Biology Program, Faculty of Natural Sciences, Universidad del Rosario, Bogotá, Colombia

³Department of Physics and Astronomy, The University of Sheffield, Hicks Building, Hounsfield Road, Sheffield S3 7RH, UK

⁴Biology and Research Department, Mashpi Lodge, Ecuador

⁵Institute of Biotechnology, 00014 University of Helsinki, Finland

⁶ESRF - The European Synchrotron, 38043 Grenoble Cedex 9, France

AJP, 0000-0001-8606-8644; NJN, 0000-0002-9319-921X

Structural colours, produced by the reflection of light from ultrastructures, have evolved multiple times in butterflies. Unlike pigmentary colours and patterns, little is known about the genetic basis of these colours. Reflective structures on wing-scale ridges are responsible for iridescent structural colour in many butterflies, including the Müllerian mimics *Heliconius erato* and *Heliconius melpomene*. Here, we quantify aspects of scale ultrastructure variation and colour in crosses between iridescent and non-iridescent subspecies of both of these species and perform quantitative trait locus (QTL) mapping. We show that iridescent structural colour has a complex genetic basis in both species, with offspring from crosses having a wide variation in blue colour (both hue and brightness) and scale structure measurements. We detect two different genomic regions in each species that explain modest amounts of this variation, with a sex-linked QTL in *H. erato* but not *H. melpomene*. We also find differences between species in the relationships between structure and colour, overall suggesting that these species have followed different evolutionary trajectories in their evolution of structural colour. We then identify genes within the QTL intervals that are differentially expressed between subspecies and/or wing regions, revealing likely candidates for genes controlling structural colour formation.

This article is part of the theme issue 'Genetic basis of adaptation and speciation: from loci to causative mutations'.

1. Introduction

Structural colours are some of the most vivid and striking colours found in nature. They are formed from the reflection and refraction of light from physical ultrastructures and examples of these can be found in nearly all groups of organisms. The structural colours of butterflies and moths are among the best described and play diverse roles, including initiation of courtship and mating behaviour [1,2], sex and species discrimination [3], long-distance mate recognition [4] signalling of quality and adult condition [5], and possibly predator avoidance [6,7].

Butterflies and moths have evolved several mechanisms of structural colour production by modifying different components of wing-scale morphology [8,9]. Scales typically consist of a flat lower lamina connected to an upper lamina by pillar-like trabeculae, with a small space separating the upper and lower laminae (figure 1). The lower lamina can act as a thin film reflector that produces hues ranging from violet to green depending on its thickness [10–12]. The

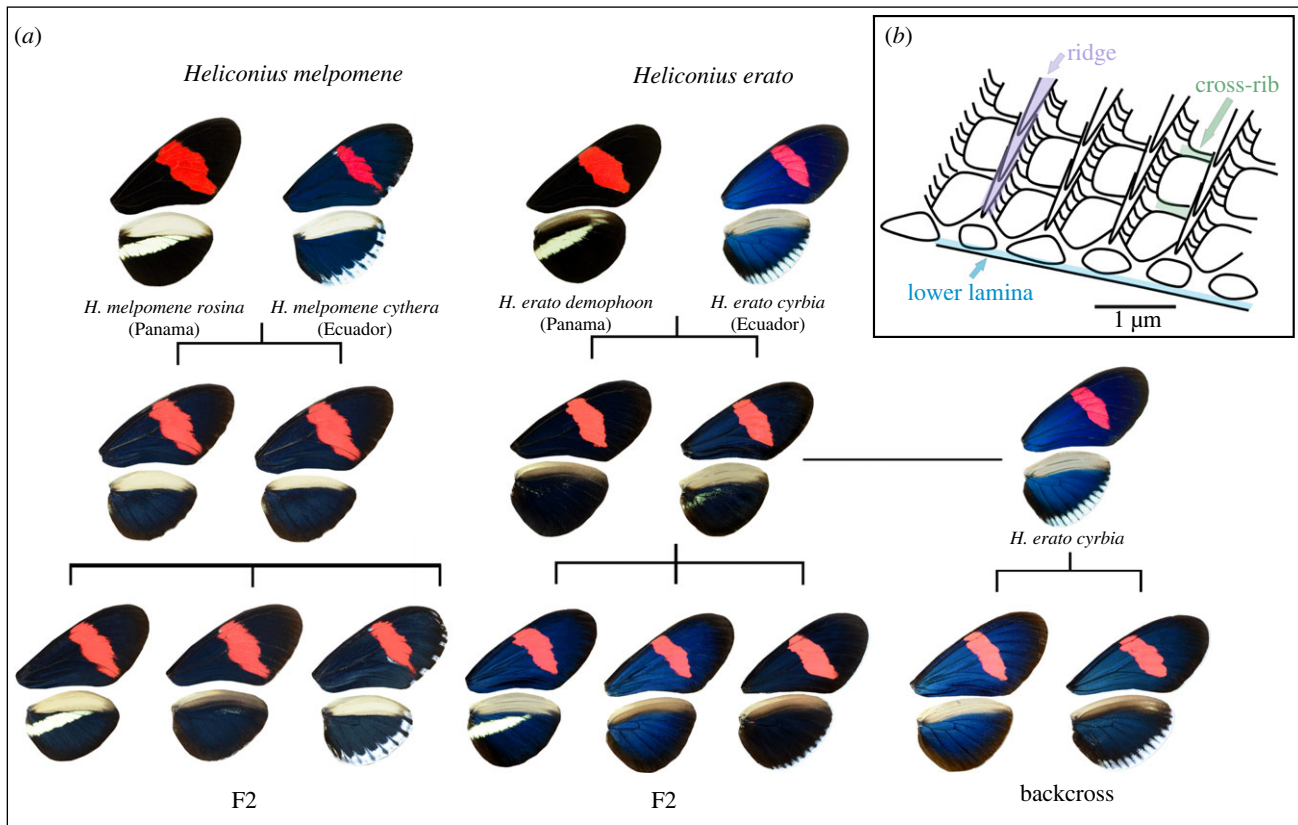


Figure 1. (a) Crosses between iridescent and non-iridescent morphs of *Heliconius melpomene* and *Heliconius erato*. For *H. melpomene*, we used F2 crosses, plus one cross thought to be F1 × F2 (not shown). For *H. erato*, we used F2 crosses and a backcross to the iridescent subspecies. (b) Schematic of part of a scale showing the lower lamina (blue) and upper longitudinal ridges (purple) connected by cross-ribs (green).

upper-scale surface has a more complex structure; it consists of a parallel array of ridges connected by cross-ribs, and modifications to these can yield diverse optical effects. For example, a lamellar structure in the ridges forms multi-layer reflectors that produce the iridescent (angle-dependent) blue in *Morpho* butterflies [13] and UV reflectance in *Colias eurytheme* [14,15]. The variations in hue and brightness of colour produced in the intricate structures of the upper-scale surface depend on an interplay between the number of lamellae, the thickness of each layer and the spacing between the ridges [16].

Recent studies have begun to uncover the genetic and developmental basis of structural colours in some species [9], revealing a common pattern in *Bicyclus anynana* and *Junonia coenia*; artificial selection for colourful phenotypes quickly resulted in changes in lower lamina thickness, and consequently hue, in a relatively small number of generations [10,12]. Knock-outs of known colour pattern genes [17], and genes involved in pigment synthesis pathways [18,19], have shown that modification of these can result in altered scale ultrastructure and, moreover, have brought about unexpected instances of the structural colour [18]. Interestingly, there are butterflies (*Junonia coenia*) for which the gene *optix*, a known major colour pattern gene [20], can jointly control pigment-based coloration and thickness of the lower lamina, producing blue structural colour [12]. Knock-outs of *optix* do not have an effect on structural colour in *Heliconius* [18]. Furthermore, the microevolutionary changes required for structural colour evolution are largely unknown.

Wing colour patterns have been widely studied in the *Heliconius* butterflies, a group of butterflies with a diverse set of aposematic colour patterns. These patterns show

examples of both convergent evolution between distantly related species and divergent evolution within species. Some species form mimicry rings, in which wing patterning is under strong positive frequency-dependent selection due to predation [21]. Pigment colour patterns are largely determined by a small number of genes that are homologous across species. Extensive research has uncovered a toolkit of five loci that control much of the colour pattern variation in *Heliconius* species and some other Lepidoptera [22]. *Heliconius* also display structural colour, and in comparison to the well-studied pigmentary colours, very little is known about the development and genetic basis of these. While overall scale morphology is similar between iridescent and non-iridescent scales in *Heliconius*, those with blue structural colour have overlapping ridge lamellae that act as multi-layer reflectors (as in *Morpho*), along with a greater density of ridges on the scale (narrower ridge spacing) [16,23].

Structural colour has evolved multiple times within the *Heliconius* genus [16]. In some species, all subspecies have iridescent colour, while others exhibit interspecific variation in iridescence. *Heliconius erato* and *Heliconius melpomene* are two co-mimicking species that diverged around 10–13 Mya [24], with each evolving around 25 different colour pattern morphs [25]. Most of the different colour patterns are produced by pigment colours, but subspecies found west of the Andes in Ecuador and Colombia also have an iridescent blue structural colour. *H. erato cyrbia* and *H. melpomene cythera* found in Western Ecuador have the brightest iridescence, while subspecies *H. erato demophoon* and *H. melpomene rosina*, found to the north in Panama, are matt black in the homologous wing regions (figure 1). A hybrid zone forms between the iridescent and

non-iridescent groups where they meet near the border between Panama and Colombia, and here, populations with intermediate levels of iridescence can be found [26]. Continuous variation in iridescent colour is observed in the centre of the hybrid zone and in experimental crosses [23], suggesting that this trait is controlled by multiple genes. The evolution of pigmentation and simple colour pattern traits has frequently been shown to involve the reuse of a small number of genes across animal species [22,27,28]. However, we may expect the genetic basis of a quantitative trait controlled by multiple genes, such as iridescence in these species, to be less predictable [29]. In addition, iridescence in *H. e. cyrbia* is much brighter than in *H. m. cythera* [16], suggesting some differences in scale structure and presumably genetic control of this structure formation process.

Here, we use crosses between subspecies of iridescent and non-iridescent *Heliconius* to determine the genetics of both colour and scale ultrastructure traits for the first time. We measure the intensity of blue colour and overall luminance (brightness) to assess variation in colour. We complement our estimates of colour variation with high-throughput measurements of ridge spacing and cross-rib spacing using ultra-small-angle X-ray scattering (USAXS). Using a quantitative trait locus (QTL) mapping approach, we can identify the location and effect sizes of loci in the genome that are controlling variation in iridescent colour. We then use RNA sequencing data from the same subspecies of each species to identify genes that are differentially expressed (DE), both between subspecies and between wing regions that differ in scale type. Comparison of the genetic basis of these traits between *H. melpomene* and *H. erato*, two distantly related mimetic species, allows us to ask whether, like pigment colour patterns, variation in iridescent colour and scale structure is also an example of gene reuse.

2. Methods

(a) Experimental crosses

Experimental crosses were performed using geographical morphs of both *Heliconius erato* and *Heliconius melpomene*. In both species, morphs from Panama (*H. e. demophoon* and *H. m. rosina*) were crossed with morphs from Western Ecuador (*H. e. cyrbia* and *H. m. cythera*), then the F1 generations crossed with each other to produce an F2. For *H. erato*, we also analysed a backcross between the F1 and *H. e. cyrbia* (figure 1). Due to a mix-up in the insectary, one of our largest *H. melpomene* broods, named 'EC70', was obtained from a cross between an F1 father and a mother of unknown parentage, likely an F2 individual. Further details of the crosses are in the electronic supplementary material, table S1. A total of 155 *H. erato* individuals from five broods were used to generate linkage maps and perform QTL mapping (3 *demophoon* and 3 *cyrbia* grandparents, 11 F1 parents and 40 backcross and 99 F2 offspring). For *H. melpomene*, data from four broods made up of 228 individuals were used (1 *rosina* and 2 *cythera* grandparents, 6 parents and 219 offspring, electronic supplementary material, table S1). Some of these crosses have previously been used for an analysis of quantitative pattern variation [30]. Details of sequencing and linkage map construction are given in Bainbridge *et al.* [30] and in the electronic supplementary material.

(b) Phenotypic measurements

In the offspring of these crosses, we measured four phenotypes—blue colour (BR), luminance, ridge spacing and cross-rib spacing.

Wings were photographed under standard lighting conditions (full details in [23]). A colour checker in each photograph was used to standardize the photographs using the levels tool in Adobe Photoshop (CS3). RGB values (red, green and blue) were extracted from two blue/black areas of each wing (proximal areas of both the forewing and hind-wing, electronic supplementary material, figure S1) and averaged. Blue-red (BR) values were used as a measure of blue iridescent colour. These were calculated as $(B - R)/(B + R)$, where 1 is completely blue and -1 is completely red. Luminance was measured as overall brightness and was calculated as $R + G + B$, with each colour having a maximum value of 255.

Scale structure measurements were extracted from USAXS data, from a single family of each species ($n = 56$ *H. erato* F2 and $n = 73$ *H. melpomene* (mother of unknown ancestry)). We measured between 33 and 113 points per individual along a linear proximo-distal path across the proximal part of the forewing, which has the most vivid iridescence in the blue subspecies (electronic supplementary material, figure S1). The raw images were corrected for dark current and spatial distortion. SEM data from a subset of individuals were used to interpret the scattering patterns and develop robust methods for extracting mean ridge and cross-rib spacing values for the dorsal wing scales of all individuals (see electronic supplementary material for details).

(c) Quantitative trait locus mapping

The R package R/qtl was used for the QTL analysis [31]. For *H. erato*, initially the F2 crosses were analysed together and the backcross analysed separately. Genotype probabilities were calculated for these two groups using *calc.genoprob* in R/qtl. We ran standard interval mapping to estimate LOD (logarithm of the odds) scores using the *scanone* function with the Haley-Knott regression method. In the F2 analysis, sex and family were included as additive covariates, and family was included as an interactive covariate, to allow multiple families to be analysed together. Sex was included as a covariate in the backcross analysis to account for any sexual dimorphism. To determine the significance level for the QTL, we ran 1000 permutations, with $perm.Xsp = T$ to get a separate threshold for the Z chromosome. A single F2 family ($n = 56$) was used to analyse scale structure variation (ridge spacing and cross-rib spacing) using the same method, albeit that a higher number of permutations was used for determining the significance level of the QTL (4000). For analyses of BR colour and luminance, LOD scores for the F2 crosses and the backcross were added together, to allow analysis of all individuals together to increase power, and the significance level recalculated in R/qtl.

Confidence intervals for the positions of QTL were determined with the *bayesint* function and we used a *fitqtl* model to calculate the phenotypic variance that each QTL explained. Genome scan plots and genotype plots were made with R/qtl2 [32]. Genetic distances in the QTL results are based on the observed recombination rate and expressed in centimorgans (cM), which is the distance between two markers that recombine once per generation. These were related to physical distances based on the marker positions in the assembled reference genome of each species. Where we discuss individual markers, these are the markers with the highest LOD scores in each QTL.

The same method was used to run genome scans for BR colour and luminance in *H. melpomene*. Since the parentage of the mother of the EC70 brood is unknown, the maternal alleles in the offspring could not be assigned as being from either a *cythera* or a *rosina* grandparent. Therefore, in this family, only paternal alleles were taken into account (and all maternal alleles were assigned to a *rosina* grandparent), and the cross was treated as if a backcross. LOD scores of the three F2 families were added to the LOD score from the EC70 family, as in *H. erato*, and the

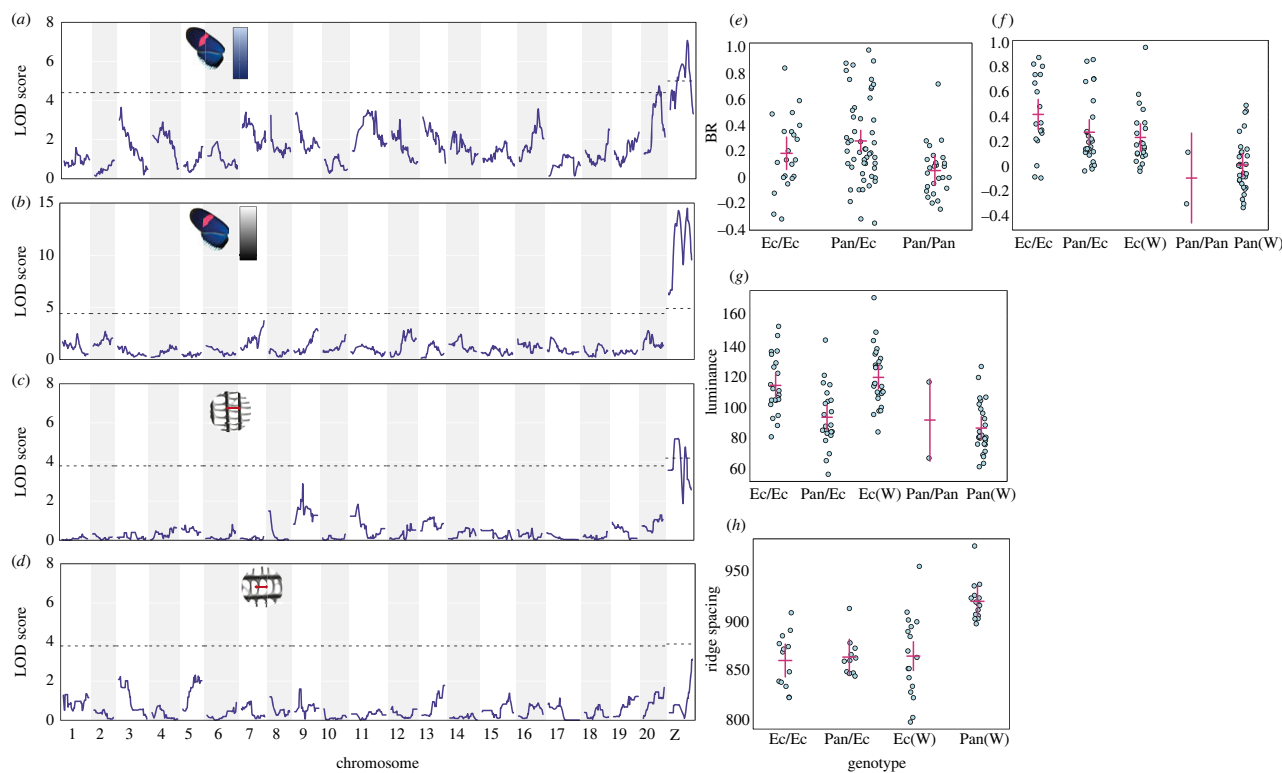


Figure 2. *H. erato* QTL analysis of all families for BR colour (a) and luminance (b), and for a single family for ridge spacing (c) and cross-rib spacing (d). Dotted lines show $p = 0.05$ significance level; (e–h) show the phenotypes of F2 individuals grouped by genotype at the most significant marker within each QTL ((e) top BR marker on chromosome 20; (f) top BR marker on Z; (g) top luminance marker on Z; (h) top ridge spacing marker on Z). ‘Pan’ denotes alleles from the Panama subspecies *demophoon*, and ‘Ec’ the Ecuador subspecies *cyrbia*. Only two individuals have homozygous Panama-type *demophoon* genotypes at the Z chromosome marker due to the small number of individuals with a *demophoon* maternal grandfather (electronic supplementary material, table S1). Points are individuals, red crosses show confidence intervals. Marker positions are shown in table 1.

significance level recalculated. Again, a single family was used for analysis of scale structures (EC70, $n = 73$).

(d) Gene expression analysis

RNA sequence data were generated from 32 *H. erato* pupal wing samples (16 *H. e. demophoon* and 16 *H. e. cyrbia*) and *H. melpomene* pupal wing samples (16 *H. m. rosina* and 16 *H. m. cythera*), with individuals sampled from the same captive populations as those used for the crosses. Each of these samples contained two wing regions (the anterior hind-wing or ‘androconial’ region, which has a different scale type, was dissected from the rest of the wing and sampled separately; electronic supplementary material, figure S1), and two developmental stages, 50% total pupation time (5 days post-pupation) and 70% total pupation time (7 days post-pupation). Overall this gave four biological replicates for each tissue type/developmental stage/subspecies combination (electronic supplementary material, table S2).

Quality-trimmed reads were aligned to the respective *Heliconius* reference genomes using HISAT2 (v. 2.1.0) (see <https://doi.org/10.1038/s41587-019-0201-4>). Clustering of samples by multidimensional scaling (MDS) on expression levels revealed that one of the *H. m. rosina* individuals had been incorrectly labelled (which was also confirmed by analysis of nucleotide variants) and this was removed from subsequent analyses. Each species was analysed separately to identify genes that were DE between subspecies and between the wing regions for the iridescent blue subspecies (electronic supplementary material, figure S1), using the quasi-likelihood F-test in R/Bioconductor package EdgeR (v.3.28.1) (see <https://doi.org/10.1093/bioinformatics/btp616>). For the wing region comparison, we used a general linear model approach, with the two wing regions nested within ‘individual ID’ for each individual. We then determined if any significantly DE genes (between subspecies or wing region)

were within the mapped QTL intervals. We further determined if any genes were DE in parallel between species. Details of further analyses of these data including gene set enrichment analysis are given in the electronic supplementary material.

3. Results

(a) Quantitative trait locus mapping in *Heliconius erato*

We found significant correlations between scale structure and colour measurements: ridge spacing is negatively correlated with both luminance and BR values (electronic supplementary material, figure S2). Cross-rib spacing is positively correlated with ridge spacing and also negatively correlates with BR values (electronic supplementary material, text). Significant QTL were found for three phenotypes in *H. erato*—BR colour, luminance and ridge spacing (figure 2, table 1; electronic supplementary material, table S3). When analysing the colour measurements, F2 and backcross genome scans were combined, and for BR values, these showed two significant QTL on chromosomes 20 and the Z sex chromosome. These QTL were also found when analysing the F2 broods separately from the backcross brood (electronic supplementary material, figure S3). At both markers, individuals with Panama-type genotypes (Pan/Pan and Pan(W)) had lower BR values than Ecuador-type and heterozygous genotypes, following the expected trend (figure 2). The QTL on the Z chromosome explained the largest proportion of the phenotypic variation in BR colour in both the F2 crosses (19.5%) and the backcross (24.6%), and the chromosome 20 QTL explained a further 12.3% in the F2 crosses.

Table 1. Significant QTL were found for three phenotypes in *H. erato* and *H. melpomene*.

phenotype	marker	chromosome	position (cM)	LOD	<i>p</i>
<i>Heliconius erato</i>					
BR colour (all families)	Herato2101_12449252	Z	38.0	7.07	0.001
	Herato2001_12633065	20	32.9	4.75	0.022
luminance (all families)	Herato2101_12449398	Z	41.6	14.50	<0.001
ridge spacing (single family)	Herato2101_7491127	Z	23.0	5.21	0.013
<i>Heliconius melpomene</i>					
BR (all families)	Hmel203003o_2119654	3	15.22	7.26	0.001
luminance (all families)	Hmel203003o_2635435	3	17.97	13.61	<0.001
ridge spacing (EC70)	Hmel207001o_11550301	7	53.61	5.71	<0.001

Luminance (overall brightness of the wing region) was highly associated with the Z chromosome (figure 2b). The significant marker did not map exactly to the same position as for the BR values but was apart by only 3.6 cM, and confidence intervals for each overlap. Individuals with Ecuador-type alleles had higher luminance values than those with Panama-type alleles, showing the same trend as the BR values (figure 2g). This QTL explained 40.2% of the variance in luminance values in the F2 crosses and 24.2% in the back-cross. This was the only significant QTL for luminance, with nothing appearing on chromosome 20.

A single QTL on the Z chromosome was also significant for ridge spacing (figure 2c). This marker was at a different position from the markers for BR and luminance, but mapped to the same marker as luminance when using the same individuals (electronic supplementary material, figure S3). All genotypes with one or two Ecuador-type alleles had similar ridge spacing, but those with a hemizygous Panama-type genotype ('Pan(W)' in figure 2h) had significantly wider ridge spacing. This QTL explained 34.8% of variance in ridge spacing in this family. No significant QTL were found for cross-rib spacing, although the highest LOD score was seen on the Z chromosome (figure 2d).

(b) Quantitative trait locus mapping in *Heliconius melpomene*

In contrast with *H. erato*, scale structure measurements in *H. melpomene* did not correlate with either of the colour measurements (supplementary material, figure S2, text). A single significant QTL for BR colour was found on chromosome 3 (figure 3a, table 1; electronic supplementary material, table S4) when combining the F2 families with EC70 (and for EC70 only; electronic supplementary material, figure S4). The marker explains 15.3% of phenotypic variation in EC70 (which should be an underestimate due to all maternal alleles being ignored) and 9.2% in the three F2 families. Luminance was also strongly associated with markers on chromosome 3 (figure 3b; electronic supplementary material, figure S4). The associated marker was 2.75 cM from the marker for BR colour, and the confidence intervals overlap. By contrast, for ridge spacing, we found a significant QTL on chromosome 7 (using just the EC70 brood), explaining 30.3% of variation (figure 3g). Again, no significant QTL were found for cross-rib spacing (figure 3d). These results were generally supported by a genome-wide association study

(GWAS) using all SNP variation (which allowed maternal variation in EC70 to be included) and did not reveal any additional loci (electronic supplementary material, figure S5, see electronic supplementary material for full results and methods).

Individuals with homozygous Panama-type genotypes at the mapped chromosome 3 markers had lower BR and luminance values (figure 3). Individuals carrying Ecuador-type alleles at the mapped chromosome 7 marker showed reduced ridge spacing, consistent with the observation that the Panama subspecies have greater ridge spacing.

(c) Differential expression

A total of 24 118 genes were expressed in the wings of *H. erato* and 30 721 in the wings of *H. melpomene*. In both *H. erato* and *H. melpomene*, MDS analysis of expression levels revealed strong clustering by stage (dimension 1) and subspecies (dimension 2), leading to four distinct clusters (electronic supplementary material, figure S6). Nine hundred and seven and 1043 genes were differentially expressed (DE) (false discovery rate (FDR) < 0.05) between *H. erato* subspecies at 50% and 70% development, respectively (electronic supplementary material, tables S5 and S6). In *H. melpomene*, 203 and 29 genes were DE between subspecies at 50% and 70% development, respectively (electronic supplementary material, tables S7 and S8). Much of this DE will be due to the genome-wide divergence between subspecies (which is greater in *H. erato* than in *H. melpomene*, [26]), we therefore used further comparisons to narrow down these lists of genes.

Comparing between wing regions, in iridescent *H. erato cyrba*, there was one gene at 50% and 70 genes at 70% DE (electronic supplementary material, tables S9 and S10); in iridescent *H. melpomene cythera*, there were six genes at 50% and 50 genes at 70% development DE (electronic supplementary material, tables S11 and S12). We may expect that genes involved in scale structure regulation would be DE both between subspecies and wing regions that differ in scale structure, but very few genes were found in both sets (electronic supplementary material, figure S7 and table S13). At 70%, there were two genes upregulated in *H. erato* in both comparisons: *chitin deacetylase 1* has a likely function in the deacetylation of chitin to chitosan and potential structural roles in the cuticle [33], and the other gene has similarity to the circadian clock-controlled gene *daywake*. There was no overlap in significant, downregulated genes expressed at 70% in *H. erato*. At 50% in *H. erato*, there were no significant,

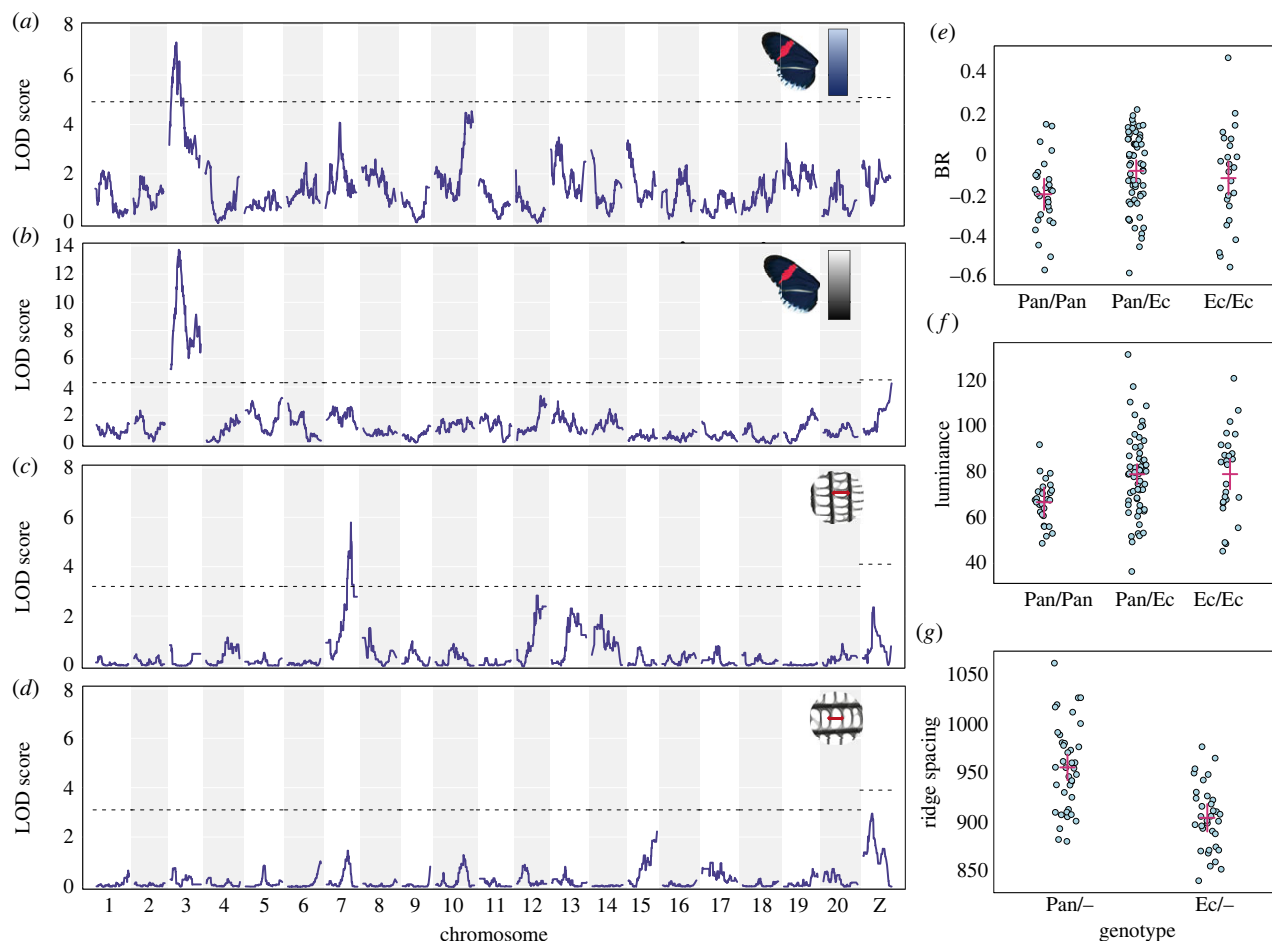


Figure 3. *Heliconius melpomene* QTL analysis of all families for BR colour (a) and luminance (b), and for a single family (EC70) for ridge spacing (c) and cross-rib spacing (d); (e–g) show the phenotypes of individuals grouped by genotype at the most significant marker within each QTL ((e) BR colour of F2 individuals by chromosome 3 marker genotype; (f) luminance of F2 individuals by chromosome 3 marker genotype; (g) Ridge spacing of EC70 brood individuals by chromosome 7 marker genotype). ‘Pan’ denotes alleles from the Panama subspecies *rosina*, and ‘Ec’ the Ecuador subspecies *cythera*. Points are individuals, red crosses show confidence intervals. Marker positions are shown in table 1.

concordantly DE genes. However, a *doublesex*-like gene on chromosome 8 narrowly missed the significance cut-off and was downregulated (Log fold change (FC) < -1.5) in both comparisons (FDR = 0.02 between subspecies, FDR = 0.08 between wing regions). In *H. melpomene*, at both 70% and 50%, there was no overlap between genes that were DE between subspecies and wing regions.

Genes involved in controlling scale structure may be similarly DE between species. Between subspecies, at 70%, there were no concordantly DE genes in either species. However, at 50%, there were two concordant genes significantly DE, *Fatty acid synthase* and *Gamma-glutamylcyclotransferase* (electronic supplementary material, table S14). For the wing region comparison, at 70%, there were four concordant genes significantly DE in both species: the homeobox gene *invected*, *Transglutaminase*, *uncharacterized LOC113401078* and the *doublesex*-like gene, which was also DE between *H. erato* subspecies (at 50%), but none at 50% (although the *doublesex*-like gene is again DE in *H. melpomene*; electronic supplementary material, table S14).

(d) Differentially expressed genes in the quantitative trait locus intervals

In order to identify candidate genes in the QTL intervals, we identified DE genes within these genomic regions. In general,

the QTL intervals were not significantly enriched for DE genes (based on expected numbers of DE genes for a given interval size; electronic supplementary material, table S15), suggesting that the QTL do not contain clusters of multiple functionally important genes. In *H. erato*, there were two and five DE genes in the ‘BR’ interval on chromosome 20 at 50% and 70% development, respectively (electronic supplementary material, table S15). One of the genes at 70% was *Fringe*, a boundary-specific signalling molecule that modulates the Notch signalling pathway and has roles in eyespot formation and scale cell spacing in butterflies [33,34].

On the Z chromosome, at 50%, there were 27, 25 and 17 genes significantly DE between subspecies in the ‘ridge spacing’, ‘luminance’ and ‘BR’ intervals, respectively, with 16 genes in the overlap of all three intervals (figure 4; electronic supplementary material, table S16). Of note, the microtubule motor protein, *dynein heavy chain 6* was within all three QTL intervals and highly upregulated (LogFC > 3.0, FDR < 0.05) in the iridescent subspecies. Additionally, an *O-GlcNAc transferase*, with strong similarity to *Drosophila* polycomb group gene *super sex combs* was highly DE (LogFC = -9.32, FDR < 0.004) and matched the exact physical location of the ‘BR’ and ‘luminance’ markers within the genome.

At 70%, on the Z chromosome, there were 24, 23 and 14 genes significantly DE in the ‘ridge spacing’, ‘luminance’ and ‘BR’ intervals, respectively, with 14 shared across all

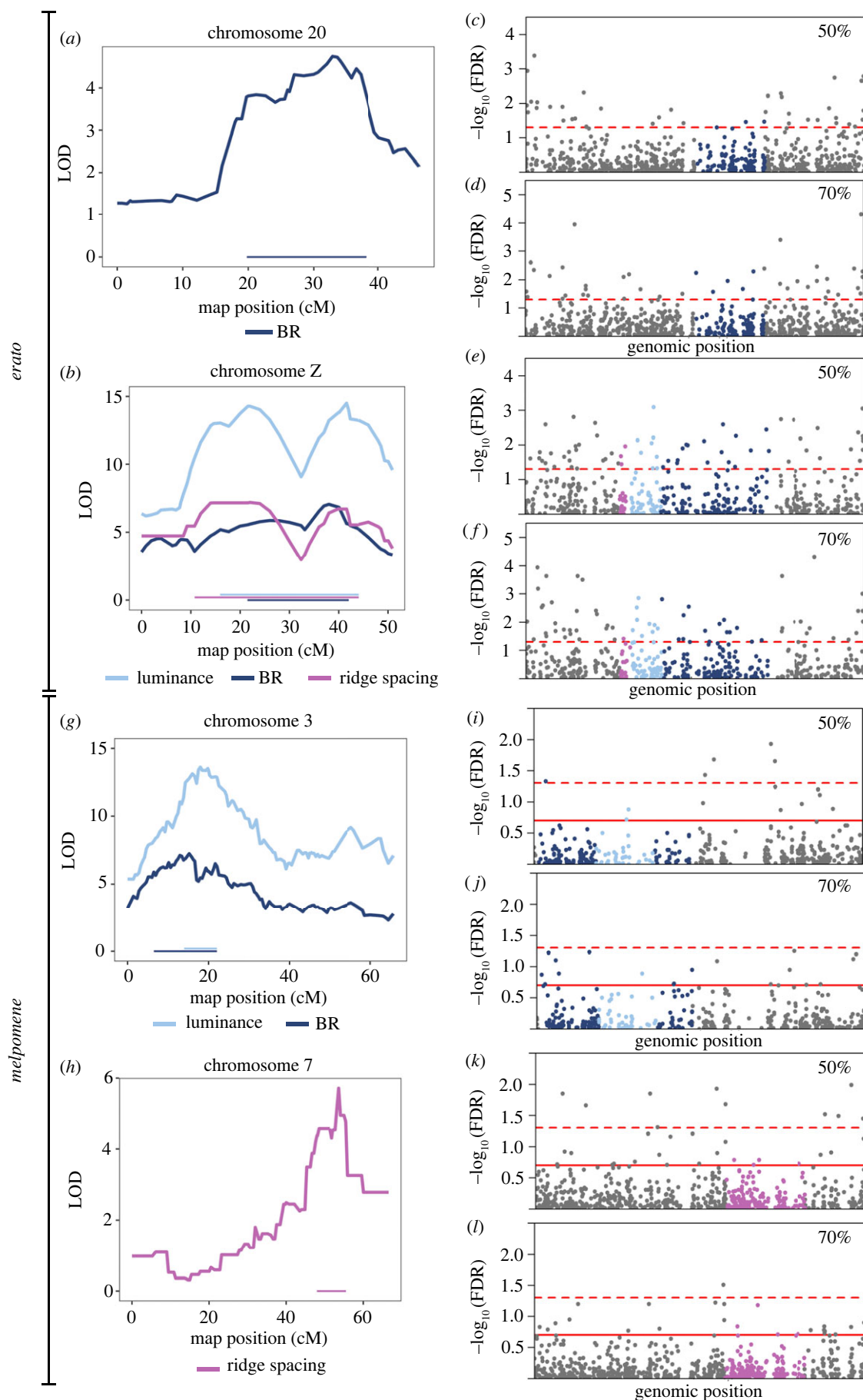


Figure 4. Differential expression of genes in the QTL in *Heliconius erato* (a–f) and *Heliconius melpomene* (g–l). LOD scores and QTL intervals in *H. erato* (a,b) and *H. melpomene* (g,h). $\log_{10}\text{FDR}$ for differential expression of all genes on the QTL-containing chromosomes for *H. erato* (c–f) and *H. melpomene* (i–l), with genes in the QTL coloured, matching those of the intervals in the panels on the left. In (e) and (f), the QTL overlap, such that all genes in the BR and ridge spacing intervals also fall within the luminance interval; see electronic supplementary material, table S16 for details. In (i) and (j) the luminance interval is within the BR interval. The dashed red lines indicate $\text{FDR} = 0.05$ (significance), solid red lines indicate $\text{FDR} = 0.2$.

three regions (electronic supplementary material, table S16). The gene *trio*, which functions in actin structure regulation through activation of Rho-family GTPases [33], was found in all three intervals with particular proximity to the ‘ridge spacing’ marker (405 kbp away from the start of this gene). In addition to the functional role of *trio*, its high expression and large fold change ($\log\text{CPM}=7.34$, $\text{LogFC}=-2.29$, $\text{FDR}=0.0015$) makes it a particularly good candidate for a role in optical nanostructure development in *H. erato*. Furthermore, a novel gene (*MSTRG.21985*) was also DE expressed ($\text{LogFC}=-1.28$, $\text{FDR}=0.0115$) and may be part of a Rho GTPase activating protein (182 bp upstream of a gene with this annotation).

In *H. melpomene*, there were no DE genes between subspecies in the ‘ridge spacing’ interval on chromosome 7 at either stage. However, at 70%, the gene *ringmaker*, which functions in microtubule organization [33], showed slight DE ($\log\text{FC}=-1.43$, $\text{FDR}=0.144$). On chromosome 3, in the BR interval, there was one novel gene (*MSTRG.3173*) DE at 50% (but this falls outside the luminance interval) and no DE genes at 70% (electronic supplementary material, table S17). The gene *miniature*, which in fly bristles is a component of the cuticulin envelope functioning in interactions between the depositing cuticle, membrane and cytoskeleton [35], falls in the overlap of the luminance and BR regions and shows slight DE at 50% ($\log\text{FC}=1.60$, $\text{FDR}=0.192$).

For the wing region comparison, in *H. erato*, there were no genes DE at either stage within any of the QTL intervals. For *H. melpomene*, there was one DE gene in the ‘BR’ interval (but outside the ‘luminance’ interval) on chromosome 3 at 70% (a *lactase-phlorizin hydrolase-like* gene) and no DE genes at 50%. For the ‘ridge spacing’ interval on chromosome 7, there was one DE gene at 50%, an *F-actin-uncapping protein* *LRRC16A* and one gene at 70%, a *cuticle protein 18.6-like* gene (electronic supplementary material, table S18).

4. Discussion

In one of the first studies to look at the genetics of structural colour variation in terms of both colour and structure, we show that the trait is controlled by multiple genes in the commimics *Heliconius erato* and *Heliconius melpomene*. While we found only a small number of QTL, these explain relatively little of the overall phenotypic variation, suggesting there are more loci that remain undetected. Some of these may be the genes that we detected as DE, but that fall outside the detected QTL intervals. Of particular interest are genes that we detected as DE both between subspecies and between wing regions that differ in scale type. *Chitin deacetylase 1* is one such candidate in *H. erato*, which is on chromosome 5 (not in a QTL interval). Chitin is the main component of the cuticle and the differential expression of a potential chitin-degrading gene could alter the formation of the scale ridges [36].

Within each species, we find that hue and brightness (BR and luminance) are controlled by loci on the same chromosomes. In *H. erato*, this was on the Z chromosome, confirming our previous phenotypic analysis [23], and in *H. melpomene*, on chromosome 3. An additional locus on chromosome 20 was also found to affect blue colour but not brightness in *H. erato*. The Z chromosome locus in *H. erato* appears to control ridge spacing, which could have

a direct effect on the brightness of the reflectance by increasing the density of reflective structures. Indeed, in the single-family analyses, luminance and ridge spacing mapped to exactly the same marker. However, the observed correlation between brightness and ridge spacing in *H. erato* may be a product of an unobserved association between tighter ridge spacing and other aspects of scale nanostructure, specifically the number of lamellae layers within the ridges. Theoretical analyses and simulations of the optical properties of multilayers have revealed that increasing the number of layers will result in a rapid increase of brightness; adding even a small number of layers produces a significant increase in the amount of reflected light [37]. Therefore, the Z chromosome locus may be affecting multiple aspects of scale structure, producing the observed correlations between the different colour and structure measurements. Indeed, some DE genes in the Z locus may control multiple aspects of scale structure. For example, *trio* acts in several signalling pathways to promote reorganization of the actin cytoskeleton through Rho GTPase activation. Its regulatory function may be repeatedly employed during scale development in the formation of different aspects of scale ultrastructure guided by the actin cytoskeleton. Interestingly, potentially related signalling genes, such as the novel gene located immediately before a Rho GTPase activating protein, also fall within this locus and are DE, potentially suggesting there are several functional genes linked together in this region.

By contrast, in *H. melpomene*, we found different loci controlling colour and ridge spacing, suggesting a more dispersed genetic architecture and different loci controlling different aspects of scale structure. We found strong evidence for a locus on chromosome 3 controlling BR and luminance, but this locus appeared to have no effect on our measurements of scale structure and so is likely controlling other aspects of scale structure not quantified here. Instead, we find a locus on chromosome 7 that partially controls ridge spacing. Combined with the lack of a correlation between ridge spacing and our colour measurements, it appears that ridge spacing has relatively little direct effect on colour in *H. melpomene*, despite the parental populations showing a similar difference in ridge spacing to that seen in *H. erato*. It appears that *H. erato* has a locus on the Z chromosome that can control multiple aspects of scale structure, while scale structure variations in *H. melpomene* involve mutations at loci dispersed around the genome. This could provide one explanation for how *H. erato* has been able to evolve brighter structural colour than that observed in *H. melpomene*, if single mutations in *H. erato* can have pleiotropic effects on multiple aspects of scale structure.

In contrast with many of the loci for pigment colour patterns that are homologous across multiple *Heliconius* species, the loci controlling iridescence in *H. erato* and *H. melpomene* appear to be largely different. Differences in the physical scale architecture and brightness of colour between the species perhaps make these genetic differences unsurprising [16,26]. A lack of genetic parallelism may also be more likely for a quantitative trait such as iridescence [29]. Nevertheless, on the Z chromosome in *H. melpomene*, we do observe elevated LOD scores in the QTL analysis and low *p*-value SNPs in the GWAS for both scale structure traits, but neither of the colour traits. This suggests that *H. melpomene* may have a locus homologous to that in *H. erato*, which is controlling some aspects of scale structure variation, but with apparently

little or no effect on colour variation. In addition, we find some genes that appear to show parallel expression patterns between species. Of particular interest is a *doublesex*-like gene that is DE between wing regions in both species and between *H. erato* subspecies. A different duplication of *doublesex* has been found to control structural colour in the Dogface butterfly (*Zerene cesonia*) [38], making this an interesting, potentially parallel candidate between species. It is possible that the evolutionary pathways may be different between species, but have triggered expression changes in similar downstream developmental pathways. However, we found very few genes that show concordant expression patterns between species.

In recent years, reverse genetics research has revealed a surprising connection between the molecular machinery underlying the development of pigmented wing patterns and the ultrastructure of butterfly scales in various species [17,18,39,40]. However, our QTL are not associated with any known colour pattern gene of large or small effect in *Heliconius* (*aristalless*, *WntA*, *vol*, *cortex* and *optix*—located on chromosomes 1, 10, 13, 15 and 18, respectively) [22]. Our findings show that *H. erato* and *H. melpomene* do not use the known molecular machinery of wing pattern production for sculpting specialized nanostructures and iridescent wings, and that the production of structural colour is completely decoupled from that of mimicry-related wing pattern regulation and pigment production.

Overall, we show major differences in the genetic basis of structural colour in *H. erato* and *H. melpomene*. Combining this with gene expression analyses, we have been able to identify novel candidate genes for the control of structural colour variation with potential functions in chitin metabolism, cytoskeleton formation, gene expression regulation and cell signalling.

Data accessibility. Genomic sequence data from the crosses are deposited in the European Nucleotide Archive under project no. PRJEB38330. RNA sequence data are deposited in the Gene Expression Omnibus (GEO) with series accession GSE190378. Photographs of all samples can be found at doi.org/10.5281/zenodo.3799188. USAXS data are

available at doi.org/10.5281/zenodo.5747416 and handling scripts at https://github.com/juanenciso14/butterfly_usaxs. Linkage maps with all phenotypic measurements and QTL scripts are available at github.com/mnbrien/Heliconius-iridescence.

The data and an abstract in Spanish are provided in the electronic supplementary material [41].

Authors' contributions. M.N.B.: data curation, formal analysis, investigation and writing—original draft; J.E.R.: data curation, formal analysis, investigation, methodology and writing—original draft; V.J.L.: data curation, formal analysis, investigation and writing—original draft; E.V.C.: investigation and writing—review and editing; A.J.P.: data curation, formal analysis, funding acquisition, investigation, methodology, project administration, resources, supervision and writing—review and editing; C.M.: investigation, resources and supervision; P.A.S.: investigation, methodology, project administration, resources, supervision and writing—review and editing; P.R.: data curation, formal analysis, methodology, software, supervision and writing—review and editing; T.Z.: data curation, investigation, methodology, project administration, resources and validation; N.J.N.: conceptualization, data curation, formal analysis, funding acquisition, investigation, methodology, project administration, resources, supervision, validation and writing—original draft.

All authors gave final approval for publication and agreed to be held accountable for the work performed therein.

Conflict of interest declaration. We declare we have no competing interests.

Funding. This work was funded by an Independent Research Fellowship (grant no. NE/K008498/1) to N.J.N. M.N.B.; E.V.C. and V.J.L. were funded by the NERC doctoral training partnership, ACCE (grant no. NE/L002450/1). J.E.R. was funded through the Leverhulme Centre for Advanced Biological Modelling as well as scholarships from Universidad del Rosario and the University of Sheffield. The scanning electron microscope is funded via a EPSRC 4CU grant (grant no. EP/K001329/1).

Acknowledgements. We thank the governments of Ecuador and Panama for permission to collect butterflies. Thanks to Darwin Chalá, Juan López and Gabriela Irazábal for their assistance with the crosses. We are grateful to the European Synchrotron Radiation Facility for the provision of X-ray beamtime under proposal LS2720, and to Andrew Dennison for assistance with USAXS data collection. We also thank Alexandre Thiery for his assistance with the differential expression analysis. Library preparation and sequencing were performed by staff at the Edinburgh Genomics Facility, at the University of Edinburgh. We thank Alan Dunbar for use of the scanning electron microscope.

References

- Silberglied RE, Taylor Jr OR. 1978 Ultraviolet reflection and its behavioral role in the courtship of the sulfur butterflies *Colias eurytheme* and *C. philodice* (Lepidoptera, Pieridae). *Behav. Ecol. Sociobiol.* **3**, 203–243. (doi:10.1007/BF00296311)
- Obara Y, Ozawa G, Fukano Y, Watanabe K, Satoh T. 2008 Mate preference in males of the cabbage butterfly, *Pieris rapae crucivora*, changes seasonally with the change in female UV color. *Zool. Sci.* **25**, 1–5. (doi:10.2108/zsj.25.1)
- Rutowski RL. 1977 The use of visual cues in sexual and species discrimination by males of the small sulphur butterfly *Eurema lisa* (Lepidoptera, pieridae). *J. Comp. Physiol.* **115**, 61–74. (doi:10.1007/BF00667785)
- Sweeney A, Jiggins C, Johnsen S. 2003 Insect communication: polarized light as a butterfly mating signal. *Nature* **423**, 31–32. (doi:10.1038/423031a)
- Kemp DJ, Rutowski RL. 2007 Condition dependence, quantitative genetics, and the potential signal content of iridescent ultraviolet butterfly coloration. *Evolution* **61**, 168–183. (doi:10.1111/j.1558-5646.2007.00014.x)
- Schultz TD. 2001 Tiger beetle defenses revisited: alternative defense strategies and colorations of two neotropical tiger beetles, *Odontocheila nicaraguensis* Bates and *Pseudoxysteira tarsalis* Bates (Carabidae: Cicindelinae). *Coleopt. Bull.* **55**, 153–163. (doi:10.1649/0010-065X(2001)055[0153:TBDRAD]2.0.CO;2)
- Kjærsmo K, Whitney HM, Scott-Samuel NE, Hall JR, Knowles H, Talas L, Cuthill IC. 2020 Iridescence as camouflage. *Curr. Biol.* **30**, 551–555. (doi:10.1016/j.cub.2019.12.013)
- Ghiradella H. 1991 Light and color on the wing: structural colors in butterflies and moths. *Appl. Opt.* **30**, 3492–3500. (doi:10.1364/AO.30.003492)
- Lloyd VJ, Nadeau NJ. 2021 The evolution of structural colour in butterflies. *Curr. Opin. Genet. Dev.* **69**, 28–34. (doi:10.1016/j.gde.2021.01.004)
- Wasik BR, Liew SF, Lilien DA, Dinwiddie AJ, Noh H, Cao H, Monteiro A. 2014 Artificial selection for structural color on butterfly wings and comparison with natural evolution. *Proc. Natl Acad. Sci. USA* **111**, 12 109–12 114. (doi:10.1073/pnas.1402770111)
- Stavenga DG, Leertouwer HL, Wilts BD. 2014 Coloration principles of nymphaline butterflies – thin films, melanin, ommochromes and wing scale stacking. *J. Exp. Biol.* **217**, 2171–2180. (doi:10.1242/jeb.098673)
- Thayer RC, Allen FI, Patel NH. 2020 Structural color in butterflies evolves by tuning scale lamina thickness. *eLife* **9**, e52187. (doi:10.7554/eLife.52187)
- Vukusic P, Sambles JR, Lawrence CR, Wootton RJ. 1999 Quantified interference and diffraction in

- single Morpho butterfly scales. *Proc. R. Soc. Lond. B* **266**, 1403–1411. (doi:10.1098/rspb.1999.0794)
14. Ghiradella H. 1974 Development of ultraviolet-reflecting butterfly scales: how to make an interference filter. *J. Morphol.* **142**, 395–409. (doi:10.1002/jmor.1051420404)
 15. Eisner T, Silberglied RE, Aneshansley D, Carrel JE, Howland HC. 1969 Ultraviolet video-viewing: the television camera as an insect eye. *Science* **166**, 1172–1174. (doi:10.1126/science.166.3909.1172)
 16. Parnell AJ *et al.* 2018 Wing scale ultrastructure underlying convergent and divergent iridescent colours in mimetic butterflies. *J. R. Soc. Interface* **15**, 20170948. (doi:10.1098/rsif.2017.0948)
 17. Concha C *et al.* 2019 Interplay between developmental flexibility and determinism in the evolution of mimetic *Heliconius* wing patterns. *Curr. Biol.* **29**, 3996–4009. (doi:10.1016/j.cub.2019.10.010)
 18. Zhang L, Mazo-Vargas A, Reed RD. 2017 Single master regulatory gene coordinates the evolution and development of butterfly color and iridescence. *Proc. Natl Acad. Sci. USA* **114**, 10 707–10 712. (doi:10.1073/pnas.1709058114)
 19. Matsuoka Y, Monteiro A. 2018 Melanin pathway genes regulate color and morphology of butterfly wing scales. *Cell Rep.* **24**, 56–65. (doi:10.1016/j.celrep.2018.05.092)
 20. Reed RD *et al.* 2011 *optix* drives the repeated convergent evolution of butterfly wing pattern mimicry. *Science* **333**, 1137–1141. (doi:10.1126/science.1208227)
 21. Mallet J, Barton NH. 1989 Strong natural selection in a warning-color hybrid zone. *Evolution* **43**, 421–431. (doi:10.1111/j.1558-5646.1989.tb04237.x)
 22. Nadeau NJ. 2016 Genes controlling mimetic colour pattern variation in butterflies. *Curr. Opin. Insect Sci.* **17**, 24–31. (doi:10.1016/j.cois.2016.05.013)
 23. Brien MN *et al.* 2018 Phenotypic variation in crosses shows that iridescent structural colour is sex-linked and controlled by multiple genes. *Interface Focus* **9**, 20180047. (doi:10.1098/rsfs.2018.0047)
 24. Kozak KM, Wahlberg N, Neild AFE, Dasmahapatra KK, Mallet J, Jiggins CD. 2015 Multilocus species trees show the recent adaptive radiation of the mimetic *Heliconius* butterflies. *Syst. Biol.* **64**, 505–524. (doi:10.1093/sysbio/syv007)
 25. Sheppard PM, Turner JRG, Brown KS, Benson WW, Singer MC, Smith JM. 1985 Genetics and the evolution of muellerian mimicry in *heliconius* butterflies. *Phil. Trans. R. Soc. Lond. B* **308**, 433–610. (doi:10.1098/rstb.1985.0066)
 26. Curran EV, Stankowski S, Pardo-Diaz C, Salazar C, Linares M, Nadeau NJ. 2020 Müllerian mimicry of a quantitative trait despite contrasting levels of genomic divergence and selection. *Mol. Ecol.* **29**, 2016–2030. (doi:10.1111/mec.15460)
 27. Manceau M, Domingues VS, Linnen CR, Rosenblum EB, Hoekstra HE. 2010 Convergence in pigmentation at multiple levels: mutations, genes and function. *Phil. Trans. R. Soc. B* **365**, 2439–2450. (doi:10.1098/rstb.2010.0104)
 28. Hubbard JK, Uy JAC, Hauber ME, Hoekstra HE, Safran RJ. 2010 Vertebrate pigmentation: from underlying genes to adaptive function. *Trends Genet.* **26**, 231–239. (doi:10.1016/j.tig.2010.02.002)
 29. Conte GL, Arnegard ME, Peichel CL, Schluter D. 2012 The probability of genetic parallelism and convergence in natural populations. *Proc. R. Soc. B* **279**, 5039–5047. (doi:10.1098/rspb.2012.2146)
 30. Bainbridge HE, Brien MN, Morochz C, Salazar PA, Rastas P, Nadeau NJ. 2020 Limited genetic parallels underlie convergent evolution of quantitative pattern variation in mimetic butterflies. *J. Evol. Biol.* **33**, 1516–1529. (doi:10.1111/jeb.13704)
 31. Broman KW, Wu H, Sen S, Churchill GA. 2003 R/qtl: QTL mapping in experimental crosses. *Bioinformatics* **19**, 889–890. (doi:10.1093/bioinformatics/btg112)
 32. Broman KW *et al.* 2019 R/qtl2: software for mapping quantitative trait loci with high-dimensional data and multiparent populations. *Genetics* **211**, 495–502. (doi:10.1534/genetics.118.301595)
 33. Thurmond J *et al.* 2018 FlyBase 2.0: the next generation. *Nucleic Acids Res.* **47**, D759–D765. (doi:10.1093/nar/gky1003)
 34. Reed RD, Serfas MS. 2004 Butterfly wing pattern evolution is associated with changes in a Notch/Distal-less temporal pattern formation process. *Curr. Biol.* **14**, 1159–1166. (doi:10.1016/j.cub.2004.06.046)
 35. Roch F, Alonso CR, Akam M. 2003 *Drosophila miniature* and *dusky* encode ZP proteins required for cytoskeletal reorganisation during wing morphogenesis. *J. Cell Sci.* **116**, 1199–1207. (doi:10.1242/jcs.00298)
 36. Yu R *et al.* 2016 Helicoidal organization of chitin in the cuticle of the migratory locust requires the function of the chitin deacetylase2 enzyme (LmCDA2). *J. Biol. Chem.* **291**, 24 352–24 363. (doi:10.1074/jbc.M116.720581)
 37. Kinoshita S, Yoshioka S. 2005 Structural colors in nature: the role of regularity and irregularity in the structure. *Chemphyschem* **6**, 1442–1459. (doi:10.1002/cphc.200500007)
 38. Rodriguez-Caro F *et al.* 2021 Novel *Doublesex* duplication associated with sexually dimorphic development of dogface butterfly wings. *Mol. Biol. Evol.* **38**, 5021–5033. (doi:10.1093/molbev/msab228)
 39. Fenner J *et al.* 2020 *Wnt* genes in wing pattern development of Coliadinae butterflies. *Front. Ecol. Evol.* **8**, 197. (doi:10.3389/fevo.2020.00197)
 40. Livraghi L *et al.* 2021 *Cortex cis*-regulatory switches establish scale colour identity and pattern diversity in *Heliconius*. *eLife* **10**, e68549. (doi:10.7554/eLife.68549)
 41. Brien MN *et al.* 2022 The genetic basis of structural colour variation in mimetic *Heliconius* butterflies. FigShare. (doi:10.6084/m9.figshare.c.5958667)